

UNIVERSIDAD DE GRANADA

PROGRAMA DE DOCTORADO EN QUÍMICA

FACULTAD DE CIENCIAS

DEPARTAMENTO DE QUÍMICA INORGÁNICA



TESIS DOCTORAL / Ph.D. THESIS

Materiales de óxido de metal / carbono como
 catalizadores para la eliminación de contaminantes

**Metal oxide/carbon materials as catalysts for the
 elimination of pollutants**

Hesham Ali Fahmy Abdalla Hamad

Granada, Noviembre 2018

Editor: Universidad de Granada. Tesis Doctorales
Autor: Hesham Hamad
ISBN: 978-84-1306-095-8
URI: <http://hdl.handle.net/10481/54774>

Materiales de óxido de metal / carbono como catalizadores
para la eliminación de contaminantes

**Metal oxide/carbon materials as catalysts for the
elimination of pollutants**

por / by

HESHAM ALI FAHMY ABDALLA HAMAD

Memoria presentada para aspirar al grado de Doctor por la Universidad de Granada

Fdo.: **Hesham Ali Fahmy Abdalla Hamad**

Directores de la Tesis / Supervisors

Prof. Dr. Francisco J. Maldonado Hódar,
Catedrático del Departamento de Química
Inorgánica, Universidad de Granada.

Prof. Dr. Agustín F. Pérez Cadenas, Profesor
Titular del Departamento de Química
Inorgánica, Universidad de Granada.

Dr. Sergio Morales Torres, Investigador de
Reincorporación – Plan Propio, Departamento
de Química Inorgánica, Universidad de
Granada.

Metal oxide/carbon materials as catalysts for the elimination of pollutants.

Tesis presentada para aspirar al grado de Doctor por

HESHAM ALI FAHMY ABDALLA HAMAD

Realizada bajo la dirección del Catedrático de Química Inorgánica Prof. Dr. Francisco J. Maldonado Hódar, del Prof. Dr. Agustín F. Pérez Cadenas y del Dr. Sergio Morales Torres, en la Facultad de Ciencias de la Universidad de Granada, y juzgada el día 9 de noviembre de 2018 en dicha Facultad, por el siguiente Tribunal:

PRESIDENTE:

Prof. Dr. Carlos Moreno Castilla, Catedrático de Química Inorgánica, Universidad de Granada.

VOCALES:

Profa. Dra. María Victoria López Ramón, Catedrática de Química Inorgánica, Universidad de Jaén.

Profa. Dra. Elena Pérez Mayoral, Profesora Titular, Universidad Nacional de Educación a Distancia, Madrid.

Dr. Fabián Suárez García, Científico Titular, Instituto Nacional del Carbón – CSIC, Oviedo.

SECRETARIA:

Dra. Luisa Pastrana Martínez, Investigadora *Ramón y Cajal*, Universidad de Granada.

Francisco J. Maldonado Hódar, Agustín F. Pérez Cadenas y Sergio Morales Torres como directores de la presente Tesis Doctoral, y el doctorando Hesham Ali Fahmy Abdalla Hamad

GARANTIZAN QUE

el trabajo ha sido realizado por el doctorando respetando los derechos de otros autores a ser citados cuando se han utilizado sus resultados o publicaciones.

Y para que conste a los efectos oportunos, en el cumplimiento de la legislación vigente, firmamos el presente certificado en Granada a 1 de octubre del 2018.

Prof. Dr. Francisco J. Maldonado Hódar,
Catedrático del Departamento de Química
Inorgánica, Universidad de Granada

Prof. Dr. Agustín F. Pérez Cadenas, Profesor
Titular del Departamento de Química
Inorgánica, Universidad de Granada.

Dr. Sergio Morales Torres, Investigador de
Reincorporación – Plan Propio, Departamento
de Química Inorgánica Universidad de
Granada.

Hesham Ali Fahmy Abdalla Hamad
B.Sc. in Special Chemistry
M.Sc. in Materials Science

"I am one of those who think that science has great beauty. A scientist in his laboratory is not just a technician: he is also a child placed before natural phenomena that impress him like a fairy tale "

Marie Curie

Nobel Prize in Physics, 1903, and Chemistry 1911.

"Specialization is the basis of excellence in the age of science"

Ahmed Zewail

Nobel Prize in Chemistry, 1999.

"The conscious mind is able to respect the idea even if it does not believe in it"

Naguib Mahfuz

Nobel Prize in Literature, 1988.

Acknowledgements.

*I would like to express my sincere thanks and profound gratitude to my Thesis directors, **Prof. Dr. Francisco J. Maldonado Hódar and Prof. Dr. Agustín Francisco Pérez Cadenas** for providing me the opportunity to pursue research in an area of great interest to me, suggestion this research project, devoting much of his precious time for supervising this work great support not only on a scientific level but also on a personal level, continuous encouragement understanding at every stage of my Ph.D. project, and careful reviewing of the Thesis.*

*I appreciate to my Thesis supervisor, **Dr. Sergio Morales Torres** for all the discussions we have had together, the good guidance they have given me throughout this project, the discerning supervision, encouragement, great support, giving me the strength and careful reviewing of the Thesis.*

*Deep thanks and sincere gratitude are extended to **Prof. Dr. Francisco Carrasco Marín**, for his guidance, encouragement during my project, and much of the work reflected here is due to his wise scientific advice. Without him, I didn't know my successful team work.*

*To **Prof. Dr. Carlos Moreno Castilla** for giving me the opportunity to do this Thesis in the Carbon Materials Research Group of the University of Granada, without forgetting the rest of the members of this group: José Rivera, Isa, M^a Ángeles, for allow me to integrate in the group easily and for the formidable environment we have in the group.*

*I feel very lucky for having had the opportunity to work in a highly cooperative group. It has been a pleasure to acknowledge **Dr. Esther Bailón García**, for her great help and efforts, especially in the work of black titania. Also, I wish to deep thank **Dr. Jose Vivo Vilches** and **Jesica Castelo Quibén** for continuous encouragement and support.*

I also want to thank all the people that I have met during these four years of work in the Adsorption and Catalysis Laboratory and that they have become more than friends. My fellow students Hakim, Maria, Adri, Abdallah, Mahmoud, David have all become the family of the carbon group, always supporting us in the face of difficulties and sharing large moments I do not want to forget all those who have spent their time in the laboratory and that have undoubtedly left their mark: Norberto, Beto Romero, Amra, Luis, Francesca, Karol, Carmen, Fran, Chris, Damaris, Camilo, Stefania Jorge Medina Valtierra, Adriana, Safa, Filipa and Alex. Special moments that you have given me.

*I wish also to express my thanks to **all members** of Inorganic Chemistry Department,*

Granada University, for their endless support during this work.

To the members of the Scientific Research Centre of the University of Granada, especially to María del Mar and Alicia (Technical specialists of TEM and SEM), Domingo and Pablo and Miguel A. Salas Peregrín (Technical specialist of DRS, TGA and DTP).

To all my friends from different countries that I met in Granada, for the good times that we have passed, Dr. Ahmed, Boubker, Ibrahim, Dr. Saied, Suhail, Biba, Boubker, Omar, Anas, Mouad, Mahmoud Hassan, Wael, Mahmoud, Mustapha, Ihab, Obid, Redwan, Dr. Mohamed Makhoulf, Ali, Dr. Osman and Dr. Rachid.

Special thanks to Dr. Tarek Younis for assistance in the structure of this Thesis.

*My deepest gratitude goes to **my family** for their unflagging love and support throughout my life.*

I would like to thank everybody who was important to the successful realization of my Thesis, as well as expressing my apology for every one that I unfortunately forgot to mention personally one by one.

Finally, Thanks for everyone who had taught me one day or still do and affect my life positively.

Hesham Hamad

November 2018

This Research Work has been funded by the Junta de Andalucía, through the RNM-172 Research Group and project P12-RNM-2892; and also by the Ministry of Economy and Competitiveness and FEDER funds through the Challenges Project CTQ2013-44789-R. Likewise, Hesham Hamad thanks the ERASMUS MUNDUS Program for the award of an Al Idrisi scholarship, Action 2.



To my spirit of my father

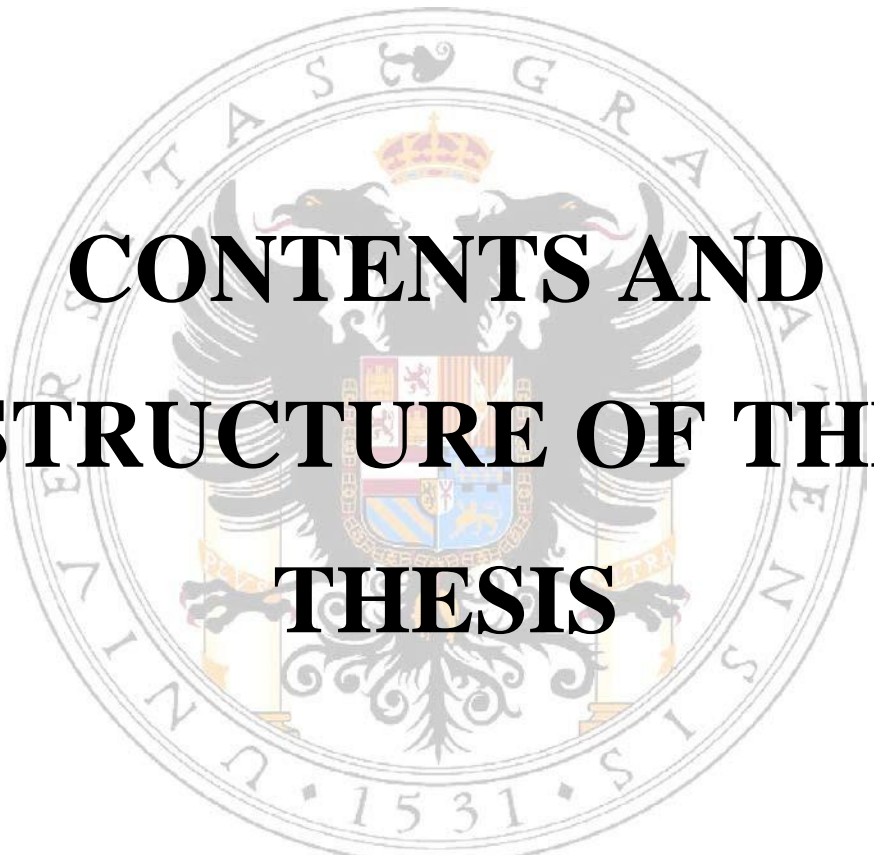
Much of the personality reflected here is due to his wise advice and morales. Without him, I didn't know my successful scientific path and descion making. I will never forget you and I always think of you, my father.

To my mother,

She is the greatest book I have read in my life. She is a school that I learnt from her the basis of values, love, sacrifice, compassion and tenderness.

To my sisters,

Thanks a lot for them for unflagging love and support throughout my life. I consider they are the most beautiful flowers in my garden.

The seal of the University of Granada is a circular emblem. It features a central shield with a crown on top, flanked by two lions. The shield is supported by two columns. The entire emblem is surrounded by a circular border containing the Latin text 'UNIVERSITAS GRANATAENSIS' and the year '1531' at the bottom.

**CONTENTS AND
STRUCTURE OF THE
THESIS**

In this Doctoral Thesis, the preparation of various series of photocatalysts based on titanium oxide is presented. Different approaches to improve the TiO₂ performance, including the preparation of composites with different composition and crystalline phase, and non-stoichiometric Ti-oxides are used. All these materials are exhaustively characterized and these properties are related with their potential as photocatalysts for the degradation of Orange G dye, which is used as a model of organic pollutant in an aqueous solution. All the photocatalytic results obtained with these innovative photocatalysts improve those obtained with commercial samples used as references.

This Doctoral Thesis has been developed in the Carbon Materials Research Group, Adsorption and Catalysis Laboratory, Inorganic Chemistry Department, University of Granada. The work developed during the realization of this Doctoral Thesis has been organized in different Chapters whose contents are the following:

Chapter I: Introduction and Objectives.

This chapter is devoted to the study of bibliographic review on the various types of titania composites for photocatalytic application and the state of the art of the alternative strategies for improving the photocatalytic activity. It begins with the literature review of the photocatalytic degradation of organic pollutants and the types of materials that used for this application is presented together with the physicochemical characteristics of the material used. Also, clarifying the importance and need to obtain solar – light – driven photocatalysts, the difficult that photocatalytic reaction implies and the possible strategies to obtain the target goals. Finally, the objectives of the work are described.

Chapter II: Materials and Methods.

This chapter described the preparation of the different materials developed in this Thesis, the used characterization techniques, and the experimental conditions of photocatalytic procedures and analysis used in chapters III, IV, V and VI.

Chapter III: Physicochemical properties of new cellulose-TiO₂ composites for the removal of water pollutants: Developing specific interactions and performances by cellulose functionalization (published in *Journal of Environmental Chemical Engineering*).

This chapter deals with the preparation of novel sustainable and green cellulose-titania hybrid composites with enhanced photocatalytic performance. The interaction of cellulose and Ti-precursors is initially too low due to the closed microcrystalline cellulose structure. For that, the synthetic strategy involves two determinant steps: (i) dissolution of MCC by acid treatments using HNO_3 or H_3PO_4 and (ii) TiO_2 impregnation by a single-step sol-gel method. We deeply study the influence of the both acids treatments on the properties (porosity, composition, crystalline structure, etc) of the corresponding cellulose – TiO_2 composites and the interactions between phases, which are a function of the nature of the surface groups generated on the cellulose structure during each acid treatment. These physicochemical and crystalline properties are correlated with the photocatalytic performance of the samples.

Chapter IV: Novel carbon-Ti composites based on functionalized cellulose for photocatalytic water decontamination.

In this work, carbon-Ti hybrid composites are obtained by carbonization of materials prepared in the previous Chapter III. Microcrystalline cellulose (MCC) works as structure-directing agent and carbon precursor to tailor the physicochemical properties and interactions between both phases. The chemical functionalization of the cellulose chains with phosphorous- or oxygen-containing surface groups strongly determines the morphological, chemical, porous and crystalline transformations during carbonization. The novel poly-hierarchical structured $\text{TiP}_2\text{O}_7/\text{carbon}$ or $\text{TiO}_2/\text{carbon}$ hybrid composite are obtained respectively from the MCC pretreated with H_3PO_4 or HNO_3 , by a facile single-step in situ sol-gel method and subsequent carbonization at different temperatures. To the best of our knowledge, the role of cellulose chemical functionalities on the characteristics of carbon-Ti composites and their photocatalytic performance has not been explored. Here, a deep analysis of chemical, crystalline, porous and morphological transformations of each composite as a function of the carbonization temperature, as well as a correlation with its photocatalytic performance is investigated.

Chapter V: On the interactions and synergism between phases of carbon–phosphorus–titanium composites synthesized from cellulose for water treatment (published in *Materials*).

Taking into account the results obtained in Chapter IV, a deep analysis on the transformation of the system cellulose-phosphorus-Titania during carbonization was carried out in this Chapter. For that, a series of samples with different Ti-precursor/functionalized cellulose ratio was designed and prepared. The physicochemical properties, including the nature of the titanium polyphosphate formed, and evidently, the photocatalytic performance is strongly influenced by this ratio.

Chapter VI: Synthesis of Ti_xO_y nanocrystals in mild synthesis conditions for the degradation of pollutants under solar light (published in *Applied Catalysis B: Environmental*)

This work presents an alternative of synthesis to obtain non-stoichiometric black titania nanoparticles (Ti_xO_y) with controlled morphology in mild conditions. Titania nanoparticles and nanofibers were synthesized at temperature of 180 °C and pressure of 8 bar by a stirred solvothermal method in presence of nitrogen, or hydrogen, for improving the visible and infrared optical absorption. Black titania was deeply characterized and tested in the photodegradation of pollutants under solar light.

*Part of the results of the research work has been already published during the development of this Thesis that is included in the following dissemination **articles**:*

1. Hesham Hamad, Esther Bailón-García, Sergio Morales-Torres, Francisco Carrasco-Marín, Agustín F. Pérez-Cadenas, Francisco J. Maldonado-Hódar, "*Physicochemical properties of new cellulose-TiO₂ composites for the removal of water pollutants: Developing specific interactions and performances by cellulose functionalization*", Journal of Environmental Chemical Engineering, 2018, Vol. 6, pp. 5032-5041. doi: [10.1016/j.jece.2018.07.043](https://doi.org/10.1016/j.jece.2018.07.043).
2. Hesham Hamad, Jesica Castelo-Quiben, Sergio Morales-Torres, Francisco Carrasco-Marín, Agustín F. Pérez-Cadenas, Francisco J. Maldonado-Hódar, "*On the interactions and synergism between phases of carbon-phosphorus-titanium composites synthesized from cellulose for water treatment*", Materials, 2018, Vol. 11(9), pp.1766-1776. doi: [10.3390/ma11091766](https://doi.org/10.3390/ma11091766).
3. Hesham Hamad, Esther Bailón-García, Sergio Morales-Torres, Francisco Carrasco-Marín, Agustín F. Pérez-Cadenas, Francisco J. Maldonado-Hódar, "*Functionalized*

cellulose as biotemplate in the synthesis of carbon-Ti composites for photocatalytic water decontamination", In progress.

4. Hesham Hamad, Esther Bailón-García, Francisco Carrasco-Marín, Agustín F. Pérez-Cadenas, Francisco J. Maldonado-Hódar, "Synthesis of Ti_xO_y nanocrystals in mild synthesis conditions for the degradation of pollutants under solar light", Applied Catalysis B: Environmental, 2019, Vol. 241, pp. 385-392. doi: [10.1016/j.apcatb.2018.09.016](https://doi.org/10.1016/j.apcatb.2018.09.016).
5. Hesham Hamad, Esther Bailón-García, Sergio Morales-Torres, Francisco Carrasco-Marín, Agustín F. Pérez-Cadenas, Francisco J. Maldonado-Hódar, "New insights and perspectives into the progress of cellulose nanocrystals to fabricate hybrid titania photocatalysts: Understanding mechanisms and future trends ", In progress.

*The most relevant results of this Thesis have been also presented at the following **national and international conferences**:*

1. Hesham Hamad, Esther Bailón-García, Francisco J. Maldonado-Hódar, Francisco Carrasco-Marín, Agustín F. Pérez Cadenas, "Photo-catalysts hybrid cellulose- TiO_2 : Effect of pre-treatment of solubilization of cellulose", Poster at SECAT 2017, Oviedo, Spain, 26-28 June 2017.
2. Hesham Hamad, Esther Bailón-García, Agustín F. Pérez Cadenas, Francisco Carrasco-Marín, Francisco Jose Maldonado-Hódar, "Sol-Gel synthesis and photocatalytic performance of Ti / Zr coated carbon microspheres highly active under visible light irradiation", Poster at 19th International Sol-Gel Conference, Liege, Belgium, 3-8 September 2017.
3. Hesham Hamad, Agustín F. Pérez Cadenas, Francisco Carrasco-Marín, Francisco Jose Maldonado-Hódar, Sergio Morales-Torres, Esther Bailón-García, "Cellulose derivatives- TiO_2 composites for the photocatalytic degradation of dyes in water", Oral Presentation at XIV Reunión del GEC, Malaga, Spain, 22-25 October 2017.
4. Hesham Hamad, Esther Bailón-García, Sergio Morales-Torres, Francisco Carrasco-Marín, Agustín F. Pérez-Cadenas, Francisco J. Maldonado-Hódar, "Novel carbon-Ti composites based on functionalized cellulose for photocatalytic water decontamination", Poster at Carbon 2018, The World Conference of Carbon, Madrid, Spain, 1-6 July 2018.

5. Hesham Hamad, Esther Bailón-García, Sergio Morales-Torres, Francisco Carrasco-Marín, Agustín F. Pérez-Cadenas, Francisco J. Maldonado-Hódar, "*New Photocatalysts for water decontamination prepared from functionalized cellulose*", Poster at XXVI Congreso Iberoamericano de Catálisis (CICat 2018), Coimbra, Portugal, 9-14 September 2018.

The doctoral student has also finished the following courses:

1. "*Web of Science*" Advanced Level- 1- Edition, Organization by FECYT, In Collaboration with Library of University of Granada, 14 may 2015.
2. "*Tools for the development of research*", Collaboration between Library of University of Granada and International School of postgraduate for doctoral students (Science, Technology and Engineering), 9-11 February 2016.
3. "*Writing a research paper in English: strategies and techniques*", Doctoral School of Sciences, Technologies and Engineering, Granada University, 2-11 March 2016.
4. "*Characterization techniques*", Doctoral Program in Chemistry, University of Granada, 11-13 July 2016.
5. "*Theoretical training - practical basic level of mercury porosimetry*", Specific Instrumentation of Materials (IESMAT), Quantachrome Instrument, 18 October 2016.
6. "*Course of LaTeX y Git*", Doctoral School of Sciences, Technologies and Engineering, University of Granada, 16 hours, November 2017.

INDEX

CONTENTS AND STRUCTURE OF THE THESIS	i-v
CHAPTER I – INTRODUCTION AND OBJECTIVES	1
1.1. PHOTOCATALYSIS FOR WATER TREATMENT.	3
1.1.1. PHOTOCATALYSIS.....	3
1.1.2. TiO ₂ AS A PHOTOCATALYST.	3
1.1.3. MECHANISM OF THE TiO ₂ PHOTOCATALYSIS.	4
1.1.4. DISADVANTAGES OF THE TiO ₂ PHOTOCATALYSIS.....	9
1.1.5. MODIFICATION OF TiO ₂ PHOTOCATALYSTS.	9
1.2. TiO ₂ / CELLULOSE HYBRID NANOCOMPOSITE.....	10
1.2.1. MOLECULAR STRUCTURE OF CELLULOSE.....	10
1.2.2. SUPERMOLECULAR STRUCTURE OF CELLULOSE.....	13
1.2.3. NANOCELLULOSE.	16
1.2.4. DISSOLUTION MECHANISMS OF CELLULOSE: MACROSCOPIC ASPECTS.....	20
1.2.5. CHEMICAL MODIFICATION OF CELLULOSE NANOCRYSTALS.	22
1.2.6. MODIFICATION OF PHOTOCATALYTIC TiO ₂ BY CELLULOSE FOR FORMATION HYBRID MICROCOMPOSITES.....	41
1.2.7. PHOTOCATALYTIC DECOMPOSITION BY TiO ₂ / CELLULOSE.....	49
1.3. BLACK TITANIA.	51
1.4. OBJECTIVES OF THE THESIS.....	52
1.5. REFERENCES.....	53
CHAPTER II – MATERIALS AND METHODS	67
2.1. CHEMICALS.	69
2.2. SYNTHESIS OF PHOTOCATALYSTS.	69
2.2.1. CELLULOSE - TiO ₂ COMPOSITES.	69
2.2.2. CARBON-TITANIUM COMPOSITES.	70
2.2.3. CARBON–PHOSPHORUS–TITANIUM COMPOSITES.	70
2.2.4. BLACK TITANIA NANOCRYSTALS.	71
2.3. CHARACTERIZATION TECHNIQUES.	71
2.3.1. MORPHOLOGICAL CHARACTERIZATION.	72
2.3.2. X-RAY DIFFRACTION (XRD).	73
2.3.3. X-RAY PHOTOELECTRON SPECTROSCOPY (XPS).	73
2.3.4. FOURIER TRANSFORM INFRARED SPECTROSCOPY (FTIR).	74
2.3.5. THERMOGRAVIMETRIC ANALYSIS (TGA).	74
2.3.6. TEMPERATURE PROGRAMMED DESORPTION (TPD).	74
2.3.7. PHYSICAL ADSORPTION OF NITROGEN.....	74
2.3.8. DIFFUSE REFLECTANCE SPECTROSCOPY (DRS).	75
2.4. PHOTOCATALYTIC EXPERIMENTS.....	75
2.5. REFERENCES.....	77
CHAPTER III - PHYSICAL PROPERTIES OF NEW CELLULOSE-TiO₂ COMPOSITES FOR THE REMOVAL OF WATER POLLUTANTS: DEVELOPING SPECIFIC INTERACTIONS AND PERFORMANCES BY CELLULOSE FUNCTIONALIZATION. 79	
3.1. MATERIALS AND METHODS.	81
3.1.1. SYNTHESIS AND CHARACTERIZATION OF THE MATERIALS.....	81
3.1.2. PHOTOCATALYTIC EXPERIMENTS.....	82
3.2. RESULTS AND DISCUSSION.....	82
3.3. CONCLUSIONS.	97
3.4. REFERENCES.....	98

CHAPTER IV- TAILORED CARBON-TITANIUM COMPOSITES FROM FUNCTIONALIZED CELLULOSE: ASSESSMENT OF THE NANOSTRUCTURE AND PHOTOCATALYTIC EFFICIENCY..... 103

4.1.	ABSTRACT.	105
4.2.	EXPERIMENTAL.	105
4.2.1.	SYNTHESIS AND CHARACTERIZATION OF CARBON-TI COMPOSITES.....	105
4.2.2.	PHOTOCATALYTIC TESTS.....	106
4.3.	RESULTS AND DISCUSSION.	106
4.3.1.	MATERIALS CHARACTERIZATION.....	106
4.3.2.	REMOVAL OF ORANGE-G (OG) AZO-DYE	120
4.4.	CONCLUSIONS.	122
4.5.	REFERENCES.....	123

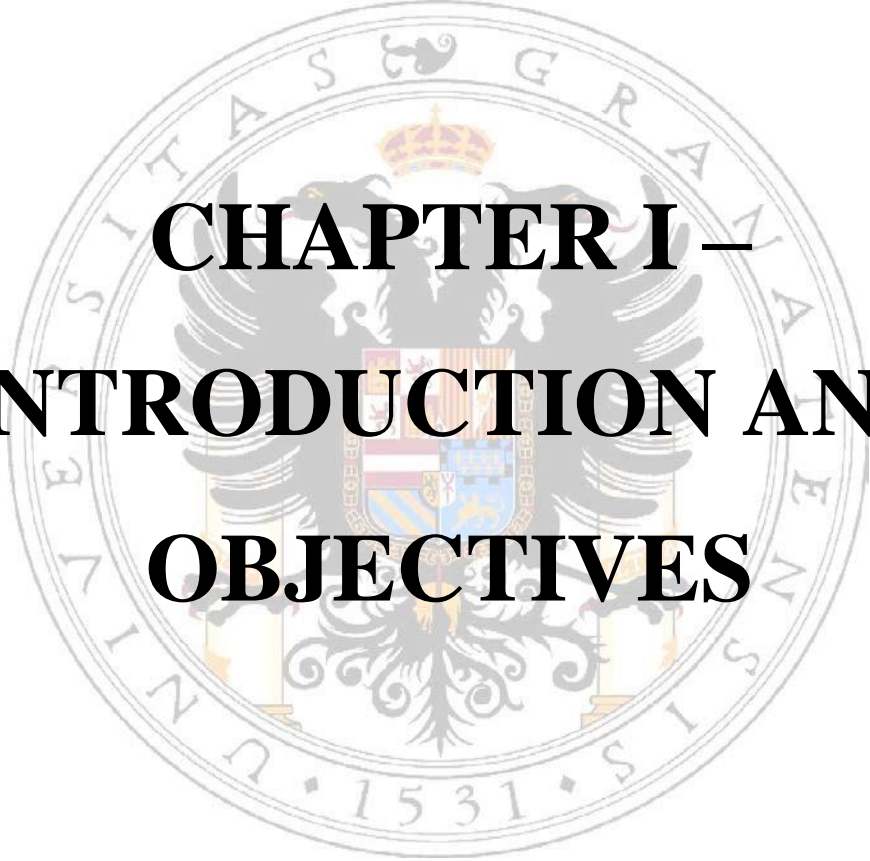
CHAPTER V - ON THE INTERACTIONS AND SYNERGISM BETWEEN PHASES OF CARBON-PHOSPHORUS-TITANIUM COMPOSITES SYNTHETIZED FROM CELLULOSE FOR THE REMOVAL OF THE ORANGE-G DYE 127

5.1.	MATERIALS AND METHODS.....	129
5.2.	RESULTS AND DISCUSSION.	130
5.3.	CONCLUSIONS	138
5.4.	REFERENCES.....	138

CHAPTER VI - SYNTHESIS OF Ti_xO_y NANOCRYSTALS IN MILD SYNTHESIS CONDITIONS FOR THE DEGRADATION OF POLLUTANTS UNDER SOLAR LIGHT 141

6.1.	MATERIALS AND METHODS.....	143
6.1.1.	SYNTHESIS AND CHARACTERIZATION OF BLACK TITANIA.	143
6.1.2.	PHOTOCATALYTIC DEGRADATION PROCEDURE IN PRESENCE OF SATURATED PHOTOCATALYSTS.....	144
6.2.	RESULTS AND DISCUSSION.	144
6.2.1.	TEXTURAL AND CHEMICAL CHARACTERIZATION.....	144
6.2.2.	PHOTOCATALYTIC ACTIVITY.....	153
6.3.	CONCLUSIONS.	156
6.4.	REFERENCES.....	157

CHAPTER VII - GENERAL CONCLUSIONS..... 159

The seal of the University of Granada is a circular emblem. It features a central shield with a crown on top, flanked by two lions. The shield is surrounded by a decorative border. The text 'UNIVERSITAS GRANADENSIS' is written around the top and sides of the circle, and '1531' is at the bottom. The seal is rendered in a light, faded style.

**CHAPTER I –
INTRODUCTION AND
OBJECTIVES**

1.1. Photocatalysis for water treatment.

Air, water, and sunlight are three basic elements for people to live on earth. As a result of the destructive nature of mankind, both water and air systems are highly contaminated. Nowadays, the wastewater of textile dyeing and finishing factories causes various environmental problems, due to its huge quantity of poisonous organic pollutants, to the large degree of aromatics present in dyes, high stability and high consumption water in this industry [1]. The dye pollutants in water causing the releasing toxic, and potential carcinogenic substances.

1.1.1. Photocatalysis.

In recent years, photocatalysis has also been actively used in environmental applications, since the semiconductor can be photoexcited to form electron-donor sites (reducing sites) and electron-acceptor sites (oxidizing sites). Photocatalytic destruction of organic contaminants like textile dyes has several important advantages rendering it an attractive process for the treatment of aqueous and gaseous wastes [2]. **First**, the reaction is nonspecific capable of degrading / destroying wide variety of organic molecules. This advantage is not available in biological processes in which organic degradation are dependent upon compound-specific enzymes. **Second**, photocatalytic reaction is immune to organic toxicity. Therefore, the process can be used to treat high strength wastes without any concern of process inhibition or upset. **Third**, the rate of photocatalytic oxidation is very fast; thereby, a high throughput is possible even for high strength wastes. **Fourth**, the reaction is so powerful that organic molecules are often destroyed completely, or mineralized, leaving no intermediates beside without forming polycyclic products. **Fifth**, the agent of treatment (UV and catalyst) can be removed easily leaving no residues in the effluent. **Finally**, highly active catalyst adaptable to specially designed reactor system.

1.1.2. TiO₂ as a photocatalyst.

The photocatalytic splitting of water into hydrogen and oxygen under ultraviolet (UV) irradiation on TiO₂ electrodes was discovered by Fujishima and Honda in 1972 [3]. TiO₂ is the most UV active photocatalyst, followed by ZnO, since TiO₂ is highly stable chemically, and highly oxidizing. Other metal oxides, such as ZrO₂, SnO₂, WO₂, and MoO₃ are much

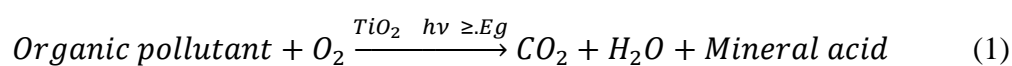
less active and do not have the same application prospects as TiO₂. In addition, TiO₂ is relatively inexpensive compared to others [4]. The advantages of using TiO₂ photocatalysts in drinking water include [2-4]:

- 1- Readily available and relatively inexpensive.
- 2- Highly stable in a broad range of pH and no addition of other chemicals.
- 3- Requirement of mild reaction conditions, non-toxic and resistance to the corrosion.
- 4- Little or no inhibitory effects by common water ions.
- 5- Strong oxidative and reductive potentials at the TiO₂ surface may lead to simultaneous oxidation and reduction of organic species.
- 6- Lower disinfectant dosages compared to traditional water treatment methods, which require massive usage of chemicals like chlorine.
- 7- Trace organics such as pesticides, hydrocarbons, chlorinated hydrocarbons, and taste and odour compounds may be mineralized.
- 8- Pathogenic bacteria can be removed by photocatalytic reactions.
- 9- Solar activation of the catalyst may be possible, (there is a small UV portion in solar energy, which can be utilized to trigger photocatalytic reactions).
- 10- The TiO₂ photocatalytic process is characterized by high reaction rates and short treatment times due to rapid oxidation reactions by hydroxyl radicals.

1.1.3. Mechanism of the TiO₂ photocatalysis.

a) Electron – hole generation.

When a photocatalyst such as TiO₂ is irradiated with light of sufficient energy equal to or larger than photocatalyst band gap ($h\nu \geq E_g$), an electron is excited from valence band (VB) to conduction band (CB), leaving an electron vacancy (“hole”) in VB. The holes generated are very oxidative, so they can directly attack and oxidize substrate molecules, or can oxidize hydroxyl groups into hydroxyl radical; electron-hole pair generated is capable of participating in chemical reactions with adsorbed molecules. The photocatalytic decomposition reaction can be summarized in equation 1. A schematic overview of the photocatalytic mechanism is depicted in Figure 1.1 [6].



The key of photocatalysis is the electron-hole pair. According to Mills, in order to

photoreduce a chemical species, the CB of the semiconductor must be more negative than the reduction potential of the chemical species; to photo-oxidize a chemical species, the potential of VB of the semiconductor must be more positive than the oxidation potential of the chemical species [7]. The VB hole is an excellent oxidant (+1.0 to +3.5 V versus the normal hydrogen electrode (NHE) depending on pH and the oxide) compared to the smaller reducing capability of the CB electron (+0.5 to -1.5 V vs. NHE).

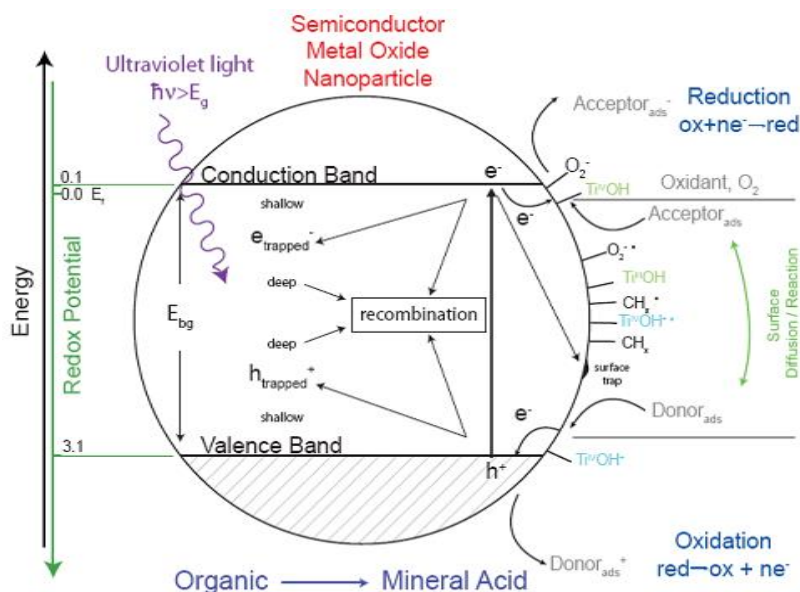


Figure 1.1. Schematic representation of photocatalytic reaction over a semiconductor nanoparticle [7].

In a photocatalytic reaction, the rate of oxidation by the holes or hydroxyl radicals must be balanced by the rate of reduction by the electrons. Figure 1.2 depicts the band structures of several oxides relative to the NHE at pH = 1.0 and several redox couples [8].

b) Hole trapping from VB.

The trapped holes have been proposed to directly oxidize adsorbate substrate. The surface of VB is that surface bound $-OH$ groups or surface adsorbed water molecules can be easily oxidized into hydroxyl radicals ($\cdot OH$). The hydroxyl radical potential is positive enough to oxidize most organic substrate.

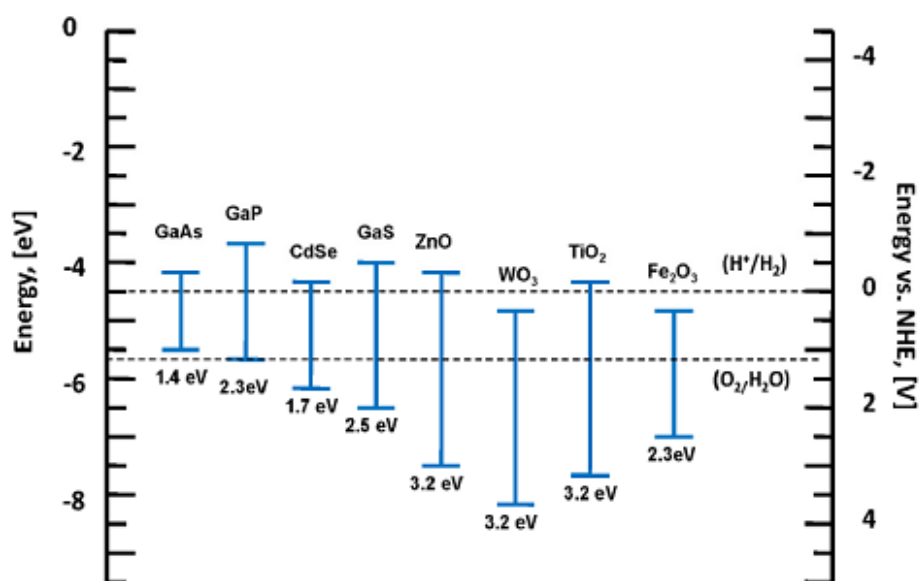


Figure 1.2. Diagram showing band gap energies and band edges of different semiconductors and relative energies with respect of the absolute vacuum scale (AVS) and normal hydrogen electrode level (NHE) in the electrolyte of pH = 1 [8].

c) Electron transferring from CB.

Additionally, most reducible species are not as efficient as adsorbed oxygen at trapping the photogenerated electrons. The rate of oxidation of organic molecules has shown to be affected by the type and concentration of the electron scavenger. Electron scavengers can be molecular oxygen, O_2 , or hydrogen peroxide, H_2O_2 , and ozone O_3 trap a photogenerated electrons e^-_{cb} to produce more hydroxyl radicals $\cdot OH$ [9]. The enhancement of photocatalytic degradation in the presence of oxygen may be attributed to the charge injection from the dye into the semiconductor. The electron from the excited dye molecule is injected into the CB of the TiO_2 and the cation radical formed at the surface quickly undergoes degradation to yield stable products as shown in equation 6-9 [10]. Oxygen adsorbed on the surface of TiO_2 prevents the recombination process by trapping the electrons according to the reaction are showed in equation (10). Carp later discussed the possible production of hydrogen peroxide via the reduction of the superoxide radical (O^{2-}). H_2O_2 and O_2 can be generated by the O^{2-} fading reaction as shown in equation 8 [11]. The superoxide radical, formed when oxygen is reduced by a CB electron via equation 9, is highly reactive and can act as both a reducing and oxidizing agent. It is highly active and can attack either organic molecules or adsorbed intermediates or, after protonation, can

provide an additional source of surface –bound hydroxyl radical. Hoffmann *et al.* suggested and confirmed by O¹⁸ isotope labelling experiment, that H₂O₂, the most frequently detected intermediate species in the photocatalytic oxidations, is partially produced from adsorbed oxygen [2].

d) Oxidation of organic compounds (hydroxyl radical attack).

A hydroxyl radical attacks an organic compound by either removing an available hydrogen atom to form water or adding itself to any unsaturated carbon bonds. Mao *et al.* found that the rate of oxidation of organics correlated with the C-H bond strength, proving that H atom abstraction by hydroxyl radical may be a rate-limiting step. Consequently, from these primary reactions, an organic radical is formed [12]. The subsequent radical transformations and radical-to-radical interactions lead to an array of intermediate products, eventually resulting in CO₂ and H₂O.

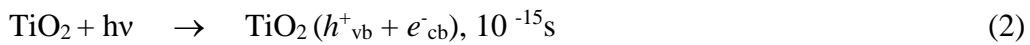
e) Charge carrier recombination.

During photocatalytic oxidations, the hole can also undergo an e⁻/h⁺ recombination process with a CB electron. The recombination (inside the volume of a semiconductor or on the surface (Figure 1.1) is a problem since it decreases the quantum yields of the photoelectron degradation reactions [13]. The recombination of the photogenerated electron and hole is so rapid (occurring on a time scale of nanoseconds) that interfacial electron transfer is kinetically competitive only when a relevant electron donor or acceptor is pre-adsorbed prior to irradiation [13].

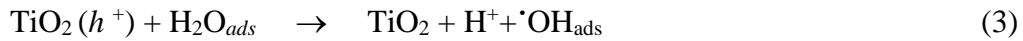
Volume recombination is a dominating process in well-crystallized large TiO₂ particles, which can be decreased by reducing particle size. Surface recombination becomes an important process. In the regime of ultrafine particle size, most of the e⁻/h⁺ pairs are generated sufficiently close to the surface that may quickly reach the surface, and undergo rapid surface recombination mainly due to abundant surface trapping sites and the lack of driving force for e⁻/h⁺ separation [6,9,13]. Since the characteristic time for surface e⁻/h⁺ recombination is much faster than that of the interfacial charge carrier transfer processes, the increase in the interfacial transfer rate will be out-weighed by the increased surface recombination rate in ultrafine particles beyond a certain size. The critical issue governing

the efficiency of photocatalytic oxidative degradation is the minimization of the electron–hole recombination rate by maximization the rate of the interfacial electron transfer to capture photogenerated charge carriers [6,9,13]. The following reactions summarize the possible mechanistic steps. Generally speaking, from irradiation on TiO₂ photocatalyst to reduction of contaminants, the process undergoes five steps: (i) electron-hole generation; (ii) hole trapping from VB; (iii) electron transferring from the CB; (iv) oxidation of organic contaminants; and (v) charge carriers recombination.

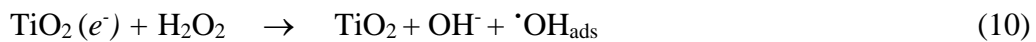
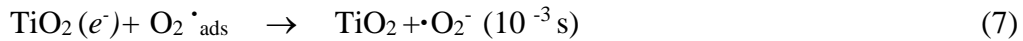
(i) *Electron–hole (charge-carrier) generation:*



(ii) *Hole trapping from VB (10×10^{-19} s):*



(iii) *Electron transferring from CB (100×10^{-12} s):*



(iv) *Oxidation of organic contaminants (10^{-3} s):*



(v) *Charge carriers recombination (100×10^{-9} for (e^-) and 10×10^{-9} for (h^+):*



In above mechanism, the primary e^-/h^+ pairs are derived from the UV irradiation in equation (2). Equation (3 – 5) are the three means of the hole trapping on the adsorbed organic species, adsorbed water molecules, and the surface hydroxyl groups. Dissolved oxygen can accept the excited electrons to form superoxide radical ions, which is another possible source of hydroxyl radicals (equation 6– 9). Thus, hydroxyl radical $\cdot\text{OH}_{\text{ads}}$ species

can be generated not only from VB hole trapping processes (equation 3 – 4), but also from the CB electron scavenging steps (equation 7-9). The highly oxidizing hydroxyl radicals or holes provide the main power for contaminant degradation (equation 11 – 13). Meanwhile, the hydrogen peroxide produced from equation 8 is also a strong oxidant, which can directly attack contaminant substrate or produce another source of hydroxyl radicals through the UV irradiation process. Equations 13 – 14 are the main reasons for the low quantum yield of TiO₂ [9,11,13].

1.1.4. Disadvantages of the TiO₂ photocatalysis.

It is unavoidable to face five issues for its practical applications. *Firstly*, is to improve the low photo-quantum efficiency of TiO₂ which is the ratio of the number of moles of contaminants degraded to the number of moles of irradiation photons, which is very low (usually less than 5 %) in aqueous reactions that arises from high band gap energy and the fast recombination of photo-generated electrons and holes [14]. *Secondly*, is to further extend its photoresponse into visible light regions since its 3.2 eV band gap results in only a small overlap of its action spectrum (<400 nm) with the solar spectrum. *Thirdly*, easy and cheap liquid – solid separation and recovery, due to very difficult photocatalyst separation from solution after reaction [14]. *Fourth*, this technology is now only efficient for low contaminant in ppm to ppb levels in the area of water treatment, which is why its research has been more focused on drinking water purification [15]. *Finally* prevent ultrafine powders will agglomerate into larger particles, resulting in an adverse effect on catalyst performance.

1.1.5. Modification of TiO₂ photocatalysts.

The rapid and extensive growth in this research activity may be attributable to the new chemical and physical properties observed in nanosized titania nanopowders which enhance the photocatalytic activity. This improvement results from changes in grain size, crystal size, crystal structure, morphology, surface area, phase composition, defect sites, extent of surface hydroxylation, light absorption properties, and resistance to mechanical stresses and surface modification [2,5]. Significant effort has been directed towards the shift of optical response of TiO₂ from UV to visible light region through modifications to TiO₂ surfaces, including addition of metal, dopants, surface sensitization and combinations with

other lower band gap semiconductor or with different carbon phases like activated carbons, Graphene, fullerenes or carbon nanotubes [16-19]. These modifications are beneficial in decreasing the recombination rate of electrons and holes, indicating increased quantum yield of photocatalytic process. The benefits of surface modification are: **(i)** inhibiting recombination by increasing the charge separation and therefore the efficiency of the photocatalytic process; **(ii)** increasing the wavelength response range (i.e. the photocatalyst can be excited in the visible light region; and **(iii)** changing the selectivity or yield of a particular product.

1.2. TiO₂ / cellulose hybrid nanocomposite.

1.2.1. Molecular structure of cellulose.

The main components of lignocellulosic biomass resources include carbohydrates polymers (e.g., cellulose (40-50%) and hemicelluloses (20-45%)), and an aromatic polymer (e.g., lignin (10-25%)) (Figure 1.3) [20] which vary depending on many factors such as the species and location of cultivation. However, cellulose is usually the dominant of the three biopolymers [21].

In plant cells, biopolymer chains are generally organized into microfibrillar bundles where nanometer diameter fibers of cellulose are encased in a thin layer of amorphous hemicellulose which serves to protect and separate it from the outer layer composed of lignin acting as the adhesive to bind together the microfibrils and provide mechanical strength to the cell wall (Figure 1.4a) [22]. Microfibrils are assembled into macrofibrils having dimensions on the order of hundreds of nanometers to microns (Figure 4b) which serve as the building units of the cell wall (Figure 1.4c). Such a complex structure therefore requires special processes to separate and recover desired lignocellulose biopolymers [23].

In general, cellulose is a condensed, chiral, crystalline, biodegradable, water-insoluble and fibrous compound. The general formula of cellulose is $(C_6H_{10}O_5)_n$ where 'n' is the number repeating monomeric β -D-glucopyranose units and the value of 'n' differs from source to source [24]. Cellulose is polydisperse, with a degree of polymerization (DP) based upon D-anhydroglucose units (AGUs).

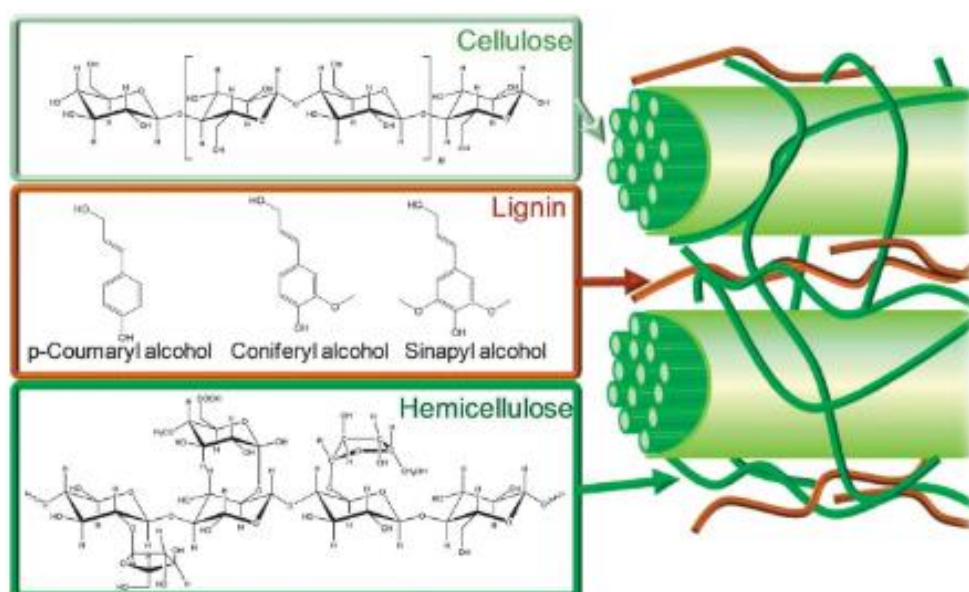


Figure 1.3. Chemical components of lignocellulosic biomass [20].

The structure of cellulose is shown in Figure 1.5 [25]. Cellulose is a higher molecular weight (10^6 or more) homoliner polysaccharide of glucose residues (AGUs) which are linked by β -1, 4-glucosidic bonds formed between the carbon atoms C(1) and C(4) of adjacent glucose units (Figure 1.5a) [25]. The β -D-glucose units combine together by covalent bonds between the equatorial OH group of C-4 of one glucose unit and the C-1 carbon atom of the next glucose unit to form cellulose [26]. The fully equatorial conformation of β -linked glucopyranose residues stabilizes the chair structure and minimizes its flexibility.

Each cellobiose unit is rotated 180° with respect its neighbours, resulting in a sterically stable and linear configuration [27]. The neighbouring glucose residues interact via intra-molecular hydrogen bonds, which give rigidity to the chains, and the polymer chains link via intermolecular hydrogen bonds to form microfibrils which results in crystalline cellulose. The microfibrils are bound together by van der Waals forces and hydrophobic interactions and are embedded within hemicellulose and lignin to form the basis of the plant cell wall [28]. The complex network of intra- and inter- molecular hydrogen bonds and van der Waal interactions stabilize the chains and microfibrils [28]. The associative nature of cellulose chains gives rise to a highly crystalline extended structure which, though hydrophilic and moisture responsive, is entirely insoluble in water and most other common solvents.

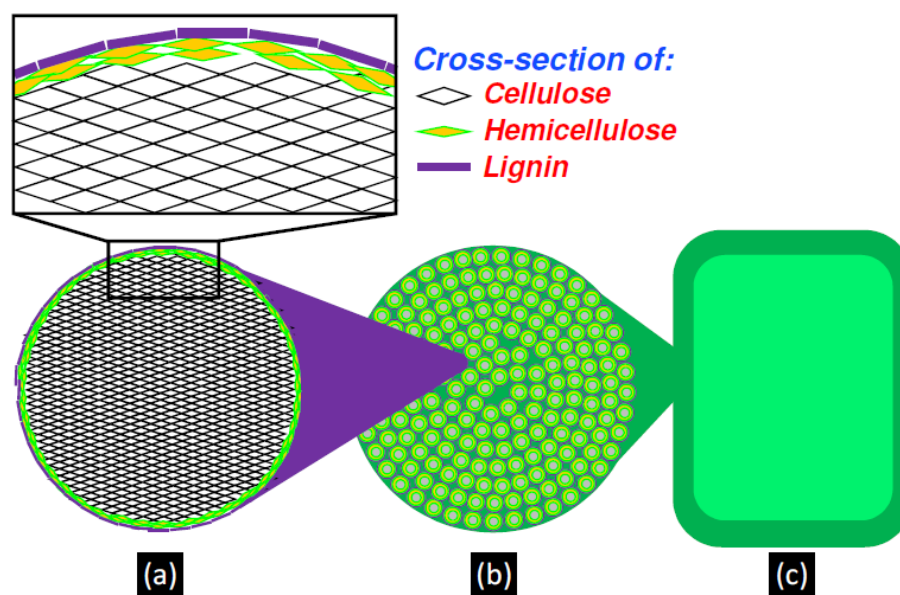


Figure 1.4. Cross-section of a lignocellulose: (a) microfibril, (b) macrofibril, and c) plant cell wall and membrane [22].

It is interesting to note that each cellulose chain has two ends which are chemically different, one with an original C₄-OH group is called the non-reducing end, which the anomeric carbon atom is involved in a closed ring structure (glycosidic linkage) whereas the other end has a D-glucopyranose unit in which the anomeric carbon atom is part of a cyclic hemiacetal functionality while the other with an original C₁-OH is called the reducing end [29]. The terminal hemiacetal group is in an equilibrium in which a small proportion is an aldehyde group which can act as a reducing group (can engage in a 2-electron reduction and transform into a carboxylic acid group) properties and hence called the terminal reducing end. The opposite end with the closed ring structure is termed as the non-reducing end [30].

The hydroxyl groups at C-2 and C-3 are secondary while the one in C-6 is primary. Due to the large presence of hydroxyl groups in the cellulose polymer the main derivatization reactions are based on alcohol chemistry, thus giving the cellulose molecule a high degree of functionality [31]. Naturally, cellulose can be randomly formed in amorphous and crystalline structure with different ratio in grassy and woody plants. It contains closely and regular packed crystalline regions along with loosely and randomly packed amorphous regions [32] (Figure 1.5b).

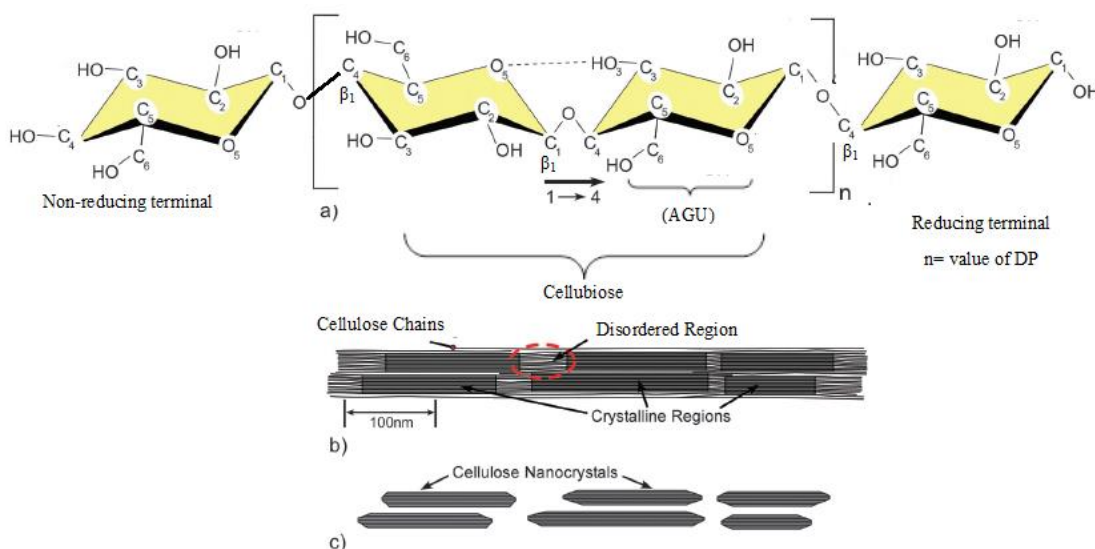


Figure 1.5. Schematics of (a) linear structure of single cellulose chain repeat unit, showing the directionality of the 1 - 4 linkage and intrachain hydrogen bonding (dotted line), (b) cellulose microfibril showing the crystalline and amorphous regions, and (c) cellulose nanocrystals after acid hydrolysis dissolved the disordered regions [25].

1.2.2. Supermolecular structure of cellulose.

Besides cellulose molecular level, the understanding of cellulose at the supermolecular level is also important to the dissolution mechanism study. This includes hydrogen bonding, crystalline types, crystallinity, crystallite size, and pore sizes and structures, which are reviewed in the following paragraphs.

a) Hydrogen bonds in cellulose crystal.

Despite the highly hydrophilic characteristics of cellulose due to the plentiful of hydroxyl groups, it is insoluble in the most common solvents due to the extensive strong of strong *inter-* and *intra-*molecular hydrogen bonding and highly crystalline structure (Figure 1.6) [33]. Generally, the hydrogen bonding organizes the chains together in a highly ordered crystal-like structures which minimizes the flexibility and increases the strength of cellulose polymer by hindering the free rotation of the pyranose rings to their adjacent glycoside bonds. So, the location of hydrogen bonds in cellulose is very decisive and determine the nature and type of different crystalline forms of the cellulose [34,35]. Because the existence of equatorial conformations of the β -D-glucopyranose units and -OH groups and electronegative O-atoms, different cellulose chains are held together by two types of

hydrogen bond to form a network which increases the thermal durability of cellulose [34].

The intra molecular hydrogen bond is high relevance with regard to the single chain conformation and stiffness. On the other hands, the intermolecular dipole-dipole interactions are responsible for the formation of microfibrils with physical and chemical stabilities along with high tensile strength. Despite the comprehensive efforts by many investigators, the exact structure of the strong hydrogen bonding network between the hydroxyl groups has not been fully resolved.

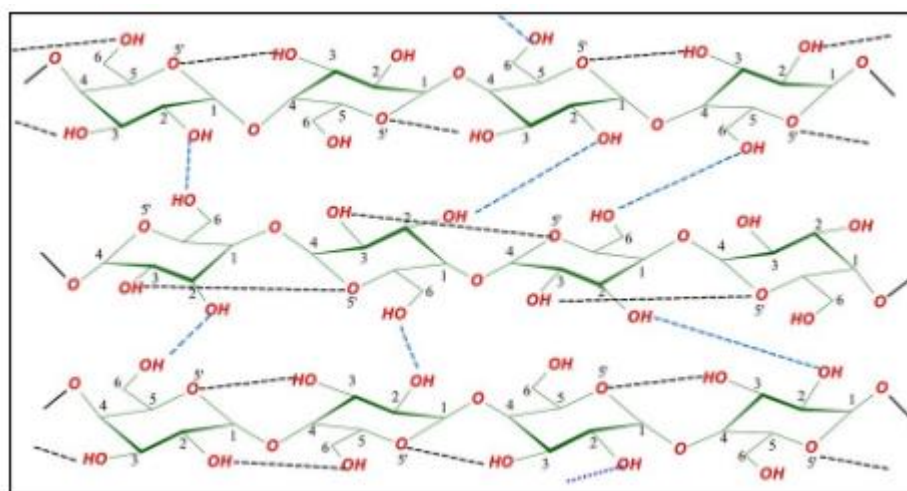


Figure 1.6. Inter (-----) and intermolecular (-----) hydrogen bonding between cellulose chains [33].

The chains of cellulose I (native cellulose) are held together which are proposed the two major intramolecular hydrogen bonds. One is between the C³ hydroxyl groups and the pyranose ring oxygen of an adjacent glucose residue (C³-OH.....O⁵) with bond length 2.707 Å and the other one is between the C² hydroxyl group and the C⁶ oxygen of a neighbouring glucose residue (C²-OH.....O-C⁶) with bond length of 2.802 Å (Figure 1.6). The intra-chain hydrogen bonding between hydroxyl groups and oxygens of the adjoining ring molecules stabilizes the linkage and results in the linear configuration of the cellulose chain. On the other hands, the major inter chain hydrogen bond is between C⁶ hydroxyl group and C³oxygen (C⁶-OH.....O-C³) along the b axis with bond length of 2.874 Å (Figure 1.6) which is responsible for the sheet like nature of the native polymer [33,36]. The intermolecular hydrogen bonding in cellulose II is insignificantly more complex compared to that of cellulose I. Other polymorphic forms III_I, III_{II}, IV_I, and IV_{II} have the same

hydrogen bonding network as the native cellulose [37]. Also, the free hydroxyl groups present in the equatorial position in the cellulose macromolecule are likely to be involved in a number of *intra* and *inter* molecular hydrogen bonds, which gives rise to a variety of ordering crystalline arrangements [31,38].

Part of a cellulose preparation is amorphous between these crystalline regions. In the amorphous or less ordered regions the cellulose chains are not so tightly packed making them more available for hydrogen bonding to other molecules, such as water. Aqueous solutions are not capable to dissolve cellulose. However, the hydrogen bonding with water makes cellulose swell, i.e., to absorb rather large quantities of water.

The hydroxyl groups in cellulose are arranged in radial orientation while the aliphatic hydrogen atoms in axial positions. Therefore, the strong inter chain hydrogen bonding between neighbouring chains are easily formed and between cellulose sheets, some weaker hydrophobic interaction exist [39]. Researchers proposed that the cellulose resistance to acid hydrolysis is due to the hydrophobic face of cellulose sheets where a dense layer of water formed near the hydrated cellulose surface [40] and the resistance to enzymatic hydrolysis is due to the inter-chain hydrogen bonding [41]. Also, both alkali mercerization and ammonia treatments reduced the void fraction. So, the research groups are motivated to design solvents for dissolving cellulose by breaking, at least, the inter-cellulose and inter-sheet dispersive force.

b) Crystal structure of cellulose.

The amorphous regions are distributed as chain dislocations on segments along the elementary fibril where the microfibrils are distorted by internal strain in the fiber and proceed to tilt and twist. The ordered regions, on the other hand, are crystalline as a result of the tight packing of cellulose chains. The relative amounts of crystalline and amorphous cellulose, are origin dependant and pretreatment of the cellulose [37].

Different chemicals can easily penetrate into the amorphous regions of cellulose, making them more susceptible to reactions, while the crystalline regions remain un-attacked. Additionally, amorphous regions can easily absorb water and become more soft and flexible [42,43]. On the other hands, the affinity to water of cellulose is greatly different

from that of amylose, another polysaccharide that has the same chemical composition. The reason is that amylose is a poly (1,4- α -D-glucan). Its stereochemistry makes a much higher proportion of hydroxyl groups not hydrogen bonded, thus are available for solvation. The hydrogen-bonding network and molecular orientation in cellulose can vary widely, which can give rise to cellulose polymorphs or allomorphs. Four polymorphs of cellulose have been characterized so far in the literature [33,37,44]. The crystal structure of native celluloses is cellulose I, whereas non-native celluloses (i.e. regenerated or derivatized) have different H-bonding patterns. There are several polymorphs of crystalline cellulose, but the currently known and accepted crystalline allomorphs are I, II, III and IV with parallel chain packing, II, IIII and IVII with anti-parallel packing [44]. The characteristics of different polymorphs of cellulose are summarized in Table 1.1.

Table 1.1. Different types of cellulosic forms, their origin, and other important characteristics [37,45-47].

Types of cellulose	Origin	Crystal structure & type of unit cells
Native cellulose exists as Cellulose I in two crystal phases I α and I β	I α rich specimens have been found in cell wall of algae. I β rich specimens have been found in cotton, wood and ramie fibers.	Crystal structures of I α and I β are different. I α has triclinic unit cell with one chain. I β has monoclinic unit cell with two chains.
Cellulose II	Thermodynamically stable form which is obtained from the alkali treatment of cellulose I.	Anti-parallel arrangement of cellulose chains with modified hydrogen bonding network.
Cellulose IIII, IIII	It is obtained from treatment of ammonia and a number of mono, di, tri amines with cellulose I and cellulose II, respectively.	One chain monoclinic unit cell with an asymmetric unit that contains one glucosyl residue.
Cellulose IVI, IVII	Obtained from heating cellulose IIII, IIII in glycerol at 206 °C.	Orthogonal unit cells

1.2.3. Nanocellulose.

Nanocellulose is a term referring to nano-structured cellulosic materials with one dimension in the nanometer range. Considering the hierarchical structure of cellulose fibers which starts from glucose chains elementary fibrils (3-5 nm), microfibrils (5-30 nm) and

ultimately forming the cellulosic wood fibers by aggregating many microfibrils (Figure 1.7) [25,48]. The nanostructures of cellulose are a broad to refer several of the particle types which depend on the distinct morphology, aspect ratio, crystallinity, crystal structure and properties. There is a distribution of length, width, and crystallinity of cellulose fibers as a result of various factors which are, (i) type and severity of the extraction process, (ii) the originality of variable biological process results in statistical variability in the production of the crystals [49].

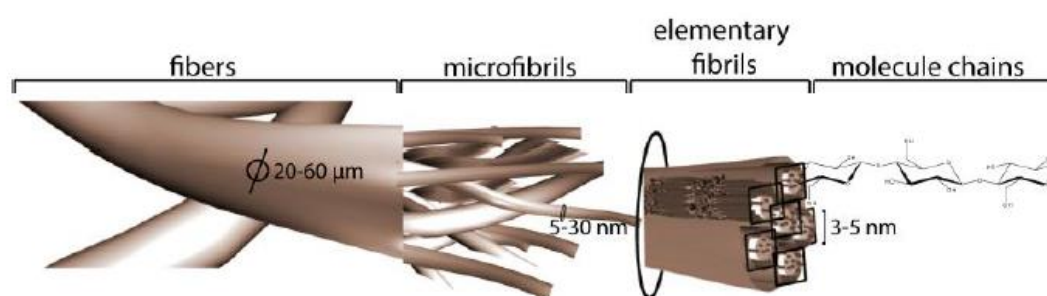


Figure 1.7. A simplified illustration of the morphological hierarchy in cellulose: the elementary fibrils contain both crystalline and amorphous regions.

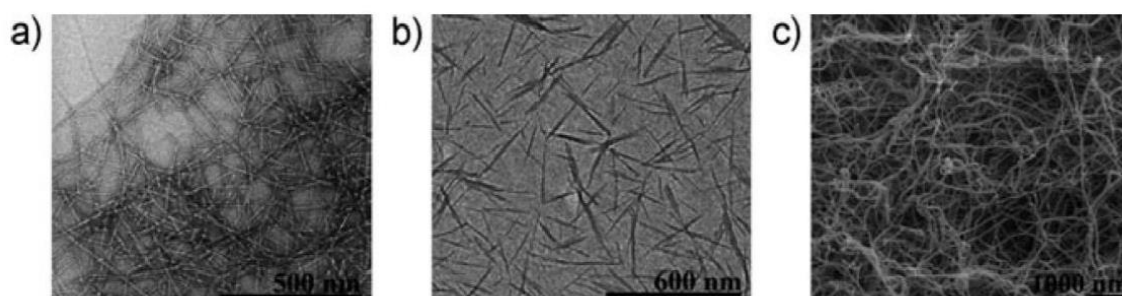
Based on their sources, dimensions, functions, and preparation methods, nanocelluloses may be classified into three main subcategories of microfibrillated cellulose (MFC), cellulose nanocrystals (CNCs), and bacterial nanocellulose (BNC) (Table 1.2) [25,50]. CNCs have also been referred to in the literature as cellulose nanowhiskers or nanocrystalline cellulose (NCC), and MFC is also sometimes called nanofibrillated cellulose (NFC) or cellulose nanofibrils (CNF) (Figure 1.8) [57-59].

Microfibrillated cellulose (MFC).

MFC is composed of more or less individualized cellulose microfibrils, expanded high-volume cellulose, very high aspect ratio (length/diameter), 100% cellulose, contain amorphous and crystalline regions, greatly expanded in surface area [25,54]. Also, typical lateral dimension of MFC are 20-60nm and longitudinal dimension is in a wide range, typically several micrometers. So, each microfibril is composed of 10-50 microfibrils if we consider that the microfibrils have a 2-10 nm-thick fibrous structure. Another noteworthy difference between these two kinds of nanoparticles is that MFC presents a web like structure [54].

Table 1.2. The family of nanocellulose materials [8,15,56].

Type of nanocellulose	Synonyms	Typical sources	Formation and average size
Microfibrillated cellulose (MFC)	Nanofibrils, microfibrils, nanofibrillated cellulose	Wood, sugar, beet, potato tuber, hemp, flax	High pressure homogenizer diameter: 5-60 nm Length: several micrometers Acid hydrolysis
Cellulose nanocrystals (CNCs)	Nanocrystalline cellulose (NCC), crystallites, whiskers, rodlike cellulose microcrystals	Wood, cotton, hemp, wheat straw, mulberry bark, ramie, Avicel, tuncin, algae, bacteria	Diameter: 5-70 nm Length: 100-250 nm (from plant celluloses; 100 nm to several micrometers (from celluloses of tunicates, algae, bacteria)
Bacterial nanocellulose (BNC)	Bacterial cellulose, microbial cellulose, biocellulose	Low-molecular-weight sugars and alcohols	Bacterials synthesis Diameter : 20-100 nm, different types of nanofiber networks

**Figure 1.8.** TEM of a) MFC [51] and b) CN [52]; c) SEM of BNC [53].

MFC may be isolated from the cellulosic fibers using the mechanical shearing forces to rip the larger fibers apart into nanofibers [55]. Different mechanical treatment procedures have been reported to prepare MFC. These processes are responsible for the high energy consumption over 25000 kWh per ton in the production of MFC as a result of the required multiple passes through the homogenizers [56]. Pre-treatments are therefore used to address this problem. Different pre-treatments such as mechanical cutting, acid hydrolysis, enzymatic degradation, and the introduction of charge groups have been proposed to

facilitate this homogenization process and thus decrease the energy consumption [51]. By combining the mechanical treatment with certain pre-treatments, it is possible to decrease the energy consumption.

Cellulose nanocrystals (CNC).

Cellulose nanocrystals are also sometimes referred to as nanocrystalline cellulose (i.e. NCC), whiskers, needles, microcrystals, monocrystals or crystallites. with the chosen term often, a question of author preference or trend. It has recently been argued that CNCs are the most dominant fundamental building block of the biosphere [57].

Indeed, here we distinguished NFC from traditional MFC not only to emphasize the size, but also that a pre-treatment is applied in the fibrillation process, which enables the nanoscale and more individual fibrils as the aggregation is reduced. The cellulose nanocrystals (CNCs) are used for the rod-like cellulose nanocrystals and tunicate nanowhiskers with the width of a few nanometers and length between 100 nm and several micrometers, are produced by the removal of amorphous sections of a purified cellulose source by acid hydrolysis, often followed by ultrasonic treatment [58]. The origin of the cellulosic material demands which of the specific hydrolysis and separation protocols are used. In addition, the geometrical dimensions (length and width) as well as the morphology of the forming CNCs are found to vary widely depending on the source of the cellulosic material, and the conditions under which the hydrolysis is performed [59].

Bacterial nanocellulose.

The biosynthesis of cellulose takes place not only in plants, but also in bacteria, with *Acetobacters*. strains being one of the most common. Bacterial nanocellulose, also called bacterial cellulose, microbial cellulose, or biocellulose, is produced by the respective bacteria strains in response to specific environmental conditions [60]. The aerobic bacteria, such as acetic acid bacteria of the genus *Gluconacetobacter*, are cultivated in common aqueous nutrient media with low-molecular weight carbon and nitrogen sources, forming highly porous nanofiber network structures (fiber diameter: 20-100 nm) with culture medium filling the voids. Unlike MFC and CNCs isolated from cellulose sources, BNC is excreted by bacteria as exopolysaccharide through biotechnological assembly processes

from nutrient media. The molar mass, molar mass distribution, and the supramolecular structure of BNC can be controlled by selecting the substrates, cultivation conditions, various additives, and bacterial strain. Although identical to cellulose from plant origins in terms of molecular formula, BNC is very pure cellulose with a high degree of polymerization (DP values of 2000-8000), high crystallinity (60-90%), and good mechanical properties [61]. As a result of the nanostructured network and morphological similarities with collagen, BNC has been extensively tested for cell immobilization, cell migration, production of extracellular matrices, and other medical applications [49]. Previous *in vitro* and *in vivo* evaluation showed that the BNC implants elicited no foreign-body reaction. In addition, fibrosis, capsule form, or giant cells were not detected around the implants, and connective tissue was nicely integrated with the BNC implants. BNC-based membranes were also functionalized with platinum nanoparticles and multiwalled carbon nanotubes to produce electrocatalytic and electrically conductive materials, respectively [61,62].

1.2.4. Dissolution mechanisms of cellulose: macroscopic aspects.

The high crystalline structure of native cellulose is stabilized by a strong intra- and intermolecular hydrogen-bond network. Therefore, the dissolution of cellulose is very difficult by chemicals or even bio-enzymes and this poses an obstacle for the easy utilization of cellulose especially in the large scale for its applications in materials science. The chemical modification of cellulose is an important avenue for the synthesis of novel and new hybrid materials with the improved performance and value-addition [63]. So, the dissolution of cellulose is necessary for impregnation of metal oxides to produce highly active hybrid materials. All of the publications related to the TiO₂/ cellulose, are synthesized without dissolving of cellulose. In order to discuss the dissolution mechanism of cellulose, it is very essential to know several aspects of issues needs to be addressed as follows:

a) Degree of polymerization (DP).

Many properties of cellulose depend on its chain length or degree of polymerization (DP) which based on the source and isolation treatment [37]. In general, the DP of cellulose based upon anhydroglucose units (AGUs) of up to 12,000 for cotton, but significantly lower for the wood pulps (DP = 600-1200) and man-made fibers (DP = 250-500) [64]. Molecules

with very small chain length, resulting from the breakdown of cellulose are known as cellodextrins; in contrast to long chain cellulose, cellodextrins are typically soluble in water and organic solvents [48].

b) Cellulose swelling vs. cellulose absorption.

The strong hydrogen bonding network within the cellulose molecules greatly affects to the properties of cellulose polymer. For instance, properties such as swelling, absorption and optical behaviour are influenced by the hydrogen bonding. Swelling of cellulose is to a certain extent reversible when the surrounding humidity level is increased or decreased. However, there is a distinct hysteresis effect in the absorption/desorption curves. Desorption curves typically show higher moisture content values than absorption curves [65]. Hysteresis is caused by the inaccessible hydroxyl groups of the cellulose in the dry state that can become accessible only after more water is absorbed, i.e., at dry state hydroxyl groups satisfy each other through adjacent free hydroxyl groups, but as the moisture increases the hydrogen bonding breaks while more water is absorbed [66].

c) Cellulose dissolution vs. cellulose swelling.

Cellulose dissolution and cellulose swelling are two completely different reactions. Although the significant change in the physical properties of cellulose and increase the volume of sample due to the uptake of the swelling agent, the cellulose swelling process maintains the overall crystalline structure of cellulose such as the moiety of solid cellulose phase particles, films or fibers [67]. On the other hand, cellulose dissolution is a transition of a two-phase system to a one system with high clarity of the solution due to the solvent induces the changes in the molecular order of superstructure of the native polymer by chemically derivatizing or the original supermolecular structure of cellulose is destroyed [68]. However, there is no visual difference between the swelling and dissolution process due to we have the same system which can act swelling or dissolution agent that are based on the operation condition and crystalline structure of cellulose [68].

d) Cellulose dissolution vs. cellulose hydrolysis.

In order to discuss the dissolution mechanism of cellulose in an aqueous solvent, it is very essential to know the difference between the cellulose dissolution and hydrolysis.

Firstly, cellulose hydrolysis or cellulose degradation is to break down the molecular weight by cutting the middle of cellulose molecule or from two ends of cellulose to obtain very low molecular weight cellulose or even cellobiose or glucose. The physical, chemical, physico-chemical and biological treatment is done for the hydrolysis step [74]. On the other hands, the cellulose dissolution is to break the intra-and inter molecular hydrogen bond, destroy the long-range order of crystalline regions of cellulose to form a molecular solution of cellulose with these novel solvents. The phenomenon of cellulose dissolution is more similar to the solid melting. Cellulose dissolution may require the certain degree of hydrolysis as a pretreatment for high molecular weight cellulose, while in the case of moderate and lower molecular weight, it is not necessary to make a pretreatment of cellulose. The ultimate research goal is to dissolve cellulose without using the hydrolysis pretreatment.

Secondly, the dissolved cellulose is used in the form of macromolecular solution, can be reformed into fiber or other shapes, and regenerated, while the complete hydrolysis of cellulose is devoted to smaller sugar molecules which cannot be regenerated back into the macromolecules of cellulose

Thirdly, the fiber dissolution does not chemically consume the solvent, but hydrolysis does. Most of the chemicals added to dissolve cellulose can be recycled.

1.2.5. Chemical modification of cellulose nanocrystals.

The poor solubility of cellulose in common solvents is due to the strong inter- and intramolecular hydrogen- bonding network and the crystallinity of cellulose. There are very few solvent systems affected on the dissolution of cellulose which are operated under restriction of temperature and composition conditions [71]. On the other hands, cellulose is amenable to chemical functionalization due to the presence of three hydroxyl groups of the cellulose polymer. It can be partially or fully reacted with various reagents to produce modified cellulosic materials for our daily and industrial needs [37,68]. To date, only a handful of solvents are known for cellulose, including more recently ionic liquids (ILs).

Cellulose solvents can be separated into two main categories: derivatizing and non-derivatizing. Derivatizing solvents, like the Viscose process, rely on a chemical reaction and bond formation for solvation, while non-derivatizing solvents are capable of dissolution

solely through physical interactions between the solvent and substrate. The chemical modification and dissolving the cellulose have been performed under homogenous and heterogeneous conditions via various solvent systems.

a) Homogenous derivatization.

One way to improve the catalytic accessibility and reduce the chemical recalcitrance of cellulose is to homogeneously dissolve it in *a non-derivatizing solvent* [72]. Homogeneous derivatization involves dissolution or, at least, by the swelling of cellulose in the reaction medium and modification of the entire cellulose chains. This remains extremely challenging as a result of the limited solubility of cellulose in common solvents [73].

Ionic liquids as greener solvents.

It has been difficult to achieve a homogeneous solution of cellulose without using harsh conditions, which in turn often affects negatively to the DP. In addition, the hydrogen-bonding pattern diminishes the reactivity of cellulose, and often the DS values achieved from heterogeneous modification reactions which have ranged from poor to moderate. To overcome these obstacles, the ILs are the new class of green solvents that has been a phenomenal burst of interest and research at both academic and industrial level in the solubilization, separation, and processing of cellulosic materials because these are highly versatile [74].

Not only do ILs have very unique properties that very few other liquids have, such as being non-volatile, having very large electronic and ionic conductivities, a wide range of miscibilities and wettabilities, and broadly variable optical behaviour, but their properties are highly switchable and tuneable [75]. The ILs is capable of disrupting the hydrogen bonds between different cellulose chains. This interaction decreases the crystallinity of cellulose and makes the cellulose fraction more susceptible to derivatization reactions [76]. The chemical modification of cellulose in ILs is relatively straightforward and products such as cellulose acetates, tosylates and benzoates have been achieved with high degrees of substitutions [77].

ILs is a pure liquid phase composed mostly if not solely of ions having a melting point near room temperature which is commonly referred to as room temperature ionic

liquids (RTILs) [78]. Biomass dissolution in ILs was discovered in the 1930's by Graenacher using *N*-ethylpyridiniumchloride with nitrogen-containing bases [79]. This was considered to be of little practical interest and the use of ILs for cellulose dissolution was largely abandoned until 2002 when Dr. Robin Roger's group demonstrated solvation of cellulose by dialkyl substituted imidazolium-based ILs [79]. Generally, ILs are 1:1 electrolyte salt where the cation is a bulky, organic molecule based on nitrogen or phosphorous in its first oxidized state, which provides the positive charge, while the anion can be either mono atomic or polyatomic, organic or inorganic, can have metals, and be acidic, neutral, or basic. Since the cationic species are usually less variable than the anionic species, ILs are commonly distinguished and referred to by their type of cation.

Although the dissolution is greatly affected by the source of cellulose, different DP, and the dissolution conditions (heating methods, irradiation, heating temperature, time, etc.), generally, with the same cation, the solubility of cellulose in ILs decrease in the order: $[(\text{CH}_3\text{CH}_2)_2\text{PO}_4]^- \approx [\text{OAc}]^- > [\text{SHCH}_2\text{COO}]^- > [\text{HCOO}]^- > \text{Cl}^- > \text{Br}^- \approx [\text{SCN}]^-$ [80]. By choosing or modifying ions, improvement in the notable physical properties of ILs such as non-volatility, non-flammability, high dissolution capacity, chemical and thermal stability, wide liquid range, low melting point and vapor pressure, low viscosity and low/no toxicity which needed for specific tasks will be achieved, and subsequently, followed by the development of advanced materials through the synthesis of new ILs with specific chemical properties.

Some enzymes are catalytically active in ILs. But, these studies have focused mainly on the use of hydrophobic ILs such as [C4mim] [PF6], where enzyme activity is similar to that in hydrophobic organic solvents because hydrophobic media do not strip the enzymes of the thin layer of surrounding water which is essential to their functionality [81]. ILs which are capable of dissolving cellulose, in contrast, tend to be hydrophilic and capable of forming strong hydrogen bonds. Unfortunately, the interactions needed to dissolve biopolymers (the ability to form hydrogen bonds with the biopolymer to disrupt its internal hydrogen bonding) also tend to denature enzymes. The investigations into cellulase activity in ILs thus far have determined that cellulase enzymes are not viable in aqueous IL mixtures (for ILs capable of dissolving cellulose) and enzymatic hydrolysis after the removal of the IL is instead preferred.

As an alternative to enzymatic hydrolysis, acid catalysts can be used to hydrolyze

the cellulose in the IL-phase [82]. But for this process, a separation step to isolate cellulose from the IL is necessary, and, because the ILs are miscible with water and the sugars are soluble in the IL/water system, a cost-effective and easy separation of sugars is required for this process to be advantageous over enzymatic hydrolysis. Such a separation process has not yet been demonstrated.

There is no question that the ability of ILs to directly dissolve cellulose has generated intense worldwide academic and industrial interest in a relatively short period of time, but ILs solvents still have not been commercialized because of the high cost involved and solvent recovery problems. Intensive research is going on to come up with the effective solvents for dissolving the cellulose.

Sodium hydroxide (NaOH).

The native cellulose (cellulose I) can be converted into cellulose II by one of two processes, mercerization and regeneration [37].

Mercerization: It is the process of treating cotton cellulose I with concentrated sodium hydroxide solution to form cellulose II. In 1850, Mercer is patented for treatment of cotton fabric by highly concentrated NaOH to improve the reactivity with chemicals and strength of the fibers. During the mercerization process, the sodium hydroxide concentration was high around 18-20% because of which NaOH stayed close to the cellulose chains forming Na/cellulose crystal [83]. Many decades later, Sarko's group created a possible mechanism of mercerization of cellulose by sliding chain model [84]. The native cellulose (cellulose I) has a parallel arrangement of crystal structure. In order to state the direction of chains, the vector was defined from cellulose reducing end to the non-reducing end (C4-C1). But the crystallites were distributed along the fiber axis with equal probability in up and down direction. The cellulose chains consist of some amorphous region in between the crystalline regions in both directions. When the NaOH was introduced in this structure, it disturbed the amorphous region first without affecting the crystalline region and the cellulose fibers were swollen in this region. The chain mobility increased due to which they were rearranged into antiparallel Na cellulose I. After the initial conversion step, the NaOH-cellulose I adsorbed the additional NaOH to form Na-Cell II. The sodium hydroxide was

then washed from the cellulose structure to form two-fold helical conformation of Cellulose II. [84].

Regeneration: This involves dissolving of cellulose I in a alkali solvent followed by re-precipitation via diluting in water to form cellulose II. In details, NaOH-water mixture is regarded as a potential solvent for dissolving cellulose. It has not been commercialized due to minimal solubility, chemical degradation of cellulose and recovery problems. The dissolution of cellulose in aqueous sodium hydroxide solution is not well understood.

In order to better understand the NaOH dissolution process, it is essential to describe the phase diagram of NaOH-water alone (Figure 1.9) [85]. There is strict operating conditions of composition of sodium hydroxide and temperature to dissolve cellulose. NaOH can cause cellulose to swell and in a narrow range of the phase diagram, even can dissolve cellulose. The liquidus curve represents the melting of ice. At the concentration range of 20% NaOH- 80% water there was no pure ice melting at higher temperature. Only the eutectic mixture of NaOH · 5H₂O and 4H₂O was formed at the melting temperature of around -33 to -34 °C [85]. The presence of sodium pentahydrate is important to dissolve cellulose [83,85]. The interaction of cellulose and NaOH-water mixture takes place in a limited range of NaOH concentration of 6-10% at temperature from - 10 to -5 °C [86]. Noticeably, there is small triangle region marked as cellulose-Q region.

Later, the scientists found that NaOH can be a direct solvent of cellulose. In swelling, the soda hydrates can penetrate the amorphous area of cellulose. Then, solvate the cellulose to destruct the neighbouring the crystalline regions. The formation of complex Na-cellulose is a temporary reaction step from crystalline cellulose I to cellulose II. Cellulose I and Na-Cellulose I coexisted between NaOH concentration in the range 10-14% [87].

The molecular weight, crystalline form and degree of crystallinity of cellulose samples also play a great role in the solubility values. Isogai suggested that the optimum conditions for dissolving microcrystalline cellulose and other cellulose samples in sodium hydroxide solution. This involved swelling cellulose in 8-9 wt% NaOH, then freezing the mixture at -20 °C to form a tight mass, followed by thawing at room temperature and diluting with water to 5% NaOH [88]. After their investigation, they found some conclusions. Firstly, the cellulose with DP < 200 could easily dissolve in NaOH solution. Secondly, most regenerated cellulose could dissolve in NaOH solution; Thirdly, cellulose I has a higher than

levelling-off DP which can be partially dissolved; fourthly, the presence of lignin reduces the solubility, whereas the hemicellulose does not affect much. Finally, the dimension over 100 nm in the long-range order of solid cellulose is preventing the cellulose dissolution in caustic soda solution. Table 1.3 clearly indicated that the high DP cellulose samples have lower solubility in aqueous sodium hydroxide solution irrespective of their crystal form and crystalline index [88].

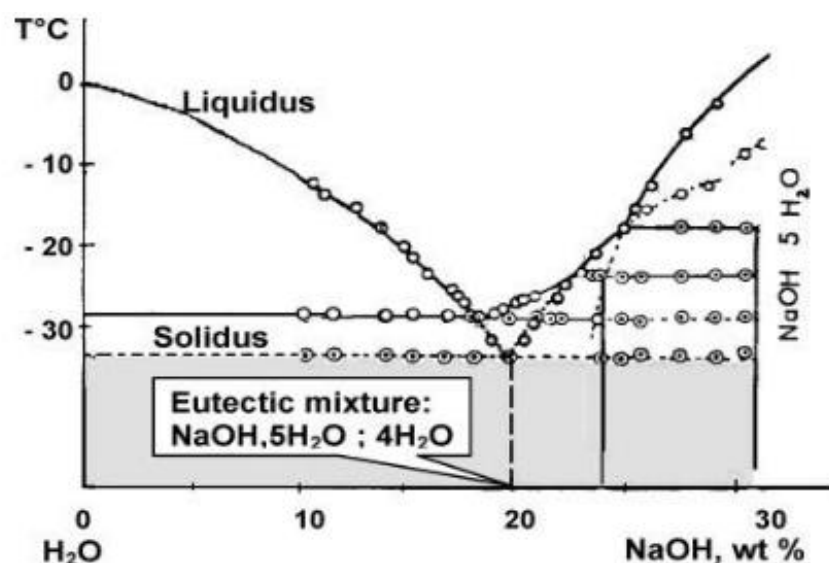


Figure 1.9. NaOH-water binary phase diagram at the sodium hydroxide concentration of 0-30% [85].

Cuissinat and Navard presented a series of five papers on the concept of swelling and dissolution of cellulose in the novel organic, aqueous and ionic liquids. The five modes of dissolution were as follows [89]:

Mode 1: fast dissolution by disintegration into fragments.

Mode 2: large swelling by ballooning and dissolution of the whole fiber.

Mode 3: large swelling by ballooning and partial dissolution of the fiber.

Mode 4: homogeneous swelling and no dissolution of any part of the fiber.

Mode 5: no swelling, and no dissolution.

The swelling and dissolution mechanism of cotton and wood cellulosic fibers were studied at different sodium hydroxide concentrations and temperatures [89c]. They were then categorized into one of the five modes as described above [89c]. They identified that optimum condition for dissolving cellulose was by Mode 3 mechanism at -5 °C and 7.6% of NaOH. There was no dissolution of the fibers by increasing the NaOH concentration and

the temperature [89c].

Table 1.3. Solubility values of linter cellulose –derived samples with different crystal forms [88].

Samples	Crystal form	Crystallinity index (%)	Dp	Solubility (%)
Original linter cellulose	Cellulose I	75	850	32
Mergerized linter	Cellulose II	50	800	32
Regenerated linter from cuen	Cellulose II	-	-	100
Regenerated linter from SO ₂ -diethylamine-DMSO (dried)	Amorphous	0	850	99
Mergerized and EDTA treated linter	Cellulose III _{II}	25	750	37

In the last decade, many research groups have found that the composition of NaOH/urea, LiOH/urea and NaOH/ thiourea have been regarded as a better solvent than NaOH alone for dissolving cellulose at low temperatures [90]. They advised the compositions are 6% NaOH /4% Urea, 7% NaOH /12% Urea, and 6% NaOH /5% thiourea. In these percentages, they explored novel fibers and after that lead to the new composites [90]. Cai investigated behaviour and the solubility of cellulose in different alkali solvent systems such as LiOH/urea, KOH/urea and NaOH/ urea [90c]. The cellulose was in the form of cotton linters having the concentration of 4 wt%. The dissolution power followed the order LiOH/urea>NaOH/Urea>KOH/urea. The KOH/urea was regarded as a weak solvent while the NaOH/urea and LiOH/urea were the good non-derivatizing cellulose solvent systems.

The mechanism of treatment of cellulose is that when put solvents and cellulose in water, NaOH hydrates –urea hydrates –free water –cellulose form a special complex in the solution. NaOH or LiOH destroys the inter- and intra- hydrogen bonds between the cellulose molecules. Urea hydrates are used as a hydrogen bond donor and receptor between solvent molecules and prevents the reassociation of cellulose molecules. The hydrates from alkali

hydroxide and urea were bound to cellulose due to which it was swollen in the solution. Stable and transparent cellulose solution was formed as the cellulose was surrounded by an overcoat of alkali hydrates, urea hydrate and free water [90c and g].

Qi [90d] investigated the dissolution of cellulose in the 7 wt. % NaOH/ 12 wt.% urea aqueous solution at different range of temperature and molecular weight. The viscosity average molecular weight (M_n) of cellulose varied from 3.1×10^4 to 13.1×10^4 and temperature from -60°C to -12.6°C . They reported following observations for the cellulose sample (4wt.%) having M_n equal to 13.1×10^4 dissolved in 7wt. % NaOH/12 wt.% at different temperature for 2 mins. a) The degree of swelling in the cellulose fibers increased with lowering of temperature and the solubility values increased from 17.7% to 100% for temperature varying from 0 to -12.6°C . b) There was hardly any change in the cellulose at temperature of 0 to 25°C . The solubility value was at the constant value of 7.6-8.3%. The molecular weight of cellulose was directly related to the crystallinity value. If the crystallinity value is greater than it would be very difficult to break the inter and intra molecular hydrogen bonding, this would affect the solubility of cellulose. Ramos [91] proposed that the dissolution of cellulose in solvents is a heterogeneous polymer dissolution which takes place in a number of steps starting from breaking of cellulose crystalline region, change in an amorphous region to the highly elastic state, interaction/salvation of polymer molecules followed by diffusion of the solvated polymers into solvents. Jin [90b] studied the dissolution mechanism of cellulose in the ternary solvent system. The solvent used was the combination of NaOH/urea/thiourea for dissolving the untreated cellulose. This confirmed that the NaOH/urea/thiourea was a better solvent in comparison to NaOH/urea and NaOH/thiourea. In conclusion, various parameters need to be studied and optimized simultaneously such as NaOH concentration, addition of urea and thiourea, cooling bath temperature and time to obtain the best dissolution conditions for cellulose.

b) Heterogenous derivatization (chemical functionalization).

As most of these limitations and drawbacks are related to the chemical nature of nanocellulose surface, they can be suppressed or limited by chemical functionalization. For instance, the introduction of surface charge by oxidation can be a successful pathway to limit the aggregation of the nanofibres upon drying and subsequently reduce the shipping

cost of NFC. In another approach, hydrophobic functions can be grafted at the NFC surface to decrease the interfacial energy and improve their interaction with hydrophobic environments (physical or chemical interactions). A decrease in the hydrophilicity of the NFC composites and foams can be also obtained by this method.

By virtue of the hydroxyl groups of cellulose polymers, it can be partially or fully reacted with various reagents to yield derivative which is the actual applied ones in the industrial production. The reducing end of the cellulose contains three hydroxyl groups and a free hemi-acetal group at C-1 whereas the non-reducing end contains four hydroxyl groups at C-2, C-3, C-4 and C-6. Moreover, each of the anhydro glucopyranose repeating units contains three hydroxyl groups at C-2, C-3 and C-6. The hydroxyl groups at C-2 and C-3 are secondary while the one in C-6 is primary.

The reactivity of the three hydroxyl groups under heterogeneous methods can be affected by their inherent chemical reactivity as well as the steric effects due to the supramolecular structure of cellulose. For example, it has been found that the primary alcohol group can react ten times faster than the other two secondary alcohol groups for esterification.

Functionalization via surface modifications.

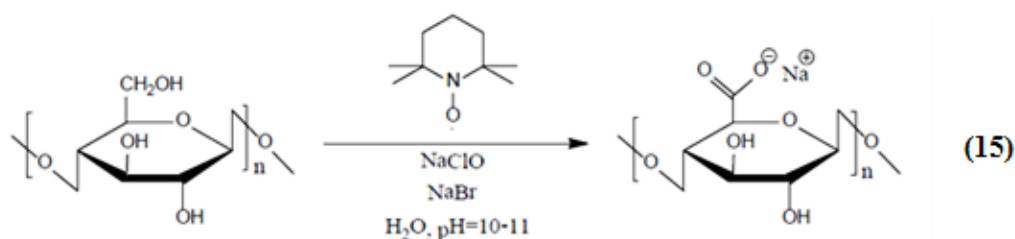
Surface modification of cellulose is through direct chemical modification and/ or covalent attachment of molecules. It is an important approach for synthesis of new and novel materials with improved the performance and value-additions. A broad range of chemical modification has been focused on the functionalization of NFC. Five main categories of reactions are oxidation, esterification, etherification, carbomethylation, and silanisation. We give details of the reaction procedure hereafter.

Basically, the chemical modification of nanocellulose fibers by selective oxidation reactions of primary and secondary hydroxyl groups of the pyranose ring in the cellulose, which present an attractive means do creates new characteristics by the introduction of carboxyl and aldehyde active groups on the polymer surface [92]. From the general formula of cellulose, different oxidation- reduction properties could be expected which the specificity of the end-chain terminal hemiacetal must be added. NFC is still hydrophilic

after oxidation, but increase in the contact angle with water was observed as compared with the parent cellulose, suggesting a change in the H-bonding network at the surface [93].

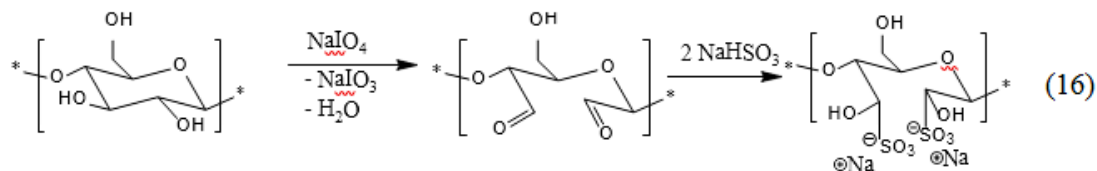
The partial oxidation of cellulose tends to have a high adsorption capacity on the such way introduced the functionalities for the suitable modification of its surface, in order to incorporate metal oxide into its structure [94]. The new binding (incorporation) of metal oxides on the surface of the cellulose, which gain novel properties, highly advantageous and changing from those initial.

The most popular route involves NFC suspension is oxidized by 2,2,6,6-tetramethylpiperidine-1-oxyl radical (TEMPO) with NaClO as a primary oxidant and NaBr as an additional catalyst, at pH of 10-11 to form carboxylate negatively charged group on the surface of NFC (eq.15) [95]. The reaction is selective to the primary alcohol at the C6 position of the anhydroglucose unit to aldehydes and further to carboxylates. The only hydroxyl methyl groups of cellulose are oxidized, while the secondary hydroxyls remain unaffected. As a result, the nanofibrils within the fibers separate from each other easier, as the electrostatic repulsion among the ionized carboxylates holds the hydrogen bonding between the fibrils. When the carboxylate contents reach approximately 1.5 mmol/g, the oxidized cellulose slurries are mostly converted to transparent, highly viscous dispersions with nanofibrils of 3-4 nm in width and a few microns in length [95]. Afterwards, they have developed the oxidation in neutral or slightly acidic conditions, utilizing TEMP/NaClO/NaClO₂ system [96]. Thus, the undesirable side reactions such as depolymerization and discoloration, taking place under alkaline conditions, are avoided [96]. Consequently, aldehyde-free nanofibrils with the uniform fibril distribution can be achieved, almost completely maintaining of the original DP.

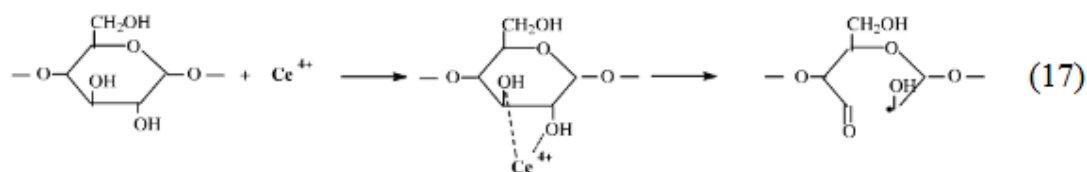


Other oxidation processes have been investigated recently to overcome the drawback of TEMPO oxidation. By pre-treating cellulose pulp with periodate and sodium bisulfite before mechanical disintegration, Liimatainen et al. is obtained a similar effect than

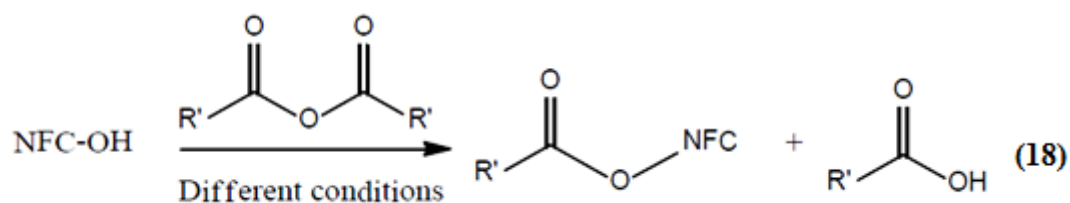
with the TEMPO-oxidation method by regioselective periodate oxidation and sulfonation of cellulose pulp (eq.16) [97].



Stenstad *et al.* [98] used ammonium cerium (IV) nitrate as a powerful oxidation agent for the post-oxidation of 1,2-glycol groups of NFC by Ce^{+4} , with the objective to further react the oxidized NFC with glycidyl methacrylate (eq.17).



Esterifications include acetylations with acetic acid and acetic anhydride which produce cellulose derivatives with different properties depending on the degree of substitution (DS) [69]. These cellulose esters have long played an important role in applications such as coating on semiconductors, biodegradable plastics, composites, optical films, and membranes. Esterification of NFC with anhydride is shown in eq.18. The most commonly used anhydride is acetic anhydride, which has been employed either as a fibrillation pre-treatment [100], or for the post-modification of NFC [101].



Esterification in which hydroxyl groups are partially replaced by less hydrophilic ester groups is not more a novelty for tailoring CNF polarity. Generally, esterification treatments do not alter either morphology, thermal stability or the crystal structure of NFC which occurs at C6 that responsible for the change of DS range from 0,02 to 0.24 [92]. Catalysts such as pyridine [101] or perchloric acid in combination with acetic acid have been reported [100], but the reaction could be also performed without catalyst [102]. Other anhydrides, such as trifluoroacetic anhydride, have been also envisaged [103].

In comparison with neat NFC, acetylated NFC (ac-NFC) can be more easily dispersed in organic solvents of low polarity such as chloroform [101]. Regarding the barrier properties, oxygen permeation was found to increase after acetylation, but water sorption decreased [101, 102, 104]. Ac-NFC has been incorporated in polymer matrices, such as PLA [100,101] or acrylic resins [100,104], but mixed results were found regarding the mechanical performances.

Etherification is an important method for the industrial production of cellulose derivatives. Cellulose ethers can be prepared by treating alkali cellulose with a number of various reagents including alkyl or aryl halides, alkene oxides, and unsaturated compounds activated by electron-attracting groups [105].

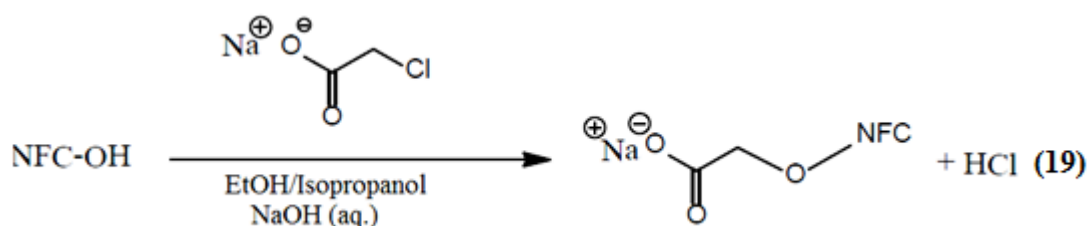
Commercial cellulose ethers are normally graded based on the chemical nature of the substituent, the degree of substitution (DS) or molar substitution (MS), and solution viscosity [105]. The DS denotes the average number of alcoholic groups substituted per anhydroglucose unit, and can thus vary between 0 and 3. Since etherification reactions generate new reactive sites that are capable of chain branching, the extent of reaction or MS is used occasionally. MS is defined as the moles of reagent combined per mole of anhydroglucose. Therefore, the ratio of MS to DS is a measure of the average length of the hydroxyalkyl chain. These cellulose ethers are relatively amphiphilic as a result of chemical grafting of hydrophobic alkyl chains.

The etherification of NFC has been mostly conducted using halogenated or epoxy-based reactants, through nucleophilic substitutions and ring-opening reactions, respectively. Cellulose ethers can be either soluble in organic or aqueous media, but for the context of this review, only water-soluble cellulose ethers will be discussed.

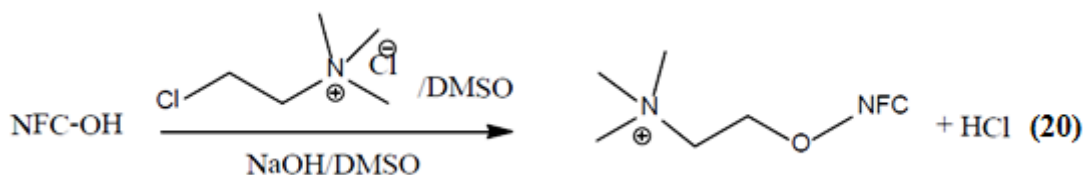
Methyl cellulose (MC) has the most straightforward chemical composition among cellulose derivatives with a partial replacement of hydroxyl groups with methoxy moieties. The balance between hydrophilic hydroxyl and hydrophobic methoxy groups determines the aqueous solubility of the polymer. If the DS is too low, sufficient hydrogen bonds remain that this MC is still insoluble, whereas MC with a high DS is hydrophobic and is also insoluble in water [106]. Therefore, the commercial products usually have an intermediate DS, ca. 1.7-2.0.

Commercial MC is a heterogeneous polymer consisting of highly substituted zones called “hydrophobic zones” and less substituted ones called “hydrophilic zones. MC exhibits lower critical solution temperature (LCST) phase behaviour in aqueous systems; at low temperature the polymer is readily soluble in water, whereas, sufficiently concentrated solutions gel above the LCST. Depending on DS, heating rate, and polymer concentration, the sol-gel transition generally resides in the range of 50-60 °C [106]. At low temperatures, the water-polymer interactions are stronger than the polymer-polymer interactions and “cagelike” water structures surrounding the hydrophobic methoxy groups were formed, leading to MC solubilization in water.

The carboxymethylation of NFC with chloro acetic acid, sodium salt has been used to introduce negative charges at the NFC surface (eq.19) [107]. In contrast to TEMPO oxidation, this reaction is not selective to primary alcohols.

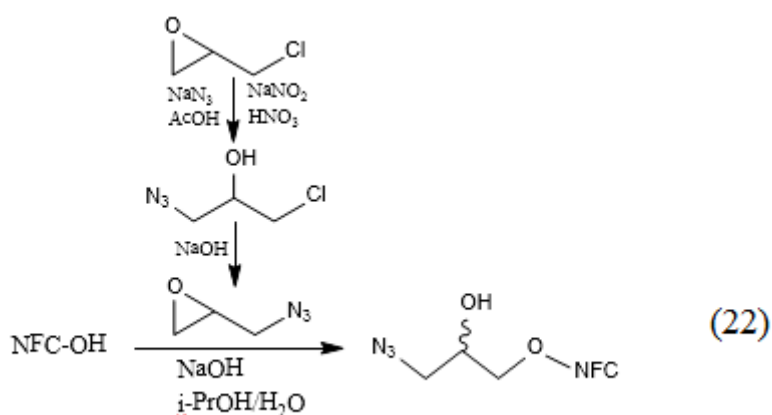
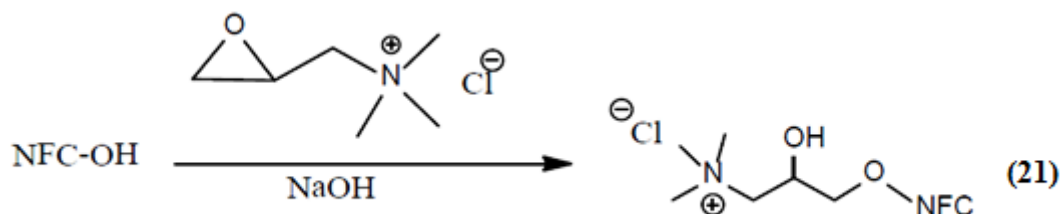


Similarly to TEMPO oxidation, this reaction has been applied as a pre-treatment before mechanical disintegration, to decrease the energy consumption in NFC production, to increase the hydrophilicity and to decrease the thermal stability of NFC after carbomethylation [107]. Aerogels of carboxy methylated NFC (cm-NFC) have been investigated, with the objective to prepare porous materials with tuneable oleophobicity [108]. Etherification can be also used to introduce cationic functionalization at the NFC surface, by reacting NFC with choline chloride (eq.20) [109].

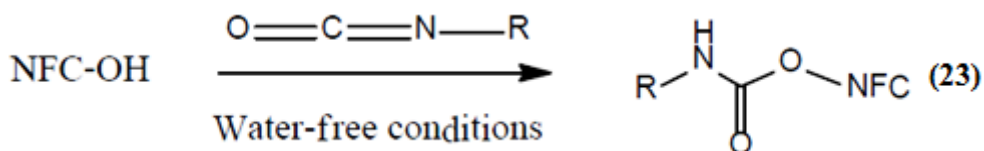


Pei *et al.* used another etherification route to prepare cationic NFC: they first modified cellulose pulp with glycidyl trimethylammonium chloride (eq.21), then subsequently passed the etherified material in a microfluidizer [110]. The quaternized NFC

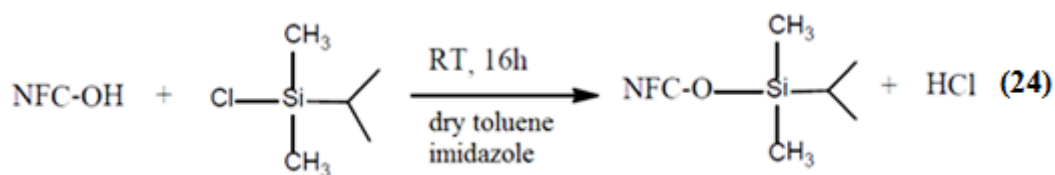
obtained was able to adsorb anionic dyes from aqueous systems. In another study, ring-opening etherification was used to introduce azidealkyne groups (eq.22), which were further grafted by click chemistry [111].



Carbomethylation with isocyanates is another route to covalently bond organic functions on the surface of NFC (eq.23). Siqueira *et al.* have used this functionalization pathway to introduce hydrophobic noctadecylchains at the NFC surface and to reinforce poly(ϵ -caprolactone) matrices [112]. Stenstad *et al.* grafted hexamethylene diisocyanate at the NFC surface, which they further cross-linked into a hydrophobic polymer layer, or reacted with amines to introduce a positive charge at the NFC surface [113].

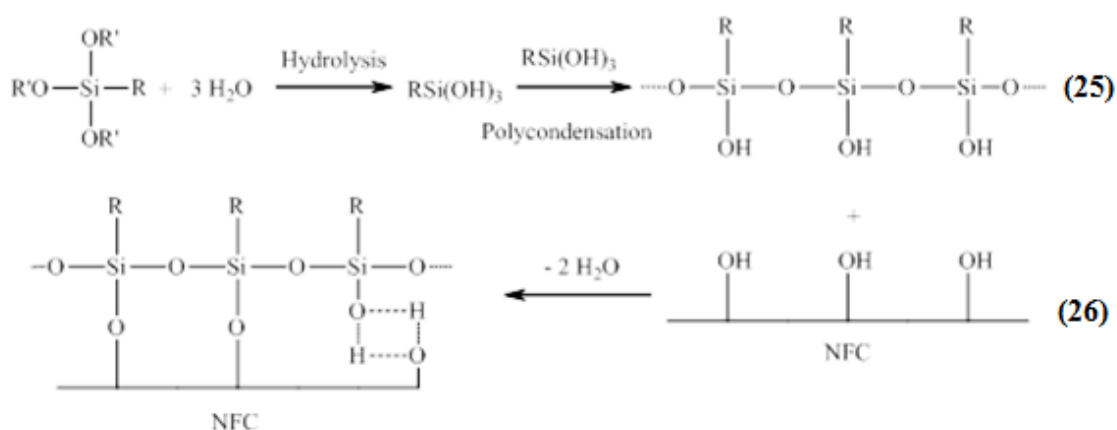


Chlorosilanes can react with NFC hydroxyl groups according to eq.24. This reaction liberates HCl as a by-product, which is generally trapped by amine-based molecules [114]. This reaction allowed producing highly hydrophobic nanofibers, which could be dispersed in THF, toluenediethyl ether, chloroform, dichloromethane and rapeseed oil.



Chemical vapour deposition (CVD) has been also envisaged, to graft various chlorosilanes on NFC foams [115]. The main purpose and achievement of these works was to create superhydrophobic materials with tuneable oleophilicity/oleophobicity, which could float on the water surface and show selective absorption of non-polar solvents and oil.

Alkoxysilanes react with hydroxylated substrates such as cellulose, according to the sol-gel process presented in eq. 25 and 26 [116]. Compared with the chlorosilanesilylation, the grafted silanestructure is rather complex and depends on reaction conditions. Alcohol/water mixtures are generally used as solvent. Tingaut *et al.* performed silylation with vinyl trimethoxy silane (MeOSiVi) or 3-mercaptopropyl trimethoxy silane (MeOSiSH) to introduce vinyl or thiol group at the NFC surface for further thiol-ene coupling with click chemistry [117]. Qu *et al.* performed the mechanical disintegration of cellulose pulp in ethanol to produce an NFC suspension which was further modified with 3-methacryloxypropyl trimethoxysilane (MEMO) [116]. Polylactic acid (PLA) nanocomposites reinforced with the MEMO-modified NFC displayed improved mechanical properties, but the thermal stability of the NFC decreased after silylation.



Lu *et al.* modified NFC with (3-aminopropyl) triethoxysilane (APS) and 3-glycidoxypropyl trimethoxysilane (GLYMO) in acetone, and incorporated the silylated NFC in epoxy resins. They observed an increase in the storage modulus of the epoxide composites

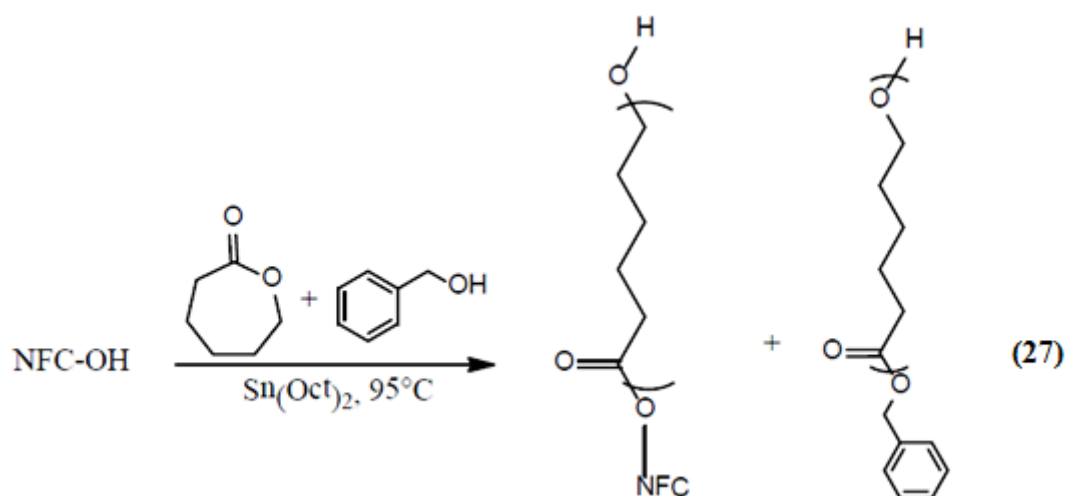
when NFC was modified with the amino silane. Frone *et al.* modified NFC with APS in an ethanol/water mixture prepared PLA composites which displayed better interfacial adhesion after silylation [118]. Qua *et al.* performed the 3-glycid oxy propyl tri methoxysilane (GLYMO) for silylation during the disintegration process, when preparing the NFC. This is the only work reporting silylation in a 100% water system. The nanofibrils obtained were thinner, as the silylation treatment prevented the re-agglomeration of nanofibrils.

The “Click chemistry” concept was firstly introduced by Kolb *et al.* for production with very high yields, inoffensive by-products, simple reaction conditions, and use of easily removable solvents, or water or no solvent [119]. This concept has been applied to the functionalization of NFC by a few authors. A preliminary functionalization of the substrate is usually required in order to introduce a reactive site (azide, alkene, alkyne group, etc.) that will be later reacted with appropriate molecules.

The Copper-Catalyzed Azide Alkyne Cycloaddition (CuAAC) “click” reaction has been recently used by Pahimanolis *et al.* to graft 1,2,3-triazole-4-methanamine (route A) or 5-(dimethylamino)-N-(2-propyl)-1-naphthalenesulfonamide (route B) at the NFC surface, in water medium [120].

Thiol-Ene coupling reactions have also been recently envisaged as an alternative to the azidealkynemethod. These reactions can be catalyzed by acids or bases, or photochemically [117]. Nielsen *et al.* used methacrylic acid to introduce ene entities at the surface of cellulose nanocrystals, which further underwent thiol-ene reaction with cysteamine [121]. The objective was to prepare fluorescent labelled nanocelluloses. In the work of Tingaut *et al.* [117] ene or thiol groups were first introduced at the surface of the NFC films by silylation with MeOSiVi or MeOSiSH, respectively. The resulting films were subsequently coupled with thiol or ene-functionalized molecules, under UV irradiation and at room temperature, leading to materials with tuneable surface properties.

It is also possible to graft polymer chains directly at the NFC surface by applying the *graft from* the method. Poly(ϵ -caprolactone) (PCL) has been accordingly grafted at the surface of NFC by ring opening polymerization and the polymer chain length was controlled by adding different initiator/monomer ratio (eq.27) [122]. The grafted NFC could be dispersed in low polarity solvents such as THF.



Functionalization and dissolution via synthesis of CNF.

The major drawback in covalent functionalization to increase the hydrophobicity of nanocellulose is the tedious solvent extraction process and the use of organic solvents in these reactions. So, one-pot process for surface modification to prepare the CNF consists of strong acid hydrolysis under controlled conditions followed by sonication to separate the crystals. The acid hydrolysis is considered to be a heterogenous acid diffusion process where the less ordered amorphous regions are attacked by acid resulting in cleavage of glycosidic bonds. It is proved that the longer hydrolysis time leads to shorter nanocrystals and also to an increase in their surface charge. On the contrary, the lower reaction times yields large, undispersable fibers and aggregates. The influence of the reaction conditions on the surface charge is not significant and controlled by other factors than hydrolysis conditions such as; hydrolysis temperature and acid type and concentration [123]. Hydrochloric and sulfuric acids have been extensively used, but phosphoric and hydrobromic acids have been also reported, but with minor methods [123]. Such processes for surface functionalization of CNF have the potential for application in large volume or even online and one-pot composite processing.

Hydrochloric acid.

The synthesis of nanocrystals of cellulose through hydrolysis of hydrochloric acid has weakly charged surfaces and low dispersion in water [124] and leads to degradation and formation of hydroxylated cellulose surface with weakly negative charges. So, the colloidal

is unstable [142].

Sulphuric acid

Through the hydrolysis by concentrated sulfuric acid become strongly negatively charged due to the grafted sulphate ester groups on the surface of groups and consequently stabilizes the aqueous suspension and exhibits an excellent dispersibility in water because the electrostatic repulsion mechanism [58,125]. Beck-Candanedo *et al.* produce stable suspensions of colloidal-sized cellulose Nano crystals by sulfuric acid by hydrolysis of wood and cotton cellulose [126]. Sulphonation is the only regioselective C6>C2>C3, while leading to severe depolymerization and major modification of the crystal structure, with crystal structure of cellulose II polymorphous which being isolated [127]. For comparing the hydrolysis of sulfuric and hydrochloric for stable suspension of CNF, it noted that the sulfuric acid provides more stable aqueous suspension than hydrochloric acid due to the esterification of surface hydroxyl groups to give completely negative charged of sulphate ester groups while hydrochloric acid produce CNF with minimum surface charge [128].

The same authors emphasized the importance of time and temperature of hydrolysis together with the sulfuric acid concentration as important single factors in the process of preparation of negatively charged isolated nanocellulose whiskers in water. Cellulose whiskers with a length ranging between 200 and 400 nm were obtained by using a 63.5 wt% sulfuric acid concentration for approximately 2 h and with a yield of 30% [129].

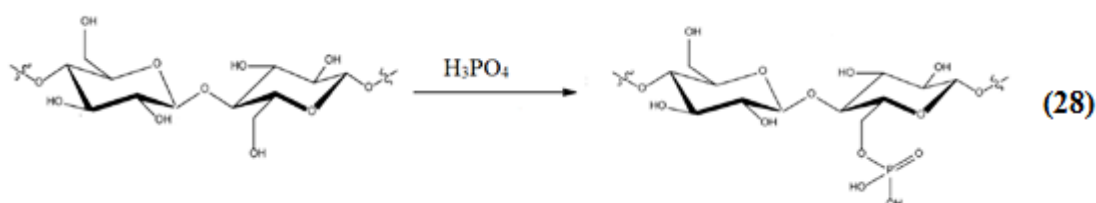
Phosphoric acid

Phosphoric acid has many advantages for dissolution and functionalization of cellulose such as; its non-toxic, non-corrosive, safe, in expensive as compared to other inorganic mineral acids [130]. Phosphoric acid is a special acid due to it can form dimers, oligomers and even polymeric forms. The dissolution by phosphoric acid generates nanocrystals with good dispersibility in polar solvents as a result of surface phosphate groups [131]. Interestingly, the difference in the surface functionalization also causes the phosphorylated CNF to display a much higher thermal stability than sulphated CNF.

The high reactivity of cellulose which is appropriate for functionalization of cellulose by swelling in 85 % phosphoric acid with quick dissolution of cellulose [132].

However, the drawback he sees is that once dissolved in phosphoric acid, the cellulose is difficult to isolate.

Cellulose dissolving involves two processes; one is the esterification reaction between the hydroxyl groups in cellulose and phosphoric acid to form anisotropic solution of cellulose phosphate over a wide range of degree of substitution (eq.28) and then it generates a competition for producing a hydrogen bond between the hydroxyl groups in cellulose chains and water molecule or with hydrogen ion that result from the acid hydrolysis of the β -glucosidic bonds of cellulose [133]. It has been demonstrated that the DS by phosphate group depends on the molar ratio of cellulose and phosphorylating agent, anhydroglucose units of cellulose, time and temperature of reaction .



It is found that water plays a detrimental role in the solvent quality. The problem then is, however, that anhydrous orthophosphoric acid is a solid with melting point of 42 °C. Cellulose phosphate can be returned back to free phosphoric acid and amorphous cellulose without any significant substitution or recrystallization through the phosphoric acid regeneration by water [132]. If cellulose is to be dissolved therein, the temperature has to be raised. Under such conditions, the rapid degradation occurs. Apart from that there is always still about 1-2 % w/w water in the acid, and approximately 5 % w/w water in the cellulose, which might both account for the relatively poor solubility of cellulose. Both problems can be overcome by increasing the orthophosphoric acid concentration to over 100 % w/w.

The pretreatment of cellulosic fiber by phosphorylation, which can help the synthesis of CNF by precharging the fiber by introduction of anionic phosphate groups using phosphorylating agents such as phosphorous pentoxide (P_2O_5), diammonium hydrogen phosphate ($(NH_4)HPO_4$), phosphoric acid (H_3PO_4), phosphorous oxychloride ($POCl_3$) and organophosphates has been studied in the recent years [134]. During activation by H_3PO_4 , it will transform into polyphosphoric acids. So, H_3PO_4 is known as a dehydration agent by

heating in different polycondensed forms such as; pyrophosphoric acid ($H_2P_2O_7$), metaphosphoric acid (HPO_3), and polyphosphoric acid ($H_6P_4O_{13}$) and so on [135]. It is reported that the different polycondensed degrees of these phosphorous oxyacids (POA) make different roles in the activation process and could have a great effect on the physical and chemical properties of the final nanofiber. Phosphorylation usually takes place in the presence of an organic solvent such as N,N-dimethylformamide (DMF), pyridine, or urea, which has a swelling effect on the cellulose-rich fibers and is a medium for phosphorylation reaction [134].

The irreversible adsorption of CNF depends on the amphiphilic features of cellulose nanocrystals residing in the crystalline organization at the elementary brick level [136]. On the other hands, the change of cellulose properties through chemical modification by phosphate helps in the synthesis of new metal oxides associated with immobilized cellulose groups. However, the colloidal stability of cellulose nano crystals which produce a specific interactions of counter ions with the deprotonated carboxyl groups and the screening effect of the salt [137].

1.2.6. Modification of photocatalytic TiO_2 by cellulose for formation hybrid microcomposites.

Recently, significant effort has been focused on developing innovative synthetic approaches to control the morphology and structures of titanium dioxide nanoparticles and its subsequent combination with organic materials to produce novel hybrid nanocomposite materials with an improved combination of mechanical, thermal, chemical and optical properties [138]. Inorganic/organic hybrid materials are generating many novel, exciting properties which not only depend on the properties of their individual component, but also the characteristics of their inner interfaces [139]. Much attention has been given to the fabrication of polymer-titania microcomposites as a means of overcoming the ensuring aggregation and separation difficulties that have been frequently encountered. Towards this end, few researchers have explored using supercritical fluids as a means to incorporate insoluble inorganic particles such as titania into the polymeric network like cellulose [140]. Nature-derived materials such as cellulose is an ideal bio template for the immobilization and stabilization of metal oxide nanoparticles to yield functional metal oxide/cellulose composites [141]. It exhibits not only topological variety and diversity and control the

growth of nanoparticles, but also sophisticated multifunctionality and mechanical support. The hierarchical structure of cellulose is a unique which inspired to create novel functional materials. There are many different ways to obtain titania / cellulose hybrid microcomposite. We have classified the strategies to associate titania and cellulose as a biotemplate in the following sections.

a) Coating of TiO₂ on the cellulosic fiber.

There are approaches generally adopted for the fabrication of titania / cellulose composites via in situ synthetic process, where the titania precursors are firstly absorbed onto the surface cellulose substances, and subsequently hydrolyzed to form titania [142]. The unique properties of nanoparticles render them of interest as property modifiers for cellulosic paper due to their quantum-confined properties. It has functionalized by titania nanoparticles to modify or induce the electronic, optical and catalytic properties of cellulose paper. A very low concentration of nanoparticles can result in an excellent photo-catalytic performance. Ngo *et al.* presented different methods based on their ability to control the structure of paper have been reviewed in the preparation of the nanoparticle-functionalized cellulose paper (Figure 1.10) [143].

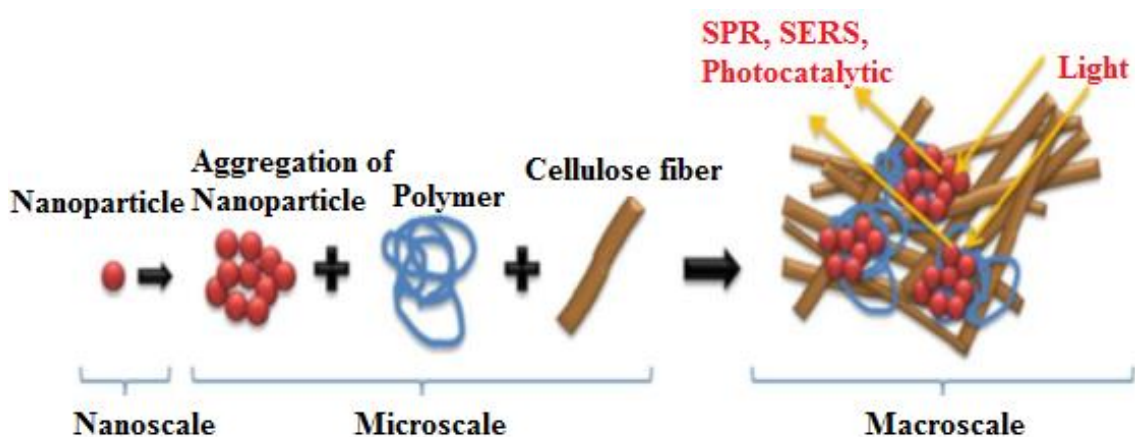


Figure 1.10. Different scales of the constituents of nano-modified cellulose paper [143].

Koskinen *et al.* proposed a method to modify the wetting properties of cellulose surfaces by depositing plasma-polymerized fluorocarbon films on cellulose to achieve hydrophobic surfaces. They investigated the moisture-absorption features of fluorocarbon films deposited on cellulose and paper and also their resistance to lipophilic components [144]. The role titanium dioxide in the protection of cellulose works of art has been

investigated as a protective coating against bacteria, pollutant gasses and the damaging effect of ultraviolet radiation. So, on the production site, it is important to monitor and control the nature of the cellulose surface as this monitoring provides insight on how to improve the surface properties.

Modification of cellulose surface through the interaction between nanotitania and cellulose fiber showed the relationship between the physical properties of the nanoparticle-coated cellulose and control of surface hydrophobicity were investigated [145]. Abidi *et al.* reported the successful modification of cotton fabric by titanium dioxide nanosols prepared by means of the sol-gel process with tetrabutyl orthotitanate $[\text{Ti}(\text{OC}_4\text{H}_9)_4]$ as the active ingredient [146]. The titania-nanosol treatment imparted to the cotton fabric a very good protection against UV radiation and self-cleaning properties. Nishibori's patent describes the preparation of photo-catalytic fibres from waste paper using thermoplastic binders in a dry forming process [147]. The treated fibres can then be used in papermaking or nonwoven manufacture.

Protection of textiles against photodegradation and the creation of new advantageous functions can be realized by coating of the textiles with silica nanoparticles, for example, with a diameter smaller than 50 nm using the corresponding silica sols [148]. Vegetable cellulose fibres have been surface-modified using the hydrolysis of tetraethoxysilane (TEOS), octyltrimethoxysilane (OTMS) or (PTMS), followed by the layer-by-layer deposition of previously synthesized titanium dioxide nanoparticles [138]. Recently, Koga and his co-workers introduced amino groups onto the surface of cellulose through a silane-coupling technique using APTES to modify the cellulose surface. They then investigated the mechanical strength and hydrophobicity of the amino-modified cellulose (Figure 1.11) [149]. They found that this paper modified with amino groups has great potential to be used in the chemical industry as a base catalyst.

Titania on cellulose demonstrates various activities like stain removal and self-cleaning surface via the photocatalytic degradation, antibacterial deodorizing, UV blocking, flame retardant, and deNO_x functions. It can also provide both surface hydrophobization and hydrophilization [148]. A current dominant coating technique for cellulose, are so called dip-pad-dry-cure and dip-coating methods [151,152]. It is performed with separately

prepared TiO₂ sol nanoparticles. Fabric is padded simply with a sol solution. The typical disadvantage of this technique is in the in appropriate adhesion of titania with biomacromolecules. Attempts to prepare TiO₂ directly on cellulose were done [148]. The precursor was dripped in cellulose-containing aqueous solution under the ultrasonic irradiation. Attainment of this aim is in doubt because of the fast hydrolysis–condensation reactions starting instantly after the contact of precursor with water. Evidence for that followed from loose coating on the fibers [153]. Kunitake with Huang provided first the absorption of precursor on cellulose fibers by passing its non-aqueous solution [154]. When water followed subsequently through this treated sample, it promoted the instant hydrolysis and condensation reactions resulting in the TiO₂ formation.

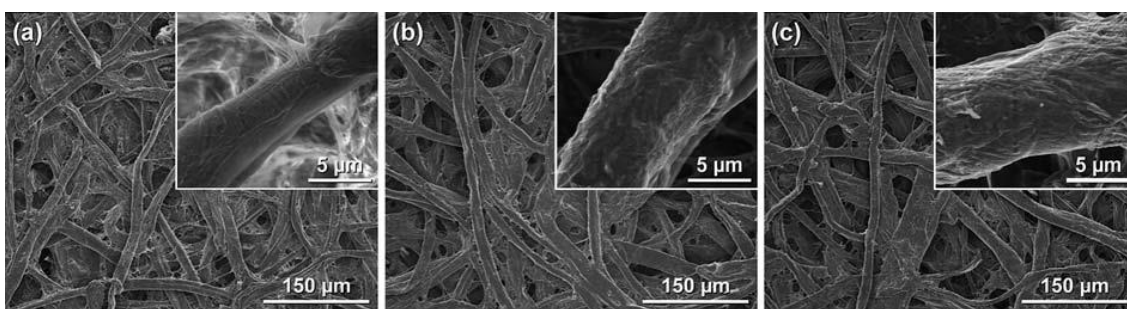


Figure 1.11. SEM images of (a) untreated paper, (b) NH₂-modified paper, and (c) PEI-modified paper investigated by Koga et. al [149].

The synthesis of titania on the cellulose fibers by the most above-considered methods did not provide sufficient binding of TiO₂ with polysaccharide. It causes the poor operational stability and durability of bionanocomposite materials. To enhance the stability of titania coating, an additional cross linking as a binder [155] or negatively charged functional groups [156] were introduced into the cellulose substance, but, as a result, the microstructures of the composites were affected [156]. Polycarboxylic acids attached covalently to cellulose fiber surface allowed binding titania through electrostatic interactions with free carboxylic groups [157]. These cross-links improved notably functional properties of textile with TiO₂ coating. It still remains a challenge to fabricate bulk titania/ cellulose composite materials where ultrafine titania crystallites (several nanometers in size) are uniformly deposited on the cellulose nanofiber surfaces by a simple and facile methodology. Carboxylic groups were also introduced directly on the cellulose surface by using radio frequency plasma, microwave plasma and vacuum-UV irradiation

treatment [155]. Under these conditions the chemical degradation of fibers took place as well that can decrease the durability of textile.

b) Porous titania by cellulose as a sacrificial template.

Porous titania can be obtained by a broad range of chemical and physical methods, which can broadly divide into template free and templated approaches [158].

Nanostructured porous titania shows improved performance compared to flat bulk materials. First, the porosity increases the surface able to accommodate large amounts of pollutant molecules. Second, the diffusion distances of charge-carriers in nano-sized particles are much shorter than in the corresponding macroscopic materials. Therefore, the charge carriers photogenerated in nanostructured semiconductors can be scavenged without significant recombination losses.

Sintering of nanoparticles is a common way to obtain porous metal oxide in a template-free approach. For instance, titania nanoparticles can be synthesized in a separate reaction and then deposited as a film on a substrate. Sintering of such film provides connectivity between titania nanoparticles and generates porosity arising from the interstitial voids. The disadvantage of this method is a poor control over porous morphology, as the porosity is defined solely by the initial shape and packing of the preformed nanoparticles.

One attractive approach to fabricate crystalline metal oxides with a periodic mesoporous nanostructure is to use shape-persistent organic templates. Additionally, replacing expensive synthetic polymers by natural biopolymers would lead to the more cost-effective fabrication of functional metal oxides. Moreover, further carbonization of the organic natural substances under proper conditions could yield unique nanostructured carbon materials with inherited fine morphologies.

Sacrificial biotemplating of porous metal oxides such as titania can be achieved by using insoluble natural materials such as cellulose nanocrystals as moulds or templates. The function of the biotemplates is similar to that of the soft templates, i.e. block-copolymers that are employed in the sol-gel template-assisted synthesis [158]. Analogous to the soft templates, the cellulose nanocrystals first direct the formation of titania, and then introduce

the porosity and crystallize the titania after being decomposed after calcination process.

The recent progress in templating with NFC has simulated the discovery of a whole family of new chiral functional materials [159]. NFC-aided nanocasting has been successfully employed for the fabrication of materials other than silica chiral, such as chiral mesoporous carbon, chiral mesoporous titania, and flexible photonic resins.

Although titania has been successfully templated by natural materials of macroscopic dimensions, such as green leaves [160], corn stalks [161], natural cellulose fibers [162], filter paper [139], nanocellulose aerogels [163], bacterial cellulose, etc., the studies on titania nanostructured by nanoscale colloidal cellulose crystals are rather scarce.

It allows the formation of titania with unusual morphologies features, such as fibers, needles, and tubes which has never been noted with other approaches. Zhou *et al.* have applied cellulose nanocrystals in the synthesis of titania nanocubes [164]. Chen *et al.* prepared hierarchically nanostructured titania powders via one-pot hydrolysis of a titania precursor in the presence of cellulose nanocrystals [165]. Nanocrystalline cellulose sponges obtained by freeze-drying were employed as scaffolds to obtain porous titania monoliths. Nanocellulose aerogels have been used as a template for porous titania nanoparticles [166].

Moreover, the development of nanofibrous carbon materials from cellulose as a biotemplate with a uniform titania coating and possessing sufficient photocatalytic activity remains challenge. By coating each nano fibers with thin titania gel films, followed by carbonization in nitrogen, hierarchical, anatase-titania-coated, carbon nanofibrous material was obtained [139]. Carbonization of titania has been realized by vacuum heating of composites containing cellulose nano-whiskers [167]. Composites of titania and cotton-nanofibers have been studied for applications in drug delivery [168]. Shopsowitz *et al.* have translated the chiral nematic organization of the cellulose nanocrystals to porous titania by a two-step sacrificial templating approach [154]. Here, NCC derived chiral silica was employed as a hard template to replicate chiral titania.

The fabrication of different nanoporous metal oxides by combining the cellulosic templates [169] and polysaccharide nanoparticles [170] with metal precursors became a very popular technique due to the straightforward synthesis and availability of the templates.

The as-prepared powders and freestanding films are mostly employed in photocatalysis [139,159,161,164], however, more elaborated devices such as solar cells [170] and Li-ion batteries have been reported as well. Obviously, the fabrication of crystalline metal oxides, especially titania features both high crystallinity and high porosity require the development of special synthesis methods.

c) Porous titania by cellulose as a permanent template.

One possibility of using a cellulose as permanent biotemplate is to employ directly in the synthesis of porous hybrid nanocomposites by using insoluble cellulose acting as moulds for replication. This method takes advantage of the diversity and sustainability of natural materials, thus offering new opportunities in tune morphological, chemical and physical characteristics of the target products. To date, materials synthesis assisted by natural materials is a very fast-growing research area in the field of nanotechnology [138,139, 169].

Different methods for production of hierarchical nanofibrous TiO₂ / cellulose composites like gas-solid displacement reactions [171], atomic layered deposition (ALD) [172], and wet chemistry techniques, such as sol-gel processes [169], and hydrothermal methods [173] have been employed to this end. Huang and Kunitake have pioneered the facts of the replication of the morphological hierarchies of natural cellulose substances from macroscopic down to nanometer scales with metal oxides by precise ultrathin-film coating of cellulose nanofibers in the bulk cellulosic material [154]. It possesses unique properties as a result of the combination of the functional and structural characteristics of the composites formed by guest titania thin-film coated to host cellulose [172].

In addition, the nanoscale of cellulose fibers is approximately 10 to 100 nm in the form of a web-like network microstructure, which makes cellulose one of the most highly porous materials. The feasibility of the synthesis of regenerated cellulose /TiO₂ hybrid nanocomposite membrane in water and wastewater treatment has been extensively studied due to their desirable mechanical, antibacterial, electrical, and optical properties and good compatibility between the TiO₂ nanoparticles and cellulose chain. This compatibility as a result of the formation of covalent bonds between TiO₂ nanoparticles with cellulose chain that can improve the rigidity of the polymer chain and increase the energy to break down

the polymer chain [174]. For instance, Zeng *et al.* offered immobilization of titania in a cellulose matrix for photocatalytic degradation of phenol under weak UV light illumination [175]. Zhu *et al.*, developed a novel inorganic–polymer hybrid membrane by the incorporation of nano-TiO₂ into cellulose with high activity for dehydration of caprolactam by pervaporation [176]. Zhang and co-workers synthesized bacterial cellulose (BC)/TiO₂ hybrid composite membrane doped with rare earth elements, and estimated for its photocatalytic characteristics [177]. They found that, the resultant composites membrane has ultrafine nanoporosity, water absorption characteristics, and high strength, whereas the photocatalytic efficiency was sufficiently improved after the TiO₂/BC membrane was doped with rare earth ions. Moreover, reusable photocatalytic titanium dioxide-cellulose based films showed the potential for degradation of organic pollutants in natural water sources [178]. Recently, the novel regenerated cellulose/N-doped TiO₂ nanocomposites membranes are prepared by the phase inversion method with the utilization of recycled newspaper as the cellulose source in NaOH/urea aqueous solvent system to provide new, green and highly efficient photocatalytic hybrid composite membranes under visible light to be used in waste water treatment [179].

Because of the limitation of cellulose such as toxicity, agglomeration, and big particles, it can be overcome by immersion methods that can be further modified by reduction, sol-gel, or precipitation reaction to add functionalities to the cellulose membrane. Metal oxides nanoparticles can be impregnated in the porous nanofibrous structure by physical adsorption methods, hydrogen bonding, and covalent bonding. Furthermore, the BC sheets of specific size can be used instead of having no control on the sample size in the case of an *in-situ* incorporation method [180]. Conductive films of TiO₂/BC composite had been prepared by a sol-gel technique. Electrostatic force microscopy (EFM) had been used to measure the conductive properties. When negative applied voltage had been applied, the EFM image showed higher contrast, indicating the response of TiO₂ nanoparticles. These TiO₂ nanoparticles are located on the surface of BC fibers by H-bonding between the BC fibers and hydrophilic inorganic TiO₂ sol-gel network [181].

Similarly, a solvent exchange and sol-gel techniques had been used to prepare inorganic/organic composite such as TiO₂/BC, vanadium oxide (V)/BC and hybrid TiO₂/V/BC (2np) composite (Figure 1.12). The hydrogen bond formation and between OH

and hydrophilic sol-gel network decreased the crystallinity of composite materials. The 2np/BC composite showed increase in mechanical and reversible photochromic property [182].

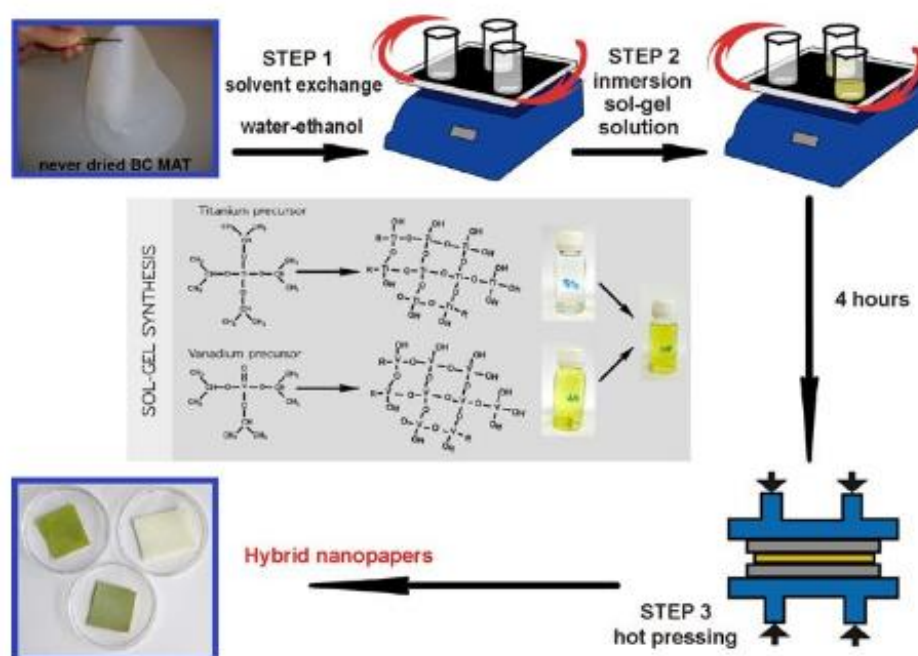


Figure 1.12. Illustration of the mechanism of composite nanopapers formation by solvent exchange and a sol-gel technique [182].

Bacterial cellulose had been used as a substrate to prepare BC/TiO₂ hybrid fibers by controlled surface hydrolysis for the photocatalytic degradation of methyl orange. Uniform and well-defined hybrid nanofibers structures were prepared by arraying the spherical TiO₂ nanoparticles on the BC nanofibers. The disordered water molecules were orderly arranged by a solvent exchange method and then dispersing in a mixture of titanium butoxide (Ti(OBu)₄) in an ethanol/urea solution for TiO₂ nanoparticles to deposit on BC nanofibers with molecular precision as shown in Figure 1.13. The high specific surface area and smaller crystallite size resulted in higher photocatalytic activity under UV light [183].

1.2.7. Photocatalytic decomposition by TiO₂/ cellulose.

TiO₂ photocatalysis has received much attention also for degradation of environmentally harmful compounds. Whereas the photo-induced hydrophilicity is caused by a top most surface structural change, conventional photocatalytic oxidation activity depends on the total amount of generating electron-hole pairs [184]. Also, photocatalytic

activity of TiO_2 coatings depends strongly on the phase, the crystallite size and the porosity of the coatings [185]. Furthermore, studies to control the morphology of TiO_2 are abundant, since both, the structural properties and the accessible surface area play a significant role in the efficiency of TiO_2 in many of its applications. On the other hand, cellulose fibers have been shown to serve as a good matrix for highly efficient TiO_2 photocatalysts [175,185,186]. Further, TiO_2 containing pulp, filter paper, and regenerated cellulose films showed good photocatalytic efficiency to decompose toxic organic pollutants and dyes [175,185,186]. Moreover, TiO_2 -cellulose based photocatalysts exhibit also good photostability under weak illumination without any loss of photocatalytic activity after several cycles, or damage in the fiber matrix structure [186,187]. However, if highly crystalline photoactive TiO_2 powder and intensive UV light is utilized, cellulose matrix can be damaged [186].

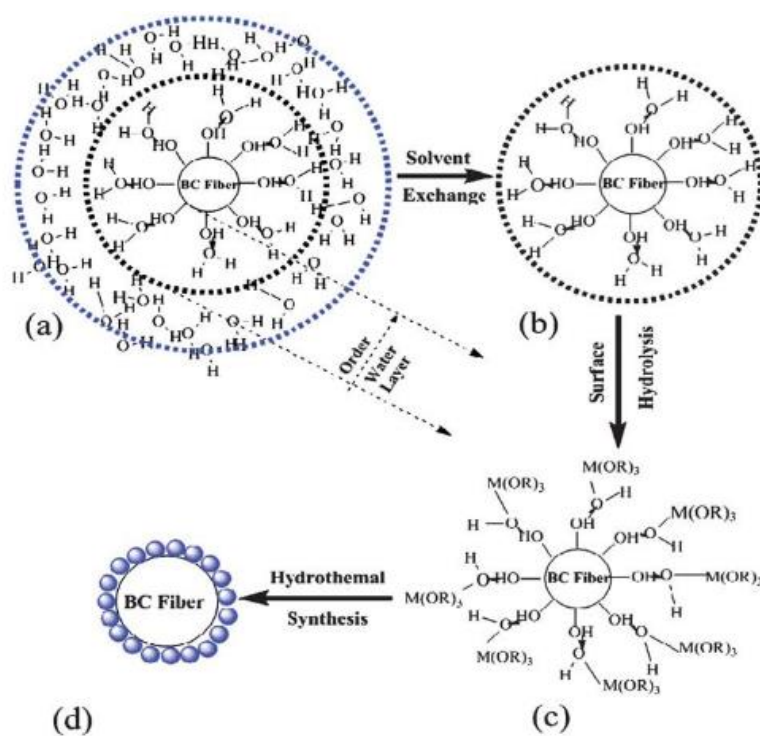


Figure 1.13. Illustration of arraying the TiO_2 nanoparticles on the BC nanofibers by solvent exchange, surface hydrolysis, and followed by a hydrothermal process [183].

Reducing the particle size is generally beneficial for surface-dependent photocatalysis because it increases the specific surface area and hence the number of the reactive sites [187]. As mentioned earlier, one of the examples is applying the cellulose fibrils in the filter papers as templates for synthesis of TiO_2 using sol-gel processes or

atomic layer deposition. Furthermore, particular effort is put on complex or hierarchical and/or porous hetero nano structures to facilitate the separation of photogenerated electron-hole pairs, which further improves the photocatalytic activity [187,188]. Photo-catalysis has been described dealing with a series of tasks involving optoelectronic conversion, surface/interface catalysis, and the post-treatment or recycling of the photocatalyst [187]. Therefore, it is important that all the above-mentioned functions should be optimized and integrated into the photocatalytic system, in order to be practical in use. This has generated the design and fabrication of advanced photocatalytic materials based on hierarchical composite nanostructures [187]. Thus, TiO₂-coated nanocellulose aerogels could be considered as an option. To date, no single composition or structure is able to fulfil all the above-mentioned tasks satisfactorily on its own. As the stability and reasonable cost of the photocatalytic materials are called for, it is important to identify and design new photocatalytically active materials that are efficient, stable and abundant [187].

1.3. Black titania.

Since the early 1990s, much effort has been made to enhance its optical absorption of photocatalytic activity through metal, non-metal or self-doping that generates donor or acceptor states in band gap [189-191]. Although there are many efforts in extending TiO₂ into the visible light region to improve the photocatalytic activity, the results are not up to the mark. At present, nitrogen doped titania displayed the greatest optical response to solar radiation, but its absorption in the visible and infrared remains insufficient.

Theoretically, the bandgap required by semiconductor for photoelectrocatalytic water splitting should be around 1.23 eV due to the hydrogen production potential is only 1.23V. This band gap corresponds 1000 nm in wavelength. Therefore, ideally, the colour of TiO₂ should be turned to black, with an energy band gap of 1.23 eV and the optical absorption near 1000 nm in the near of infrared region. The recent appreciation of engineering disorder of nanophase TiO₂ has opened a new and novel approach for enhancement the solar light absorption and triggered a great amount of interest [192,193]. To justify the improvement of optical properties and photocatalytic activity of hydrogenated black TiO₂, different factors were known such as oxygen vacancies; Ti⁺³ ions, Ti-OH and Ti-H groups, surface lattice disorders, and band gap shifting. However, all of these

properties were different that mainly depending on the synthetic methods [194].

The synthesis of black titania nanocrystals is depending on the ease of penetration of the surface of the titania crystal lattice by hydrogen [195]. Later on, different synthesis methods like hydrogen plasma, chemical reduction, chemical oxidation, and electrochemical reduction have been employed to obtain black TiO₂ [194,196-201]. In addition, various incorporation of impurities that produces Ti³⁺ and oxygen vacancy defects that turn white TiO₂ to yellow or blue and it is reasonable to think that Ti³⁺ is also responsible to turn the colour of white titania into yellow, blue, brown, or black material [202,203]. The observed hydrogen diffusion into TiO₂ (110) surface with a barrier of 1 eV indicated that the hydrogen incorporation into TiO₂ lattice [204].

Very recently, a review article on black TiO₂ materials was published by Chen *et al.* [194] describing the different synthesis methods and the improvement of different properties of black TiO₂ materials. It was suggested that “more efforts are needed for synthesis to property and application in order to finally improve the efficiency of black TiO₂ nanomaterials for practical applications in renewable energy, the environment, and others”. Therefore, a black TiO₂ material with optimized properties would be highly desired for visible light photocatalysis.

1.4. Objectives of the Thesis.

The overall objective of Thesis is to improve the photocatalytic efficiency of titania-based photocatalysts with economic benefits by the synthesis of advanced materials composed of only titania nanocrystals, including both pure oxide phases and/or non-stoichiometric ones, or combinations of them with carbon or functionalized cellulose. All the synthesized materials were used in the photocatalytic degradation of Orange G as a target pollutant. Special attention is paid to achieve high surface area, low recombination rate and to increase the spectral response from UV to visible or solar region. For that, two research approaches have been studied. Firstly to develop a green, sustainable, cheap and facile method for synthesis of functionalized cellulose - TiO₂ composites and their corresponding carbon – titania composites. In the second approach, a study of the effect of hydrogenation conditions on TiO₂ structures which is directly related to its crystal phase, crystallite size, defect structures, and its structural properties, including surface area, porosity, morphology,

and pore size distribution.

The specific objectives of this work are discussed and summarized as follows:

- (i) Controlled functionalization of cellulose as a way for the introduction of oxygen and/or phosphate groups on the surface of titania (Chapter III).
- (ii) Deep knowledge on the subsequent structure modifications to select the appropriate method for the synthesis of carbon / titania composites by carbonization (Chapter IV).
- (iii) Development and characterization of the carbon-phosphorous-Ti composites as photocatalysts (Chapter V).
- (iv) Novel progress in the synthesis of non-stoichiometric black titania with controlled morphology (Chapter VI).

1.5. References.

- [1] D.G. Bassyouni, H.A. Hamad, E-S.Z. El-Ashtoukhy, N.K. Amin, M.M. Abd El-Latif, Comparative performance of anodic oxidation and electrocoagulation as clean processes for electrocatalytic degradation of diazo dye Acid Brown 14 in aqueous medium, *J. Hazard. Mater.* 335 (2017)178–187.
- [2] M. R. Hoffmann, S. T. Martin, W. Choi, D. W. Bahnemann, Environmental applications of semiconductor photocatalysis, *Chem. Rev.*, 95 (1995) 69 – 96.
- [3] A. Fujishima, K. Honda, Electrochemical photolysis of water at a semiconductor electrode, *Nature*, 238 (1972) 37 – 38.
- [4] A. Fujishima, T. N. Rao, D.A. Tryk, Titanium dioxide photocatalysis, *J. Photochem. Photobiol. C*, 1 (2000) 1 – 21.
- [5] N. Serpone, E. Pelizzetti, *Photocatalysis fundamental and applications*, Wiley Interscience, New York, 8 (1989) 991 – 997.
- [6] J. M. Herrmann, Heterogeneous photocatalysis: fundamentals and applications to theremoval of various types of aqueous pollutants, *Catal. Today*, 53 (1999) 115 – 129.
- [7] A Mills, S Le Hunte, An overview of semiconductor photocatalysis, *J. Photochem. Photobiol. C*, 108 (1997) 1-35.
- [8] A.L. Linsebigler, G.Q. Lu, J.T. Yates, Photocatalysis on TiO₂ surfaces: principles, mechanisms, and selected results, *Chem. Rev.*, 95 (1995) 735 – 758.
- [9] J. M. Herrmann, Heterogenous Photocatalysis: State of the art and present applications, *Top. Catal.*, 34(2005) 49 – 65.
- [10] C. Nasar, K. Vinodgopal, L. Fisher, S. Hotchandani, A. K. Chattopadhyay, P.V. Kamat, Environmental photochemistry on semiconductor surfaces. Visible light induced degradation of a textile dye, naphthol blue black, on TiO₂ nanoparticles, *J. Phys. Chem.*,

100 (1996) 8436 – 8442.

[11] O. Carp, C. L. Huisman, A. Reller, Photoinduced reactivity of titanium dioxide : Review, *Prog. Solid State Chem.*, 32(2004), 33 – 177.

[12] Y. Mao, C. Schoneich, K. Asmus, Radical mediated degradation mechanisms of halogenated organic compounds as studied by photocatalysis at TiO₂ and by radiation chemistry” in: *Photocatalytic Purification and Treatment of Water and Air*, Ollis, D. F. and Al-Ekabi, H. (Eds.), Elsevier Science Publishers, Amsterdam, (1993), 49 – 66.

[13] J. Schneider, M. Matsuoka, M. Takeuchi, J. Zhang, Y. Horiuchi, M. Anpo, D. W. Bahnemann, Understanding TiO₂ photocatalysis: Mechanisms and materials, *Chem. Rev.*, 114 (2014) 9919-9986.

[14] H. Hamad, M. Abd El-latif, A. Kashyout, W. Sadik, M. Feteha, Synthesis and characterization of core-shell-shell magnetic (CoFe₂O₄-SiO₂-TiO₂) nanocomposites and TiO₂ nanoparticles for the evaluation of photocatalytic activity under UV and visible irradiation. *New J. Chem.*, 39 (2015) 3116-3128.

[15] R. Molinari, A. Caruso, P. Argurio, T. Poerio, Degradation of the drugs Gemfibrozil and Tamoxifen in pressurized and de-pressurized membrane photoreactors using suspended polycrystalline TiO₂ as catalyst. *J. Membr.Sci.*, 319(2008)54-63.

[16] H. Park, Y. Park, W. Kim, W. Choi, Surface modification of TiO₂ photocatalyst for environmental applications, *J Photochem Photobiol C-Photochem Rev.*, 15 (2013)1-20.

[17] K.K. Akurati, A. Vital, J-P. Dellemann, K. Michalow, T. Graule, D. Ferri et al. Flame-made WO₃/TiO₂ nanoparticles: Relation between surface acidity, structure and photocatalytic activity, *Appl. Catal. B-Environ.*, 79 (2008)53-62.

[18] A. D. Paola, E. García-López, G. Marci, L. Palmisano, A survey of photocatalytic materials for environmental remediation, *J. Hazard. Mater.*, 211-212 (2012)3-29.

[19] S. Morales-Torres, L.M. Pastrana-Martínez, J.L. Figueiredo, J.L. Faria, A.M.T. Silva AMT. Graphene oxide-P25 photocatalysts for degradation of diphenhydramine pharmaceutical and methyl orange dye, *Appl. Surf. Sci.*, 275 (2013) 361-368.

[20] D.M. Alonso, S.G. Wettsteinab, J.A. Dumesic, Bimetallic catalysts for upgrading of biomass to fuels and chemicals, *Chem. Soc. Rev.*, 24 (2012) 8075-8098.

[21] J.B. Sluiter, R.O. Ruiz, C.J. Scarlata, A.D. Sluiter, D.W. Templeton, Compositional analysis of lignocellulosic feedstocks. 1. Review and description of methods, *J. Agric. Food. Chem.*, 2010, 58 (2010) 9043-9053.

[22] E.M. Rubin, Genomics of Cellulosic Biofuels, *Nature*, 454 (2008) 841-845.

[23] S.P. Chundawat, G. Bellesia, N. Uppugundla, L. Costa Sousa, D. Gao, A.M. Cheh, U.P. Agarwal, C.M. Bianchetti, Jr. G. N. Phillips, P. Langan, V. Balan, S. Gnanakaran, B.E. Dale, Restructuring the crystalline cellulosehydrogen bond network enhances its depolymerization rate, *J. Am. Chem. Soc.*, 133 (2011) 11163-11174.

[24] R. Kumar, R. K. Sharma, A. P. Singh, Cellulose based grafted biosorbents - Journey from lignocellulose biomass to toxic metal ions sorption applications - A review, *J.Mol. Liquids*, 232 (2017) 62–93.

[25] R. J. Moon, A. Martini, J. Nairn, J. Simonsen, J. Youngblood, Cellulose nanomaterials

review: structure, properties and nanocomposites, *Chem. Soc. Rev.*, 40 (2011) 3941–3994.

[26] J.A. Figueiredo, M.I. Ismael, C.M.S. Anjo, A.P. Duarte, Cellulose and derivatives from wood and fibers as renewable sources of raw-materials. In: Rauter, A.P., Vogel, P., Queneau, Y. (Eds.), *Carbohydrates in sustainable development I: Renewable Resources for Chemistry and Biotechnology*, 294 (2010) 117–128.

[27] D. N-S. Hon, Cellulose: a random walk along its historical path, *Cellulose*, 1 (1994) 1–25.

[28] C. Somerville, Cellulose Synthesis in Higher Plants. *Annual Review of Cell and Developmental Biology*, 22(2006) 53-78.

[29] V. K. Suhas, P.J.M. Gupta, R. Carrott, M. Singh, S. Chaudhary, S. Kushwaha, Cellulose: A review as natural, modified and activated carbon adsorbent, *Bioresour. Technol.*, 216 (2016) 1066–1076.

[30] P. Fardim, T. Moreno, B. Holmbom, Anionic groups on cellulosic fiber surfaces investigated by XPS, FTIR-ATR, and different sorption methods, *J. Colloid Interface Sci.*, 290 (2005) 383-391.

[31] A. Gandini, The irruption of polymers from renewable resources on the scene of macromolecular science and technology, *Green Chem.*, 13 (2011) 1061-1083.

[32] S. Park, J.O. Baker, M.E. Himmel, P.A. Parilla, D.K. Johnson, Cellulose crystallinity index: measurement techniques and their impact on interpreting cellulase performance, *Biotechnol. Biofuels*, 3 (2010) 10.

[33] R. Kumar, R. Kr. Sharma, A. P. Singh, Cellulose based grafted biosorbents - Journey from lignocellulose biomass to toxic metal ions sorption applications - A review, *J. Mol. Liq.*, 232 (2017) 62–93.

[34] R. Parthasarathi, G. Bellesia, S.P.S. Chundawat, B.E. Dale, P. Langan, S. Gnanakaran, Insights into hydrogen bonding and stacking interactions in cellulose, *J. Phys. Chem. A*, 115 (2011) 14191–14202.

[35] T. Heinze, Cellulose: Structure and properties, *Adv. Polym. Sci.*, 271 (2015) 1–52.

[36] P. Zugenmaier, Conformation and packing of various crystalline cellulose fibers, *Prog. Polym. Sci.*, 26 (2001) 1341-1417.

[37] A.C. O'Sullivan, Cellulose: the structure slowly unravels, *Cellulose*, 4 (1997) 173-207.

[38] Y. Nishiyama, G. P. Johnson, A.D. French, V.T. Forsyth, P. Langan, Neutron crystallography, molecular dynamics, and quantum mechanics studies of the nature of hydrogen bonding in cellulose I β , *Biomacromolecules*, 9 (2008) 3133-3140.

[39] M. E. Himmel, S-Y. Ding, D.K. Johnson, W.S. Adney, M.R. Nimlos, J.W. Grady, T.D. Foust, Biomass recalcitrance: Engineering plants and enzymes for biofuels production, *Science*, 315 (2007) 804-807.

[40] J. F. Matthews, C.E. Skopec, P.E. Mason, P. Zuccato, R.W. Torget, J. Sugiyama, M. E. Himmel, J.W. Brady, Computer simulation studies of microcrystalline cellulose I β , *Carbohydr. Res.* 341(2006) 138-152.

[41] Y. Nishiyama, P. Langan, H. Chanzy, Crystal structure and hydrogen-bonding system in cellulose I β ; from synchrotron X-ray and neutron fiber diffraction, *J. Am. Chem. Soc.*,

124 (2002) 9074-9082.

[42] D. Ciolacu, F. Ciolacu, V.I. Popa, Amorphous cellulose – structure and characterization, *Cellul. Chem. Technol.*, 45 (2011) 13–21.

[43] H.V. Lee, S.B.A. Hamid, S.K. Zain, Conversion of lignocellulosic biomass to nanocellulose: structure and chemical process, *Sci. World J.*, 2014 (2014) 631013.

[44] T. P. Nevell, S. H. Zeronian, *Cellulose chemistry and its applications: Book Review*. Eds., Halsted Press, John Wiley, New York, USA, (1985), 552 pages.

[45] K. Fleming, D. G. Gray, S. Matthews, Cellulose crystallites, *Chem.Eur. J.*, 7(2001) 1831-1835.

[46] K.H. Gardner, J. Blackwel, Structure of Native Cellulose, *Biopolymers*, 13 (1974) 1975-2001.

[47] M. Wada, H. Chanzy, Y. Nishiyama, P. Langan, Cellulose III Crystal structure and hydrogen bonding by synchrotron X-ray and neutron fiber diffraction. *Macromolecules*, 37 (2004) 8548-8555.

[48] Y. Nishiyama, Structure and properties of the cellulose microfibril, *J. Wood Sci.*, 55 (2009) 241-249.

[49] D. Klemm, F. Kramer, S. Moritz, T. Lindstrom, M. Ankerfors, D. Gray, A. Dorris, Nanocelluloses: A new family of nature-based materials, *Angew. Chem., Int. Ed.*50 (2011) 5438-5466.

[50] M. Pääkkö, M. Ankerfors, H. Kosonen, A. Nykänen, S. Ahola, M. Österberg, J. Ruokolainen, J. Laine, P.T. Larsson, O. Ikkala, T. Lindström, Enzymatic hydrolysis combined with mechanical shearing and high-pressure homogenization for nanoscale cellulose fibrils and strong gels, *Biomacromolecules*, 8 (2007) 1934-1941.

[51] L. Wågberg, G. Decher, M. Norgren, T. Lindström, M. Ankerfors, K. Axnäs, The build-up of polyelectrolyte multilayers of microfibrillated cellulose and cationic polyelectrolytes, *Langmuir*, 24 (2008) 784-795.

[52] K. Fleming, D. Gray, S. Prasanna, S. Matthews, Cellulose crystallites: A new and robust liquid crystalline medium for the measurement of residual dipolar couplings, *J. Am. Chem. Soc.*, 122 (2000) 5224-5225.

[53] A.N. Nakagaito, S. Iwamoto, H. Yano, Bacterial cellulose: the ultimate nano-scalar cellulose morphology for the production of high-strength composites, *Appl. Phys. A*, 80 (2005) 93-97.

[54] J. Lu, P. Askeland, L.T. Drzal, Surface modification of microfibrillated cellulose for epoxy composite applications, *Polymer*,49 (2008) 1285-1298.

[55] P. Stenstad, M. Andresen, B.S. Tanem, P. Stenius, Chemical surface modifications of microfibrillated cellulose, *Cellulose*, 15 (2008) 35-45.56

[56] T. Zimmermann, N. Bordeanu, E. Strub, Properties of nanofibrillated cellulose from different raw materials and its reinforcement potential, *Carbohydr. Polym.*, 79 (2010) 1086-1093.

[57] Y. Habibi, L. A. Lucia, O. J. Rojas, Cellulose nanocrystals: chemistry, self-assembly, and applications, *Chem. Rev.*, 110 (2010) 3479-3500.

- [58] R.M. A. Domingues, M. E. Gomes, R.L. Reis, The potential of cellulose nanocrystals in tissue engineering strategies, *Biomacromolecules*, 15 (2014) 2327-2346.
- [59] S. Elazzouzi, Y. Nishiyama, J-L. Putaux, L. Heux, F. Dubreuil, C. Rochas, The shape and size distribution of crystalline nanoparticles prepared by acid hydrolysis of native cellulose, *Biomacromolecules*, 9 (2008) 57 -65.
- [60] Y. Huang, C. L. Zhu, J. Z. Yang, Y. Nie, C. T. Chen, D. P. Sun, Recent advances in bacterial cellulose, *Cellulose*, 21 (2014) 1-30.
- [61] S. H. Yoon, H-J. Jin, M-C. Kook, Y.R. Pyun, Electrically conductive bacterial cellulose by incorporation of carbon nanotubes, *Biomacromolecules*, 7 (2006) 1280-1284.
- [62] W. Si, W. Lei, Y. Zhang, M. Xia, F. Wang, Q. Hao, Electrodeposition of graphene oxide doped poly(3,4-ethylenedioxythiophene) film and its electrochemical sensing of catechol and hydroquinone, *Electrochim. Acta*, 85 (2012) 295-301.
- [63] Y. Xu, X. Liu, X. Liu, J. Tan, H. Zhu, Influence of $\text{HNO}_3/\text{H}_3\text{PO}_4\text{-NaNO}_2$ mediated oxidation on the structure and properties of cellulose fibers, *Carbohydr. Polym.*, 111 (2014) 955-963.
- [64] D. Klemm, B. Heublein, H. P. Fink and A. Bohn, Cellulose: Fascinating biopolymer and sustainable raw material: Review, *Angew. Chem., Int. Ed.*, 44 (2005) 3358-3393.
- [65] J. Sugiyama, R. Vuong, H. Chanzy, Electron diffraction study on the two crystalline phases occurring in native cellulose from an algal cell wall, *Macromolecules*, 24 (1999) 4168-4175.
- [66] M. B. Turner, S.K. Spear, J.D. Holbrey, R.D. Rogers, Production of bioactive cellulose films reconstituted from ionic liquids, *Biomacromolecules*, 5 (2004) 1379-1384.
- [67] Y-H. P. Zhang, J. Cui, L. R. Lynd, L. R. Kuang, A transition from cellulose swelling to cellulose dissolution by o-Phosphoric Acid: Evidence from enzymatic hydrolysis and supramolecular structure, *Biomacromolecules*, 7 (2006) 644-648.
- [68] D. Klemm, B. Philipp, T. Heinze, U. Heinze, W. Wagenknecht, *Comprehensive cellulose chemistry I: Fundamentals and analytical methods*; Wiley-VCH: Weinheim, Germany (1998).
- [69] M.G. Maximino, A. M. Adell, Acid hydrolytic treatment of cotton linters, *Cellul. Chem. Technol.*, 34 (2000) 229-240.
- [70] L.A. Ramos, J.M. Assaf, O.A. ElSeoud, E. Frollini, Influence of the supramolecular structure and physicochemical properties of cellulose on its dissolution in a lithium chloride N, N -dimethylacetamide solvent system, *Biomacromolecules*, 6 (2005) 2638-2647.
- [71] J. Cai, Y. Liu, L. Zhang, Dilute solution properties of cellulose in LiOH/urea aqueous system, *J. Polym. Sci., Part B: Polym. Phys.*, 44 (2006) 3093-3101.
- [72] R. Rinaldi, F. Schüth, F. Acid hydrolysis of cellulose as the entry point into biorefinery schemes, *Chem.Sus.Chem.*, 2 (2009) 1096-1107.
- [73] B. Medronho, B. Lindman, Competing forces during cellulose dissolution: From solvents to mechanisms, *Curr. Opin. Colloid Interface Sci.*, 19 (2014) 32-40.
- [74] J. Zhang, J.Wu, J.Yu, X. Zhang, J. He, J. Zhang, Application of ionic liquids for dissolving cellulose and fabricating cellulose-based materials: state of the art and

futuretrends: Review, *Mater. Chem. Front.*, 1 (2017)1273-1290.

[75] D. A. Fort, R.C. Remsing, R. P. Swatloski, P. Moyna, G. Moyna, R.D. Rogers, Can ionic liquids dissolve wood? Processing and analysis of lignocellulosic materials with 1-n-3-methylimidazolium chloride, *Green Chem.*, 9 (2007) 63-69.

[76] I. Anugwom, P. Mäki-Arvela, P. Virtanen, S. Willför, R. Sjöholm, J.P. Mikkola, Selective extraction of hemicelluloses from spruce using switchable ionic liquids, *Carbohydr. Polym.*, 87 (2012) 2005-2011.

[77] M. Kadokawa, Y. Murakami, Y. Kaneko, A facile preparation of gel materials from a solution of cellulose in ionic liquid, *Carbohydrate Res.*, 343 (2008) 769-772.

[78] M. Freemantle, *An introduction to ionic liquids*; Royal Society of Chemistry: Cambridge, UK, 2010.

[79] R.P. Swatloski, S.K. Spear, J.D. Holbrey, R.D. Rogers, Dissolution of cellulose with ionic liquids, *Am. Chem. Soc.*, 124 (2002) 4974-4975.

[80] a) J.-P. Mikkola, A. Kirilin, J. C. Tuuf, A. Pranovich, B. Holmbom, L. M. Kustov, D. Y. Murzina, T. Salmia, Ultrasound enhancement of cellulose processing in ionic liquids: from dissolution towards functionalization, *Green Chem.*, 9 (2007) 1229-1237; b) B. Kosan, C. Michels, F. Meister, Dissolution and forming of cellulose with ionic liquids, *Cellulose*, 15 (2008) 59-66; c) S. Barthel, T. Heinze, Acylation and carbanilation of cellulose in ionic liquids, *Green Chem.*, 8 (2006) 301-306; d) T. Heinze, K. Schwikal, S. Barthel, Ionic liquids as reaction medium in cellulose functionalization, *Macromol. Biosci.*, 5 (2005) 520-525; e) S. Köhler, T. Liebert, T. Heinze, Interactions of ionic liquids with polysaccharides. VI: Pure cellulose nanoparticles from trimethylsilyl cellulose synthesized in ionic liquids, *J. Polym. Sci. A*, 46 (2008) 4070-4080; f) M. Mazza, D.-A. Catana, C. Vaca-García, C. Cecutti, Influence of water on the dissolution of cellulose in selected ionic liquids, *Cellulose*, 16 (2009) 207-215.

[81] S. Cantone, U. Hanefeld, A. Basso, Biocatalysis in non-conventional media-ionic liquids, supercritical fluids and gas phase, *Green Chem.*, 9 (2007) 954-971.

[82] T.C.R. Brennan, S. Datta, H.W. Blanch, B.A. Simmons, B.M. Holmes, Recovery of sugars from ionic liquid biomass liquor by solvent extraction, *Bioenergy Res.*, 3(2010) 123-133.

[83] Y. Wang, Y. Deng, The kinetics of cellulose dissolution in sodium hydroxide solution at low temperatures, *Biotechnol. Bioeng.*, 102 (2009), 1398-1405.

[84] T. Okano, A. Sarko, Mercerization of cellulose. II. Alkali cellulose intermediates and a possible mercerization mechanism, *J. Appl. Polym. Sci.*, 30 (1985) 325-332.

[85] M. Egal, T. Budtova, P. Navard, Structure of aqueous solutions of microcrystalline cellulose/sodium hydroxide below 0 °C and the limit of cellulose dissolution, *Biomacromolecules*, 8 (2007) 2282-2287.

[86] C. Roy, T. Budtova, P. Navard, O. Bedue, Structure of cellulose-soda solutions at low temperatures, *Biomacromolecules*, 2 (2001) 687-693.

[87] P. Zugenmaier, Conformation and packing of various crystalline cellulose fibers, *Prog. Polym. Sci.*, 26 (2001) 1341-1417.

[88] A. Isogai, R.H. Atalla, Dissolution of cellulose in aqueous NaOH solutions, *Cellulose*,

5 (1998) 309-319.

[89] a) C. Cuissinat, P. Navard, Swelling and dissolution of cellulose part II: free floating cotton and wood fibers in NaOH-water-additives systems, *Macromol. Symp.*, 244 (2006) 19-30; b) C. Cuissinat, P. Navard, T. Heinze, Swelling and dissolution of cellulose. Part IV: Free floating cotton and wood fibres in ionic liquids, *Carbohydr. Polym.*, 72 (2008) 590-596; c) C. Cuissinat, P. Navard, Swelling and dissolution of cellulose, Part III: plant fibres in aqueous systems, *Cellulose*, 15 (2008) 67-74; d) C. Cuissinat, P. Navard, Swelling and dissolution of cellulose part 1: free floating cotton and wood fibers in N-methylmorpholine-N-oxide-water mixtures, *Macromol. Symp.*, 244 (2006) 1-18; e) C. Cuissinat, P. Navard, Swelling and dissolution of cellulose, Part III: plant fibres in aqueous systems, *Cellulose*, 15 (2008) 67-74.

[90] a) Y. Wang, Y. Zhao, Y. Deng, Effect of enzymatic treatment on cotton fiber dissolution in NaOH/urea solution at cold temperature, *Carbohydr. Polym.*, 72 (2008) 178-184; b) H. Jin, C. Zha, L. Gu, Direct dissolution of cellulose in NaOH/thiourea/urea aqueous solution, *Carbohydr. Res.*, 342 (2007) 851-858; c) J. Cai, L. Zhang, Rapid dissolution of cellulose in LiOH/urea and NaOH/urea aqueous solutions, *Macromol. Biosci.*, 5 (2005) 539-548; d) H. Qi, C. Chang, L. Zhang, Effects of temperature and molecular weight on dissolution of cellulose in NaOH/urea aqueous solution, *Cellulose*, 15 (2008) 779-787; e) A. Ehrhardt, H.M. Bui, H. Duelli, T. Bechtold, NaOH/urea aqueous solutions improving properties of regenerated-cellulosic fabrics, *J. Appl. Polym. Sci.*, 115 (2010) 2865-2874; f) R. Sescousse, T. Budtova, Influence of processing parameters on regeneration kinetics and morphology of porous cellulose from cellulose-NaOH-water solutions, *Cellulose*, 16 (2009) 417-426, and g) J. Kunze, J. H-P. Fink, Structural changes and activation of cellulose by caustic soda solution with urea, *Macromol. Symp.*, 223 (2005) 175-188.

[91] L. A. Ramos, J. M. Assaf, O.A. El Seoud, E. Frollini, Influence of the supramolecular structure and physicochemical properties of cellulose on its dissolution in a lithium chloride/N, N dimethylacetamide solvent system, *Biomacromolecules*, 6 (2005) 2638-2647.

[92] M.L. Foresti, A. Vázquez, B. Boury, Applications of bacterial cellulose as precursor of carbon and composites with metal oxide, metal sulfide and metal nanoparticles: A review of recent advances, *Carbohydr. Polym.*, 157 (2017) 447-467.

[93] C. Lai, L. Sheng, S. Liao, T. Xi, Z. Zhang, Surface characterization of TEMPO-oxidized bacterial cellulose, *Surf. Interface Anal.*, 45(2013)1673-1679.

[94] S. Hokkanen, Amit Bhatnagar, Mika Sillanpää, A review on modification methods to cellulose-based adsorbents to improve adsorption capacity, *Water Res.*, 91 (2016) 156-173.

[95] A. Isogai, T. Saito, H. Fukuzumi, TEMPO-oxidized cellulose nanofibers, *Nanoscale*, 2011, 3, 71-85.

[96] T. Saito, M. Hirota, N. Tamura, S. Kimura, H. Fukuzumi, L. Heux, Akira Isogai, Individualization of nano-sized plant cellulose fibrils by direct surface carboxylation using TEMPO catalyst under neutral conditions, *Biomacromolecules*, 10 (2009) 1992-1996

[97] H. Liimatainen, M. Visanko, J. Sirviö, O. Hormi, J. Niinimäki, Sulfonated cellulose nanofibrils obtained from wood pulp through regioselective oxidative bisulfite pretreatment, *Cellulose*, 20 (2013) 741-749.

[98] P. Stenstad, M. Andresen, B.S. Tanem, P. Stenius, Chemical surface modifications of microfibrillated cellulose, *Cellulose*, 15, (2008), 35-45.

- [99] D. Klemm, B. Heublein, H-P. Fink, A. Bohn, Cellulose: Fascinating biopolymer and sustainable raw material, *Angew. Chem. Int. Ed.*, 36 (2005) 3358-3393.
- [100] J. Dlouhá, L. Suryanegara, H. Yano, The role of cellulose nanofibres in supercritical foaming of polylactic acid and their effect on the foam morphology, *Soft Matter*, 8 (2012) 8704-8713.
- [101] P. Tingaut, T. Zimmermann, F. Lopez-Suevos, Synthesis and characterization of bionanocomposites with tuneable properties from poly (lactic acid) and acetylated microfibrillated cellulose, *Biomacromolecules*, 11(2010) 454-464.
- [102] G. Rodionova, M. Lenes, Ø. Eriksen, Ø. Gregersen, Surface chemical modification of microfibrillated cellulose: Improvement of barrier properties for packaging applications, *Cellulose*, 18 (2011) 127-134.
- [103] G. Rodionova, B. Hoff, M. Lenes, O. Eriksen, O. Gregersen, Gas-phase esterification of microfibrillated cellulose (MFC) films, *Cellulose*, 20 (2013) 1167–1174.
- [104] M. Nogi, K. Abe, K. Handa, F. Nakatsubo, S. Ifuku, H. Yano, Property enhancement of optically transparent bionanofiber composites by acetylation. *Appl. Phys. Lett.*, 89, (2006) 233123.
- [105] K.J. Edgar, C.M. Buchanan, J.S. Debenham, P.A. Rundquist, B.D. Seiler, M.C. Shelton, D. Tindall, Advances in cellulose ester performance and application, *Prog. Polym. Sci.*, 26 (2001) 1605-1688.
- [106] S.A. Arvidson, J.R. Lott, J.W. McAllister, J. Zhang, F.S. Bates, T.P. Lodge, R.L. Sammler, Y. Li, M. Brackhagen, Interplay of phase separation and thermoreversible gelation in aqueous methylcellulose solutions, *Macromolecules*, 46 (2012) 300-309.
- [107] C. Eyholzer, N. Bordeanu, F. Lopez-Suevos, D. Rentsch, T. Zimmermann, K. Oksman, Preparation and characterization of water-redispersible nanofibrillated cellulose in powder form, *Cellulose*, 17 (2010) 19-30.
- [108] C. Aulin, J. Netrval, L. Wågberg, T. Lindström, Aerogels from nanofibrillated cellulose with tuneable oleophobicity, *Soft Matter*, 6 (2010) 3298-3305.
- [109] T.T.T. Ho, T. Zimmermann, R. Hauert, W. Caseri, Preparation and characterization of cationic nanofibrillated cellulose from etherification and high-shear disintegration processes, *Cellulose*, 18 (2011) 1391-1406.
- [110] A. Pei, N. Butchosa, L.A. Berglund, Q. Zhou, Surface quaternized cellulosenanofibrils with high water absorbency and adsorption capacity for anionic dyes, *Soft Matter*, 9 (2013) 2047-2055.
- [111] N. Pahimanolis, U. Hippi, L.S. Johansson, T. Saarinen, N. Houbenov, J. Ruokolainen, J. Seppälä, Surface functionalization of nanofibrillated cellulose using click-chemistry approach in aqueous media, *Cellulose*, 18 (2011) 1201-1212.
- [112] G. Siqueira, J. Bras, A. Dufresne, New process of chemical grafting of cellulose nanoparticles with a long chain isocyanate, *Langmuir*, 26 (2010) 402-411.
- [113] P. Stenstad, M. Andresen, B.S. Tanem, P. Stenius, Chemical surface modifications of microfibrillated cellulose, *Cellulose*, 15 (2008) 35-45.
- [114] C. Gousse, H. Chanzy, M. L. Cerrada, E. Fleury, Surface silylation of cellulose microfibrils: preparation and rheological properties. *Polymer*, 45 (2004) 1569-1575.

- [115] J.T. Korhonen, M. Kettunen, R.H. Ras, O. Ikkala, Hydrophobic nanocellulose aerogels as floating, sustainable, reusable, and recyclable oil absorbents, *ACS Appl. Mater. Interfaces*, 3 (2011) 1813-1816.
- [116] P. Qu, Y. Zhou, X. Zhang, S. Yao, L. Zhang, Surface modification of cellulose nanofibrils for poly (lactic acid) composite application, *J. Appl. Polym. Sci.*, 125 (2012) 3084-3091.
- [117] P. Tingaut, R. Hauert, T. Zimmermann, Highly efficient and straightforward functionalization of cellulose films with thiol-ene click chemistry, *J. Mater. Chem.*, 21 (2011) 16066-16076.
- [118] A.N. Frone, S. Berlioz, J.F. Chailan, D.M. Panaitescu, Morphology and thermal properties of PLA–cellulose nanofibers composites, *Carbohydr. Polym.*, 91 (2013) 377-384.
- [119] H. C. Kolb, M.G. Finn, K.B. Sharpless, Click chemistry: Diverse chemical function from a few good reactions, *Angew. Chem.-Int. Edit.*, 40 (2001) 2004-2021.
- [120] N. Pahimanolis, U. Hippi, L.S. Johansson, T. Saarinen, N. Houbenov, J. Ruokolainen, J. Seppälä, Surface functionalization of nanofibrillated cellulose using click-chemistry approach in aqueous media, *Cellulose*, 18 (2011) 1201-1212.
- [121] L.J. Nielsen, S. Eyley, W. Thielemans, J.W. Aylott, Dual fluorescent labelling of cellulose nanocrystals for pH sensing, *Chem. Commun.*, 46 (2010) 8929-8931.
- [122] H. Lönnberg, L. Fogelström, L. Berglund, E. Malmström, A. Hult, Surface grafting of microfibrillated cellulose with poly(ϵ -caprolactone) - Synthesis and characterization, *Eur. Polym. J.*, 44 (2008) 2991-2997.
- [123] S. Beck-Candanedo, M. Roman, D.G. Gray, Effect of reaction conditions on the properties and behavior of wood cellulose nanocrystal suspensions, *Biomacromolecules*, 6 (2005) 1048-1054.
- [124] X. Hao, W. Shen, Z. Chen, J. Zhu, L. Feng, Z. Wu, P. Wang, X. Zeng, T. Wu, Self-assembled nanostructured cellulose prepared by a dissolution and regeneration process using phosphoric acid as a solvent, *Carbohydr. Polym.*, 123(2015)297-304.
- [125] X.Jia, Y.Chen, C.Shi, Y. Ye, P. Wang, X. Zeng, T. Wu, Preparation and characterization of cellulose regenerated from phosphoric acid, *J. Agric. Food Chem.*, 61 (2013) 12405–12414.
- [126] S. Beck-Candanedo, M. Roman, D. Gray, Effect of conditions on the properties behavior of wood cellulose nanocrystals suspensions, *Biomacromolecules*, 6 (2005) 1048-1054.
- [127] Z. Qin, L. Ji, X. Yin, L. Zhu, Q. Lin, J. Qin, Synthesis and characterization of bacterial cellulose sulfates using a $\text{SO}_3/\text{pyridine}$ complex in DMAc/LiCl, *Carbohydr. Polym.*, 101(2014) 947–953.
- [128] J. Araki, M. Wada, S. Kuga, T. Okano, Low properties of microcrystalline cellulose suspension prepared by acid treatment of native cellulose, *Colloids Surf. A*, 142 (1998) 75-82.
- [129] G. Siqueira, J. Bras, A. Dufresne, Cellulosic bionanocomposites: A review of preparation, properties and applications, *Polymers*, 2 (2010) 728-765.
- [130] N. Mosier, C. Wyman, B. Dalem, Features of promising technologies for pretreatment

of lignocellulosic biomass, *Bioresour. Technol.*, 96 (2005) 673–686.

[131] S. Camarero Espinosa, T. Kuhnt, E.J. Foster, C. Weder, Isolation of thermally stable cellulose nanocrystals by phosphoric acid hydrolysis, *Biomacromolecules*, 14 (2013) 1223–1230.

[132] J. Zhang, B. Zhang, J. Zhang, L. Lin, S. Liu, P. Ouyang, Effect of phosphoric acid pretreatment on enzymatic hydrolysis of microcrystalline cellulose, *Biotechnol. Adv.*, 28 (2010) 613–619.

[133] J. Zhang, J. Zhang, L. Lin, T. Chen, J. Zhang, S. Liu, Z. Li, P. Ouyang. Dissolution of microcrystalline cellulose in phosphoric acid—Molecular changes and kinetics. *Molecules*, 14 (2009) 5027–5041.

[134] M. Ghanadpour, F. Carosio, P. T. Larsson, L. Wagberg, Phosphorylated cellulose nanofibrils: A renewable nanomaterial for the preparation of intrinsically flame retardant materials, *Biomacromolecules*, 16 (2015) 3399–3410.

[135] C. Cheng, J. Zhang, Y. Mu, J. Gao, Y. Feng, H. Liu, Z. Guo, C. Zhang, Preparation and evaluation of activated carbon with different polycondensed phosphorus oxyacids (H_3PO_4 , $H_4P_2O_7$, $H_6P_4O_{13}$ and $C_6H_{18}O_{24}P_6$) activation employing mushroom roots as precursor, *J. Anal. Appl. Pyrolysis*, 108 (2014) 41–46.

[136] I. Kalashnikova, H. Bizot, B. Cathala, I. Capron, Modulation of cellulose nanocrystals amphiphilic properties to stabilize oil/water interface, *Biomacromolecules*, 13(2012) 267–275.

[137] L.X. Zhong, S.Y. Fu, X.W. Peng, H.Y. Zhan, R.C. Sun, Colloidal stability of negatively charged cellulose nanocrystalline in aqueous systems, *Carbohydr. Polym.*, 90 (2012) 644–649.

[138] G. Goncalves, P. A.A.P. Marques, R. J.B. Pinto, T. Trindade, C. P. Neto, Surface modification of cellulosic fibres for multi-purpose TiO_2 based nanocomposites, *Compos. Sci. Technol.*, 69 (2009) 1051–1056.

[139] Y. Luo, J. Huang, Hierarchical-structured anatase-titania/cellulose composite sheet with high photocatalytic performance and antibacterial activity, *Chem. Eur. J.*, 21(2015) 2568 – 2575.

[140] B. Yue, Y. Wang, C.Y. Huang, R. Pfeffer, Z. Iqbal, Polymeric nanocomposites of functionalized carbon nanotubes synthesized in supercritical CO_2 , *J. Nanosci. Nanotechnol.*, 7 (2007) 994–1000.

[141] J. Gutierrez, S. C. M. Fernandes, I. Mondragon, A. Tercjak, Multifunctional hybrid nanopapers based on bacterial cellulose and sol–gel synthesized titanium/vanadium oxide nanoparticles, *Cellulose*, 20 (2013) 1301 – 1311.

[142] N. S. Venkataramanan, K. Matsui, H. Kawanami, Y. Ikushima, Green synthesis of titania nanowire composites on natural cellulose fibers, *Green Chem.*, 9 (2007) 18– 19.

[143] Y. H. Ngo, D. Li, G. P. Simon, G. Garnier, Paper surfaces functionalized by nanoparticles, *Ad. Colloid & Interface Sci.*, 163 (2011) 23–38.

[144] S. Vaswani, J. Koskinen, D. W. Hess, Surface modification of paper and cellulose by plasma-assisted deposition of fluorocarbon films, *Surf. Coat. Technol.*, 195(2005) 121–129.

[145] P. Samyna, M. Deconincka, G. Schoukens, D. Stanssens, L. Vonck, H. V. D.

Abbeele, Modifications of paper and paperboard surfaces with a nanostructured polymer coating, *Prog. Org. Coat.*, 69 (2010) 442–454.

[146] N. Abidi, L. Cabrales, E. Hequet, Functionalization of a cotton fabric surface with titania nanosols: Applications for self-cleaning and UV-protection properties, *ACS Appl. Mater. Interfaces*, 1 (2009) 2141–2146.

[147] S. Nishibori, Photocatalytic pulp composition, foam, moulded pulp, as well as processes and apparatus for their preparation and application, 2001.

[148] B. Mahltig, H. Haufe, H. Bottcher, Functionalisation of textiles by inorganic sol–gel coatings, *J. Mater. Chem.*, 15 (2005) 4385–4398.

[149] H. Koga, T. Kitaoka, A. Isogai, In situ modification of cellulose paper with amino groups for catalytic applications, *J. Mater. Chem.*, 21 (2011) 9356–9361.

[150] I. Postnova, E. Kozlova, S. Cherepanova, S. Tsybulya, A. Rempel, Y. Shchipunov, Titania synthesized through regulated mineralization of cellulose and its photocatalytic activity, *RSC Adv.*, 5 (2015) 8544–8551.

[151] Nelson and Y. Deng, Enhanced light scattering from hollow polycrystalline TiO₂ particles in a cellulose matrix, *Langmuir*, 24 (2008) 975–982.

[152] T. Yuranova, D. Laub, J. Kiwi, Synthesis, activity and characterization of textiles showing self-cleaning activity under daylight irradiation, *Catal. Today*, 122 (2007) 109–117.

[153] F. A. Sadr and M. Montazer, In situ sonosynthesis of nano TiO₂ on cotton fabric, *Ultrason. Sonochem.*, 21 (2014) 681–691.

[154] Ji. Huang, T. Kunitake, Nano-precision replication of natural cellulosic substances by metal oxides, *J. Am. Chem. Soc.*, 125 (2003) 11834–11835.

[155] L. Karimi, M. Mirjalili, M. E. Yazdanshenas, A. Nazari, Effect of nano TiO₂ on self-cleaning property of cross-linking cotton fabric with succinic acid under UV irradiation, *Photochem. Photobiol.*, 86 (2010) 1030–1037.

[156] N. A. Ibrahim, R. Refaie, A. F. Ahmed, Novel approach for attaining cotton fabric with multi-functional properties, *J. Ind. Text.*, 40 (2010) 65–83.

[157] A. L. Ahmad, M. A. T. Jaya, D. C. J. Chieh, The effects of organic binders on palladium impregnated in TiO₂ membrane synthesis: X-Ray diffraction analysis, *J. Am. Ceram. Soc.* 93 (2010) 3595–3599.

[158] D. Fattakhova-Rohlfing, A. Zaleska, T. Bein, T. Three-dimensional titanium dioxide nanomaterials, *Chem. Rev.*, 114 (2014) 9487–9558.

[159] M. Giese, L.K. Blusch, M.K. Khan, M. J. MacLachlan, Functional materials from cellulose-derived liquid-crystal templates, *Angew. Chem. Int. Ed.*, 54 (2015) 2888–2910.

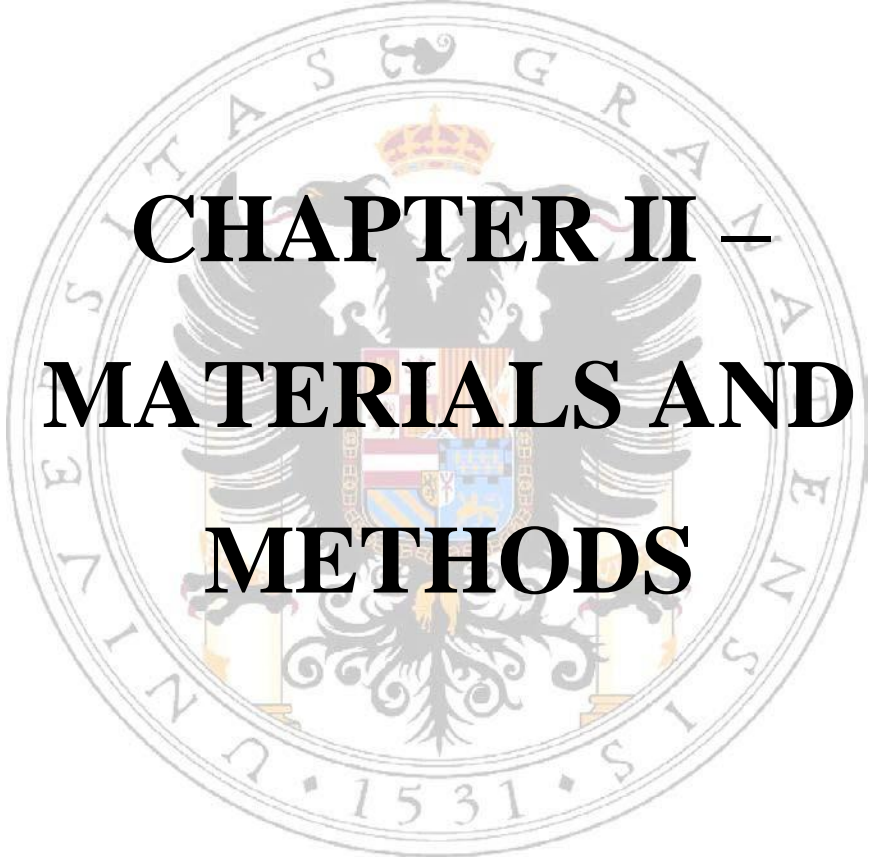
[160] X. Li, T. Fan, H. Zhou, S-K. Chow, W. Zhang, D. Zhang, Q. Guo, H. Ogawa, Enhanced light-harvesting and photocatalytic properties in morph-TiO₂ from green-leaf biotemplates, *Adv. Funct. Mater.*, 19 (2009) 45–56.

[161] P. Jiang, H. Lin, R. Xing, J. Jiang, F. Qu, Synthesis of multifunctional macroporous-mesoporous TiO₂-bioglasses for bone tissue engineering, *J. Sol-Gel Sci. Technol.*, 61(2012) 421–428.

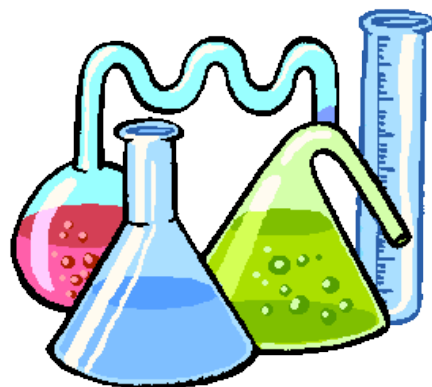
- [162] J. T. Korhonen, P. Hiekkataipale, J. Malm, M. Karppinen, O. Ikkala, R.H.A. Ras, Inorganic hollow nanotube aerogels by atomic layer deposition onto native nanocellulose templates *ACS Nano*, 5 (2011) 1967-1974.
- [163] Y. Zhou, E-Y. Ding, W.D. Li, Synthesis of TiO₂ nanocubes induced by cellulose nanocrystal (CNC) at low temperature, *Mater. Lett.*, 61 (2007) 5050-5052.
- [164] T. Chen, Y. Wang, Y. Wang, Y. Xu, Biotemplated synthesis of hierarchically nanostructured TiO₂ using cellulose and its applications in photocatalysis, *RSC Adv.*, 5 (2015) 1673-1769.
- [165] H. Cai, W. Mu, W. Liu, X. Zhang, Y. Deng, Sol-gel synthesis highly porous titanium dioxide microspheres with cellulose nanofibrils-based aerogel templates, *Inorg. Chem. Commun.*, 51 (2015)71-74.
- [166] A. Vuorema, S. Shariki, M. Sillanpaa, W. Thielemans, G.W. Nelson, J.S. Foord, S.E.C. Dale, S. Bending, F. Marken, Enhanced TiO₂ surface electrochemistry with carbonised layer-by-layer cellulose-PDDA composite films, *Phys. Chem. Chem. Phys.*, 13 (2011) 9857-9862.
- [167] O.L. Galkina, V.K. Ivanov, A.V. Agafonov, G.A. Seisenbaeva, V.G. Kessler, Cellulose nanofiber-titania nanocomposites as potential drug delivery systems for dermal applications, *J. Mater. Chem. B*, 3 (2015)1688-1698.
- [168] K.E. Shopsowitz, A. Stahl, W.Y. Hamad, M.J. MacLachlan, Hard templating of nanocrystalline titanium dioxide with chiral nematic ordering, *Angew. Chem. Int. Ed.*, 51 (2012) 6886-6890.
- [169] B. Boury, S. Plumejeau, Metal oxides and polysaccharides: an efficient hybrid association for materials chemistry, *Green Chem.*, 17 (2015)72-88.
- [170] C. Li, F. Wang, J.C. Yu, Semiconductor/biomoleculares composites for solar energy applications, *Energ. Environ. Sci.*, 4 (2011)100-113.
- [171] Z. Bao, M. R. Weatherspoon, S. Shian, Y. Cai, P. D. Graham, S. M. Allan, G. Ahmad, M. B. Dickerson, B. C. Church, Z. Kang, H. W. Abernathy III, C. J. Summers, M. Liu, K. H. Sandhage, Chemical reduction of three-dimensional silica micro-assemblies into microporous silicon replicas, *Nature*, 446 (2007) 172 –175.
- [172] M. Kemell, V. Pore, M. Ritala, M. Leskela, M. Linden, Atomic layer deposition in nanometer-level replication of cellulosic substances and preparation of photocatalytic TiO₂/cellulose composites, *J. Am. Chem. Soc.*, 127 (2005) 14178–14179.
- [173] Y. Luo, J. Xu, J. Huang, Hierarchical nanofibrous anatase-titania-cellulose composite and its photocatalytic property, *Cryst. Eng. Comm.*, 16 (2014) 464-471.
- [174] J. Zeng, S. Liu, J. Cai, L. Zhang, TiO₂ immobilized in cellulose matrix for photocatalytic degradation of phenol under weak UV light irradiation, *J. Phys. Chem. C.*, 114 (2010) 7806–7811.
- [175] H. Yano, Optically transparent composites reinforced with networks of bacterial nanofibers, *Adv. Mater.*, 17 (2005) 153–155.
- [176] X. Zhang, W. Chen, Z. Lin, J. Yao, S. Tan, Preparation and photocatalysis properties of bacterial Cellulose/TiO₂ composite membrane doped with rare earth elements, *Synth. React. Inorganic, Met. Nano-Metal Chem.*, 41 (2011) 997–1004.

- [177] T. Zhu, Y. Lin, Y. Luo, X. Hu, W. Lin, P. Yu, et al., Preparation and characterization of TiO₂-regenerated cellulose inorganic-polymer hybrid membranes for dehydration of caprolactam, *Carbohydr. Polym.*, 87 (2012) 901–909.
- [178] X.J. Jin, J. Xu, X.F. Wang, Z. Xie, Z. Liu, B. Liang, et al., Flexible TiO₂/cellulose acetate hybrid film as a recyclable photocatalyst, *RSC Adv.*, 4 (2014) 12640–12648.
- [179] M. A. Mohamed, W.N.W. Salleh, J. Jaafar, A.F. Ismail, M. A. Mutalib, N.A.A. Sani, S.E.A.M. Asri, C.S. Ong, Physicochemical characteristic of regenerated cellulose/N-doped TiO₂ nanocomposite membrane fabricated from recycled newspaper with photocatalytic activity under UV and visible light irradiation, *Chem. Eng. J.*, 184 (2016) 202–215.
- [180] S. Yano, H. Maeda, M. Nakajima, T. Hagiwara, T. Sawaguchi, Preparation and mechanical properties of bacterial cellulose nanocomposites loaded with silica nanoparticles, *Cellulose*, 15 (2008) 111–120.
- [181] J. Gutierrez, A. Tercjak, I. Algar, A. Retegi, I. Mondragon, Conductive properties of TiO₂/bacterial cellulose hybrid fibres, *J. Colloid Interface Sci.*, 377 (2012) 88–93.
- [182] J. Gutierrez, S.C. Fernandes, I. Mondragon, A. Tercjak, Multifunctional hybrid nanopapers based on bacterial cellulose and sol-gel synthesized titanium/vanadium oxide nanoparticles, *Cellulose*, 20 (2013) 1301–1311.
- [183] D. Sun, J. Yang, X. Wang, Bacterial cellulose/TiO₂ hybrid nanofibers prepared by the surface hydrolysis method with molecular precision, *Nanoscale*, 2 (2010) 287–292.
- [184] H. Hamad, M. Abd El-latif, A. Kashyout, W. Sadik, M. Feteha, Optimizing the preparation parameters of mesoporous nanocrystalline titania and its photocatalytic activity in water: physical properties and growth mechanisms, *Process Saf. Environ. Prot.*, 98 (2015) 390–398.
- [185] M.J. Uddin, F. Cesano, F. Bonino, S. Bordiga, G. Spoto, D. Scarano, A. Zecchina, Photoactive TiO₂ films on cellulose fibres: synthesis and characterization, *J. Photochem. Photobiol. A*, 189 (2007) 286–294.
- [186] L. Ye, C. D. M. Filipe, M. Kavooosi, C. A. Haynes, R. Pelton, M. A. Brook, Immobilization of TiO₂ nanoparticles onto paper modification through bioconjugation, *J. Mater. Chem.*, 19 (2009) 2189–2198.
- [187] H. Tong, S. Ouyang, Y. Bi, N. Umezawa, M. Oshikiri, J. Ye, Nano-photocatalytic materials: Possibilities and challenges: Review, *Adv. Mater.*, 24 (2012) 229–251.
- [188] X. Wang, R. A. Caruso, Enhancing photocatalytic activity of titania materials by using porous structures and the addition of gold nanoparticles, *J. Mater. Chem.*, 21 (2011) 20–28.
- [189] S.U.M. Khan, M. Al-Shahry, W. B. Ingler, Efficient photochemical water splitting by a chemically modified n-TiO₂. *Science*, 297(2002)2243–2245.
- [190] F. Zuo, L. Wang, T. Wu, Z. Zhang, D. Borchardt, P. Feng, Self-doped Ti³⁺ enhanced photocatalyst for hydrogen production under visible light. *J. Am. Chem. Soc.*, 132 (2010) 11856–11857.
- [191] B. Liu, H. M. Chen, C. Liu, S. C. Andrews, C. Hahn, P. Yang, Large-scale synthesis of transition-metal-doped TiO₂ nanowires with controllable overpotential, *J. Am. Chem. Soc.*, 135 (2013) 9995–9998.

- [192] A. Naldoni, M. Allieta, S. Santangelo, M. Marelli, F. Fabbri, S. Cappelli, C. L. Bianchi, R. Psaro, V. D. Santo, Effect of nature and location of defects on bandgap narrowing in black TiO₂ nanoparticles. *J. Am. Chem. Soc.*, 134 (2012) 7600–7603.
- [193] O.A. Syzgantseva, P. Gonzalez-Navarrete, M. Calatayud, S. Bromley, C. Minot, Theoretical investigation of the hydrogenation of (TiO₂)_N clusters (N = 1–10). *J. Phys. Chem. C*, 115 (2011) 15890–15899.
- [194] X. Chen, L. Liu, F. Huang, Black titanium dioxide (TiO₂) nanomaterials, *Chem. Soc. Rev.*, 44 (2015) 1861–1885.
- [195] M. M. Islam, M. Calatayud, G. Pacchioni, Hydrogen adsorption and diffusion on the anatase TiO₂ (101) surface: a first-principles investigation, *J. Phys. Chem. C*, 115 (2011) 6809–6814.
- [196] N. Liu, C. Schneider, D. Freitag, M. Hartmann, U. Venkatesan, J. Müller, E. Spiecker, P. Schmuki, Black TiO₂ nanotubes: cocatalyst-free open-circuit hydrogen generation, *Nano Lett.*, 14 (2014) 3309–3313.
- [197] X. Chen, L. Liu, Z. Liu, M. A. Marcus, W.-C. Wang, N. A. Oyler, M. E. Grass, B. Mao, P.-A. Glans, P. Y. Yu, J. Guo, S. S. Mao, Properties of disorder-engineered black titanium dioxide nanoparticles through hydrogenation, *Sci. Rep.*, 3 (2013) 1510.
- [198] J. Dong, J. Han, Y. Liu, A. Nakajima, S. Matsushita, S. Wei, W. Gao, Defective black TiO₂ synthesized via anodization for visible-light photocatalysis, *ACS Appl. Mater. Interfaces*, 6 (2014) 1385–1388.
- [199] T. Lin, C. Yang, Z. Wang, H. Yin, X. Lu, F. Huang, J. Lin, X. Xie, M. Jiang, Effective nonmetal incorporation in black titania with enhanced solar energy utilization, *Energy Environ. Sci.*, 7 (2014) 967–972.
- [200] Z. Wang, C. Yang, T. Lin, H. Yin, P. Chen, D. Wan, F. Xu, F. Huang, J. Lin, X. Xie, M. Jiang, Visible-light photocatalytic, solar thermal and photoelectrochemical properties of aluminium-reduced black Titania, *Energy Environ. Sci.*, 6 (2013) 3007–3014.
- [201] G. Zhu, T. Lin, X. Lu, W. Zhao, C. Yang, Z. Wang, H. Yin, Z. Liu, F. Huang, Black brookite titania with high solar absorption and excellent photocatalytic performance, *J. Lin, J. Mater. Chem. A*, 1 (2013) 9650–9653.
- [202] C. D. Valentin, G. Pacchioni, A. Selloni, Reduced and n-type doped TiO₂: nature of Ti³⁺ species. *J. Phys. Chem. C*, 113(2009) 20543–20552.
- [203] G. Wang, H. Wang, Y. Ling, Y. Tang, X. Yang, R. C. Fitzmorris, C. Wang, Z. J. Zhang, Y. Li, Hydrogen-treated TiO₂ nanowire arrays for photoelectrochemical water splitting, *Nano Lett.*, 11 (2011) 3026–3033.
- [204] X.-L. Yin, M. Calatayud, H. Qiu, Y. Wang, A. Birkner, C. Minot, Diffusion versus desorption: complex behavior of H Atoms on an oxide surface. *ChemPhysChem.*, 9(2008)253–256.



**CHAPTER II –
MATERIALS AND
METHODS**



This chapter describes how the photocatalysts were prepared and the characterization techniques used for the investigation of their physical and chemical properties. The methodology and experimental conditions used in the reactions of photo-degradation of Orange G, as a target organic molecule, are also described.

2.1. Chemicals.

Microcrystalline cellulose (MCC, Merck), and titanium (IV) isopropoxide (TTIP, >97%, Aldrich), and zirconium butoxide (99%, Aldrich)] as carbon, and metal oxide precursors, respectively, while o-phosphoric (85% w/w) acid, nitric acid (70% w/w) and solvents (heptane, acetone and ethanol) were acquired from VWR chemicals. Methanol (99.9%, Applichem-Panreac), acetonitrile (99.9%, Panreac), and hexa decyl trimethyl ammonium bromide (CTAB, > 99%, Sigma-Aldrich) were purchased from Sigma-Aldrich. All aqueous solutions were prepared using distilled water from the Millipore instrument. TiO₂-P25 (Degussa) was used as reference materials. Orange G (OG, CAS 1936-15-8, Aldrich) is the target dye for the investigation of photocatalysis.

2.2. Synthesis of photocatalysts.

In this Thesis, composite materials were prepared for their use as photocatalysts. These materials are classified into two groups: i) cellulose/titania and its carbon/titania hybrid composites; and ii) black titania.

2.2.1. Cellulose - TiO₂ composites.

Hybrid cellulose-TiO₂ composites were synthesized by a two-step method, in which MCC was initially dissolved with acids (H₃PO₄ or HNO₃) to facilitate the subsequent impregnation with the TiO₂ pre-cursor. In a typical procedure, 10 g of MCC was suspended in 50 mL of distilled water, heated at 50 °C under vigorous stirring for 15 min and then, 100 mL of the selected acid was added drop wise to the MCC suspension, the MCC being completely dissolved under these conditions overnight. In the second step, an appropriate amount of TTIP (cellulose-TiO₂ mass ratio = 1:6) was dissolved in 150 mL of heptane under stir-ring at 50 °C and then, the MCC solution was added dropwise. A solid suspension was formed progressively due to the hydrolysis of TTIP and consequently, the formation of TiO₂

particles. After that, the suspension was aged for 24 h at 60 °C under stirring and finally the solid filtered, washed with distilled water and acetone and dried at 120 °C in an oven. The cellulose-TiO₂ composites were referred as CPT or CNT, according to the type of acid treatment applied to the cellulose, i.e., H₃PO₄ or HNO₃, respectively.

Two pure cellulose derivatives, i.e. without TiO₂, were also synthesized to study the effects of acid treatments on the cellulose. Therefore, MCC was dissolved in the selected acid media following the procedure described above during the first step and then, the acid-treated cellulose was recovered by heating the solution until it was dried. After that, the resulting solid was washed with deionized water to completely remove phosphates or nitrates in the solution and dried again at 120 °C in an oven. The obtained materials were referred as CP and CN, for cellulose treated in H₃PO₄ or HNO₃, respectively. Analogously, two pure titania materials, i.e., in absence of cellulose, were also prepared for comparison by hydrolysing TTIP in each acid media. These samples were labelled as PT and NT, for titania treated in H₃PO₄ or HNO₃, respectively.

2.2.2. Carbon-titanium composites.

The synthesis of these materials is based in the carbonization of CPT and CNT composites prepared in Section 2.2.1. Therefore, they were carbonized in a tubular furnace at 500 or 800 °C in N₂ flow (100 cm³ min⁻¹). The final carbon-Ti composites were referred as CPT1, CPT2, CNT1 and CNT2, following the same nomenclature above mentioned but adding 1 and 2 if the carbonization temperature was 500 °C or 800 °C, respectively. Additionally, pure carbon materials were prepared as reference to follow the functionalization of cellulose by H₃PO₄ (CP1 and CP2 samples) and HNO₃ (CN1 and CN2 samples) during thermal treatments.

2.2.3. Carbon-phosphorus-titanium composites.

The synthesis of the carbon-phosphorus-titanium composites was carried out using a modification of the procedure used to prepare CPT samples in Section 2.2.1. Briefly, MCC was suspended in distilled water (200 g L⁻¹) and then, it was completely dissolved by adding 100 mL of H₃PO₄ under stirring at 50 °C overnight. After that, an appropriated amount of TTIP in heptane was dropped to the previous cellulose solution to obtain different cellulose-Ti composites by changing the corresponding Ti:cellulose mass ratio, namely 1:1, 6:1 or

12:1. The solid suspension formed during the TTIP hydrolysis was aged under continuous stirring at 60 °C for 24 h and then, the composites were filtered, washed with distilled water and acetone and dried at 120 °C in an oven. Finally, the carbon-phosphorus-Ti composites were obtained by carbonization of the corresponding cellulose-Ti composites in a tubular furnace at 500 or 800 °C under 100 cm³ min⁻¹ N₂ flow. The samples will be labelled as CPTX-Y where the letters CPT have the same meaning already described while “X” refers the Ti:cellulose ratio used (i.e., 1, 6 or 12) and “Y” states the carbonization temperature (500 or 800 °C). For instance, CPT6-500 corresponds to the composite prepared in a 6:1 ratio and at 500 °C.

2.2.4. Black titania nanocrystals.

Black titania was prepared by a controlled hydrolysis of TTIP in methanol/acetonitrile medium using CTAB as structure-directing agent. In a typical preparation, 0.546 g of CTAB was added to 150 ml of methanol/acetonitrile solution. After stirring for 10 min, 1 ml of TTIP was added and then quickly transferred into a sealed stirred reactor (Parr reactor model 5500) to avoid the hydrolysis under atmospheric conditions. This mixture was heated at 60 °C under stirring (2000 rpm) and pressurized with hydrogen or nitrogen under flow in order to purge the reactor. Hydrolysis and condensation reactions occurs when adding 1 ml of deionized water in the pressurized stirred tank using a pump. After that, the flow was stopped, and the tank pressurized at 8 bar and heated at 180 °C under stirring for 1, 2, 3, 4 or 5 days. The obtained samples were centrifuged at 4000 rpm for 20 min and washed with methanol several times. These samples were denoted as TiAX, where A is H or N for H₂ or N₂, respectively and X is the days of treatments, i.e. TiH1 indicates that TiO₂ was synthesised in presence of H₂ after 1 day of treatment. White titania, TiO₂ anatase from sigma aldrich, was used as reference material.

2.3. Characterization techniques.

The photocatalysts were characterized by various techniques in order to study their morphology, porous structure, surface area and surface chemical characteristics, as well as the nature and dispersion of the corresponding active phases. A significant number of important characterization methods were utilized to elucidate the physico-chemical properties of photocatalysts. The morphological analysis was investigated by scanning

electron microscopy (SEM) and transmission electron microscopy (TEM). Surface area and porosity were analyzed by N_2 at $-196\text{ }^\circ\text{C}$ and CO_2 at $0\text{ }^\circ\text{C}$. The crystal structure of the prepared photocatalysts were clarified by X-ray diffraction (XRD). The chemical nature was studied through the techniques of elemental analysis, Fourier Transform-Infrared spectroscopy (FT-IR), temperature programmed desorption (TPD), X-ray photoelectron spectroscopy (XPS), and thermogravimetric analysis (TGA). For the determination of the dispersion and chemical nature of the metallic phase of the catalysts, the techniques of XRD, TEM and XPS were used. The optical properties of the photocatalysts were analyzed by diffuse reflectance spectroscopy (DRS). UV-visible spectroscopy was utilized to determine the concentration of the OG dye before and after adsorption and photocatalysis processes.

2.3.1. Morphological characterization.

2.3.1.1. Scanning electron microscopy (SEM).

The morphology of photocatalysts was performed by SEM. A common preparation technique is to coat the sample with several nanometer layer of conductive materials such as gold by the use of Carbon Sputter Coater. After coating the sample were placed in an AURIGA (FIB-FESEM) microscope from Carl Zeiss SMT equipped with an EDAX microanalysis system for the work in cellulose/ titania composites. SEM can get images with increases of up to 500,000 X. On the other hands, SEM with model LEO (Carl Zeiss) GEMINI-1530 microscope were used for analysis of black titania samples.

2.3.1.2. Transmission electron microscopy (TEM).

Crystallite sizes and shapes of the prepared samples were observed using TEM. Cellulose / titania for TEM measurements were suspended in ethanol and ultrasonically dispersed. A small amount of well milled sample is dispersed in ethanol under ultrasound and mounted on a 300-mesh carbon-coated cooper grid. TEM observations were carried out using a LIBRA (Carl Zeiss) 120 PLUS microscope. A number of grids were prepared accordingly for each sample and examined by TEM.

For black titania, HRTEM images were recorded using a FEI TITAN G2 80-300 microscope equipped with a scanning TEM (STEM) detector-type HAADF (high-angle annular dark-field detector), corrector of spherical aberration (CEOS), and EDX

microanalysis system (Super X). This equipment has a maximum resolution of 0.8 Å (TEM) or 1.4 Å (STEM), working with an acceleration voltage of 300 kV.

2.3.2. X-Ray diffraction (XRD).

In this study, Bruker D8 Advance X-ray diffractometer, using CuK α radiation of wavelength ($\lambda = 1.541$ Å), and the K β radiation was eliminated by a Ni filter at room temperature. The 2θ range for all samples was in the range of scan step size $20^\circ < 2\theta > 70^\circ$ with scan speed of 0.2°/s. The average crystallite sizes (D) were estimated by the Debye-Scherrer equation, $D = 0.95 \lambda / (\beta \cos \theta)$ where θ is the diffraction angle and β is the full width at half-maximum (FWHM). The FWHM was determined with an extrapolated baseline between the beginning (low-angle side) and the end (high-angle side) of a diffraction peak with the highest intensity.

2.3.3. X-Ray photoelectron spectroscopy (XPS).

The surface chemistry of the samples was studied by XPS. The grinded samples were placed in a steel sample holder and introduced into the analysis chamber, degassing them at a pressure lower than 10⁻⁸ Torr. The XPS spectra were obtained on a Kratos Axis Ultra-DLD X-ray photoelectron spectrometer equipped with a hemispherical electron analyzer connected to a detector DLD (delay-line detector). Survey and multi-region spectra were recorded at C1s, O1s, N1s, P2p, and Ti2p photoelectron peaks. Each spectral region of photoelectron interest was scanned several times to obtain good signal-to-noise ratios.

The spectra obtained, once the background was subtracted, were deconvolved by means of an iterative adjustment method, using Gaussian-Lorentzian asymmetric sum functions to determine the number of components, the power of ligating the peaks (EL) and the areas of the themselves (quantitative analysis). The binding energy of the peak of the C1s region, corresponding to C=C (aromatic-aliphatic) was taken as the reference peak, assigning it the value of 284.6 eV.

For XPS analysis of the samples used in reaction, the procedure was the following: once the reaction was finished, the sample was dried under He flow, impregnated with n-octane, and then transferred to the pre-treatment chamber of the XPS instrument. Prior to the XPS analysis the samples were evacuated at high vacuum and room temperature, and

then introduced into the analysis chamber. A base pressure of 10^{-9} mbar was maintained during data acquisition.

2.3.4. Fourier transform infrared spectroscopy (FTIR).

FTIR spectra of cellulose/titania a composite were recorded using a NICOLET 20SXB spectrometer, with software package OMNIC v.1.1, in the range from 400 to 4000 cm^{-1} with scanning rate was $0.5 \text{ cm}^{-1} \text{ s}^{-1}$. To make the spectra, tablets with KBr were prepared in which the sample was diluted to 0.1% by weight.

2.3.5. Thermogravimetric analysis (TGA).

The carbonization process of cellulose / titania composites was studied by thermogravimetric (TG) and differential thermogravimetric (DTG) analyses by heating the sample in nitrogen flow from $50 \text{ }^{\circ}\text{C}$ to $900 \text{ }^{\circ}\text{C}$ at $20 \text{ }^{\circ}\text{C min}^{-1}$ using a Mettler-Toledo TGA/DSC1 thermal balance; the TiO_2 content in cellulose/titania was determined by burning the carbon fraction in air flow until constant weight.

2.3.6. Temperature programmed desorption (TPD).

The chemical properties of the acid-treated cellulose and composite samples were analysed by TPD experiments. The procedures were as follows; the samples were heated in He flow ($60 \text{ cm}^3 \cdot \text{min}^{-1}$) at $50 \text{ }^{\circ}\text{C} \cdot \text{min}^{-1}$ heating rate up to $1000 \text{ }^{\circ}\text{C}$. The analysis of gases desorbed as a function of time was carried out with a thermo balance and gases evolved that were analyzed using a FTIR spectrophotometer (Thermo fisher Nicolet mod. IS10-detector). The exact content of TiO_2 in the composites was obtained by a thermogravimetric analysis burning the cellulose fraction in air flow until constant weight using a Mettler–Toledo TGA/DSC1 thermo balance. The spectrometer was controlled by a computerized data acquisition system, which analyzed the amounts of CO , CO_2 and H_2O desorbed by recording the following m/z signals: 12, 14, 16, 17, 18, 22, 28 and 44.

2.3.7. Physical adsorption of nitrogen.

Textural characterization of all photocatalysts was carried out by N_2 adsorption at $-196 \text{ }^{\circ}\text{C}$ using Quantachrome Autosorb-1 equipment. Prior to measuring the adsorption isotherms, the samples were outgassed overnight at $110 \text{ }^{\circ}\text{C}$ under high vacuum (10^{-6} mbar). The N_2 -adsorption isotherms were fitted using the BET equation and DFT method were

applied to determine the apparent surface area (S_{BET}), while and mesopore volume of the samples (V_{meso}), respectively. The BJH method was applied to the desorption branch of the N_2 adsorption isotherms to obtain the pore size distribution (PSD) curves and mesopore volume (V_{BJH}). The Dubinin–Radushkevich equation was applied to calculate the micropore volume (V_{micro}), the mean micropore width (L_0) and the microporous surface (S_{DR}) [1,2]. The total pore volume (V_{T}) was considered as the volume of N_2 adsorbed at $P/P_0=0.95$, while the mesopore volume (V_{meso}) was obtained by the difference of V_{T} and V_{micro} [3]. S_{DFT} is the cumulative surface area obtained from the pore size distribution determined applying the quenched solid state functional theory (QSDFT) method for slit-shaped pores [4].

2.3.8. Diffuse reflectance spectroscopy (DRS).

Optical absorption spectra of samples were obtained on a double-beam UV–vis spectrophotometer (CARY 5E from VARIAN) equipped with a Praying Mantis diffuse reflectance accessory (DRS). The reflectance spectra were analyzed according to the Kubelka–Munk (KM) method in order to calculate the band gap (E_{g}) of samples. The graphic representations $(F(R) \cdot h\nu)^n$ versus $E = h\nu$ were used to calculate E_{g} ; where $F(R)$ is a function of the reflectance; $F(R) = (1-R)^2/2R$, R is the absolute reflectance of the sample layer and $h\nu$ is the photon energy (eV), assuming also a value of $n = 1/2$ for an indirect allowed transition and $n = 2$ for a direct allowed transition. The E_{g} value was obtained by extrapolating the slope to $a = 0$ [5].

2.4. Photocatalytic experiments.

The photocatalytic decomposition of organic pollutant in photocatalysts under UV and visible irradiations was investigated in order to evaluate the photocatalytic activity. Polluted waste water was prepared by dissolving a known weight of dye in distilled water. The degradation reaction was carried out in a slurry photocatalytic reactor as shown in Figure 2.1. The reaction mixture was maintained as a suspension by magnetic stirring. The prepared photocatalysts and Organic-G (disodium salt of 1-phenylazo-2-naphthol-6,8-disulfonic acid, CAS 1936, OG) dye were placed in a glass photoreactor (inner diameter of 8.5 cm and height of 20 cm) which equipped with an inner quartz tube of 2.5 cm of diameter that placed in the reactor center. A tubular UV (TNN 15/32, 15 W, HNG, Germany) or a visible sun lamp of 14 W (ReptoLux 2.0, Spain) was placed inside at the center of the

photoreactor to ensure an uniform irradiation of all volume solution. The degradation reaction was carried out in a slurry photocatalytic reactor. The reaction mixture was maintained as a suspension by magnetic stirring to ensure the uniform homogeneity throughout the reaction medium.

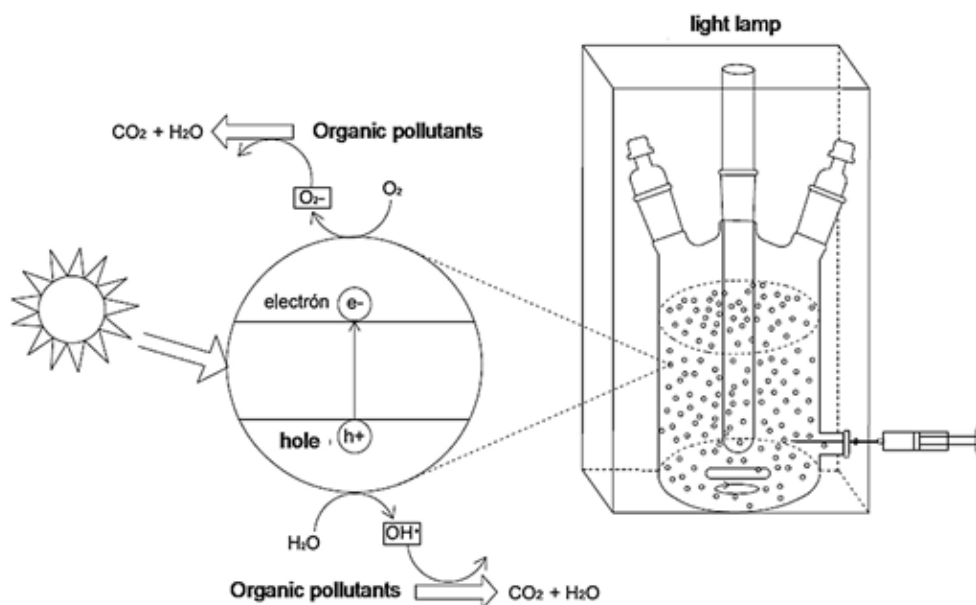


Figure 2.1. Diagram of the device used for the photo-degradation of the Orange G.

The kinetics of adsorption of Orange G on the photocatalytic material was initially determined, obtaining the necessary time to reach the saturation equilibrium. A 800 mg of the photocatalyst was saturated in 800 ml dye solution in dark to avoid the effect of different adsorption efficiency of catalyst on the evolution of the dye concentration.

After saturation, at regular interval of 10 min., aliquots were taken out and then filtered through Millex GP sterile syringe filter of 0.22 μm (Merck Millipore, Germany). The photo-degradation was carried out taking aliquots of the reactor every certain time, and analyzing them by means of (5625 Unicam Ltd., Cambridge, UK) at a $\lambda = 487 \text{ nm}$. Spectrometry All photocatalytic experiment was kept at a natural pH and room temperature. The colour removal efficiency (R , %) of OG dye could be calculated according to the following equation

$$\text{Color removal } (R, \%) = 1 - \frac{C}{C_0} \times 100 = 1 - \frac{A}{A_0} \times 100 \quad (1)$$

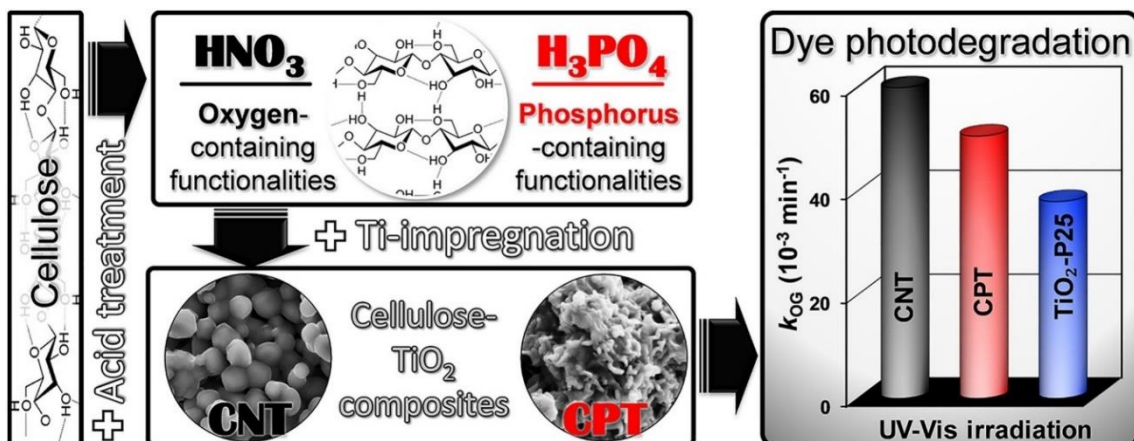
where, C_0 (mg/L) is the initial concentration of dye solution, C (mg/L) is the concentration

of dye solution after photoirradiation at time t (min), A_0 is the value of absorbance of dye aqueous solution after adsorption in the dark, and A is the value of absorbance of dye aqueous solution after reaction.

2.5. References.

- [1] S. Brunauer, P.H. Emmett, E. Teller, Adsorption of gases in multimolecular layers, *J. Am. Chem. Soc.*, 60 (1938) 309–319.
- [2] M.M. Dubinin, Generalization of the theory of volume filling of micropores to nonhomogeneous microporous structures, *Carbon*, 23 (1985) 373–380.
- [3] F. Stoeckli, In: *Porosity in Carbons—Characterization and Applications*, Arnold, London, 1995.
- [4] A.V. Neimark, Y. Lin, P.I. Ravikovitch, M. Thommes, Quenched solid density functional theory and pore size analysis of micro-mesoporous carbons, *Carbon*, 47 (2009) 1617-1628.
- [5] R. López, R. Gómez, Band-gap energy estimation from diffuse reflectance measurements on sol-gel and commercial TiO_2 : a comparative study, *J. Sol-Gel Sci. Technol.*, 61 (2012) 1–7.

CHAPTER III - PHYSICAL PROPERTIES OF NEW CELLULOSE-TiO₂ COMPOSITES FOR THE REMOVAL OF WATER POLLUTANTS: DEVELOPING SPECIFIC INTERACTIONS AND PERFORMANCES BY CELLULOSE FUNCTIONALIZATION





Contents lists available at ScienceDirect

Journal of Environmental Chemical Engineering

journal homepage: www.elsevier.com/locate/jece

Physicochemical properties of new cellulose-TiO₂ composites for the removal of water pollutants: Developing specific interactions and performances by cellulose functionalization



Hesham Hamad¹, Esther Bailón-García, Sergio Morales-Torres, Francisco Carrasco-Marín, Agustín F. Pérez-Cadenas, Francisco J. Maldonado-Hódar*

Carbon Materials Research Group, Department of Inorganic Chemistry, Faculty of Sciences, University of Granada, Avenida de Fuentenueva, s/n., ES18071 Granada, Spain

ARTICLE INFO

Keywords:

Cellulose functionalization
Ti-active phases
Synergism
Photocatalytic composites
Water dye oxidation

ABSTRACT

Cellulose-TiO₂ composites are developed using microcrystalline cellulose (MCC). The closed MCC structure was solubilized by liquid-phase treatments with nitric (HNO₃) or phosphoric acids (H₃PO₄) to improve the TiO₂-dispersion. These pretreatments simultaneously generate different types of oxygen and phosphorus functionalities on the cellulose chains that determine the interactions with Ti-alkoxide precursor during impregnation, leading to composite materials with different Ti-loadings and physicochemical characteristics. The morphological, textural, chemical and crystalline properties of both cellulose derivatives and cellulose-TiO₂ composites were studied by complementary techniques. Microporous composites with round-shaped anatase TiO₂ microcrystals were obtained by using HNO₃ treatments, while H₃PO₄ favours the formation of mesoporous composites with flat and non-crystalline TiO₂ particles. The photocatalytic efficiency of the obtained cellulose-TiO₂ composites always improve the results obtained with the commercial TiO₂-photocatalysts used as reference materials; this behaviour was analysed taking into account the physicochemical characteristics of the samples.

3.1. Materials and methods.

3.1.1. Synthesis and characterization of the materials.

Hybrid cellulose-TiO₂ composites were synthesized by a two-step method, in which MCC was initially dissolved with acids (H₃PO₄ or HNO₃) to facilitate the subsequent impregnation with the TiO₂ precursor. The amount of TTIP was that according to obtain a cellulose-TiO₂ mass ratio = 1:6. The cellulose-TiO₂ composites were referred as CPT or CNT, according to the type of acid treatment applied to the cellulose, i.e., H₃PO₄ or HNO₃, respectively. Two pure cellulose derivatives, i.e. without TiO₂, were also synthesized to study the effects of acid treatments on the cellulose. The obtained materials were referred as CP and CN, for cellulose treated in H₃PO₄ or HNO₃, respectively. Analogously, two pure titania materials, i.e., in absence of cellulose, were also prepared for comparison by hydrolysing TTIP in each acid media. These samples were labelled as PT and NT, for titania treated in H₃PO₄ or HNO₃, respectively. More information about the synthesis of all these materials can be found in Section 2.2.1.

The characterization of the samples was carried out using physical adsorption of N₂, scanning electron microscopy (SEM), elemental analysis, FTIR spectroscopy, temperature programmed desorption (TPD), thermogravimetric analysis (TGA), X-ray diffraction (XRD), X-ray photoelectron spectroscopy (XPS) and Diffuse reflectance spectroscopy (DRS). The performance of cellulose-TiO₂ composites in the photodegradation of the orange-G (OG) dye in aqueous solutions was studied under UV irradiation.

3.1.2. Photocatalytic experiments.

The experiments were performed using a glass photoreactor (inner diameter of 8.5 cm × height of 20 cm) equipped with an inner quartz tube of 2.5 cm of diameter placed in the reactor center, which fits and ensures the uniform irradiation of all solution volumes by a low-pressure mercury vapour lamp (TNN 15/32, 15 W, HNG-Germany) emitting at 254 nm. The concentration of OG was determined by a UV–vis spectrophotometer (5625 Unicam Ltd., Cambridge, UK). Before catalytic experiments, all photocatalysts (800 mg) were saturated with the dye solution (800 mL) in dark to re-move the different adsorptive contribution of each sample on the evolution of the total dye concentration. After saturation, the initial dye concentration (C_0) was fitted again to 10 mg/L in all cases, and then, a UV lamp was turned on, this time being considered $t = 0$. Samples were taken from the reactor and centrifuged to separate the catalyst particles before analysis by UV–vis spectrophotometer.

3.2. Results and discussion.

The changes induced on the cellulose by each acid treatment are observed even at a glance. The original MCC is white, while CN and CP samples are brown and black, respectively (Figures 3.1a-c). The morphology of the acid treated cellulose samples was analysed by SEM (Figures 3.1d-f). The microstructure of MCC is compact, formed by long structures more or less parallel between them, where cellulose microfibers are clearly observed (Figure 3.1d). This morphology is similar to that reported by other authors [1] and is clearly maintained after the HNO₃ treatments, as observed for CN (Figure 3.1e). However, the morphology of the CP sample is different (Figure 3.1f), showing a rough and denser surface, without the original microfibers, but with a granular appearance. The results of the textural analysis carried out by N₂-adsorption are in agreement with these dense structures,

very low pore volumes and BET surface areas below $10 \text{ m}^2 \text{ g}^{-1}$ being obtained in all cases. These results point out that the acid treatments performed are unable to develop porosity on the original cellulose.

Changes in the cellulose crystallinity were studied by analysing the XRD-patterns (Figure 3.2). The original crystalline structure of MCC corresponds to the cellulose type I [2]. The diffraction peaks are approximately located at $2\theta = 14^\circ$ (101), 16° (101), 23° (002) and 35° (004). Nevertheless, the shoulders between 20 - 23° can also indicate the presence of a certain proportion of a cellulose type II, which presents peaks at 20 and 22° , corresponding to the diffractions (101) and (002), respectively. The crystalline arrangement of the cellulose is destroyed by H_3PO_4 treatments, an amorphous cellulose being obtained in agreement with other works [3, 4]. However, the crystallinity of MCC is maintained after HNO_3 treatments. These crystalline differences should be related to the different chemical transformations induced by each acid treatment, as well as the different ability of establishing interactions (H-bonds) between cellulose chains during the drying process [5].

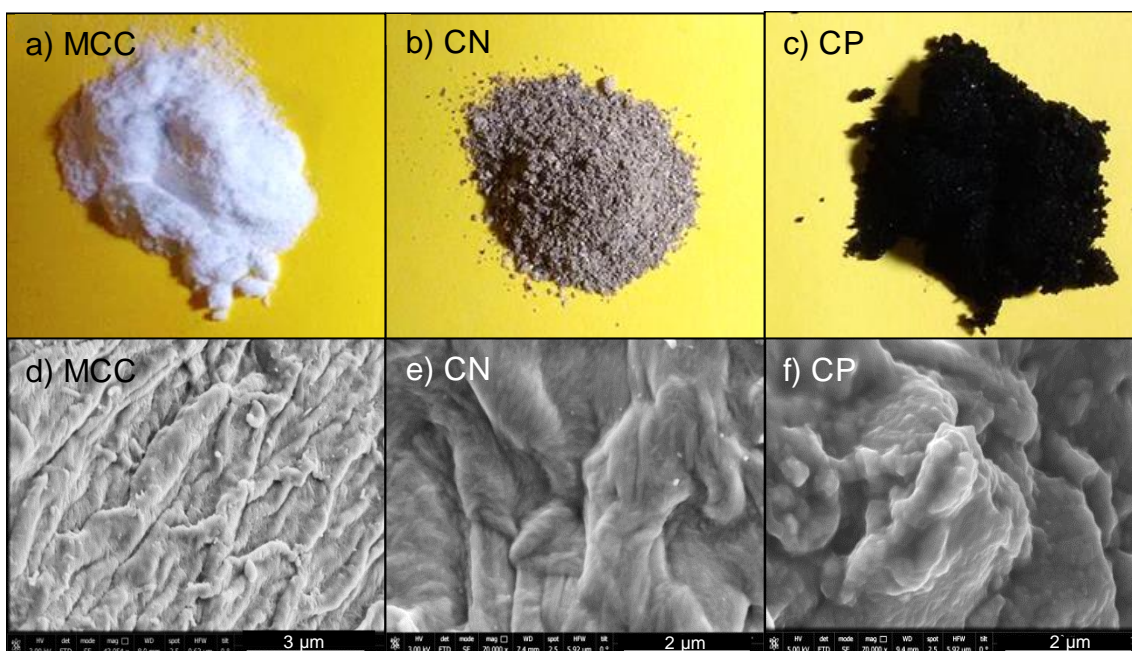


Figure 3.1. (a-c) Photographs and (d-f) SEM images of raw cellulose (MCC), cellulose after nitric acid treatment (CN) and cellulose after phosphoric acid treatment (CP).

The chemical surface of the cellulose before and after acid treatments was analysed by XPS. Significant changes were found in the profiles of the XPS spectra (Figure 3.3), which confirms the formation of different surface groups in each case. The surface composition of the raw cellulose and their acid-treated derivatives is summarized in Table 3.1. The strong functionalization of the CP sample is corroborated by the high phosphorus content, while the nitrogen content is practically negligible. The oxygen content significantly decreases after both acid treatments denoting the esterification or hydrolysis processes [6, 7].

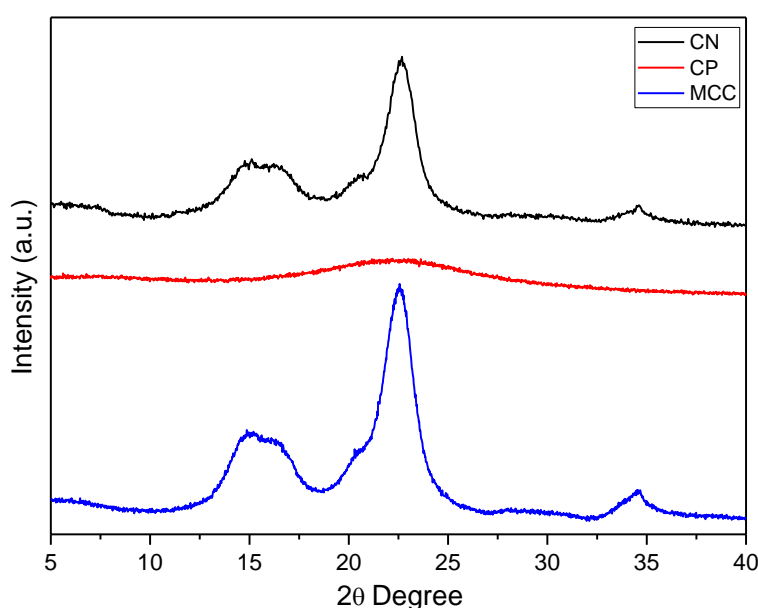


Figure 3.2. XRD patterns of the raw cellulose and their acid-treated derivatives.

Different contributions are used to fit the C_{1s} region of raw MCC (Figure 3.3a). The main peak located at 284.1 eV is associated to the C-C bonds while the component with a binding energy (BE) at 285.3 eV is assigned to C-O or C-OH bonds [8]. A small shoulder is also assigned in the low BE region (282.4 eV), which could be associated with the presence of aromatic regions in the sample [9]. After HNO_3 treatments (Figure 3.3b), the main components at around 284 and 285 eV are maintained but the new peak detected at 286.8 eV denotes the formation of C=O bonds in carboxylic acid groups. The main change in the profile of the C_{1s} region is the big shoulder observed at low BE (282.6 eV), which increased up to 16% in comparison with the 4% recorded for MCC at this BE. The C_{1s} spectrum also markedly changed after H_3PO_4 treatments (Figure 3.3c), in this case, a

significant peak (around 10% of the total) is detected at 288.7 eV for CP associated with carboxylated groups or O-C-O-R groups [10, 11].

Table 3.1. Surface composition by XPS of the raw cellulose and their acid-treated derivatives.

Sample	Surface concentration (wt.%)			
	C	O	N	P
MCC	56.0	44.0	-	-
CP	48.8	32.7	-	18.5
CN	65.5	34.0	0.5	-

Two peaks were used to fit the O_{1s} region in all samples. The distribution of oxygenated surface groups (OSG) is also quite similar between MCC and CN samples (Figures 3.3d and e). The main peak (around 90 % of the total) is located at 530.6 eV, associated to C–OH groups, while the peak at 531.9 eV corresponds to the O-C-O bonds. Nevertheless, the O_{1s} profile in the case of the CP sample is wider and less symmetric (showing a big shoulder close to low BE values), appearing shifted to higher BE (Figure 3.3f) due to the formation of different oxygenated surface groups, as denoted by the C_{1s} spectral region. Thus, the peak at 531.9 eV indicates the presence of P=O bonds, but it should also contain the C-O bonds from the raw cellulose. The second peak placed at 533.2 eV corresponds to C-O-P bonds [10-12]. The P_{2p} spectral region presents two contributions located at 133.2 eV (66%) and 134.1 eV (34%) which are assigned to P-O-C and/or C-PO₃ groups and to penta-valent phosphorus in phosphates or C-O-PO₃ groups linked to the cellulose structure, respectively [10, 12], also denoting the bonds of the phosphate groups to the cellulose chains.

The nature of the surface groups created by acid treatments was studied by complementary techniques including infrared spectroscopy (FTIR) or temperature programmed desorption (TPD). The FTIR spectra are collected in Figure 3.4. The main bands in the FTIR spectrum of MCC are located at 3340 cm⁻¹ (O-H stretching), 2910 cm⁻¹ (C-H stretching), 1650 cm⁻¹ (C-H in aromatic units), 1600 cm⁻¹ (-OH hydroxyl groups and

adsorbed water), 1430 cm^{-1} ($-\text{CH}_2$ bending), 1320 cm^{-1} (C-H bending) and a strong band centred at 1060 cm^{-1} that shows different shoulders; peaks in this region are associated to the CO groups in the polysaccharide structure (1030 cm^{-1} C-O stretching or around 1160 cm^{-1} C-O-C asymmetric stretching). The position of these bands is influenced by the change of inter or intramolecular hydrogen bonds, and therefore, related with changes in the chemical surface groups and crystallinity [13] previously commented.

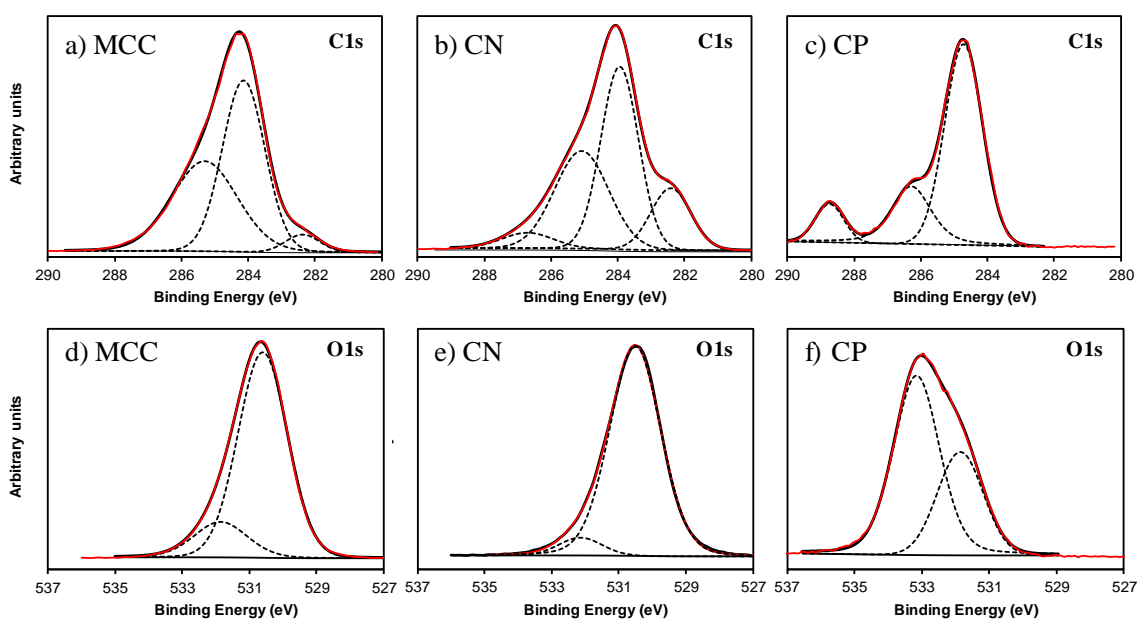


Figure 3.3. High resolution XPS spectra of the C1s and O1s regions of the raw cellulose and their acid-treated derivatives.

As observed in both XPS and XRD results, the FTIR spectrum of the CN sample is also quite similar to that for MCC. The main band is maintained at around 1060 cm^{-1} but new bands in the region of $1600 - 1700\text{ cm}^{-1}$ denoted the development of C-O and C=O groups in carboxylic acid, lactones or ketone groups after acid treatment. The major differences are observed in the FTIR spectra corresponding to the CP sample, bands being in general broader and more intense, probably influenced by the strong change in the crystallinity of this sample [13]. The main band at 1050 cm^{-1} is now broad and appears shifted to 980 cm^{-1} . This band is attributed P-OH groups stretching vibrations, P-O-C carbons asymmetric stretching, interactions between aromatic ring vibration and P-C (aromatic) stretching and/or symmetrical stretching P=O in PO_2 and PO_3 phosphate-carbon complexes [14]. There is also a broad band in the region of $1600-1700\text{ cm}^{-1}$, where C=C and C=O stretching vibrations take place. The reinforcement of this band is associated not

only to a strong oxidation degree, but also can indicate an increase of the aromatic character of the glucose derivative structure during acid treatments [15]. The suppression of the C-H and CH₂ bands in the 1300 - 1400 cm⁻¹ region and the development of a new and intense band centred at 2330 cm⁻¹ which is also associated to the C=C bonds [16] also confirm the greater aromatic character of the CP chemical structure. Finally, the bands at 2910 cm⁻¹ became also very broad and intense, while the band at 3340 cm⁻¹ is shifted to higher frequencies (3360 cm⁻¹). These changes are associated to the different interactions between C-H and C-OH groups during decrystallization.

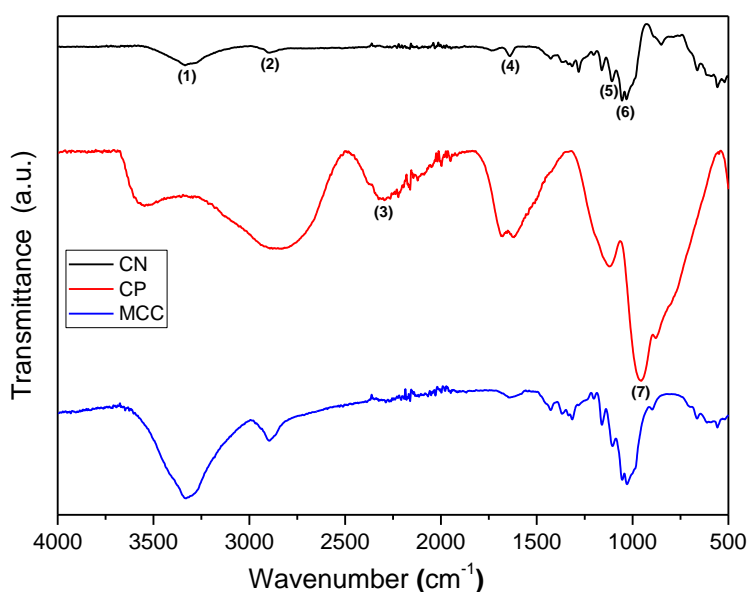


Figure 3.4. FTIR spectra of the raw cellulose and their acid-treated derivatives: O-H stretching (1), C-H stretching (2), C=C bonds (3), C-H in aromatic units (4), C-O-C asymmetric stretching (5), C-O stretching (6) and P-O-C asymmetric stretching (7).

The TPD profiles of evolved H₂O, CO and CO₂ are shown in Figure 3.5 for the raw cellulose and their acid-treated derivatives. These gases are evolved during the thermal treatments of the samples in inert atmosphere (He-flow) by decomposition of chemical groups present in the material structure depending on their thermal stability [17]. During this thermal decomposition, a sequence of depolymerisation – volatilization occurs in the cellulose structure [18, 19]. The depolymerization of solid cellulose generates levoglucosan, which by dehydration and isomerization reactions forms intermediate anhydro sugars and further, furans and glyceraldehydes. Carbon monoxide and carbon dioxide are formed from decarbonylation and decarboxylation reactions.

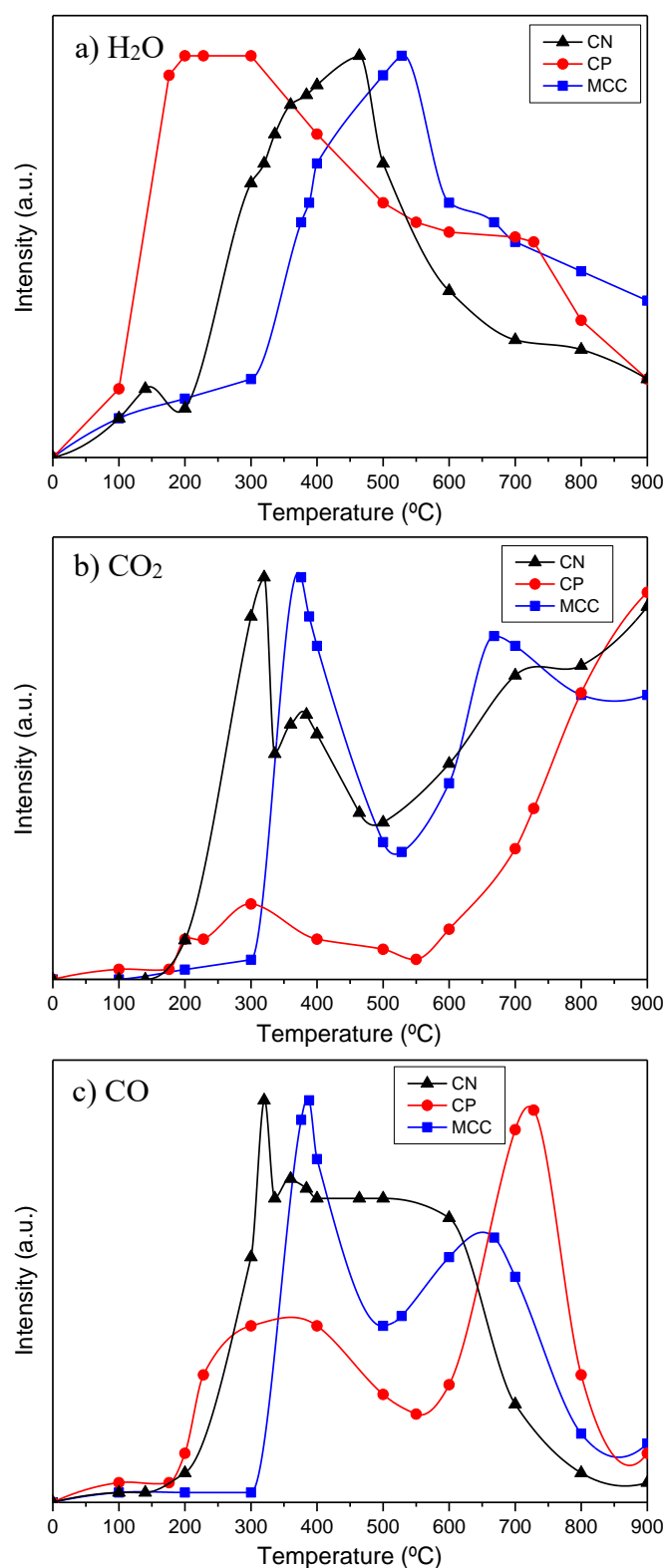


Figure 3.5. TPD profiles of H₂O, CO₂ and CO showing the influence of the acid treatments on the thermal stability of chemical groups generated on the cellulose.

Both acid treatments favour the dehydration process at a lower temperature than on raw MCC. These differences are associated to the formation of different concentrations of different oxygenated surface groups during acid treatments as previously commented, namely carboxylic acid groups, which consequently dehydrate forming anhydrides during the thermal treatment. The profiles of CO and CO₂ evolved recorded for both MCC and CN are quite similar (Figures 3.5a and b), with slight changes related to the maximum decomposition temperature as also denoted by XPS. The highest peak in the CO₂ profile at low temperature (between 250-400 °C) was assigned to carboxylic acids release while the second maxima of the CO₂-profile indicate the presence of more stable CO₂-evolving groups like anhydrides or lactones. Different CO-evolving groups are also present. According to previous works phenols evolve between 600-700 °C, ether groups at around 700 °C, carbonyls between 800-900 °C and more stable chromenes at around 1000 °C [20].

However, the TPD profiles strongly changes in the case of the CP sample. The decarboxylation only increases significantly from 550 °C and the decarbonylation is also maxima at 750 °C (Figure 3.5c), denoting the greater thermal stability of the chemical groups present in this sample. H₃PO₄ is a classical activating agent in the production of porous carbon materials from lignocellulosic materials by chemical activation [21]. The temperature of gasification induced by H₃PO₄, opening porosity by evolving gases during activation, strongly depends on the distinct biopolymeric composition of different biomass derivatives [22]. In our study, the release of CO and CO₂ from the CP sample takes place at temperatures significantly higher than those for MCC and CN, and only increase from 500 °C, pointing out that the reduction of phosphate groups by the organic cellulose do not occurs bellow this temperature range.

The direct impregnation on the MCC sample with the Ti-precursor was not homogenously achieved because of its close structure, which hinders its dissolution and leads to a poor support-active phase interaction. MCC needed to be treated with acid treatments before Ti-impregnation. The presence of the surface groups generated on the cellulose surface during acid treatments will determine the nature and strength of the interactions between the cellulose molecules in solution and the titania precursor during the synthesis of the corresponding composites, and consequently, the TiO₂ loading, nature and distribution of the cellulose derivatives.

The total TiO₂ content determined by TG in CNT and CPT composites was 62.8 and 73.7 wt.%, respectively, probably as consequence of a stronger interaction with the CP surface.

The surface composition analysed by XPS in cellulose-TiO₂ composites is summarized in Table 3.2. The carbon content decreases regarding the corresponding supports (Table 3.1) because of cellulose is coated by the TiO₂ phase. However, these results point out significant differences in the distribution of TiO₂ on the cellulose supports. Thus, in spite of the higher TiO₂ content determined by TG for the sample CPT (73.7 wt.%), the Ti content determined by XPS is significantly lower than for CNT (i.e., 17.4 and 43.8 wt.%, respectively). It is also noteworthy that the phosphor content in CPT surface even increases regarding the CP support. These facts denote that (i) phosphor groups are not covered by large TiO₂ particles, leading to high P-content but a low Ti-content (ii) these groups interacts with the TiO₂ precursor forming new Ti-P structures where the oxygen and phosphate groups are located in surface and can be detected by XPS. After impregnation, the P_{2p} region in CPT significant change regarding the corresponding CP support [10, 11]. In this case, only presents one component at 133.4 eV corresponding to pentavalent phosphate groups, denoting the interaction of phosphate groups (C-PO₃ or C-O-PO₃ groups) with the titania phase.

Table 3.2. Surface composition of TiO₂-cellulose composites determined by XPS.

Sample	Surface concentration (wt.%)				
	C	O	N	P	Ti
CPT	8.5	47.3	-	26.8	17.4
CNT	18.7	36.2	1.3	-	43.8

In Figure 3.6 are shown the corresponding C_{1s}, O_{1s} and Ti_{2p} spectral regions. Modification of the position and shapes of these curves regarding their corresponding supports are also indicative of the different interactions between phases in each composite. The Ti_{2p} region is fitted in both CNT and CPT composites (Figures 3.6c and f) with two components ascribed to Ti 2p_{3/2} and Ti 2p_{1/2} with a difference in binding energy of 5.7 eV, in good agreement with Ti⁺⁴ in TiO₂ [23]. However, it is noteworthy that both components

are shifted at around 1.7 eV to higher BE values in CPT, indicating the different electronic environment of Ti⁴⁺ in the chemical structure of the composite.

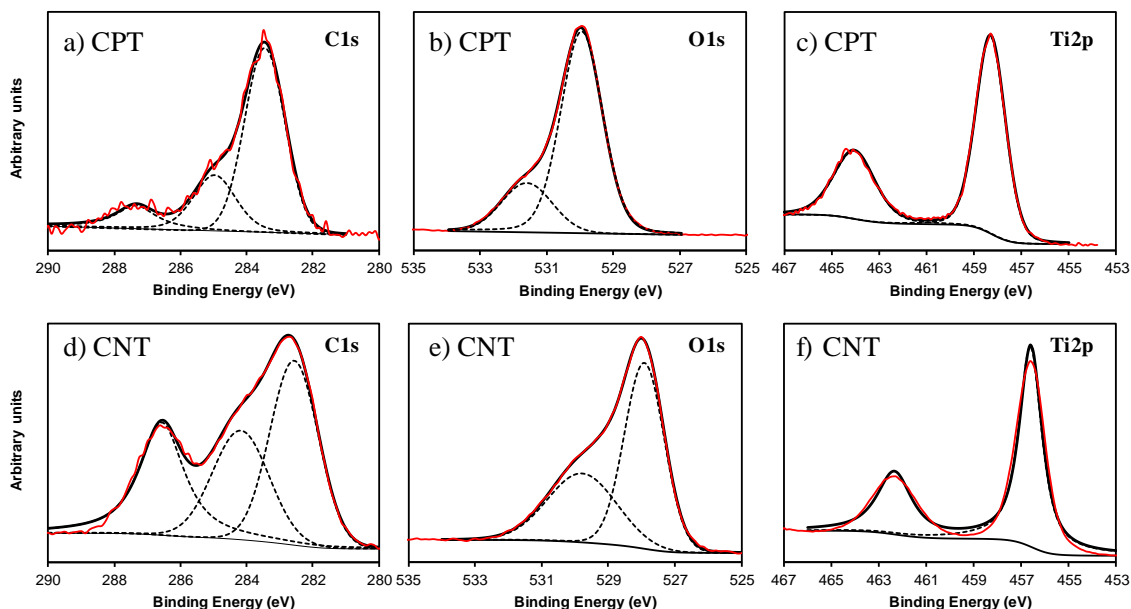


Figure 3.6. High resolution XPS spectra of the C_{1s}, O_{1s} and Ti_{2p} regions for the cellulose-TiO₂ composites.

In contrast with the strong differences in the profile of the O_{1s} region previously described for CN and CP, after TiO₂-doping a quite similar O_{1s} profile is observed for CNT and CPT (Figures 3.6b and e), denoting that in these cases oxygen groups correspond mainly to the TiO₂-coating of the cellulose particles. Two components were also used to fit the O_{1s} spectra in both composite. The peak at lower BE correspond to Ti–O–Ti (lattice O) bonds, while component at higher BE are ascribed to Ti–OH and C–O (C–OH or C–O–C), respectively [24]. Nevertheless, as occurs for the Ti_{2p} curve, the peaks are shifted around 1.5 eV to higher BE values in the case of CPT and the peak at 531.4 eV involve also to both C=O or P=O bonds [4].

The C_{1s} spectrum after TiO₂ doping is less intense for composites than for their corresponding supports, because the TiO₂-nanoparticles are covering the cellulosic chains. TiO₂ doping also modifies the shape and position of C_{1s} spectrum regarding those each support. In the case of CPT, the C_{1s} spectrum shifted to lower BE regarding CP sample, although the profile is quite similar. Also in the case of CNT, the main peak in the C_{1s} spectrum shifted from 284 to 282.6 eV. Peaks in this region (282.2–282.7 eV) were

associated with the formation of O-Ti-C or Ti-O-C bonds [24, 25]. The peak at 281-282 eV characteristic of Ti-C bonds is however missing. These results point out the interactions between both phases, namely through oxygen surface groups. The different interactions with the OSG are pointed out also by the different variations observed on the TPD-profiles regarding the corresponding supports (Figure 3.7).

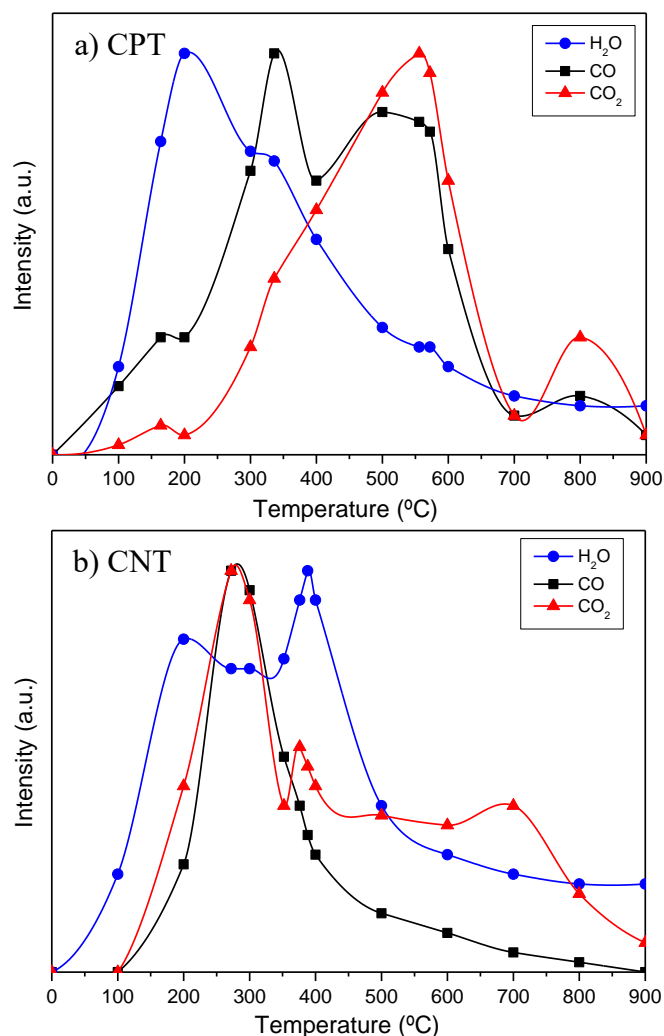


Figure 3.7. TPD-profiles of H₂O, CO and CO₂ of the cellulose-TiO₂ composites.

When comparing the TPD profiles of the cellulose-TiO₂ composites with those of their respective supports (Figure 3.7 vs. 3.5) a decrease in the temperature of decarbonylation and decarboxylation processes is clearly observed in both cases. The different profiles denote again the formation of different bonds. In the case of CPT, the maximum release of CO₂ occurs at 550 °C, while in the CP support this process is practically

starting at this temperature. Similarly, the temperature of the maximum in the CO profile decreases from 750 to 550 °C. These processes at high temperatures were previously discussed as consequence of the degradation of the phosphate groups by the organic support. In the case of CNT, both CO and CO₂ evolve more or less simultaneously, related to the anhydride groups present in the CN support. However, both the CO and CO₂ profile significantly changes. While the CO-profile presents a large shoulder at 600 °C in the CN support, in the case of CNT in this region only a large tail of the maximum peak is observed. Similarly, the CO₂ profile does not increase progressively with the temperature, but present a second maximum at around 700 °C. This means that the high stable OSG present in the supports, including the oxygen contained in the phosphorus groups [21, 22], are interacting with the TiO₂ phase in the composite, also favouring the formation of C-O-Ti or C-(O)-P-O-Ti bonds that in general have a smaller thermal stability than the original ones.

The different interactions between dissolved cellulose and the Ti-alkoxide precursor are pointed out also by the different morphology and crystallinity of the TiO₂ phase formed in each acid media (Figures 3.8a and b). In the case of CPT, TiO₂ is forming flat microstructures grouped to form a flaky solid, however, CNT present the formation of round-shaped particles. These TiO₂-composites have also different crystallinity, as shown by XRD (Figure 3.8c). CPT is an amorphous sample where therefore, both components, cellulose and TiO₂ – particles, remains amorphous. However, the XRD-pattern of the CNT sample clearly shows the formation of crystalline anatase but the XRD peaks corresponding to the cellulose phase are not observed. Because the CN sample clearly present the peaks corresponding to the cellulose type I (Figure 3.2), this means that the interaction of the dissolved cellulose with the titanium isopropoxide (TTIP) avoids the reconstruction of the crystalline cellulose structure, because the titania phase difficult the contact between cellulose chains and the formation of C-H bonds between them.

The influence of cellulose on these structures is pointed out by comparing the XRD of the CPT and CNT composites with those corresponding to pure TiO₂ synthesized in identical conditions but in absence of cellulose (Samples NT and PT). The phosphate ions preserve the crystal growth independently of the presence/absence of the cellulose phase. Both PT and CPT are amorphous materials. However, TN presents a mixture of rutile and brookite while in CNT, as commented, it is anatase. The influence of the anionic species in

the crystal structure of TiO_2 samples prepared in acid media by hydrolysis of the corresponding alkoxides was previously pointed out [26]. The low affinity of NO_3^- by titania in solutions favours the reorganization of the TiO_6 octahedron forming the rutile or brookite [27, 28] structures, while CH_3COO^- or SO_4^{2-} induces the formation of anatase. In such a way, cellulose seems to avoid the anatase-rutile transformation during the synthesis of the composite.

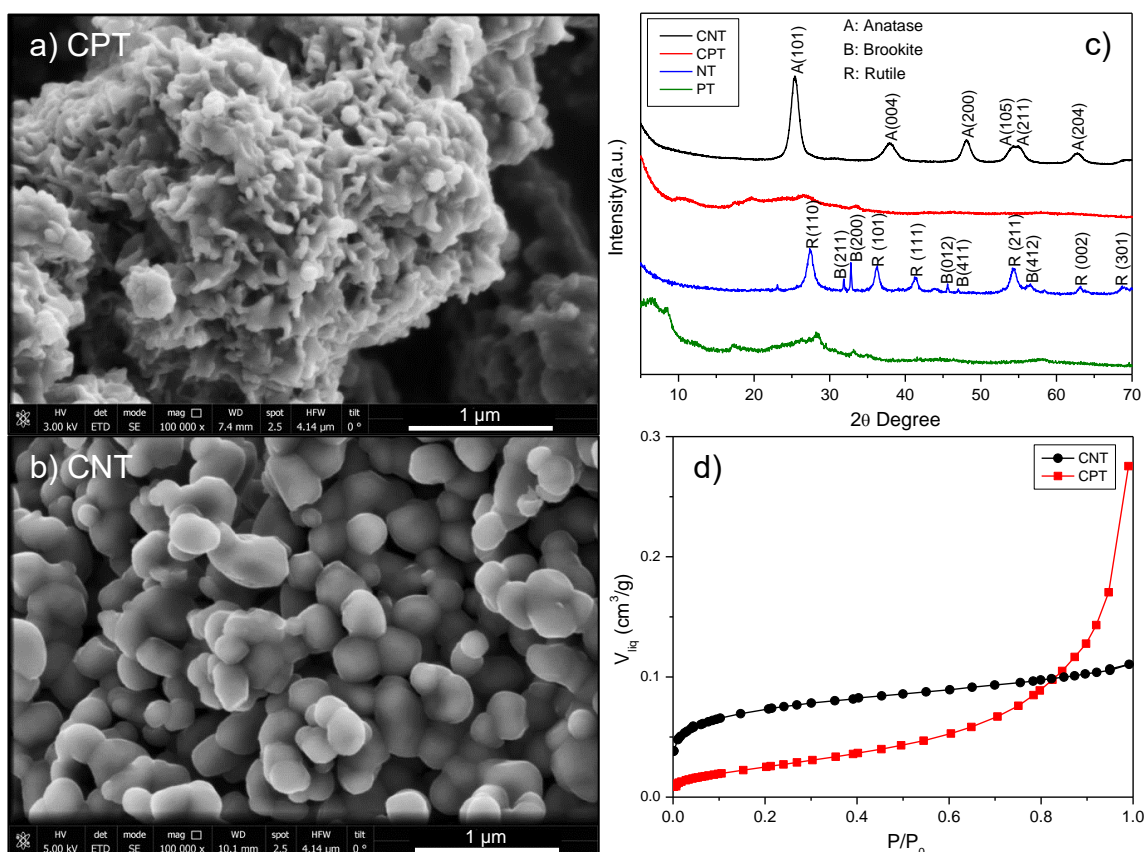


Figure 3.8. (a, b) SEM images, (c) XRD-patterns and (d) N_2 -adsorption isotherms of the cellulose- TiO_2 composites.

The different morphology leads to a different porous texture, as denoted by the shape of the corresponding N_2 -adsorption isotherms (Figure 3.8d). The porosity of the composites is always higher than in their pure phases. In the case of the CNT composite isotherm is clearly type I, associated to microporous materials. However the isotherm of CPT is type II showing a clear hysteresis cycle associated to the N_2 -condensation processes into mesopores [29]. The textural characteristics are summarized in Table 3.3. Thus, the CNT is evidently a microporous sample, which contributes to higher S_{BET} values. However, in the case of

CPT the micropore volume is low, leading to low surface values in spite of the fact that the total pore volume is larger.

Table 3.3. Textural characteristics of the cellulose-TiO₂ composites.

Sample	S_{BET} (m^2g^{-1})	V_{T} (cm^3g^{-1})	V_{micro} (cm^3g^{-1})	L_0 nm	V_{meso} (cm^3g^{-1})
CPT	49	0.271	0.020	1.78	0.251
CNT	167	0.110	0.065	1.85	0.045

Finally, composites were analysed by UV–Vis diffuse reflectance spectroscopy (Figure 3.9) to determine the corresponding band gap (E_g) values of the composites according to the procedure previously described [30, 31]. The band gap values determined for the CPT sample was 3.4 eV, which is comparable to that obtained for the pure TiO₂ (P25), while for the CNT composite the band gap was reduced down to 3.1 eV.

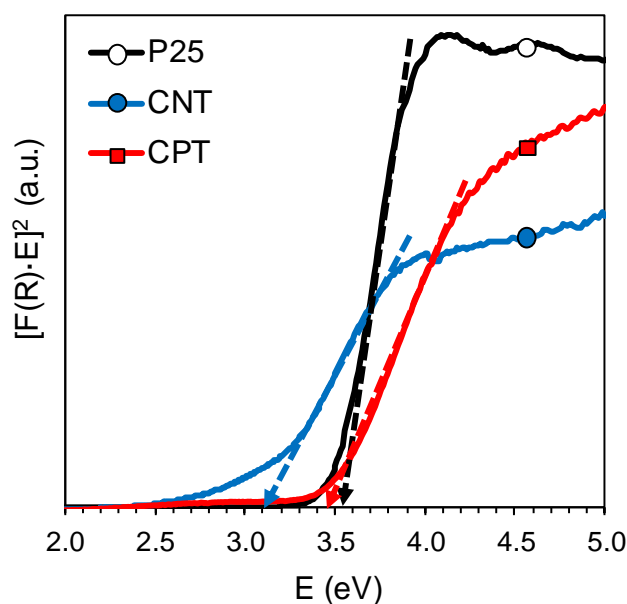


Figure 3.9. Plot of transformed Kubelka–Munk as a function of the energy of light for TiO₂-P25, CNT and CPT composites (inset: determination of the band gap).

The adsorptive performance of both CNT and CPT composites in the removal of the OG dye is compared with a benchmark TiO₂ material (P25, Degussa) (Figure 3.10a). As commented in the experimental section, materials were first saturated with the pollutant before the photocatalytic process, this methodology allowing to analyse separately both

contributions. CNT clearly presents the best adsorptive performance of OG in aqueous solution due to its largest micropore volume and BET surface area (Table 3.3), since the micropore size (L_0 , Table 3.3) and consequently, the diffusion restrictions in both composites (around 1.8 nm) were similar. The large mesoporosity of CPT has a poor influence on the adsorption behaviour, but the beneficial effect on the dye adsorption of phosphate doping in Ti-structures have been previously reported [32] and should explain the slightly higher OG adsorption compared to that for TiO_2 -P25.

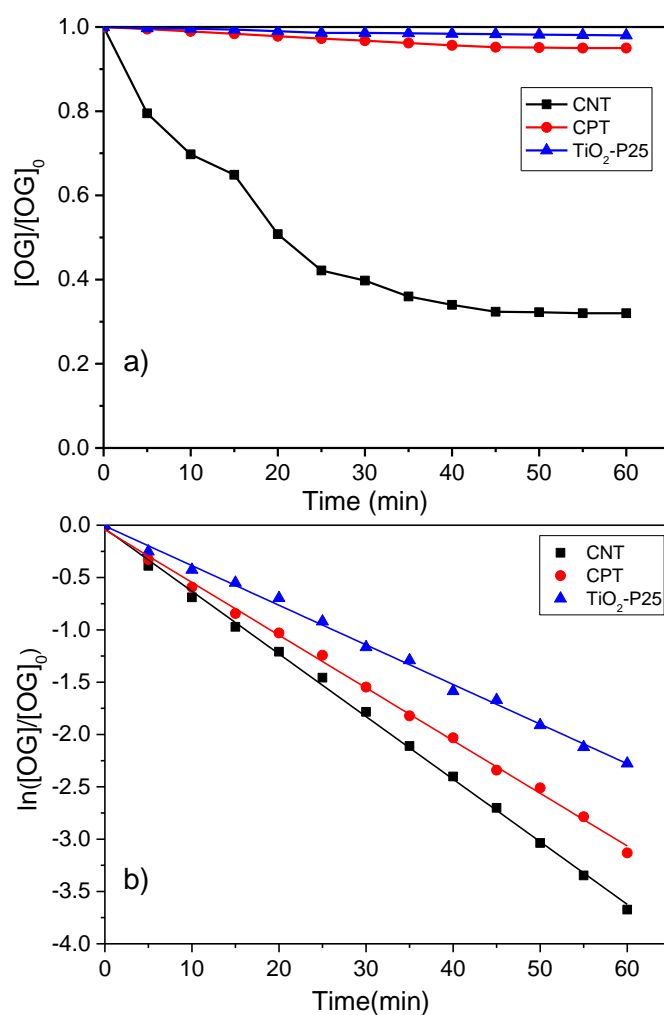


Figure 3.10. Orange-G adsorption (a) and photocatalytic degradation (b) for cellulose- TiO_2 composites and P25 under UV irradiation. Curves represent the fitting of the pseudo-first order equation to the experimental data.

The photocatalytic performance of composites was also analysed in comparison with TiO_2 -P25. The OG concentration decreases exponentially with the reaction time. The

kinetics curves for the OG degradation were therefore fitted using the pseudo first-order kinetic equation $\ln(C/C_0) = -k t$ (Figure 3.10b), obtaining in all cases high values of r^2 upon linear regression [33]. The k and $t_{1/2}$ for CNT, CPT and P25 are presented in Table 3.4. Both cellulose-TiO₂ composites presented better efficiency than the benchmark P25 material, CNT being the most active photocatalyst in the removal of OG. Different factors can influence on this behaviour such as, the higher surface area and the band-gap narrowing promoted by interactions with the cellulose through C-O-Ti bonds. The presence of phosphorus-containing groups on the CPT surface could also modify its photocatalytic efficiency, although these functionalities led to amorphous Ti-particles.

Table 3.4. Pseudo first-order rate constant (k), regression coefficient (R^2) and half-life time ($t^{1/2}$) of OG degradation under UV irradiation.

Sample	k (10^{-3} min^{-1})	R^2	$t^{1/2}$ (min)
CNT	59.8 ± 0.7	0.998	11.8
CPT	50.4 ± 0.6	0.998	13.9
P25	37.9 ± 0.6	0.996	18.7

Hamad *et al.* [33] suggested that amorphous polyphosphates embed anatase nanocrystals enhanced the mesoporosity, which is an agreement with high mesopore volume determined for CPT. However, these amorphous structures have abundant imperfections and dangling bonds favouring the e^- / h^+ recombination. Both contrary effects on the activity depend on the P/Ti ratio [34]. The increasing proportion of amorphous phases in titania (oxohydroxides) photocatalysts decreases the photocatalytic activity [35]. However, amorphous TiO₂ can be also photocatalytically active when supported on carbon materials [36]. This enhanced performance was related with the interactions with the support or the formation of nanocrystals into the macroscopically amorphous active phases.

3.3. Conclusions.

HNO₃ or H₃PO₄ acids were selected to dissolve MCC. Simultaneously, oxygenated and phosphorus groups are linked to the cellulose chains. The functionalization degree is larger in the case of cellulose CP, which becomes black and amorphous, while sample CN

is brown and maintains the crystallinity. The impregnation with the Ti-alkoxide is influenced by these functionalities, which determines the loading, morphology, porosity and band-gap values of the composites. Higher TiO₂ loading is obtained when pretreated with H₃PO₄ acid. However, in spite of the higher loading, TiO₂ remains amorphous in CPT while in CNT is forming round-shaped anatase crystallites. The different morphology leads to a different porosity. Thus, CNT composite is microporous with a high surface area, while CPT is mainly a macro-mesoporous material. The interactions between the surface groups present on the cellulose chains and the titania-precursor allow a band gap narrowing and a developed active surface, in particular for the CNT composite, thus leading to more active photocatalyst.

3.4. References.

- [1] I.F. Amaral, P.L. Granja, M.A. Barbosa, Chemical modification of chitosan by phosphorylation: an XPS, FT-IR and SEM study, *Journal of Biomaterials Science, Polymer Edition*, 16 (2005) 1575-1593.
- [2] A.E. Oudiani, Y. Chaabouni, S. Msahli, F. Sakli, Crystal transition from cellulose I to cellulose II in NaOH treated *Agave americana* L. fibre, *Carbohydrate Polymers*, 86 (2011) 1221-1229.
- [3] Y.H.P. Zhang, J. Cui, L.R. Lynd, L.R. Kuang, A Transition from Cellulose Swelling to Cellulose Dissolution by *o*-Phosphoric Acid: Evidence from Enzymatic Hydrolysis and Supramolecular Structure, *Biomacromolecules*, 7 (2006) 644-648.
- [4] J. Zhang, J. Zhang, L. Lin, T. Chen, J. Zhang, S. Liu, Z. Li, P. Ouyang, Dissolution of Microcrystalline Cellulose in Phosphoric Acid—Molecular Changes and Kinetics, *Molecules*, 14 (2009) 5027.
- [5] X. Hao, W. Shen, Z. Chen, J. Zhu, L. Feng, Z. Wu, P. Wang, X. Zeng, T. Wu, Self-assembled nanostructured cellulose prepared by a dissolution and regeneration process using phosphoric acid as a solvent, *Carbohydrate Polymers*, 123 (2015) 297-304.
- [6] T. Marzialetti, M.B. Valenzuela Olarte, C. Sievers, T.J.C. Hoskins, P.K. Agrawal, C.W. Jones, Dilute Acid Hydrolysis of Loblolly Pine: A Comprehensive Approach, *Industrial & Engineering Chemistry Research*, 47 (2008) 7131-7140.
- [7] E.A. Skiba, V.V. Budaeva, O.V. Baibakova, V.N. Zolotukhin, G.V. Sakovich, Dilute nitric-acid pretreatment of oat hulls for ethanol production, *Biochemical Engineering Journal*, 126 (2017) 118-125.
- [8] M. Božič, P. Liu, A.P. Mathew, V. Kokol, Enzymatic phosphorylation of cellulose nanofibers to new highly-ions adsorbing, flame-retardant and hydroxyapatite-growth induced natural nanoparticles, *Cellulose*, 21 (2014) 2713-2726.

- [9] M. Smith, L. Scudiero, J. Espinal, J.-S. McEwen, M. Garcia-Perez, Improving the deconvolution and interpretation of XPS spectra from chars by ab initio calculations, *Carbon*, 110 (2016) 155-171.
- [10] A. Elmouwahidi, E. Bailón-García, A.F. Pérez-Cadenas, F.J. Maldonado-Hódar, F. Carrasco-Marín, Activated carbons from KOH and H₃PO₄-activation of olive residues and its application as supercapacitor electrodes, *Electrochimica Acta*, 229 (2017) 219-228.
- [11] J. Zhang, B. Zhang, J. Zhang, L. Lin, S. Liu, P. Ouyang, Effect of phosphoric acid pretreatment on enzymatic hydrolysis of microcrystalline cellulose, *Biotechnology Advances*, 28 (2010) 613-619.
- [12] M. Ghanadpour, F. Carosio, P.T. Larsson, L. Wågberg, Phosphorylated Cellulose Nanofibrils: A Renewable Nanomaterial for the Preparation of Intrinsically Flame-Retardant Materials, *Biomacromolecules*, 16 (2015) 3399-3410.
- [13] S.Y. Oh, D.I. Yoo, Y. Shin, H.C. Kim, H.Y. Kim, Y.S. Chung, W.H. Park, J.H. Youk, Crystalline structure analysis of cellulose treated with sodium hydroxide and carbon dioxide by means of X-ray diffraction and FTIR spectroscopy, *Carbohydrate Research*, 340 (2005) 2376-2391.
- [14] F.W. Shaarani, B.H. Hameed, Ammonia-modified activated carbon for the adsorption of 2,4-dichlorophenol, *Chemical Engineering Journal*, 169 (2011) 180-185.
- [15] X. Liu, Y. Gu, J. Huang, Hierarchical, Titania-Coated, Carbon Nanofibrous Material Derived from a Natural Cellulosic Substance, *Chemistry – A European Journal*, 16 (2010) 7730-7740.
- [16] F. Kaouah, S. Boumaza, T. Berrama, M. Trari, Z. Bendjama, Preparation and characterization of activated carbon from wild olive cores (oleaster) by H₃PO₄ for the removal of Basic Red 46, *Journal of Cleaner Production*, 54 (2013) 296-306.
- [17] S. Morales-Torres, L.M. Pastrana-Martínez, J.L. Figueiredo, J.L. Faria, A.M.T. Silva, Design of graphene-based TiO₂ photocatalysts-a review, *Environmental Science and Pollution Research*, 19 (2012) 3676-3687.
- [18] Y.-C. Lin, J. Cho, G.A. Tompsett, P.R. Westmoreland, G.W. Huber, Kinetics and Mechanism of Cellulose Pyrolysis, *The Journal of Physical Chemistry C*, 113 (2009) 20097-20107.
- [19] M.I.G. Miranda, C.I.D. Bica, S.M.B. Nachtigall, N. Rehman, S.M.L. Rosa, Kinetic thermal degradation study of maize straw and soybean hull celluloses by simultaneous DSC-TGA and MDSC techniques, *Thermochimica Acta*, 565 (2013) 65-71.
- [20] J.F. Vivo-Vilches, E. Bailón-García, A.F. Pérez-Cadenas, F. Carrasco-Marín, F.J. Maldonado-Hódar, Tailoring the surface chemistry and porosity of activated carbons: Evidence of reorganization and mobility of oxygenated surface groups, *Carbon*, 68 (2014) 520-530.
- [21] M.J. Prauchner, F. Rodríguez-Reinoso, Chemical versus physical activation of coconut shell: A comparative study, *Microporous and Mesoporous Materials*, 152 (2012) 163-171.
- [22] Y. Guo, D.A. Rockstraw, Physical and chemical properties of carbons synthesized from xylan, cellulose, and Kraft lignin by H₃PO₄ activation, *Carbon*, 44 (2006) 1464-1475.

- [23] L. Luo, Y. Yang, M. Xiao, L. Bian, B. Yuan, Y. Liu, F. Jiang, X. Pan, A novel biotemplated synthesis of TiO₂/wood charcoal composites for synergistic removal of bisphenol A by adsorption and photocatalytic degradation, *Chemical Engineering Journal*, 262 (2015) 1275-1283.
- [24] M.A. Mohamed, W.N. W. Salleh, J. Jaafar, Z.A. Mohd Hir, M.S. Rosmi, M. Abd. Mutalib, A.F. Ismail, M. Tanemura, Regenerated cellulose membrane as bio-temple for in-situ growth of visible-light driven C-modified mesoporous titania, *Carbohydrate Polymers*, 146 (2016) 166-173.
- [25] M.A. Mohamed, W.N. Wan Salleh, J. Jaafar, M.S. Rosmi, Z.A. Mohd. Hir, M. Abd Mutalib, A.F. Ismail, M. Tanemura, Carbon as amorphous shell and interstitial dopant in mesoporous rutile TiO₂: Bio-template assisted sol-gel synthesis and photocatalytic activity, *Applied Surface Science*, 393 (2017) 46-59.
- [26] M.A. Reddy, M.S. Kishore, V. Pralong, V. Caignaert, U.V. Varadaraju, B. Raveau, Room temperature synthesis and Li insertion into nanocrystalline rutile TiO₂, *Electrochemistry Communications*, 8 (2006) 1299-1303.
- [27] J.H. Lee, Y.S. Yang, Synthesis of TiO₂ nanoparticles with pure brookite at low temperature by hydrolysis of TiCl₄ using HNO₃ solution, *Journal of Materials Science*, 41 (2006) 557-559.
- [28] H. Kominami, M. Kohno, Y. Kera, Synthesis of brookite-type titanium oxide nanocrystals in organic media, *Journal of Materials Chemistry*, 10 (2000) 1151-1156.
- [29] K.S.W. Sing, D.H. Everett, R.A.W. Haul, L. Moscou, R.A. Pierotti, J. Rouquerol, T. Siemieniewska, Reporting physisorption data for gas/solid systems with special reference to the determination of surface area and porosity, *Pure Appl Chem*, 57 (1985) 603-6019.
- [30] E. Bailón-García, A. Elmouwahidi, M.A. Álvarez, F. Carrasco-Marín, A.F. Pérez-Cadenas, F.J. Maldonado-Hódar, New carbon xerogel-TiO₂ composites with high performance as visible-light photocatalysts for dye mineralization, *Applied Catalysis B: Environmental*, 201 (2017) 29-40.
- [31] R. López, R. Gómez, Band-gap energy estimation from diffuse reflectance measurements on sol-gel and commercial TiO₂: a comparative study, *Journal of Sol-Gel Science and Technology*, 61 (2012) 1-7.
- [32] M. Jose, N. Harsha, K. Suhailath, A.P. Mohamed, S. Shukla, Hydrogen phosphate anions modified hydrogen titanate nanotubes for methylene blue adsorption from aqueous solution: Validating novel method of predicting adsorption capacity, *Journal of Environmental Chemical Engineering*, 4 (2016) 1295-1307.
- [33] H.A. Hamad, W.A. Sadik, M.M. Abd El-latif, A.B. Kashyout, M.Y. Feteha, Photocatalytic parameters and kinetic study for degradation of dichlorophenol-indophenol (DCPIP) dye using highly active mesoporous TiO₂ nanoparticles, *Journal of Environmental Sciences*, 43 (2016) 26-39.
- [34] X. Fan, T. Yu, Y. Wang, J. Zheng, L. Gao, Z. Li, J. Ye, Z. Zou, Role of phosphorus in synthesis of phosphated mesoporous TiO₂ photocatalytic materials by EISA method, *Applied Surface Science*, 254 (2008) 5191-5198.

- [35] V.A. Lebedev, D.A. Kozlov, I.V. Kolesnik, A.S. Poluboyarinov, A.E. Becerikli, W. Grünert, A.V. Garshev, The amorphous phase in titania and its influence on photocatalytic properties, *Applied Catalysis B: Environmental*, 195 (2016) 39-47.
- [36] N. Justh, T. Firkala, K. László, J. Lábár, I.M. Szilágyi, Photocatalytic C₆₀-amorphous TiO₂ composites prepared by atomic layer deposition, *Applied Surface Science*, 419 (2017) 497-502.

CHAPTER IV-

TAILORED CARBON-TITANIUM COMPOSITES FROM FUNCTIONALIZED CELLULOSE: ASSESSMENT OF THE NANOSTRUCTURE AND PHOTOCATALYTIC EFFICIENCY



4.1. Abstract.

Carbon-Ti composites were prepared by a two step-method using cellulose as raw material. The synthesis involves the solubilization of cellulose microcrystals in an acid media (H_3PO_4 or HNO_3), which improves the dispersion of the Ti-precursor and favours simultaneously the functionalization of cellulose chains with phosphorus or oxygen functionalities. These groups determine the interactions between both cellulose-titanium phases during impregnation and consequently, define the loading and crystalline phase of Ti during carbonizations. Thus, when carbonization takes place at low temperature ($500\text{ }^\circ\text{C}$), phosphorous groups avoid the crystallization of Ti-species leading to amorphous composites, while oxygen functionalities induce the rutile formation. An increase of the carbonization temperature up to $800\text{ }^\circ\text{C}$ favours, respectively, the progressive crystal growth of rutile and the formation of TiP_2O_7 crystals by reaction between the Ti-precursor and the phosphorous functionalities of the cellulose. Both carbon-Ti composites, containing TiO_2 rutile or TiP_2O_7 nanocrystals, present a band gap narrowing compared to their corresponding pure Ti-phases. The degradation of Orange-G azo-dye in aqueous solutions was used to determine the photocatalytic efficiency, all composites being more active than the benchmark TiO_2 material (Degussa P25). Composites with a high surface area, developed micro-mesoporosity, reduced band gap and rutile crystalline phase were the most active.

4.2. Experimental.

4.2.1. Synthesis and characterization of carbon-Ti composites.

The synthesis of these materials is based in the carbonization of CPT and CNT composites and the detailed preparation can be found in Section 2.2.2. The carbon-Ti composites were referred as CPT1, CPT2, CNT1 and CNT2, where C = cellulose, P = H_3PO_4 , N = HNO_3 , T = TiO_2 , 1 or 2= carbonization temperature of $500\text{ }^\circ\text{C}$ or $800\text{ }^\circ\text{C}$, respectively. Additionally, pure carbon materials were prepared as reference to follow the functionalization of cellulose by H_3PO_4 (CP1 and CP2 samples) and HNO_3 (CN1 and CN2 samples) during thermal treatments.

The characterization of the samples was carried out using physical adsorption of N_2 , scanning electron microscopy (SEM), transmission electron microscopy (TEM),

thermogravimetric analysis (TGA), X-ray diffraction (XRD), X-ray photoelectron spectroscopy (XPS) and Diffuse reflectance spectroscopy (DRS). The performance of carbon-Titanium composites in the photodegradation of the orange-G (OG) dye in aqueous solutions was studied under UV irradiation.

4.2.2. Photocatalytic tests

The performance of carbon-Ti composites in the photodegradation of the Orange-G (OG) dye in aqueous solutions was studied under UV irradiation. The experiments were performed using a glass photoreactor (inner diameter of 8.5 cm x height of 20 cm) equipped with an inner quartz tube of 2.5 cm of diameter placed in the reactor center and a low-pressure mercury vapour lamp (TNN 15/32, 15 W, HNG-Germany) emitting at 254 nm. The concentration of OG was determined by a UV–Vis spectrophotometer (5625 Unicam Ltd., Cambridge, UK). Before catalytic experiments, all photocatalysts (800 mg) were saturated with the dye solution (800 mL) in dark to remove the different adsorptive contribution of each sample on the evolution of the total dye concentration. After saturation, the initial dye concentration (C_0) was fitted again to 10 mg L^{-1} in all cases, and then, a UV lamp was turned on, this time being considered $t=0$. Samples were taken from the reactor and centrifuged to separate the catalyst particles before analysis by the UV–Vis. Spectrophotometer.

4.3. Results and discussion.

4.3.1. Materials characterization.

Cellulose was first dissolved by HNO_3 or H_3PO_4 acid treatments to facilitate the impregnation and dispersion of the TiO_2 phase according to the procedure described in the experimental section, and then, carbon-Ti composites were prepared by carbonization of Ti-impregnated cellulose samples. The carbonization processes of raw (commercial) and acid-treated MCCs were simulated by TG and used as reference processes, pointing out the strong changes on the thermal stability of cellulose after HNO_3 or H_3PO_4 pretreatments (Figure 4.1). The thermal decomposition of the raw cellulose (MCC) occurs in a single step at around $340 \text{ }^\circ\text{C}$, in agreement with that previously described in the literature [1], indicating the absence of both hemicellulose and lignin in this sample. The theoretical total carbon content is 44 wt.% taking into account the chemical composition of cellulose $(\text{C}_6\text{H}_{10}\text{O}_5)_n$. However, the yield of carbon residue after pyrolysis is significantly lower (around 17 wt.%)

because the depolymerization of the cellulose molecular structure takes place during heating and evolves carbon oxides (CO and CO₂) from intermediate aldehydes and carboxylic acids, consequently decreasing the yield of carbon residues [2].

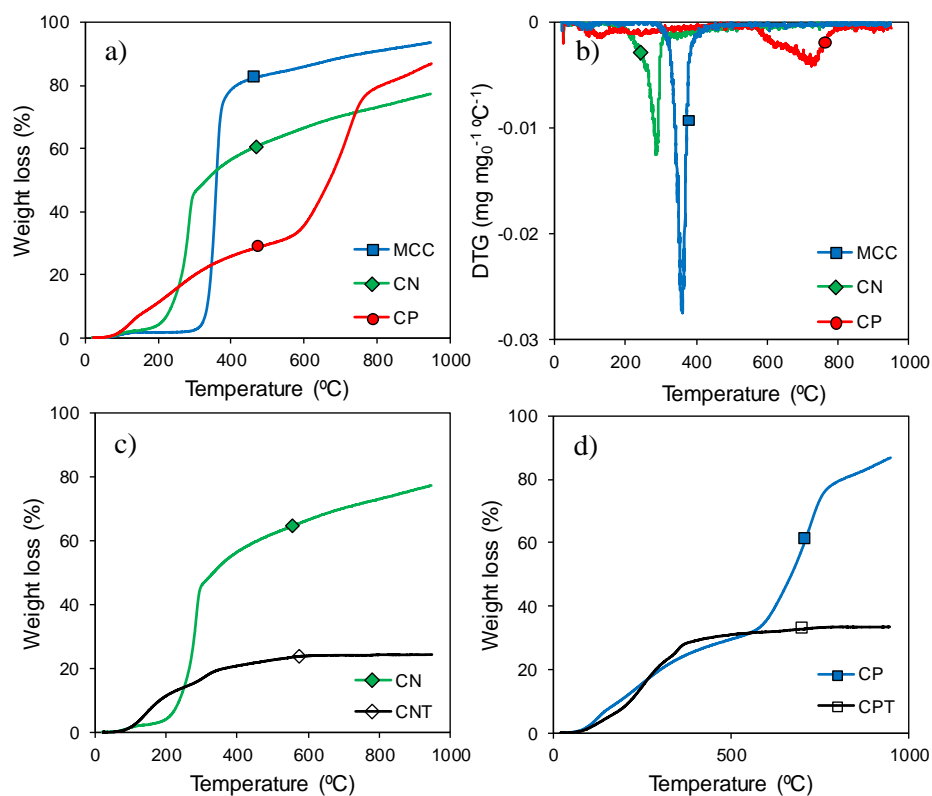


Figure 4.1. a) TG and b) DTG profiles showing the influence of acid treatments on the cellulose carbonization process; c) TG profiles of nitric-treated cellulose before and after impregnation; and d) TG profiles of phosphoric acid-treated cellulose before and after impregnation (experiments carried out in N₂ flow at 5 °C min⁻¹).

The thermal decomposition of acid-treated cellulose presents significant differences regarding the original MCC. After HNO₃ treatment, the CN sample decomposes mainly in one step, as the raw MCC, but the decomposition occurs at lower temperatures (Figure 4.1a). This smaller thermal stability is associated with the incorporation of new oxygenated groups, in particular carboxylic acid groups. Dehydration processes of adjacent carboxylic acid groups and/or the decomposition of these groups into CO₂ occurs at temperatures below 300 °C [3]. Nevertheless, after this main decomposition step, a slow but continuous weight loss also occurs with increasing temperature, indicating the decomposition of additional oxygenated surface groups that typically evolve as CO (phenol, carbonyl or quinone) [3].

After H_3PO_4 treatment, carbonization takes place clearly in two steps at around 200 and 700 °C. The first decomposition step may be also due to dehydration and decomposition of carboxylic acids and anhydrides derivative groups, but the decomposition temperature range (from around 150 to 500 °C) is wider in MCC or CN samples than in CP, indicating a more heterogeneous distribution of surface groups. The second carbonization step is associated with the reduction of phosphate groups by the organic cellulose, which increases the cellulose gasification in this temperature range. Chemical activation of H_3PO_4 -impregnated lignocellulosic materials [4, 5] is a classical method for the preparation of activated carbons, the activation temperature depending on the nature of the raw biopolymer [6]. In the case of the CP sample, the weight loss associated with the activation process occurs at 700 °C, while, as an example, coconut activation has been reported between 400-450 °C [5]. Evidently, the yield of solid residue strongly increases after impregnation of these functionalized cellulose samples with the Ti-precursor (Figure 4.1c and 1d), obtaining the corresponding carbon-Ti composites (CNT and CPT). It is noteworthy the significant change in the TG-profiles of composites regarding their supports (CN and CP), denoting the formation of new bonds between the cellulose supports and Ti-precursor. At low temperature (below 200 °C), the weight loss in the CNT sample even increases regarding CN by decomposition of organic precursors, but after that the slope of the curve strongly decreases, there is not a significant weight loss from around 600 °C, showing the thermal stabilization of the cellulose oxygenated surface groups by interaction with the Ti-phases. The cellulose – Ti interactions are also observed for the CPT sample. In this case, the first decomposition step remains more or less unchanged, but the second decomposition step is not observed, indicating therefore that in this case, the phosphate groups are not reduced by the organic cellulose phase during the thermal treatments and thus, being also clearly stabilized by reactions with the Ti-phase.

The inorganic content in the composites was also determined by TG, in this case by burning a small portion of each sample in air flow. Although both samples were prepared using a constant cellulose: TiO_2 ratio of 1:6 by weight, the residue percentage was 63 and 74 wt.% for CNT and CPT, respectively. Thus, the highest residue content determined for CPT is favoured by the presence of phosphorus functionalities. The surface chemical nature and composition of Ti-impregnated cellulose and their carbon derivatives were analyzed by XPS (Table 4.1). The highest oxygen content detected on the surface of the CPT sample regarding

the CNT sample, together the high phosphorus content, suggest the presence of phosphate groups. However, the Ti-content of CPT is smaller than in CNT in spite the highest solid residue detected by TG, indicating therefore a different Ti-distribution in surface than in the sample bulk. During carbonization, CPT composites undergo stronger changes than CNT samples, increasing the carbon content and decreasing the oxygen and Ti contents.

Table 4.1. Surface composition determined by XPS of the Ti-impregnated cellulose and their carbon derivatives.

Sample	Atomic content (wt.%)					
	C	O	N	P	Ti	
CPT	8.5	47.3	-	26.8	17.4	
CPT1	22.0	42.7	-	21.9	13.4	
CPT2	27.3	36.4	-	22.8	13.5	
CNT	18.7	36.2	1.2	-	43.9	
CNT2	16.4	35.4	-	-	48.2	

The changes in the profiles of the different XPS spectral regions also show the interactions of surface groups on the organic cellulose with the TiO₂ phases (Figures 4.2 and 4.3), as well as their transformations during carbonization. The profiles of C1s and O1s for raw cellulose (MCC) and the corresponding nitric-treated cellulose samples (i.e., CN, CNT, CNT2) are collected in Figure 4.2. The deconvolution of the C1s spectral region of raw cellulose shows a main contribution at 284.6 eV associated to C-C bonds and other small component at a higher BE (286.0 eV) associated to the presence of C-O-C or C-OH oxygenated surface groups [7]. After nitric treatments, an increase of the peak at lower B.E. (282.7 eV) is observed and associated with the presence of aromatic part in the CN material [8]. On the other hand, the interaction between carbon-Ti phases is clearly pointed out by the strong peak appearing at 286 eV after impregnation (i.e., CNT) and due to C=O or carboxyl groups [4, 9]. This peak was also previously associated to the presence of carbon in the lattice of TiO₂ [7, 10], but in the case of CNT should be assigned to C=O bonds, since this peak is not observed after carbonization at 800 °C (i.e., CNT2), taking into account the

weak thermal stability of these groups, as previously showed by TG.

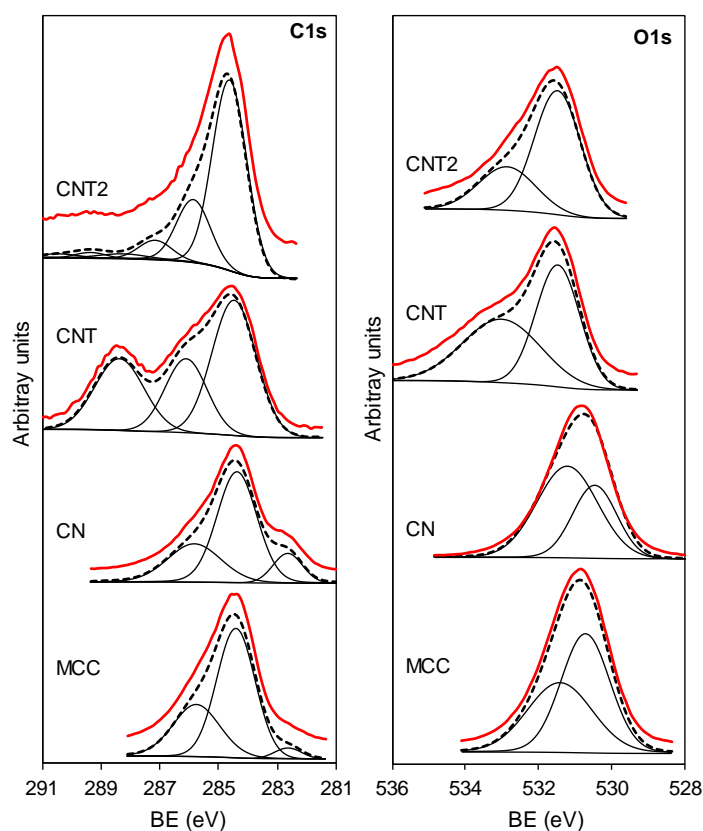


Figure 4.2. High resolution XPS spectra of C1s and O1s regions for raw cellulose, nitric-treated cellulose derivatives and the corresponding Ti composites.

In general, two components located at 530.8 and 531.6 eV corresponding to C-O-C or C-OH bonds, respectively, were used to fit the O1s region. After impregnation (i.e., CNT), the profile of the spectra is shifted to higher B.E., showing a big shoulder associated to the Ti-phase, although it also is fitted using two components located at 531.5 and 533.1 eV, the first one would correspond to C-O bonds, as previously commented, but also to the Ti-O bonds, while the large shoulder at 533.1 eV is due to C=O and Ti-OH bonds or chemisorbed oxygen [11]. These contributions decrease significantly after carbonization (i.e., CNT2). The low N-content of the raw cellulose leads to a very poor XPS signal (not shown) of the N1s region in both MCC and CN samples. This low N-content is completely removed after carbonization. The N1s region was also fitted using two components at 398.2 and 399.8 eV that can be assigned to N pyridinic and pyrrolic, respectively [12].

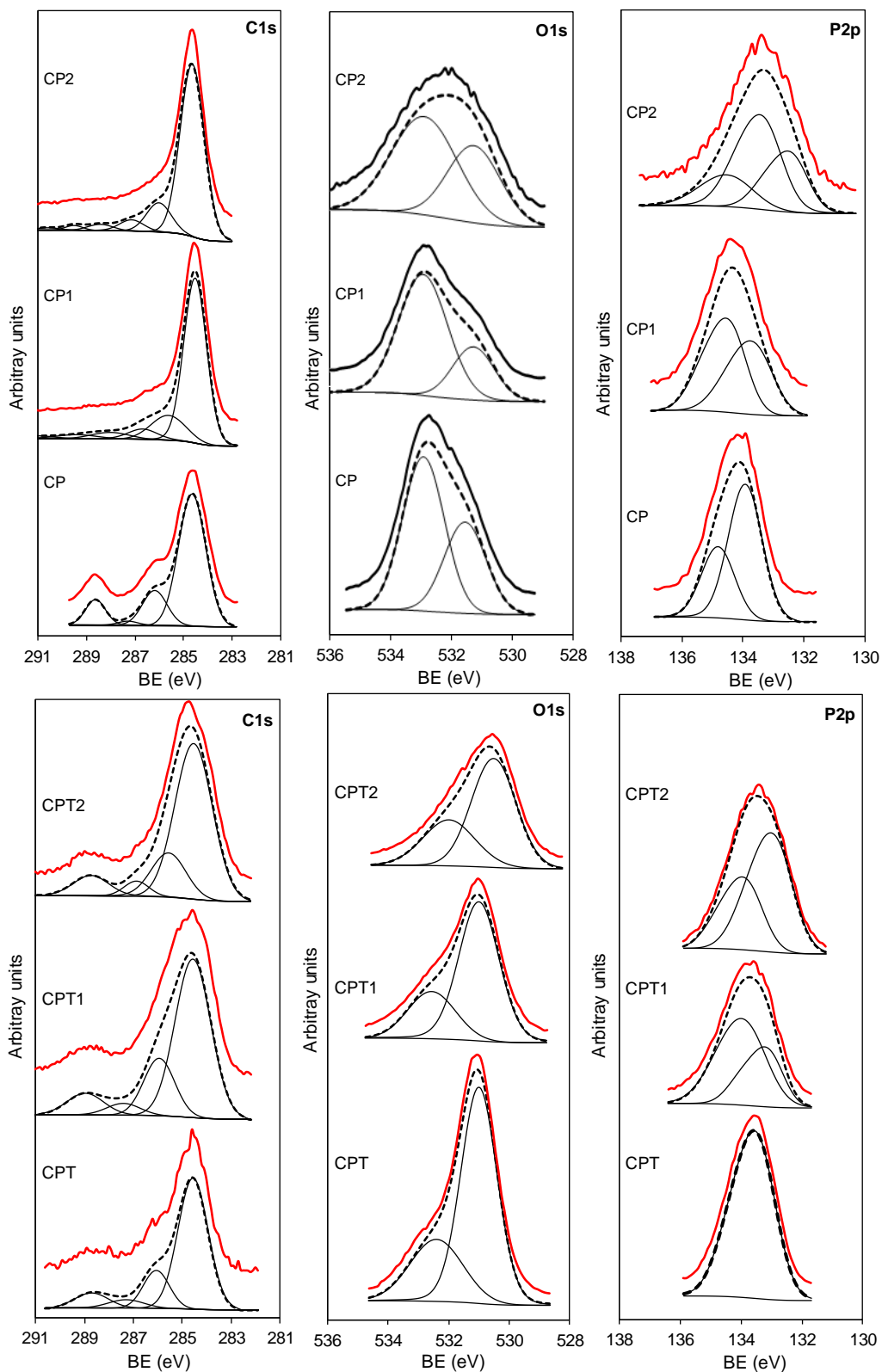


Figure 4.3. High resolution XPS spectra of C1s, O1s and P2p regions for phosphoric-treated cellulose derivatives and their corresponding Ti composites.

The C1s, O1s and P2p spectral regions of the phosphoric-treated cellulose derivatives (i.e., CP, CP1 and CP2) and the corresponding Ti-composites (i.e., CPT, CPT1 and CPT2) were also analyzed (Figure 4.3). The treatment with phosphoric acid generated a strong concentration of C=O bonds (contribution at 288.6 eV) in the CP sample, which is not observed in the CN sample. In fact, the contribution of these oxygenated groups in the O1s region (peak at 533 eV) is clearly predominant (73% of the total area), although it evidently tends to decrease after carbonization by the low thermal stability of these groups. On the other hand, when CP results are compared with those for the CPT sample (i.e. after Ti-impregnation), the peak at 288.6 eV is less significant, but it is maintained even after carbonization showing the interaction between the Ti-phase and these surface groups. Analogously to CNT, the O1s spectral region of CPT is also shifted to higher BE regarding to the CP support due to the contribution of Ti-O and Ti-OH bonds, as previously described, and to the phosphorus surface groups containing P=O and C-O-P bonds [4, 13], which are incorporated to the cellulose fibres after phosphoric acid treatments. The analysis of the P2p spectral region also allows to point out the interaction of Ti-phases with the phosphorus groups. This region is fitted in two components placed at 133.9 and 134.7 eV for the CP sample, while after Ti-impregnation, an only peak at 133.4 eV is used for CPT. Peaks at ca. 134 eV and 135 eV were assigned [14] to phosphorus linked to carbon (C-PO₃) and to pentavalent tetracoordinated phosphorus in phosphates or polyphosphates as (C-O-PO₃), respectively. After carbonization, the peak at 135 eV is favoured at low carbonization temperature (CPT1), but it decreases when carbonized at 800 °C (CPT2). The gradual decrease of the BE of the P2p band was previously justified on basis of a progressive dehydration and condensation of phosphates into polyphosphates and the progressive interactions of phosphorus with the aromatic carbon system [15]. After carbonization at 800 °C, a new peak is formed at ca. 132.5 eV in the CP2 support, but not in the case of the CPT2 composite. This peak was assigned [14, 16] to reduced phosphorus linked to carbon (C-P), which it is avoided by the presence of Ti in the case of CPT2. Regarding the Ti2p region (Figure 4.4), only Ti⁺⁴ is detected on the impregnated samples and on the carbonized composites obtained at low temperature, which is corroborated by the peak at 459.4 eV. However, the spectra of both CNT2 and CPT2 carbonized at 800 °C is wider and shifted to lower BE values, showing the presence of a mixture of Ti⁺⁴ and Ti⁺³ and denoting the influence of the carbonization temperature on the nature of the active phase. In spite of the

certain reduction observed, the difference in BE between Ti $2p_{3/2}$ and Ti $2p_{1/2}$ components is always maintained at 5.7 eV, in agreement with TiO₂ results previously reported [7].

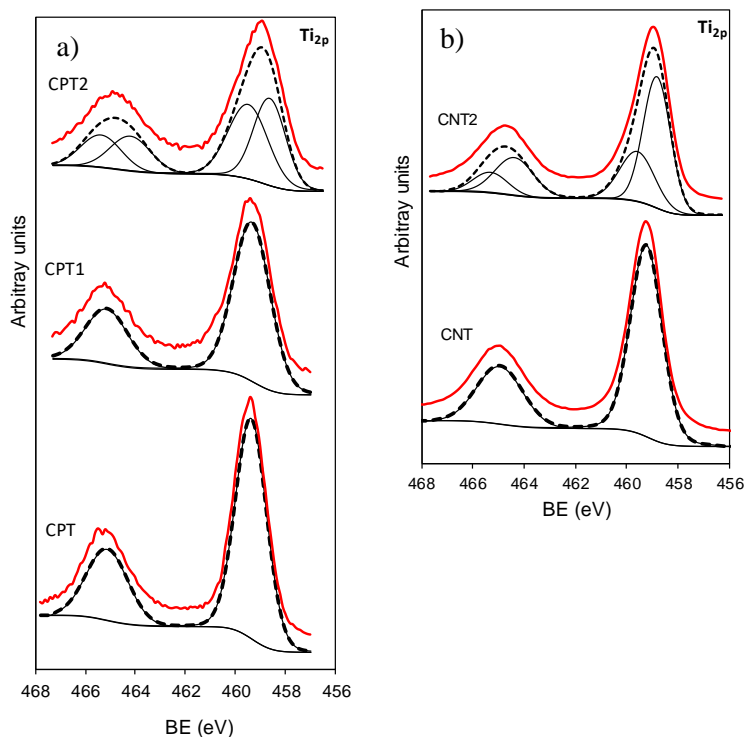


Figure 4.4. High resolution XPS spectra of Ti_{2p} region for the Ti-impregnated cellulose and the corresponding carbonized derivatives.

The analysis of the XRD-patterns also pointed out the different transformations of the samples as a function of the temperature carbonization in the composites (Figure 4.5), and consequently the different metal-support interactions. Thus, the absence of XRD-peaks is observed for CPT carbonized at 500 °C (CPT1), while XRD-patterns denoting a total transformation to the rutile phase can be detected in the case of CNT1. In previous works [17, 18] we have pointed out how the carbon phase prevents both the sintering and phase transformation of the inorganic oxides in carbon/oxide composites, including TiO₂, SiO₂ or Al₂O₃/C. In this case, the phosphate groups on the cellulose support should avoid the crystal growth during carbonization at low temperatures. However, the formation of rutile at 500 °C observed for CNT1 was not expected taking into account the transformation of the anatase phase to rutile normally occurs at 750 °C, although it can be induced at lower temperatures in some cases, as by doping with metals like V⁺⁵ [19]. By increasing the carbonization temperature up to 800 °C, an increase of the rutile crystallinity is observed in CNT2 compared to CNT1, as denoted by the narrower and more intense diffraction peaks.

However, because rutile is the phase stable at high temperature no additional transformations can be expected. At this carbonization temperature, the CPT2 XRD-pattern showed the formation of a crystalline phase that do not correspond to any TiO_2 phase, but it was indexed as cubic TiP_2O_7 with the space group $\text{Pa}\bar{3}$ and $3\times 3\times 3$ superstructure (JCPDS no. 38-1468) [20, 21]. The formation of TiP_2O_7 nanocrystals is only obtained at higher temperatures than 1000°C [22] and thereby, it should be favoured by the phosphorus surface groups on the functionalized cellulose. These results are also in agreement with the TG and XPS results, which suggested the stabilization of the phosphate groups by interaction (reaction) with the Ti-species with increasing temperature. In summary, the functionalities incorporated during cellulose solubilization determine the Ti-phase formed in the corresponding composites. The oxygenated surface groups, namely carboxylic acid species, generated on the cellulose chains by HNO_3 treatments induce the formation of rutile at low temperature, while the phosphorus groups generated by H_3PO_4 treatments avoid the formation of Ti-crystalline phases when treated at low temperatures and the formation of TiP_2O_7 nanocrystals with increasing this parameter, but reaction occurs at lower temperatures than those typically reported.

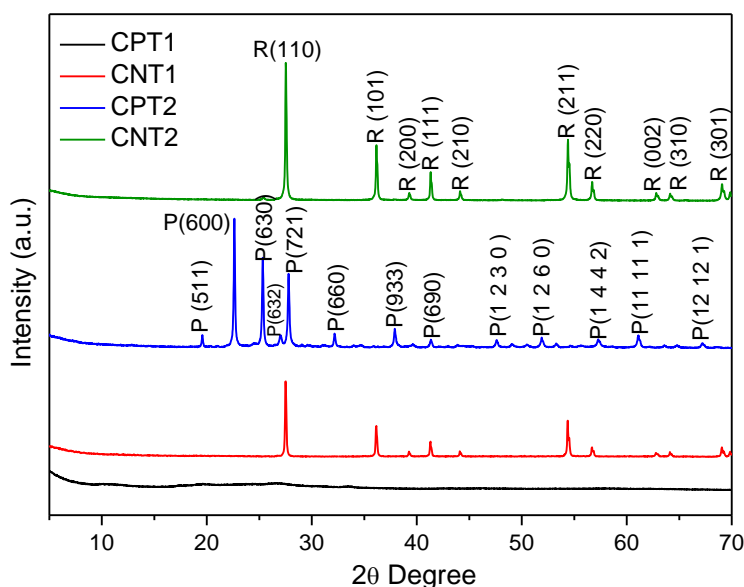


Figure 4.5. XRD patterns of the carbon-Ti composites. (R = rutile, P = TiP_2O_7).

The chemical and crystalline transformations previously indicated are simultaneously accompanied by a marked change in the morphology of the samples, mainly for CPT carbonized derivatives. Thus, the CPT sample carbonized at low temperature (500

°C) presents an opened structure composed by grouping sheets leading to a solid with flaky aspect (Figure 4.6a). When the composite is carbonized at 800 °C (CPT2, Figure 4.6b), the structure becomes more compact showing a granular aspect that corresponds to the formation of the TiP_2O_7 crystalline phase, according to XRD results. The morphology of CNT1 is formed by round shaped particles overlapped forming also an opened structure (Figure 4.6c). These particles should correspond to rutile crystals identified by XRD (Figure 4.5). The composite carbonized at higher temperature (CNT2) presents also a denser surface than CNT1 by sintering, and due to the referred crystal growth the crystallites show now sharp edges on clearly cubic structures (Figure 4.6d).

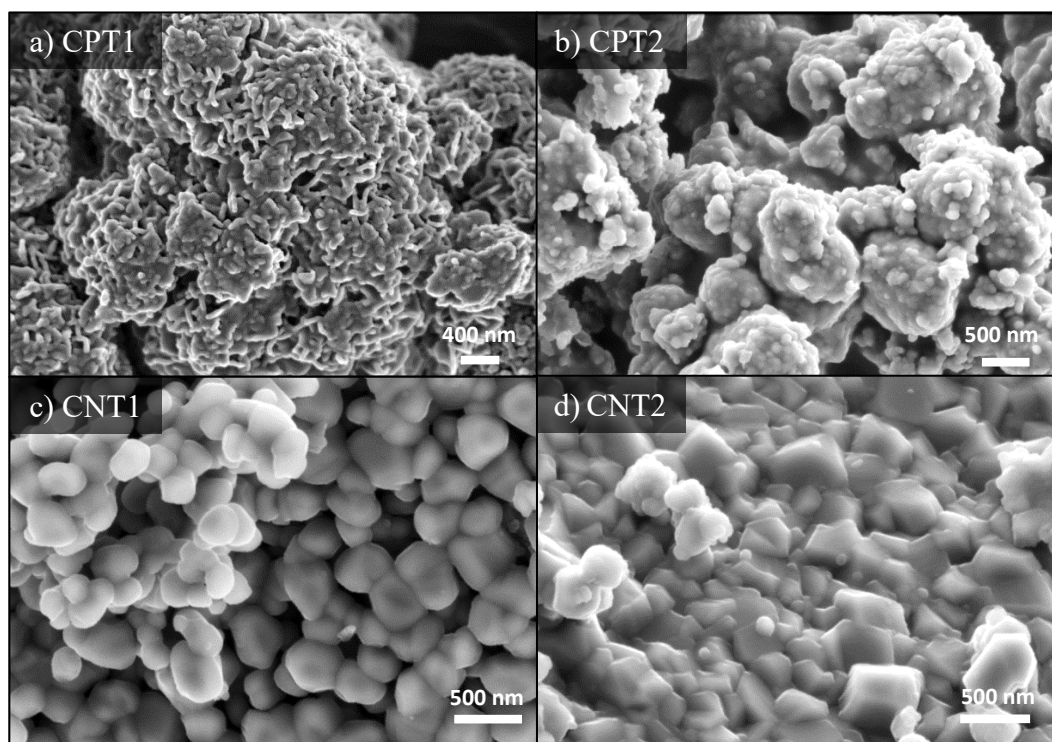


Figure 4.6. SEM images of the carbon-Ti composites.

The EDX spectrum corroborates the presence of C-O-P-Ti in the CPT composite (Figure 4.7a). HRTEM micrographs of CPT1 (Figure 4.7b) shows the formation of ultrathin carbon layers, in which a homogeneous distribution of Ti is deposited throughout the composite, as confirmed by mapping (Figure 4.7c). After carbonization at 800 °C, the formation of needle shaped structures, more or less aggregated between them are also observed together large carbon flakes previously described (Figures 4.7d and e). These flat and transparent carbon structures were also previously observed after sulfuric acid

hydrolysis and carbonization of *eucalyptus* kraft wood pulp [23]. Filaments, aggregates of films can be developed depending on the thermal treatments of cellulose nanocrystals, although the mechanism of formation of these nanostructures is still unclear, seem to be related with the H-bonding interactions and the transformations during carbonization.

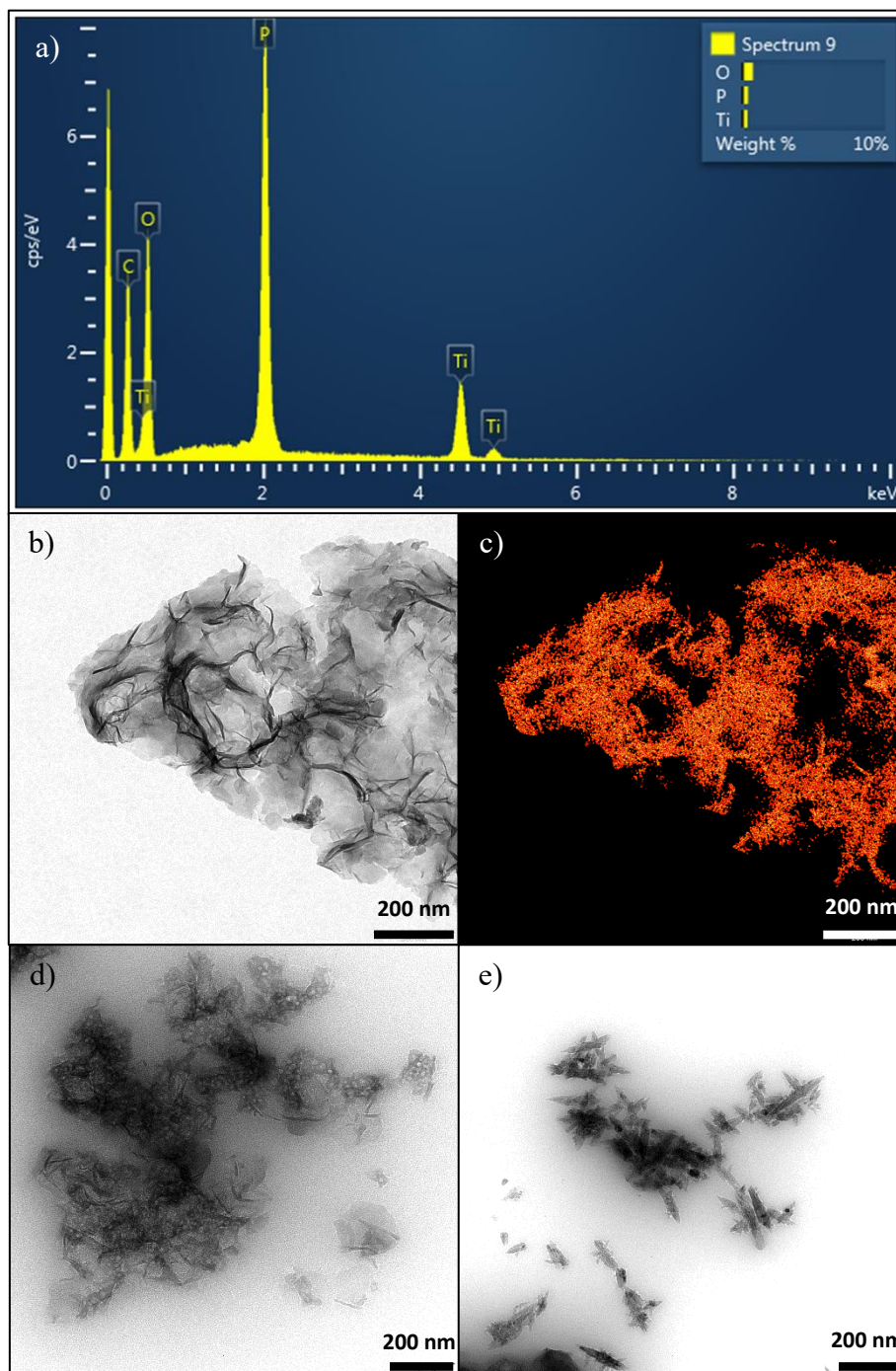


Figure 4.7. Characterization of CPT composites: (a) EDX spectrum, (b) HRTEM micrograph and (c) Ti-mapping on CPT1. (d, e) HRTEM micrographs of CPT2.

The different morphologies observed for the carbon-Ti composites influences on their porosity, which was analyzed by N₂ adsorption-desorption isotherms (Figure 4.8). The shape of the isotherms already points out the different porosity of the samples. When compared the isotherms of pure carbon samples (Figure 4.8a) and their corresponding composites (Figure 4.8b), a different porous texture due to the interactions and transformations between phases is clearly pointed out. Thus, the porosity of the CP sample carbonized at 500 °C (i.e., CP1) is quite poor, while CP2, carbonized at 800 °C, presents a high surface area associated to the microporosity development generated during the activation processes by the reduction of the phosphate groups at ~ 700 °C, as previously observed by TG. In fact, CP2 is mainly microporous as denoted by its type-I adsorption isotherm (Figure 4.8a) and pore size distribution (Table 4.2). On contrary, the CN1 sample, pretreated in nitric acid and carbonized at low temperature, showed a higher porosity than CP1, due to the evolution of low stable oxygenated surface groups. However, the porosity and surface area of CN samples decrease after increasing carbonization temperature with a progressive micropore widening (Table 4.1). CN1 and CN2 samples showed type-III adsorption isotherms.

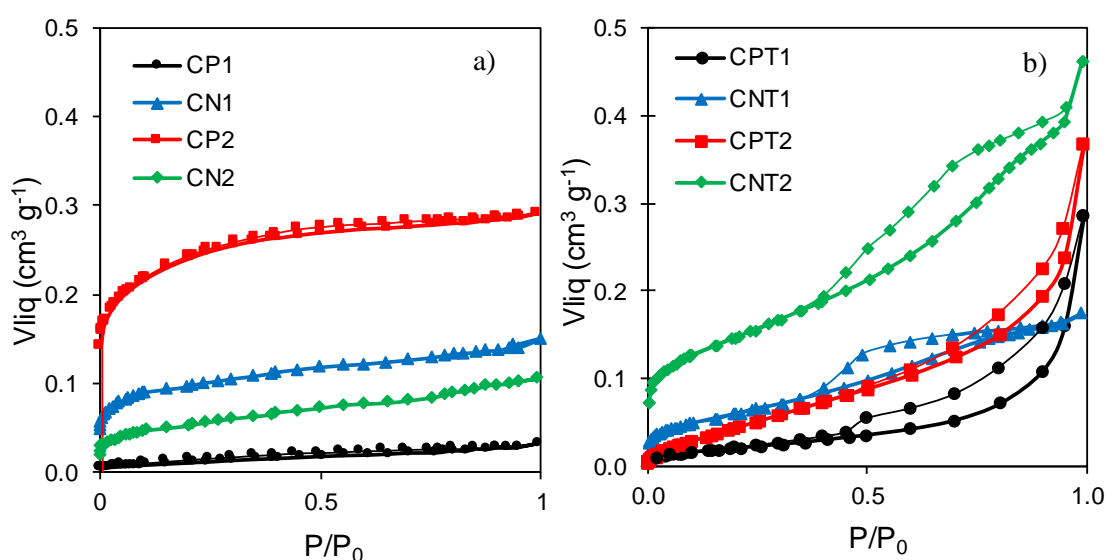


Figure 4.8. N₂ adsorption-desorption isotherms of a) the pure carbon materials and b) the carbon-Ti composites.

After Ti-precursor impregnation, both CNT1 and CNT2 showed type-IV adsorption isotherms characteristics of micro-mesoporous materials, while basically type-III isotherms

were obtained for both CPT1 and CPT2. These samples showed a similar microporosity and surface area, on the contrary that the previous non-impregnated samples (e.g., CP1 and CP2), which corroborates that the interaction of the carbon with the Ti-phase avoids the reduction of the phosphate groups. Nevertheless, a certain delay in the desorption branch of both CPT1 and CPT2 samples also denotes a hysteresis cycle associated to N₂-condensation. In all composites, the shape of the isotherm is maintained with increasing the carbonization temperature, but the total porosity and BET surface areas increases (Table 4.2). This increase is due to a larger weight loss and on the other hand, to the progressive sintering and crystal growth of the Ti-phase (Figures 4.6 and 4.7) leading to narrow pores where N₂ condensate during the porosity filling. CNT derivative samples present mainly a developed micropore structure that strongly favours high surface area values compared to those for the CPT ones. In addition, CNT2 presented the largest development of porosity, sintering favouring the formation of mesopores from macropores or interparticle voids present in the sample obtained at lower carbonization temperature. Porosity, namely mesoporosity, is favoured in the carbon-Ti composites regarding to their pure carbon materials, an evolution directly related to the transformations of the Ti-phase being established.

Table 4.2. Textural characteristics of the carbon-Ti composites.

Sample	S _{BET} (m ² g ⁻¹)	S _{DR} (m ² g ⁻¹)	L ₀ (nm)	W ₀ (cm ³ g ⁻¹)	V _{meso} (cm ³ g ⁻¹)
CP1	17	20	2.2	0.007	0.024
CP2	552	624	1.5	0.222	0.069
CN1	226	253	1.5	0.090	0.060
CN2	115	122	1.7	0.043	0.062
CPT1	28	35	1.4	0.013	0.273
CPT2	30	48	1.8	0.017	0.351
CNT1	124	141	1.6	0.050	0.125
CNT2	319	360	1.5	0.128	0.335

The optical properties of the carbon-Ti composites were analyzed using UV/Vis diffuse reflectance (DRUV) spectroscopy. All reflectance spectra (Figure 4.9a) recorded were converted to equivalent absorption Kubelka–Munk (K-M) units (Figure 4.9b) and the band gap (E_g) determined from the plots $(F(R) \times hv)^n$ vs. E by extrapolating the slope to $a = 0$ according to the procedure previously reported [24–26]. The band gap for all composites synthesized from cellulose decreased regarding the value determined for P25, which was used as reference material (Figure 4.9b). CNT samples with rutile as active phase, presented E_g values at ~ 2.4 eV regardless the carbonization temperature, this value of band gap being significantly lower than 3.0 eV corresponding to the pure rutile phase. Analogously, the strong influence of the carbonization temperature on the crystalline and morphological properties previously discussed for CPT composites do not produce however, a significant change in the profile of their corresponding spectra, and consequently also similar band gap values, at ~ 3.0 eV are obtained (Figure 4.9b) for CPT1 and CPT2. However, these values are also significantly smaller than the band gap of 3.5 eV reported in the bibliography for the TiP_2O_7 phase [26].

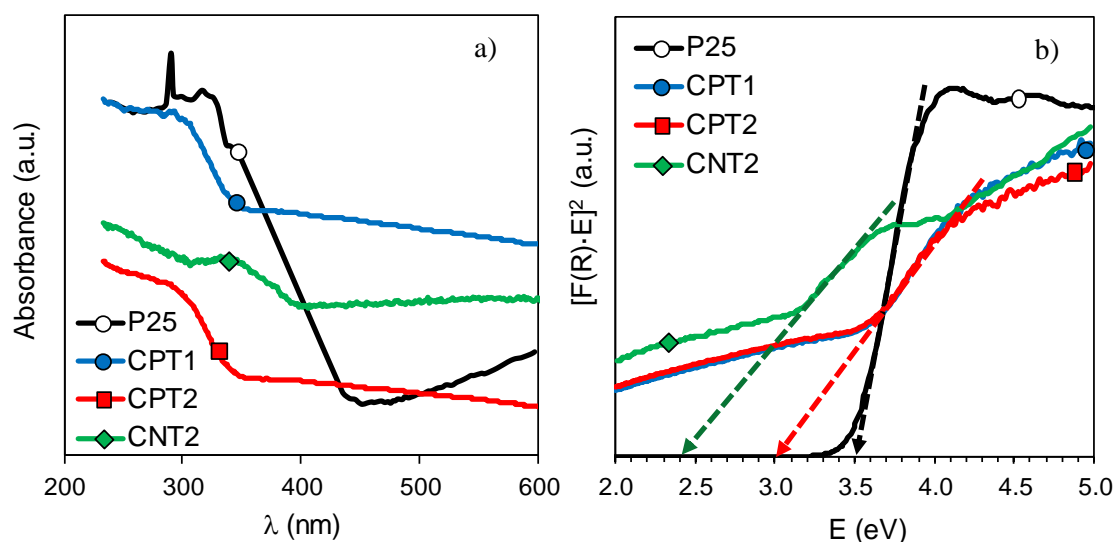


Figure 4.9. a) DRUV spectra of P25 and different carbon-Ti composites. b) Plot of transformed Kubelka–Munk as a function of the energy of light (inset: determination of the band gap).

Thus, a clear influence of the functionalized cellulose on the semiconductor properties of both series of composites is evidenced. On the other hand, the carbonization temperature did not influence markedly on the band gap values of the carbon-Ti composites,

despite of presenting different physicochemical properties. Different effects can contribute to the similar band gap values observed. For instance, with increasing the carbonization temperature the formation of Ti^{+3} species were pointed out by XPS, which can contribute to the band gap narrowing. However, in this way also progressively increases the crystal size of the composites, which evidently favours the recombination electron-hole. Otherwise, the low band gaps determined for all composites should significantly improve their photocatalytic efficiency compared to the pure TiO_2 materials, as P25.

4.3.2. Removal of Orange-G (OG) azo-dye

The adsorptive and photocatalytic performance of the carbon-Ti composites was analyzed for the removal of OG, a textile dye typically present in industrial wastewater and used as target molecule, following the procedure described in our previous works with other semiconductors [24, 27]. Firstly, all samples were saturated during 4h using a concentrated OG solution in dark experiments, which allows to analyze the interactions of pollutants with the sample surface, but also avoids the contribution of the adsorption process on the OG removal during the subsequent photocatalytic degradation experiment. The initial adsorption kinetic curves for pure carbon materials and the corresponding composites are shown in Figures 4.10a and 10b, respectively. When analyzed the OG-adsorptive performance of the pure carbon materials, a direct relationship between the OG removal and the micropore volume (W_0 , Table 4.2) of the samples can be established. The high micropore development in CP2 allows the complete removal of OG in solution in only 25 min, while CP1 with the lowest W_0 leads to the worst adsorptive behaviour (Figure 4.10a). In the case of CN materials, the OG-adsorption capacity decreases as carbonization temperature increases due to a micropore destruction probably by widening (Table 4.2). For the case of composites, CPT2 also showed a better performance than CPT1, although the microporosity of both samples is quite similar (Figure 4.10b). The increased microporosity with the carbonization temperature explains the better OG-adsorptive performance of CNT2 compared to CNT1 (Figure 4.10b). In these composites, the mesoporosity also increased as the carbonization temperature, which can favour the accessibility and adsorptive performance of the samples. The fast adsorption processes of the CPT2 composite could be favoured by chemical interactions of the carbon surface with the dye in solution. The beneficial effect on the dye adsorption of phosphate doping in Ti-structures have been

previously reported [28, 29] due to the modification of the electrostatic interactions. Nevertheless, the best final performance of CNT samples confirms the importance of a developed porosity in the interactions with the pollutant.

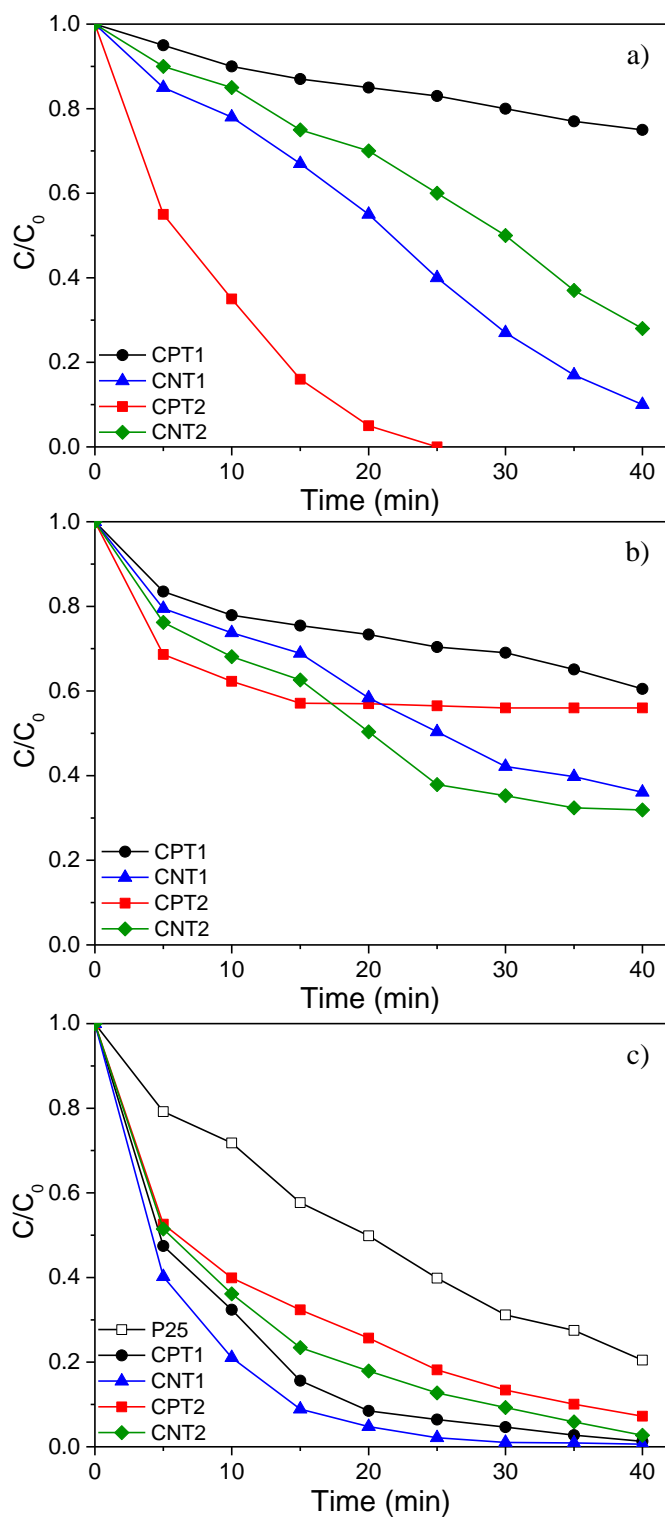


Figure 4.10. Removal of Orange-G from water solution by adsorption (a, b) and photocatalysis (c) using pure carbon materials (a) and carbon-Ti composites (b, c).

When analyzed the photocatalytic performance of the composites (Figure 4.10c), the best efficiency is observed for the CNT1 sample. In the CNT composite series, the catalytic activity decreases with increasing carbonization temperature despite the higher porosity and similar band gap values of CNT2. A similar influence of the carbonization temperature on the catalytic activity can be described for CPT1 and CPT2 composites. All carbon-Ti composites present however a better performance than the reference TiO₂ photocatalyst (P25), reaching the total OG removal for 40-60 min. The activity order follows the sequence CNT>CPT>P25 in agreement to the evolution of the band gap values. This fact should be associated with the increasing crystallinity of the rutile or TiP₂O₇ phases and confirms the importance of the particle size in the interaction with the support and the electron-hole recombination processes. The reaction pathway for the photodegradation of the azo-dye acid Orange 7 in TiO₂ suspensions was studied by Styliidi *et al.* [30], reporting that the mineralization to CO₂ occurs with the formation of aromatic and aliphatic acids as intermediates. In previous works [24, 27], we have pointed out that the photocatalytic experiments carried out using C-Ti or C-Zr composites produces the mineralization of the dye to CO₂. In the current work, a similar behaviour was observed; no intermediates were expected in solution after reaction, because the TOC analysis of the samples decreased accordingly with the OG removal. The best photocatalytic performance of the CNT1 sample should be related with an adequate porous texture, the narrow band gap associated to the rutile phase in combination with the carbon support and an intermediate particle size. In the case of the CPT1 composite, the low surface area can be compensated by the favourable role of phosphate groups on the adsorption and a very small particle size (not detectable by XRD). Therefore, this study demonstrates the possibility to enhance the photocatalytic activity of TiO₂ by preparing cheap composites using biopolymers like cellulose through an easy procedure and highlighting the importance of the cellulose pretreatment conditions on the final properties and catalytic performance.

4.4. Conclusions.

Cheap and sustainable carbon–Ti composites with improved adsorptive and photocatalytic performances were obtained using cellulose as raw material. The oxygen- and phosphorus-containing surface groups generated on the cellulose chains during the acid solubilization of the microcrystalline structure determine the interactions with the Ti-

precursor during impregnation and the transformations of both cellulose and Ti-phases during thermal treatments. Thus, the chemical nature and physicochemical properties of the active phases can be fitted by adjusting the surface chemistry and carbonization temperature.

Phosphorus functionalities, in particular phosphate groups, avoid the crystal growth when composites are carbonized at low temperature (500 °C) while oxygen functionalities favour the transformation of anatase nanocrystals into rutile phase. Increasing carbonization temperature (800 °C), Ti-precursors react with the phosphate surface groups forming TiP_2O_7 nanocrystals, sintering is favoured and Ti^{+4} is partially reduced to Ti^{+3} . These interactions with the carbon phase produce a significant narrowing of the band gap regarding rutile or TiP_2O_7 pure phases. The combination of a developed porosity and surface area, a narrow band gap and small crystal size favour the dye adsorption and prevent the electron-hole recombination, consequently enhancing the dye mineralization in all carbon-Ti composites regarding the commercial P25.

4.5. References.

- [1] M.I.G. Miranda, C.I.D. Bica, S.M.B. Nachtigall, N. Rehman, S.M.L. Rosa, Kinetic thermal degradation study of maize straw and soybean hull celluloses by simultaneous DSC–TGA and MDSC techniques, *Thermochimica Acta*, 565 (2013) 65-71.
- [2] A.G. Dumanlı, A.H. Windle, Carbon fibres from cellulosic precursors: a review, *Journal of Materials Science*, 47 (2012) 4236-4250.
- [3] J.L. Figueiredo, M.F.R. Pereira, M.M.A. Freitas, J.J.M. Órfão, Modification of the surface chemistry of activated carbons, *Carbon*, 37 (1999) 1379-1389.
- [4] A. Elmouwahidi, E. Bailón-García, A.F. Pérez-Cadenas, F.J. Maldonado-Hódar, F. Carrasco-Marín, Activated carbons from KOH and H_3PO_4 -activation of olive residues and its application as supercapacitor electrodes, *Electrochimica Acta*, 229 (2017) 219-228.
- [5] M.J. Prauchner, F. Rodríguez-Reinoso, Chemical versus physical activation of coconut shell: A comparative study, *Microporous and Mesoporous Materials*, 152 (2012) 163-171.
- [6] Y. Guo, D.A. Rockstraw, Physical and chemical properties of carbons synthesized from xylan, cellulose, and Kraft lignin by H_3PO_4 activation, *Carbon*, 44 (2006) 1464-1475.
- [7] L. Luo, Y. Yang, M. Xiao, L. Bian, B. Yuan, Y. Liu, F. Jiang, X. Pan, A novel biotemplated synthesis of TiO_2 /wood charcoal composites for synergistic removal of bisphenol A by adsorption and photocatalytic degradation, *Chemical Engineering Journal*, 262 (2015) 1275-1283.
- [8] M. Smith, L. Scudiero, J. Espinal, J.-S. McEwen, M. Garcia-Perez, Improving the deconvolution and interpretation of XPS spectra from chars by ab initio calculations, *Carbon*, 110 (2016) 155-171.

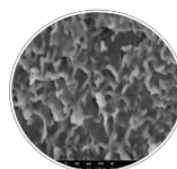
- [9] J.F. Vivo-Vilches, E. Bailón-García, A.F. Pérez-Cadenas, F. Carrasco-Marín, F.J. Maldonado-Hódar, Tailoring the surface chemistry and porosity of activated carbons: Evidence of reorganization and mobility of oxygenated surface groups, *Carbon*, 68 (2014) 520-530.
- [10] H. Li, D. Wang, H. Fan, P. Wang, T. Jiang, T. Xie, Synthesis of highly efficient C-doped TiO₂ photocatalyst and its photo-generated charge-transfer properties, *Journal of Colloid and Interface Science*, 354 (2011) 175-180.
- [11] M.A. Mohamed, W.N. Wan Salleh, J. Jaafar, M.S. Rosmi, Z.A. Mohd. Hir, M. Abd Mutalib, A.F. Ismail, M. Tanemura, Carbon as amorphous shell and interstitial dopant in mesoporous rutile TiO₂: Bio-template assisted sol-gel synthesis and photocatalytic activity, *Applied Surface Science*, 393 (2017) 46-59.
- [12] M. Pérez-Cadenas, C. Moreno-Castilla, F. Carrasco-Marín, A.F. Pérez-Cadenas, Surface Chemistry, Porous Texture, and Morphology of N-Doped Carbon Xerogels, *Langmuir*, 25 (2009) 466-470.
- [13] M.A. Mohamed, W.N. W. Salleh, J. Jaafar, Z.A. Mohd Hir, M.S. Rosmi, M. Abd. Mutalib, A.F. Ismail, M. Tanemura, Regenerated cellulose membrane as bio-template for in-situ growth of visible-light driven C-modified mesoporous titania, *Carbohydrate Polymers*, 146 (2016) 166-173.
- [14] J.M. Rosas, J. Bedia, J. Rodríguez-Mirasol, T. Cordero, HEMP-derived activated carbon fibers by chemical activation with phosphoric acid, *Fuel*, 88 (2009) 19-26.
- [15] A.M. Puziy, O.I. Poddubnaya, R.P. Socha, J. Gurgul, M. Wisniewski, XPS and NMR studies of phosphoric acid activated carbons, *Carbon*, 46 (2008) 2113-2123.
- [16] G. Hasegawa, T. Deguchi, K. Kanamori, Y. Kobayashi, H. Kageyama, T. Abe, K. Nakanishi, High-Level Doping of Nitrogen, Phosphorus, and Sulfur into Activated Carbon Monoliths and Their Electrochemical Capacitances, *Chemistry of Materials*, 27 (2015) 4703-4712.
- [17] C. Moreno-Castilla, F.J. Maldonado-Hodar, Synthesis and surface characteristics of silica- and alumina-carbon composite xerogels, *Physical Chemistry Chemical Physics*, 2 (2000) 4818-4822.
- [18] C. Moreno-Castilla, F.J. Maldonado-Hódar, F. Carrasco-Marín, E. Rodríguez-Castellón, Surface Characteristics of Titania/Carbon Composite Aerogels, *Langmuir*, 18 (2002) 2295-2299.
- [19] N. Khatun, Anita, P. Rajput, D. Bhattacharya, S.N. Jha, S. Biring, S. Sen, Anatase to rutile phase transition promoted by vanadium substitution in TiO₂: A structural, vibrational and optoelectronic study, *Ceramics International*, 43 (2017) 14128-14134.
- [20] A. Muto, K. Ida, T. Bhaskar, M.A. Uddin, S. Takashima, T. Hirai, Y. Sakata, Preparation of novel TiP₂O₇ carbon composite using ion-exchanged resin (C467) and evaluation for photocatalytic decomposition of 2-propanol, *Applied Catalysis A: General*, 260 (2004) 163-168.
- [21] Y. Sun, L. Gai, Y. Zhou, X. Zuo, J. Zhou, H. Jiang, Polyhierarchically structured TiP₂O₇/C microparticles with enhanced electrochemical performance for lithium-ion batteries, *CrystEngComm*, 16 (2014) 10681-10691.

- [22] S. Patoux, C. Masquelier, Lithium Insertion into Titanium Phosphates, Silicates, and Sulfates, *Chemistry of Materials*, 14 (2002) 5057-5068.
- [23] D.R.d.S. Souza, J.P.d. Mesquita, R.M. Lago, L.D. Caminhas, F.V. Pereira, Cellulose nanocrystals: A versatile precursor for the preparation of different carbon structures and luminescent carbon dots, *Industrial Crops and Products*, 93 (2016) 121-128.
- [24] E. Bailón-García, A. Elmouwahidi, M.A. Álvarez, F. Carrasco-Marín, A.F. Pérez-Cadenas, F.J. Maldonado-Hódar, New carbon xerogel-TiO₂ composites with high performance as visible-light photocatalysts for dye mineralization, *Applied Catalysis B: Environmental*, 201 (2017) 29-40.
- [25] R. López, R. Gómez, Band-gap energy estimation from diffuse reflectance measurements on sol-gel and commercial TiO₂: a comparative study, *Journal of Sol-Gel Science and Technology*, 61 (2012) 1-7.
- [26] X. Meng, M. Hao, J. Shi, Z. Cao, W. He, Y. Gao, J. Liu, Z. Li, Novel visible light response Ag₃PO₄/TiP₂O₇ composite photocatalyst with low Ag consumption, *Advanced Powder Technology*, 28 (2017) 1047-1053.
- [27] E. Bailón-García, A. Elmouwahidi, F. Carrasco-Marín, A.F. Pérez-Cadenas, F.J. Maldonado-Hódar, Development of Carbon-ZrO₂ composites with high performance as visible-light photocatalysts, *Applied Catalysis B: Environmental*, 217 (2017) 540-550.
- [28] M. Jose, N. Harsha, K. Suhailath, A.P. Mohamed, S. Shukla, Hydrogen phosphate anions modified hydrogen titanate nanotubes for methylene blue adsorption from aqueous solution: Validating novel method of predicting adsorption capacity, *Journal of Environmental Chemical Engineering*, 4 (2016) 1295-1307.
- [29] R.C. Bansal, J.B. Donnet, F. Stoeckli, *Active Carbon*, Marcel Dekker, New York, 1988.
- [30] M. Styliadi, D.I. Kondarides, X.E. Verykios, Pathways of solar light-induced photocatalytic degradation of azo dyes in aqueous TiO₂ suspensions, *Applied Catalysis B: Environmental*, 40 (2003) 271-286.

CHAPTER V - ON THE INTERACTIONS AND SYNERGISM BETWEEN PHASES OF CARBON- PHOSPHORUS-TITANIUM COMPOSITES SYNTHETIZED FROM CELLULOSE FOR THE REMOVAL OF THE ORANGE-G DYE



- Cellulose
- Acid treatment
- Ti-impregnation
- Carbonization
- Carbon-Ti Composites



Integrating Bioresources



Article

On the Interactions and Synergism between Phases of Carbon–Phosphorus–Titanium Composites Synthetized from Cellulose for the Removal of the Orange-G Dye

Hesham Hamad [†], Jesica Castelo-Quibén , Sergio Morales-Torres ^{*},
Francisco Carrasco-Marín , Agustín E Pérez-Cadenas and Francisco J. Maldonado-Hódar

Carbon Materials Research Group, Department of Inorganic Chemistry, Faculty of Sciences, University of Granada, Avenida de Fuentenueva, s/n. E518071 Granada, Spain; heshamaterials@hotmail.com (H.H.); jesicacastelo@ugr.es (J.C.-Q.); fmarin@ugr.es (F.C.-M.); afperez@ugr.es (A.E.P.-C.); fjaldon@ugr.es (F.J.M.-H.)

^{*} Correspondence: semoto@ugr.es

[†] Current address: Fabrication Technology Department, Advanced Technology and New Materials Research Institute (ATNMRI), City of Scientific Research and Technology Applications (SRTA-City), New Borg El-Arab City, Alexandria 21934, Egypt

Received: 11 August 2018; Accepted: 15 September 2018; Published: 18 September 2018



Abstract: Carbon–phosphorus–titanium composites (CPT) were synthesized by Ti-impregnation and carbonization of cellulose. Microcrystalline cellulose used as carbon precursor was initially dissolved by phosphoric acid (H_3PO_4) to favor the Ti-dispersion and the simultaneous functionalization of the cellulose chains with phosphorus-containing groups, namely phosphates and polyphosphates. These groups interacted with the Ti-precursor during impregnation and determined the interface transformations during carbonization as a function of the Ti-content and carbonization temperature. Amorphous composites with high surface area and mesoporosity were obtained at low Ti-content (Ti:cellulose ratio = 1) and carbonization temperature (500 °C), while in composites with Ti:cellulose ratio = 12 and 800 °C, Ti-particles reacted with the cellulose groups leading to different Ti-crystalline polyphosphates and a marked loss of the porosity. The efficiency of composites in the removal of the Orange G dye in solution by adsorption and photocatalysis was discussed based on their physicochemical properties. These materials were more active than the benchmark TiO_2 material (Degussa P25), showing a clear synergism between phases.

Keywords: microcrystalline cellulose; chemical functionalization; polyphosphates; synergism; physicochemical properties; Orange G; photocatalysis

5.1. Materials and methods.

The synthesis of these materials consists in a modification of the procedure used to prepare CPT samples and the detailed information can be found in Section 2.2.3. Briefly, MCC was suspended in distilled water (200 g L^{-1}) and then, it was completely dissolved by adding 10 mL of phosphoric acid (H_3PO_4) under stirring at 50 °C overnight. After that, an

appropriated amount of titanium tetra-isopropoxide (TTIP) in heptane was dropped to the previous cellulose solution to obtain different cellulose-Ti composites by changing the corresponding Ti:cellulose mass ratio, namely 1:1, 6:1 or 12:1. The solid suspension aged at 60 °C for 24 h, washed and dried at 120 °C in an oven. Finally, the carbon-phosphorus-Ti composites were obtained by carbonization of the corresponding cellulose-Ti composites in a tubular furnace at 500 or 800 °C under 100 cm³ min⁻¹ N₂ flow. The samples will be labelled as CPTX-Y indicating the composition (C=cellulose, P= phosphoric acid, T= TTIP impregnation), “X” refers the Ti:cellulose ratio used (i.e., 1, 6 or 12) and “Y” states the carbonization temperature (500 or 800 °C). For instance, CPT6-500 corresponds to the composite prepared in a 6:1 ratio and at 500 °C.

The characterization of the samples was carried out using physical adsorption of N₂, scanning electron microscopy (SEM), thermogravimetric analysis (TGA), X-ray diffraction (XRD) and X-ray photoelectron spectroscopy (XPS). The performance of carbon-phosphorus-titanium composites in the photodegradation of the orange-G (OG) dye in aqueous solutions was studied under UV irradiation. The experiments were performed using a glass photoreactor (8.5 ×20 cm) equipped with a low-pressure mercury vapor lamp (TNN 15/32, 15 W, Heraeus Headquarters, Hanau, Germany) emitting at 254 nm. The concentration of OG was determined by a UV–vis spectrophotometer (5625 Unicam Ltd., Cambridge, UK). Before catalytic experiments, all materials (800 mg) were saturated with the dye solution (800 mL) in dark to remove the adsorptive contribution. After saturation, the initial dye concentration (C₀) was fitted again to 10 mg L⁻¹ in all cases, and then, a UV lamp was turned on, this time being considered t = 0.

5.2. Results and discussion.

The closed structure of MCC required a previous solubilization with H₃PO₄ before Ti-impregnation. This acid treatment improved the dispersion of the Ti-active phase on the cellulose support but also, functionalized it simultaneously with different phosphorus-containing groups leading to a carbon-phosphorus-Ti composites. The morphology of the composites was analyzed by SEM (Figure 5.1). The composites prepared with low and intermediate Ti:cellulose and carbonized at 500 °C, i.e., CPTi1-500 and CPT6-500, presented opened structures formed by a network of elongated particles resembling the raw

cellulose fibers (Figures 5.1a and 5.1c). These large structures become round shaped particles with increasing the Ti:cellulose ratio up to 12 wt.% (Figure 5.1e).

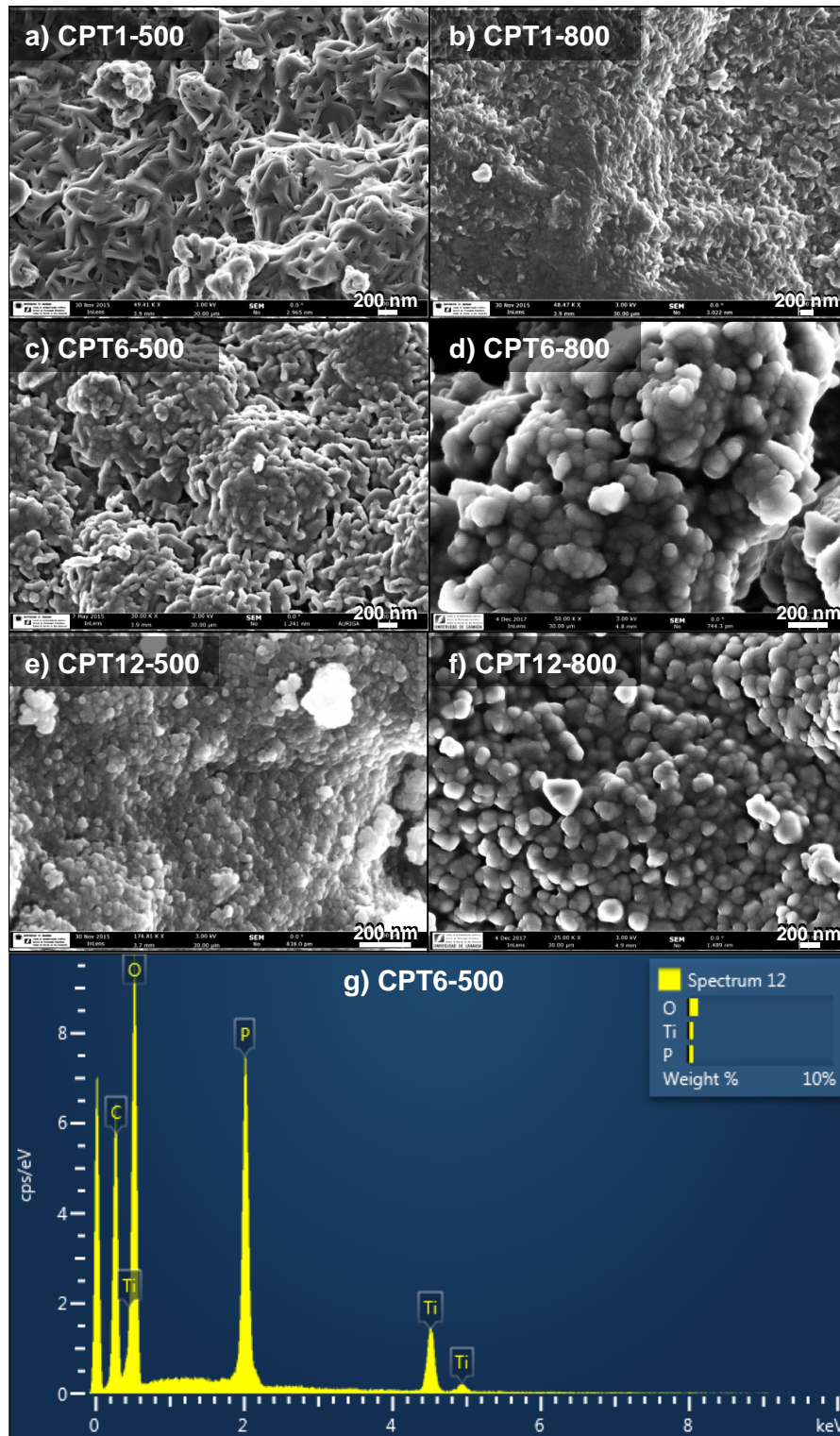


Figure 5.1. SEM micrographs for the carbon-phosphorus-Ti composites treated at 500 °C (a,c,e) and 800 °C (b,d,f), as well (g) EDX spectrum for the CPT6-500 composite.

The particle size determined for the CPT12 composite after carbonization at 500 °C was always smaller than 50 nm, while some particles larger than 300 nm were detected after carbonizing at 800 °C. After carbonization at 800 °C, round shaped particles are observed in the surface of all samples, the particle size being increased as the Ti-content (Figures 5.1b, 5.1d and 5.1e). EDX-microanalysis of all composites showed high contents of C and Ti, but also of phosphorus (Figure 5.1g for CPT6-500), which was distributed homogeneously on the composite, as confirmed by EDX.

Cellulose-phosphate structures formed during the MCC solubilization with H_3PO_4 were reported to be reversible, i.e., they are removed after washed leading to free H_3PO_4 and amorphous cellulose [1]. In our case, although amorphous cellulose was obtained, the phosphorus functionalities were stable not only after washed but also after carbonization of the composites, as corroborated below by different techniques. Thus, the stability of the phosphorus-containing groups was confirmed by XPS. As an example, the chemical composition of the CPT6 samples and the variation on the nature of the surface groups with the carbonization temperature are summarized in Table 5.1. An increase of the carbonization temperature led to the progressive reduction of the samples since the oxygen content decreases (i.e., 42.7 and 36.4 % for CPT6-500 and CPT6-800, respectively) due to the thermal decomposition of some oxygen- and/or phosphorus functionalities, which are released as CO_x . The deconvolution of the Ti_{2p} region showed for CPT6-500 an only peak placed at ≈ 459.3 eV corresponding to the presence of Ti^{+4} , while the corresponding sample carbonized at 800 °C presented an additional component at ≈ 458.6 eV due to the presence of Ti^{+3} (Table 5.1).

Table 5.1. Surface composition of CTP6 and nature of chemical groups with increasing carbonization temperature.

Sample	C	O	P	Ti	P_{2p} (%)		Ti_{2p} (%)	
					C- PO_3	C-O- PO_3	Ti^{3+}	Ti^{4+}
CPT6-500	22.0	42.7	21.9	13.4	36 (132.9)	64 (133.8)	-	100 (459.3)
CPT6-800	27.3	36.4	22.8	13.5	63 (132.8)	37 (133.8)	48 (458.6)	52 (459.5)

Analogously, a variation of the spectra of the P_{2p} region was observed for the different CPT6 samples. Thus, this region can be deconvoluted in two peaks placed at ≈ 132.8 and ≈ 133.8 eV corresponding to phosphorus linked to carbon (C- PO_3) and to pentavalent tetracoordinated phosphorus in phosphates or polyphosphates as (C-O- PO_3), respectively [2] (Table 5.1). In addition, the position of these peaks is shifted to higher binding energies (BE) with increasing the oxidation degree of the P-groups [3, 4], while the peak at low BE is favored at high carbonization temperatures.

XRD patterns for the composites treated at 500 °C did not show any peak regardless the Ti:cellulose ratio used, denoting an amorphous character for these samples. Nevertheless, sharp peaks were observed in XRD patterns when samples were treated at 800 °C, different crystalline phases being formed depending on the Ti:cellulose ratio (Figure 5.2). The TiP_2O_7 crystalline phase (JCPDS 38-1468) was present in all these composites, but also there is a small contribution of $Ti(HPO_4)_2$ (JCPDS 38-334) at low Ti-content, i.e., CPT1-800. On the other hand, when the Ti-content is increased up to 12wt.% (i.e., CPT12-800) the main crystalline phase was $(TiO)_2P_2O_7$ (JCPDS 39-0207). Thus, richer crystalline Ti-phases are favoured when increasing the Ti-content in the composite since the H_3PO_4 /cellulose ratio was always maintained. The crystal size obtained by application of the Scherrer equation was 38.9, 53.4 and 57.9 nm for CPT1-800, CPT6-800 and CPT12-800, respectively.

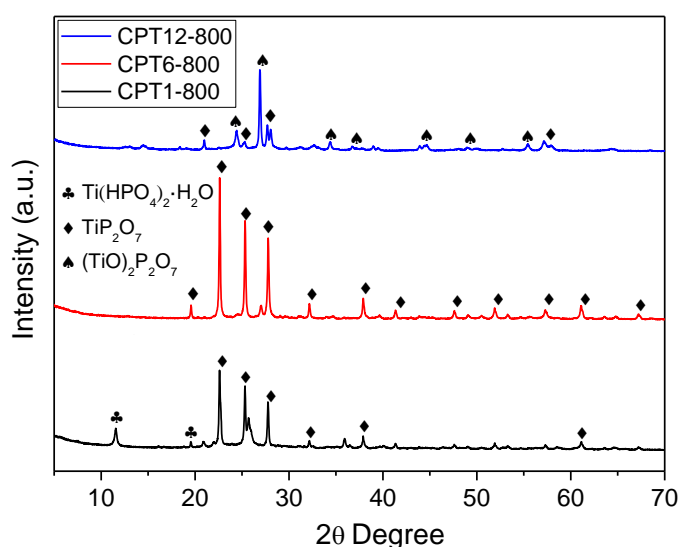


Figure 5.2. XRD patterns of the different C-P-Ti composites treated at 800 °C.

The marked influence of the carbonization temperature on the interactions of Ti-species with the phosphate surface groups was also pointed out by the thermogravimetric analysis of the samples. Thus, TG-DTG profiles obtained during the carbonization process of H₃PO₄-treated cellulose before (i.e., the CP support) and after Ti-impregnation (i.e., the CPT6 composite) are compared in Figures 5.3a and 5.3b, respectively. The support carbonization occurs in three steps denoted by the corresponding minimum in the DTG profile (Figure 5.3a). The first weight loss occurs at ≈ 120 °C and can be associated to dehydration and drying processes; a second peak at ≈ 240 °C corresponds to the release of CO_x formed by the thermal decomposition of oxygenated surface groups, namely carboxylic acids that decompose at this temperature range [5]; and the third peak can be due to the reduction of the phosphate surface groups by the organic matrix, causing the gasification of the support, as typically described in the chemical activation process of lignocellulosic materials [6]. In the carbonization of the CPT6 composite (Figure 5.3b), the Ti-support interactions leads to a certain shifting of the first peaks to slightly higher temperatures compared to the support. This fact should be related with the formation of links between the oxygenated surface groups of cellulose and the Ti-species [7]. However, Ti-species mainly interact with the phosphorus-containing groups, in such a manner that the reduction of these groups by the cellulose matrix at ≈ 750 °C does not occur during the thermal treatment (Figure 5.3b), this reduction being replaced by the reaction between these groups with the Ti species leading to crystalline Ti-phosphate or polyphosphate compounds, as previously observed by XRD. In fact, the weight loss above 500 °C is clearly negligible.

The morphological and crystalline transformations of the composites previously discussed had a clear effect on their textural properties, which were determined by analyzing the corresponding N₂-adsorption isotherms (Table 5.2 and Figure 5.4). In general, the total pore volume (V_{pore}) and the BET surface area (S_{BET}) of the composites decreased as the Ti-content and the carbonization temperature increased, due to the higher porosity of the carbon phase compared to inorganic Ti-phases and the sintering favoured under these conditions. The CPT1-500 composite presented the highest surface area (357 m² g⁻¹) due to its high micropore volume (0.144 cm³ g⁻¹) associated to a high adsorbed volume of N₂ at low relative pressure (Figure 5.4). In general, the isotherms of the composites belong to type-IV or type-II, showing from $P/P_0 > 0.4$ a clear hysteresis cycle

due to the presence of mesopores. A similar behaviour is also observed for CPT6 and CPTi12 samples with a loss of microporosity but also an enhanced mesoporosity (i.e., higher adsorbed volume of N₂ at high relative pressure), compared to composites prepared with lower Ti-content.

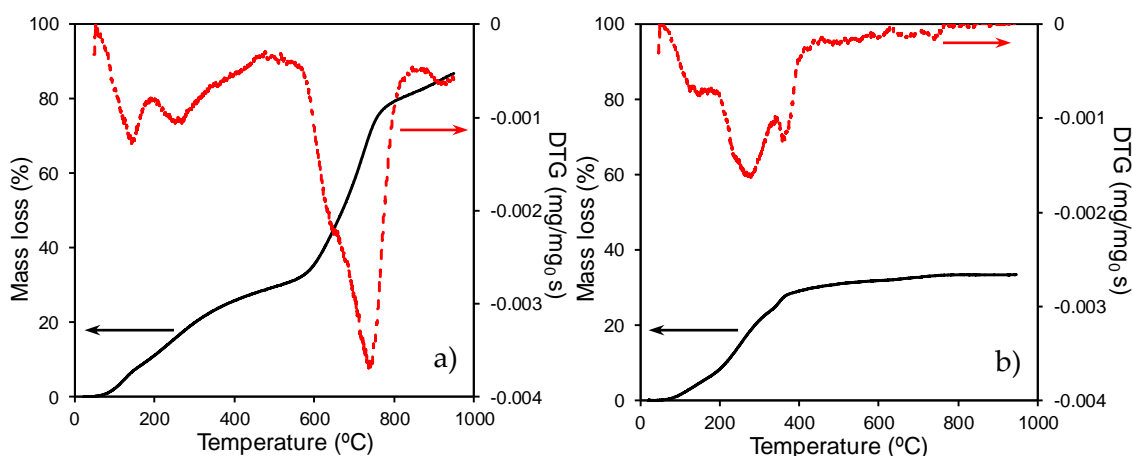


Figure 5.3. TG and DTG profiles obtained during the carbonization in N₂ flow: (a) H₃PO₄-treated cellulose support and (b) CPT6 composite.

Table 5.2. Textural properties of selected carbon-phosphorus-Ti composites treated at 500 or 800 °C.

Sample	S_{BET} (m ² g ⁻¹)	V_{micro} (cm ³ g ⁻¹)	V_{pore} (cm ³ g ⁻¹)
CPT1-500	357	0.144	0.386
CPT1-800	9	0.004	0.076
CPT6-500	28	0.013	0.160
CPT6-800	30	0.017	0.239
CPT12-500	184	0.073	0.508
CPT12-800	5	0.021	0.043

The adsorptive and photocatalytic performance of the carbon-phosphorus-Ti composites was analyzed for the removal of OG (Figures 5.5a and 5.5b, respectively). Firstly, all samples were saturated in dark experiments, which hinders the contribution of the adsorption process on the OG removal in the subsequent photocatalytic experiments.

The adsorption capacity and the adsorption rate are not exclusively related with the different porosity of the samples, as observed in Figure 5.5a. In general, composites with lower Ti-content presented a better adsorptive behaviour than those prepared with intermediate and high Ti-contents regardless of the carbonization temperature used. The maximum removal of OG was achieved after 20 min and varied as: CPT1 samples > CPT6 samples > CPT12 samples. This trend could be explained because composites with low Ti-carbon ratio present a larger carbon phase, which has a higher affinity for OG in solution. The CPT1 composites presented the best adsorptive behaviour, being the adsorption of both CPT1-500 and CPT1-800 comparable in spite of their different porous characteristics and the crystallinity of their Ti-phases.

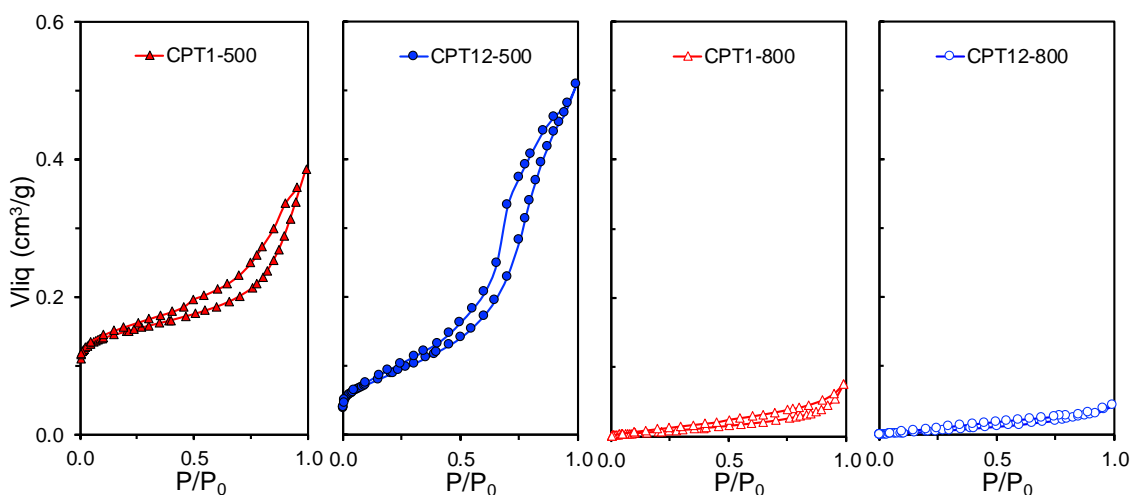


Figure 5.4. N₂-adsorption isotherms of carbon-phosphorus-Ti composites treated at 500 or 800 °C.

In Figure 5.5b is showed the photocatalytic efficiency obtained for the different carbon-phosphorus-Ti composites and the benchmark TiO₂ material (Degussa P25) for comparison. The complete OG removal was achieved after \approx 25-35 min or 40-50 min depending on composites treated at 500 or 800 °C, respectively. In general, all composites obtained at low carbonization temperature presented a better efficiency than those treated at 800 °C, in spite of that all these samples were completely amorphous since no peaks were not observed by XRD. The carbon phase retards the crystal growth and the phase transformations of metal oxides in carbon-metallic oxide composites [8, 9]. In addition, the presence of phosphorus may influence on the TiO₂-crystal structure, obtaining mixtures of TiO₂ amorphous and anatase [10]. In this context, composites obtained at 500 °C could

develop a mixture of amorphous and very small TiO₂-anatase nanoparticles (undetectable by XRD), latter being responsible for the high activity of composites treated at 500 °C. On the other hand, the photocatalytic efficiency varied as follows: CPT1-500 > CPT6-500 > CPT12-500, i.e., when the Ti-content increased in the composites, which could be related with their lower porosity (Table 5.2).

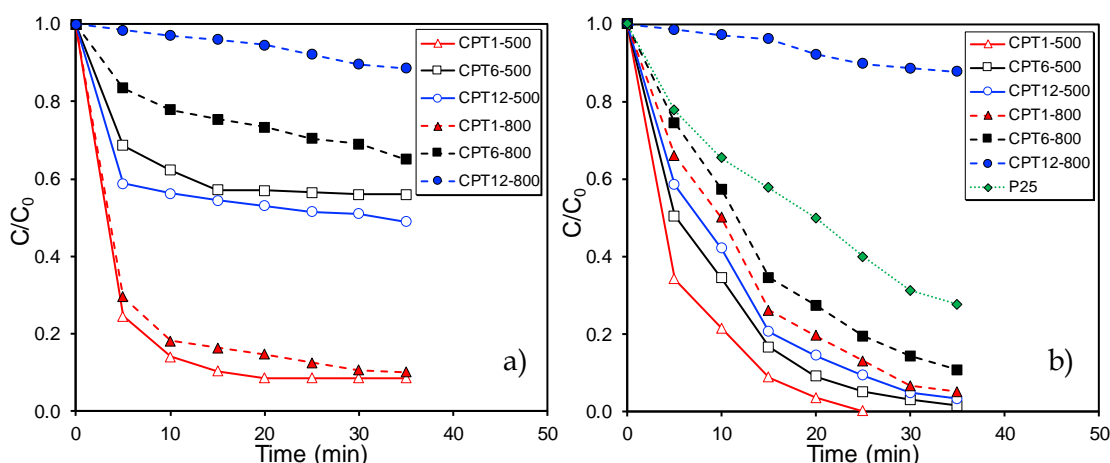


Figure 5.5. Removal of the Orange-G from water solution by adsorption (a) and photocatalytic (b) processes using carbon-phosphorus-Ti composites.

Concerning to composites treated at 800 °C, the formation of different polyphosphates was pointed out by XRD. The band gap for the titanium pyrophosphate (TiP₂O₇) was estimated to be 3.48 eV [11], being higher than that for the TiO₂ anatase or rutile phases, i.e., 3.2 and 3.0 eV, respectively. The different nature of polyphosphates can also influence on their performance [12, 13].

In addition, sintering was favoured to this range of temperature, Ti-particles larger than ≈ 39 nm being obtained. Otherwise, even the composites carbonized at this temperature, with exception of CPTi12-800, presented a better performance than the benchmark TiO₂ material (Degussa P25). This fact denotes the importance of the carbon phase in Ti-based composites, leading to an enhanced improved performance based on the synergism between both phases. Overall, carbon-phosphorus-titanium composites with low carbon content and carbonization temperature are preferred for the removal of the OG pollutant by photocatalysis because of their enhanced porosity, high dispersion of the active phase (anatase) and strong adsorption capacity (interaction) of OG.

5.3. Conclusions

The treatment of microcrystalline cellulose with H_3PO_4 leads to a simultaneous functionalization of cellulose chains by incorporating stable phosphorus-containing surface groups, namely, phosphates and polyphosphates. These functionalities interact and react progressively with Ti-species during impregnation and carbonization at high temperatures, with different polyphosphates of titanium being anchored on the carbon phase. The physicochemical properties of these carbon–phosphorus–Ti composites vary according to the Ti-content and carbonization temperature. Thus, the increase of these parameters favours Ti-particle sintering, the formation of Ti-crystalline phases and a marked loss of the porosity. The synergism between phases allows to obtain materials with enhanced photocatalytic efficiency compared to the benchmark TiO_2 material (Degussa P25), in spite of the band gap of polyphosphates being wider than that for anatase/rutile phases. Carbon–phosphorus–Ti composites with anatase TiO_2 nanoparticles and large surface areas seem to be the most active photocatalysts for OG degradation under UV irradiation.

5.4. References

- [1] Y.H.P. Zhang, J. Cui, L.R. Lynd, L.R. Kuang, A Transition from Cellulose Swelling to Cellulose Dissolution by *o*-Phosphoric Acid: Evidence from Enzymatic Hydrolysis and Supramolecular Structure, *Biomacromolecules*, 7 (2006) 644-648.
- [2] J.M. Rosas, J. Bedia, J. Rodríguez-Mirasol, T. Cordero, HEMP-derived activated carbon fibers by chemical activation with phosphoric acid, *Fuel*, 88 (2009) 19-26.
- [3] G. Hasegawa, T. Deguchi, K. Kanamori, Y. Kobayashi, H. Kageyama, T. Abe, K. Nakanishi, High-Level Doping of Nitrogen, Phosphorus, and Sulfur into Activated Carbon Monoliths and Their Electrochemical Capacitances, *Chemistry of Materials*, 27 (2015) 4703-4712.
- [4] A. Elmouwahidi, E. Bailón-García, A.F. Pérez-Cadenas, F.J. Maldonado-Hódar, F. Carrasco-Marín, Activated carbons from KOH and H_3PO_4 -activation of olive residues and its application as supercapacitor electrodes, *Electrochimica Acta*, 229 (2017) 219-228.
- [5] J.F. Vivo-Vilches, E. Bailón-García, A.F. Pérez-Cadenas, F. Carrasco-Marín, F.J. Maldonado-Hódar, Tailoring the surface chemistry and porosity of activated carbons: Evidence of reorganization and mobility of oxygenated surface groups, *Carbon*, 68 (2014) 520-530.
- [6] M.J. Prauchner, F. Rodríguez-Reinoso, Chemical versus physical activation of coconut shell: A comparative study, *Microporous and Mesoporous Materials*, 152 (2012) 163-171.
- [7] M.A. Mohamed, M. Abd Mutalib, Z.A. Mohd Hir, M.F. M. Zain, A.B. Mohamad, L. Jeffery Minggu, N.A. Awang, W.N. W. Salleh, An overview on cellulose-based material in

tailoring bio-hybrid nanostructured photocatalysts for water treatment and renewable energy applications, *International Journal of Biological Macromolecules*, 103 (2017) 1232-1256.

[8] F.J. Maldonado-Hódar, C. Moreno-Castilla, J. Rivera-Utrilla, Synthesis, pore texture and surface acid–base character of TiO₂/carbon composite xerogels and aerogels and their carbonized derivatives, *Applied Catalysis A: General*, 203 (2000) 151-159.

[9] C. Moreno-Castilla, F.J. Maldonado-Hodar, Synthesis and surface characteristics of silica- and alumina-carbon composite xerogels, *Physical Chemistry Chemical Physics*, 2 (2000) 4818-4822.

[10] L. Kőrösi, A. Oszkó, G. Galbács, A. Richardt, V. Zöllmer, I. Dékány, Structural properties and photocatalytic behaviour of phosphate-modified nanocrystalline titania films, *Applied Catalysis B: Environmental*, 77 (2007) 175-183.

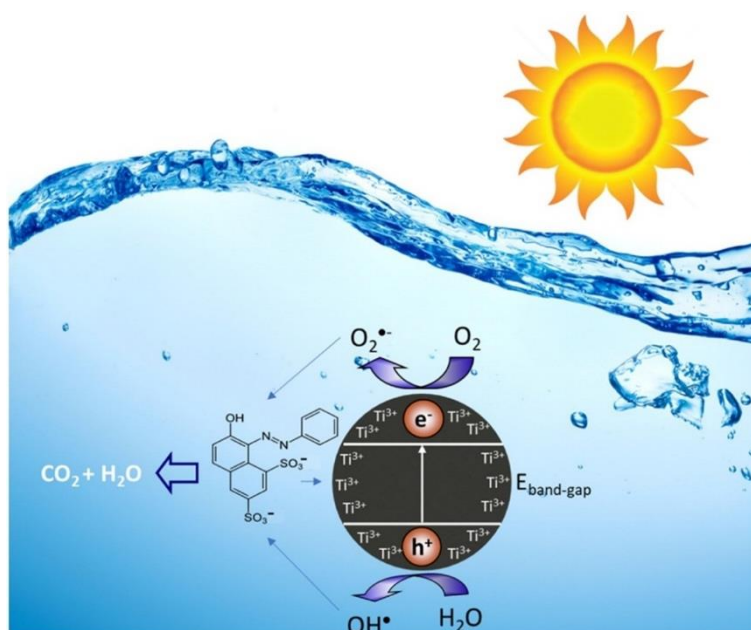
[11] X. Meng, M. Hao, J. Shi, Z. Cao, W. He, Y. Gao, J. Liu, Z. Li, Novel visible light response Ag₃PO₄/TiP₂O₇ composite photocatalyst with low Ag consumption, *Advanced Powder Technology*, 28 (2017) 1047-1053.

[12] R. Fagan, D.E. McCormack, S. Hinder, S.C. Pillai, Improved high temperature stability of anatase TiO₂ photocatalysts by N, F, P co-doping, *Materials & Design*, 96 (2016) 44-53.

[13] H.-F. Yu, Phase development and photocatalytic ability of gel-derived P-doped TiO₂, *Journal of Materials Research*, 22 (2007) 2565-2572.

CHAPTER VI -

SYNTHESIS OF Ti_xO_y NANOCRYSTALS IN MILD SYNTHESIS CONDITIONS FOR THE DEGRADATION OF POLLUTANTS UNDER SOLAR LIGHT





Synthesis of Ti_xO_y nanocrystals in mild synthesis conditions for the degradation of pollutants under solar light



Hesham Hamad¹, Esther Bailón-García*, Francisco J. Maldonado-Hódar, Agustín F. Pérez-Cadenas, Francisco Carrasco-Marín, Sergio Morales-Torres

Carbon Materials Research Group, Department of Inorganic Chemistry, Faculty of Sciences, University of Granada, Avenida de Fuentenueva, s/n., ES18071 Granada, Spain

ARTICLE INFO

Keywords:

Black titania
Oxygen vacancies
Visible light photocatalysts
Band gap narrowing
Synergetic effect

ABSTRACT

Black TiO_2 is capable to absorb the entire or part of the visible spectrum improving, a priori, the photoactivity under solar irradiation. Nevertheless, black TiO_2 materials have not been able to demonstrate the expected photocatalytic activity in visible light due to the presence of a large number of recombination centers. In addition, high temperatures or pressures ($> 400^\circ C$, 20 bar) are required for the conventional synthesis and alternative methods have high energy costs which limit the capability for mass production. In this report, a novel controlled hydrolysis method has been developed to synthesize reduced black TiO_2 in mild conditions of temperature ($180^\circ C$) and pressure (8 bar). The synergetic effect of the stabilization of small crystal sizes, strong visible light absorption, band gap narrowing, Ti^{3+} defects or oxygen vacancies concentration, improved surface area and pollutant-surface interactions, significantly enhances the photocatalytic activity in the degradation of organic pollutants (Orange G) under visible light (almost totally degraded at 40 min).

6.1. Materials and methods.

6.1.1. Synthesis and characterization of black titania.

The synthesis of these materials was prepared by a controlled hydrolysis of TTIP in methanol/acetonitrile medium using CTAB as structure-directing agent. Information detailed can be found in Section 2.2.4. These samples were denoted as TiAX, where A is H or N for H_2 or N_2 treatments, respectively and X is the number of days of treatments (1 – 5 days), i.e. TiH1 indicates that TiO_2 was synthesised in presence of H_2 after 1 day of treatment. White titania, TiO_2 anatase from sigma aldrich, was used as reference material.

The characterization of the samples was carried out using physical adsorption of N_2 , scanning electron microscopy (SEM), transmission electron microscopy (TEM), X-ray diffraction (XRD), X-ray photoelectron spectroscopy (XPS) and Diffuse reflectance spectroscopy (DRS). The performance of black titania in the photodegradation of the orange-G (OG) dye in aqueous solutions was studied under visible irradiation.

6.1.2. Photocatalytic degradation procedure in presence of saturated photocatalysts.

The photocatalytic activity was using a glass photoreactor (inner diameter of 8.5 cm x height of 20 cm) equipped with an inner tube of 2.5 cm of diameter placed in the reactor centre, allowing to fit a visible sun lamp of 14 W (ReptoLux 2.0) inside to ensure a uniform irradiation of all solution volume. The degradation kinetic was follow by UV-spectrometry using a UV-vis spectrophotometer (5625 Unicam Ltd., Cambridge, UK), previously calibrated. Catalytic photodegradation was carried out using 1 mg/ml of photocatalyst, previously saturated with the dye in the dark to avoid the influence of the different adsorptive performance of each sample on the evolution of the dye concentration. After saturation, the initial dye concentration (C_0) was fitted again in all cases to 10 mg/L, and then, visible light was turned on and this time was considered as the start degradation time. At a regular interval of 10 min, equal aliquot was removed from the reactor, filtered and the OG concentration measured by UV-spectrometry. The OG mineralization degree was followed by the evolution of total organic carbon (TOC) present in the solution during the photo-degradation experience using an analyzer Shimadzu V-CSH analyser with ASI-V autosampler and subtracting the inorganic carbon value in each sample from the total carbon value. The Orange G adsorption isotherm on black titania was carried out also in a thermostatic bath at 298 K. For this, a volume of 25 mL with different initial concentrations of dye is placed in a flask and 0.025 g of sample was added. The flask was placed inside the thermostatic bath under shaking for 4 h to ensure the equilibrium are reached. The Orange G adsorption capacity of samples (X_{ads} , mg/g) was calculated by fitting de adsorption data to the Langmuir equation.

6.2. Results and discussion.

6.2.1. Textural and chemical characterization.

Black titania nanoparticles with different colours were successfully synthesized in mild experimental conditions (8 bar and 180 °C) by the controlled hydrolysis of titanium isopropoxide, either in presence of nitrogen or hydrogen. As shown in Figure 6.1, TiO_2 powder was converted from white to intense grey-black by increasing the treatment time. Highlight that the dark colour is more intense in presence of H_2 in comparison with the N_2 samples, denoting a higher effectivity in the titania reduction.

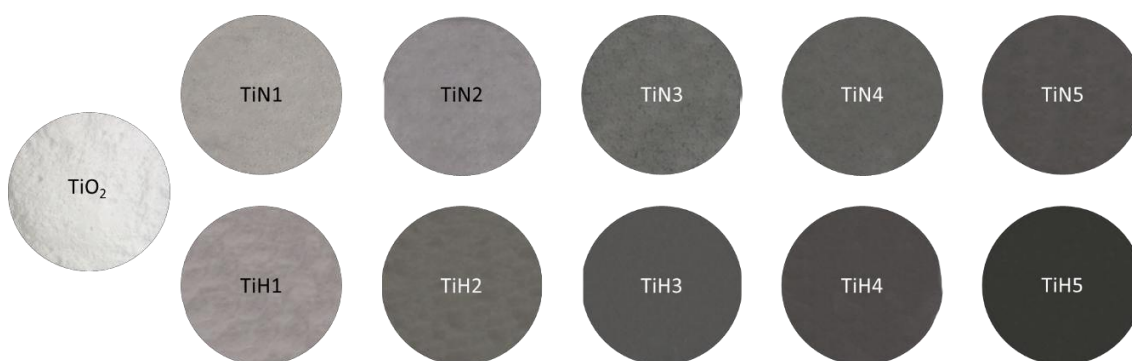


Figure 6.1. Digital photographs of Ti_xO_y samples.

The different dark colours of samples suggest excellent visible light absorption. Figure 6.2 displays the diffuse reflectance spectra of the coloured titania and TiO_2 -anatase as reference. A strong visible light absorption is observed for the synthesized samples regarding white TiO_2 ; stronger for the H_2 -treated samples. Moreover, this adsorption increases by increasing the treatment time which is in line with the visual impression of the darkness of the samples. The enhanced visible light adsorption could be attributed to the effective reduction of Ti^{4+} ions of titania into Ti^{3+} by introducing oxygen vacancies [1] during the solvothermal treatment. This means that the higher is the treatment time the higher is the amount of Ti^{3+} or oxygen vacancies in the sample and thus, the effectivity of the process. This effectivity is also improved in presence of H_2 manifesting that, in spite of the soft hydrogenation conditions, titania hydrogenation takes place.

The band gap, E_g , was calculated by the Kubelka–Munk (KM) method and results are shown in Figure 6.2c. TiO_2 is an intrinsic n-type semiconductor with a band gap of 3–3.2 eV. However, in the reduced state, the higher density of Ti^{3+} leads to a decrease in the band gap. As compared to white TiO_2 , the optical band gap of TiN_x and TiH_x samples are substantially reduced (up to band gap lower than 2.3 eV) and this decrease is linearly dependent of the treatment time. Moreover, as expected, a proportional decrease of the band gap is obtained in presence of H_2 atmosphere (same slopes).

The presence of Ti^{3+} was corroborated by X-ray photoelectron spectroscopy (XPS). Figure 6.3 displays the Ti_{2p} XPS region and Table 6.1 collects the data obtained from XPS analysis. Only a peak centered at 459.5 eV is observed for white TiO_2 which is attributed to Ti^{4+} , whereas Ti^{3+} is the main component in coloured TiO_2 (peak centered at 458.5 eV). This

means that reduction occurs mainly at the surface since TiO_2 is the unique phase detected by XRD without detection of Ti_2O_3 (data shown below); and that oxidation does not take place after the exposure of samples to the air. Moreover, as expected, the % of Ti^{3+} increases with the treatment time and the hydrogen treatment improves this reduction (86 vs. 92 % of Ti^{3+} for TiN_1 and TiH_1 , respectively, Table 1) which corroborates the results obtained from diffuse reflectance analysis.

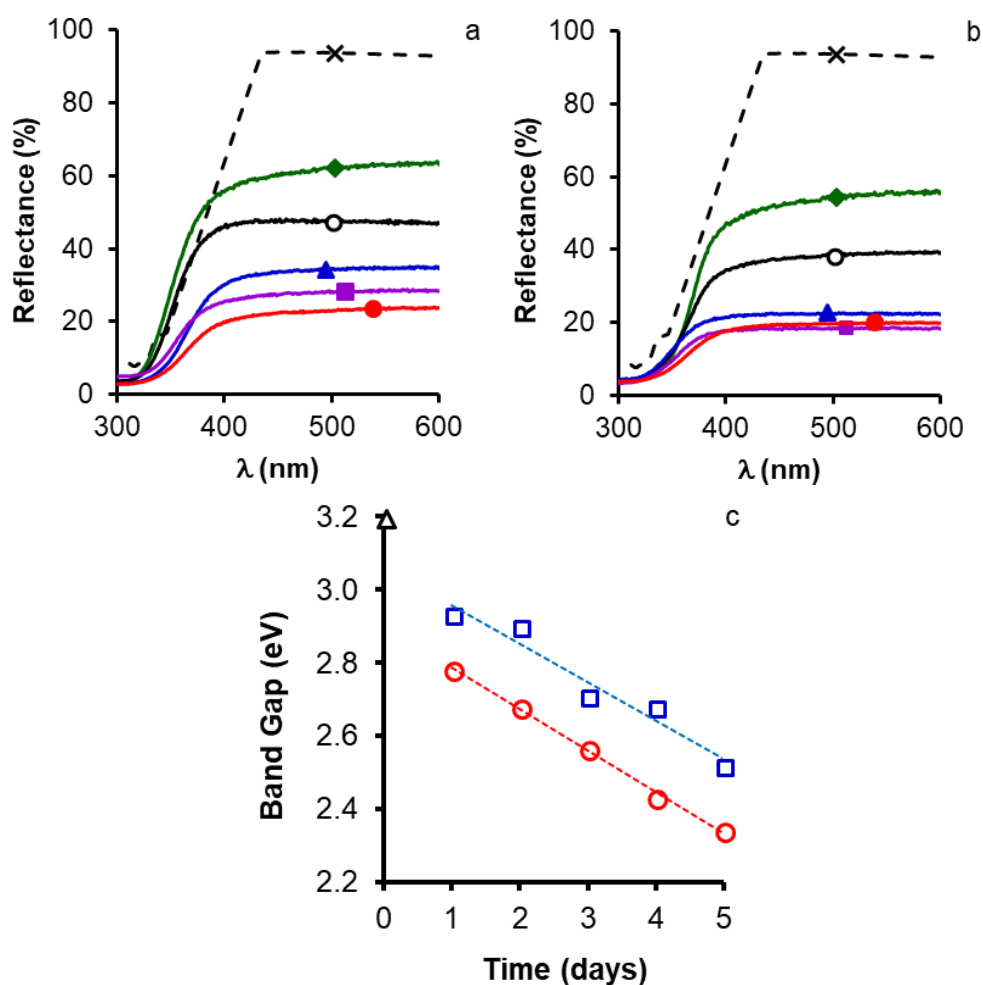


Figure 6.2. Diffuse reflectance spectra of a) TiN_x and b) TiH_x samples in comparison with white TiO_2 (x) as reference, being x : 1 (\blacklozenge), 2 (\circ), 3 (\blacktriangle), 4 (\blacksquare) or 5 (\bullet); c) Band gap of TiN_x (\square), TiH_x (\circ) and white TiO_2 (Δ).

Regarding the O1s region (Table 6.1), three peaks located at 529.8, 531.0, and 532.0 eV are needed, corresponding to Ti-O in surface bulk oxide lattices, acidic hydroxyl group and basic hydroxyl group, respectively [2]. Different authors have confirmed the formation of hydroxyl group on TiO_2 surface after hydrogenation treatments [1–4] due to the

hydrogenation helping to break up Ti-O bonds on the surfaces of anatase nanocrystals by forming Ti-H and O-H bonds [5]. An increase of Ti-OH bonds (Ti-OH/Ti-O area ratio) is observed in both TiN_x and TiH_x samples regarding TiO_2 because of the titania reduction, but this increase is more significant in presence of H_2 corroborating again that titania hydrogenation occurs in TiH_x samples during the solvothermal treatment at mild conditions.

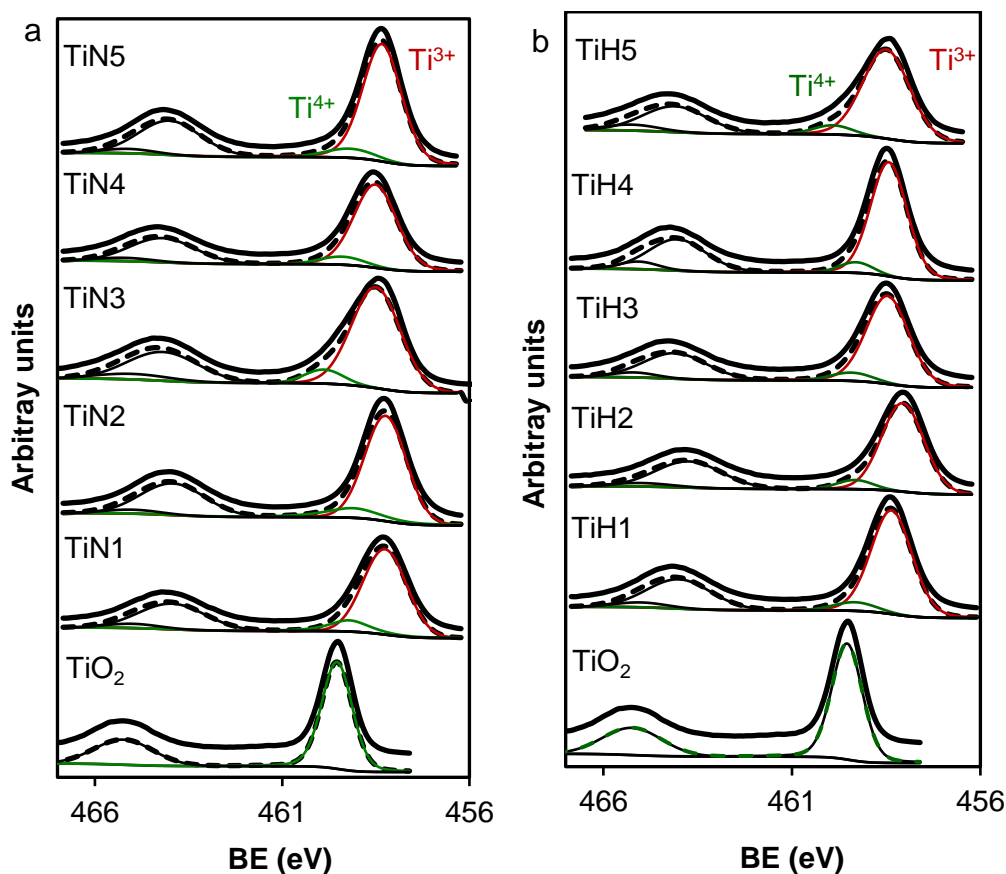


Figure 6.3. Ti_{2p} region of XPS spectra for a) TiN_x and b) TiH_x samples.

XRD was used to investigate the crystallinity and possible phase changes of the prepared samples and results are collected in Figure 6.4 and Table 6.1. XRD patterns of TiH_x and TiN_x nanoparticles was similar to that of TiO_2 , except for the lower peak intensities denoting a lower crystallinity or lower crystal size, and well matched with the anatase phase TiO_2 (21-1272, JCPDS). It is clearly noticed an increase of diffraction intensities and crystal sizes in TiN_x samples increasing the treatment time (Figure 6.4a and Table 6.1) whereas in TiH_x ones, crystal sizes are similar (around 4.5 nm) in all cases (Figure 6.4b and Table 6.1).

Table 6.1. Ti_{2p} and O_{1s} data obtained from XPS and crystal size from XRD.

Sample	Ti _{2p}		O _{1s}		Ti-OH/ Ti-O	D (nm)
	BE (eV)	% peak	BE (eV)	% peak		
TiO ₂	459.5	100	530.4	80	0.25	24.6
			532.5	17		
			534.3	3		
TiN1	459.2	13.7	458.3	86.3	0.28	3.8
			529.8	78		
			531.2	15		
TiN2	459.1	13.5	532.2	7	0.37	3.9
			458.2	86.5		
			529.7	73		
TiN3	459.9	9.7	530.9	16	0.32	4.6
			458.5	90.3		
			529.8	74		
TiN4	459.4	8.6	531.8	11	0.35	4.7
			458.5	91.4		
			529.9	74		
TiN5	459.2	8.2	530.9	19	0.35	5.1
			458.3	91.8		
			529.6	74		
TiH1	459.3	8.0	531.9	7	0.35	4.6
			458.4	92.0		
			529.7	74		
TiH2	459.3	7.9	531.9	8	0.39	4.3
			458.1	92.1		
			529.4	72		
TiH3	459.4	7.7	530.7	21	0.41	4.3
			458.5	92.3		
			529.9	71		
TiH4	459.3	7.4	531.8	7	0.41	4.5
			458.4	92.6		
			529.8	71		
TiH5	459.9	7.4	530.9	21	0.42	4.4
			458.5	92.6		
			529.8	71		
			531.0	22		
			532.1	7		

It was pointed out in literature that the intensity of the diffraction peaks decreases gradually, and peaks weaken and widened increasing the reduction effectivity of the coloured titania which are related to the amorphous phase created after the reduction process [4,6]. Usually, a surface disordered shell is observed in coloured titania due to the creation of oxygen vacancy/Ti³⁺, surface hydroxyl groups or Ti–H bonds. This shell is amorphous and consequently, crystal sizes and diffraction intensity decrease after the reduction

treatment. With that background, two considerations must to be considered: i) the crystallinity usually increases the hydrothermal treatment time [6] and ii) the crystallinity decreases by the titania reduction [4,6]. In the TiN_x series, the reduction effectivity is lower than in the case of TiH_x one and consequently, the first factor is more significant than the latter and, as results, an increase in the crystallinity and particles size is observed. Conversely, in TiH_x samples, the reduction efficiency is higher and thus, both factors are balanced resulting in a stabilization of the particle size.

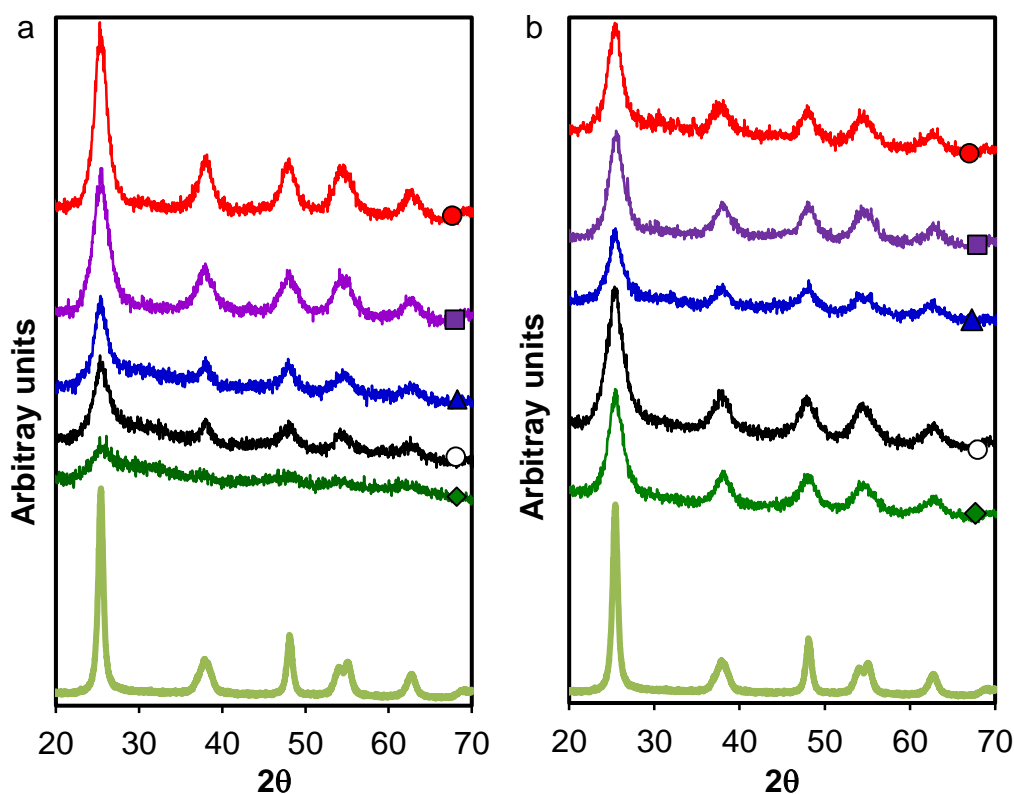


Figure 6.4. XRD patterns of a) TiN_x and b) TiH_x samples. x : 1 (\blacklozenge), 2 (\circ), 3 (\blacktriangle), 4 (\blacksquare) or 5 (\bullet).

The morphology of the black titania was analysed by SEM and HRTEM. Characteristic SEM and HRTEM images are collected in Figure 6.5. SEM images reveals the presence of titania particles interconnected by titania nanofibers (around 60 nm of diameter), independently of the treatment time and atmosphere. In turn, HRTEM images show that the white TiO_2 is completely crystalline, displaying clearly-resolved and well-defined lattice fringes and well-ordered crystal domains of around 25 nm. In contrast, TiN_x and TiH_x samples display highly-disorder nanosized crystal domains (around 4 nm) with a

relatively unclear fringe pattern owing to introduction of amorphous regions between crystal domains. Note that the size of the crystal domains observed by TEM corroborates the crystal sizes obtained by XRD. The distance between the adjacent lattice planes is 0.35 nm for white TiO₂, which matches the typical value for anatase. Conversely, this distance is slightly reduced to 0.30 nm for black titania suggesting the incorporation of H atoms within the host lattice.

The N₂ adsorption–desorption isotherms are depicted in Figure 6.6a-b and data collected in Table 6.2. All samples mainly exhibit a type-IV isotherm with a hysteresis loop, indicating the mesoporous character. However, significant differences are observed between white and coloured TiO₂. The hysteresis loop appears at 0.3-0.4 relative pressure for coloured titania, indicating the presence of narrow mesoporosity (3 nm, Figure 6.6c-d), whereas in white TiO₂, this loop begins at higher relative pressures (0.7-0.8) indicating the presence of wider mesoporosity (20 nm, data not shown). Moreover, higher N₂ uptake at low relative pressure is observed for coloured TiO₂ indicating the development of microporosity in these cases. Note also that the textural properties are improved increasing the treatment time, i.e. the surface area increases from 133 to 191 m² g⁻¹ for N₂ serial and from 137 to 212 m² g⁻¹ for H₂ samples, increasing the treatment time from 1 to 5 days (Table 6.2). The presence of H₂ during the solvothermal treatment also improves the textural properties. This improvement could be explained on the base of different crystal sizes. An increase in surface area could be attributed to a decreased crystallite size [7, 8], however, similar or even larger crystal size is observed in TiH_x and TiN_x series increasing the treatment time. This seems to indicate that the reduction effectivity and defective TiO_{2-x} play an important role in the texture. The amorphous titania typically shows BET surface areas higher than the crystalline counterparts [9,10]. This defective phase increases with the effectiveness of the titania reduction method and consequently, with the treatment time.

Therefore, the present synthesis method improves the porous texture of coloured titania regarding white one; significantly affects the pore structure and surface area of the obtained TiO_{2-x} samples, and consequently, this improved porous structure must have a beneficial effect in the photocatalytic performance of coloured TiO₂.

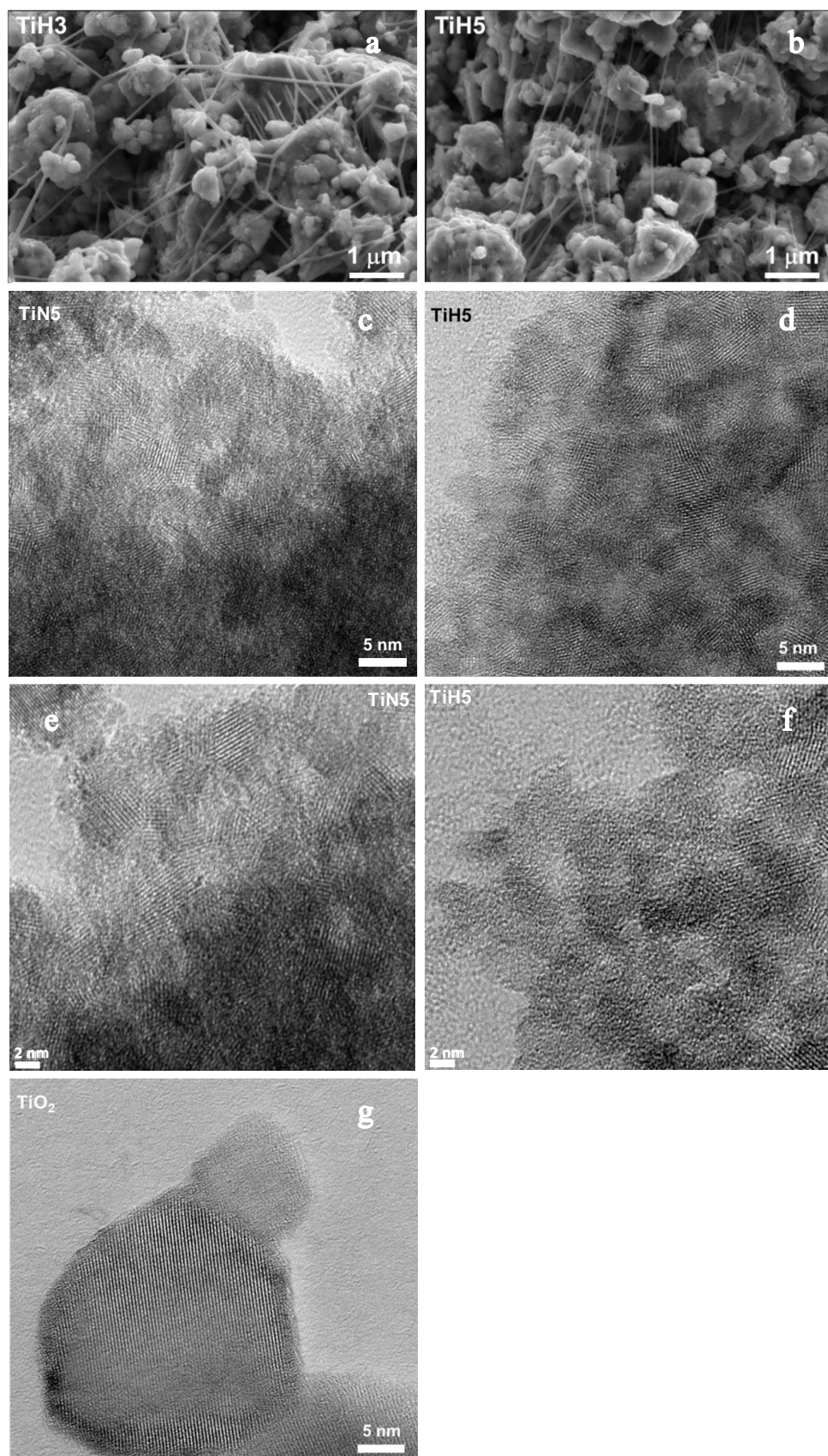


Figure 6.5. Characteristic SEM (a,b) and TEM (c-g) images of the black titania

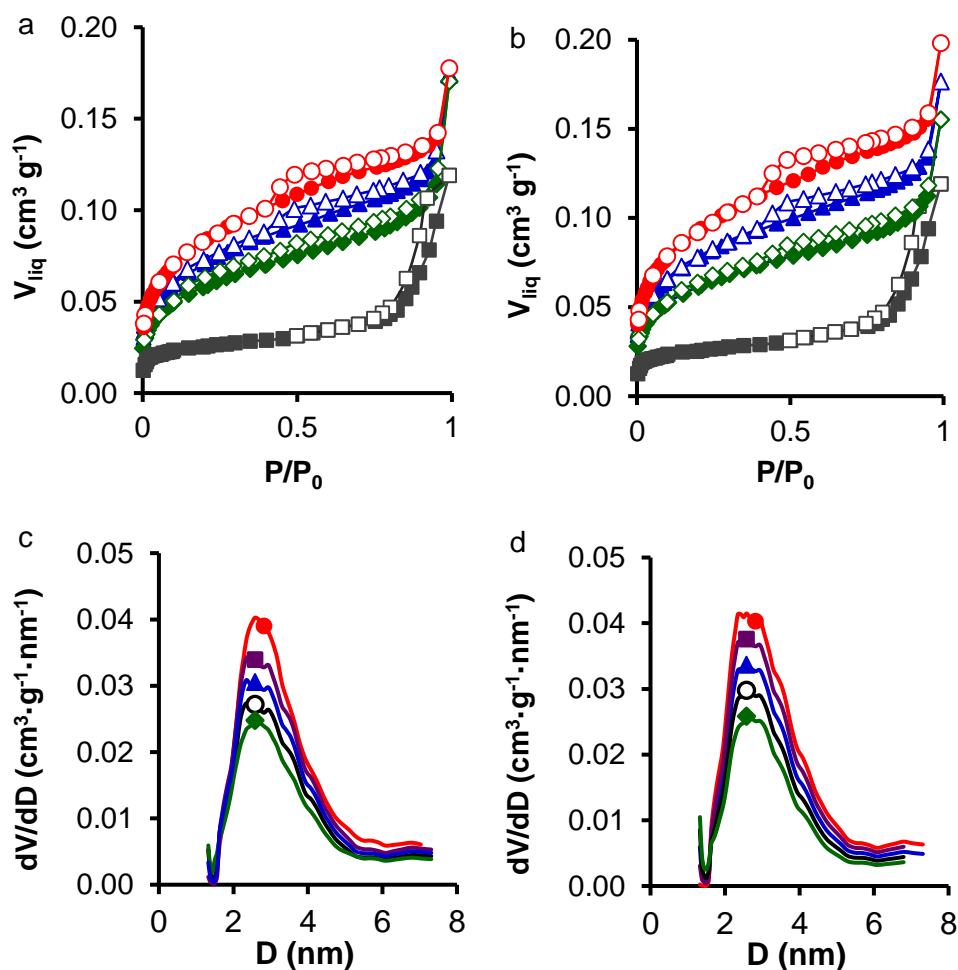


Figure 6.6. N₂-isotherms and pore size distributions for TiNx (a,c) and TiHx (b,d) samples in comparison with TiO₂ (□). x: 1 (◆), 2 (○), 3 (▲), 4 (■) or 5 (●).

Table 6.2. Textural characterization of samples

Samples	S_{BET} (m ² /g)	W_0 (N ₂) cm ³ /g	L_0 (N ₂) (nm)	$V_{0.95}$ cm ³ /g	V_{meso} cm ³ /g
TiO ₂	57	0.038	-	0.118	0.080
TiW1	133	0.052	1.81	0.114	0.063
TiW2	146	0.057	1.84	0.121	0.063
TiW3	161	0.062	1.83	0.127	0.065
TiW4	175	0.067	1.82	0.133	0.066
TiW5	191	0.075	1.89	0.139	0.064
TiH1	137	0.054	1.74	0.112	0.058
TiH2	154	0.061	1.76	0.123	0.062
TiH3	172	0.068	1.78	0.134	0.066
TiH4	190	0.074	1.79	0.145	0.071
TiH5	212	0.082	1.83	0.159	0.077

6.2.2. Photocatalytic activity.

The photocatalytic activity of coloured TiO_2 was evaluated towards the degradation of an industrial textile dye, Orange G (OG), under a low power artificial visible light (14 W). Prior to the photocatalytic test, catalysts were saturated with OG in dark in order to avoid adsorption interferences and the initial concentration fitted in 10 mg/l. In Figure 6.7, the Orange G adsorption capacity of samples was plotted as a function of the specific surface area. As could be expected, the adsorption capacity linearly increases with the surface area for both TiN_x and TiH_x samples, but significant differences are observed between them; much higher absorption capacity is obtained in TiH_x samples despite similar surface area. To explain this fact, two factors must to be considered; i) the specific surface area for the adsorption of the pollutant and ii) the electrostatic interactions of the pollutant with the surface. Zeta potential results have demonstrated an increased positive charge on titania surface increasing the Ti^{3+} defects or oxygen vacancies on the surface [11,12]. The adsorption of Orange G, a negatively charged molecule, could be favoured on positively charged oxygen vacancies. It has been pointed out that the adsorption of cationic dyes (such as methylene blue) is favoured increasing de pH of the solution due to for pH's higher than the point zero charge (pzc) of titania, the surface becomes negatively charged and its adsorption is favoured on a negatively charged surface. By contrast, OG has its adsorption inhibited by high pH's because of its negatively charged sulfonate, SO_3^- function [13,14]. In a similar way, the increase of oxygen vacancies on the surface of coloured titania creates an electron deficiency on the surface and thus, a positively charged titania surface, favouring the interaction with anionic dyes (such as Orange G). Consequently, this adsorption is favoured on the TiH_x samples regarding TiN_x due to the development of a more defective titania surface in presence of H_2 (Ti^{3+} /oxygen vacancies observed by XPS). Note that the adsorption capacity of white TiO_2 is lower than the expected according with TiN_x and TiH_x linear series due to the absence or low amount of oxygen vacancies and thus, the null or scarce contribution of the specific interactions in the adsorption capacity. Mineralization of dye was followed by the Total Organic Carbon (TOC) measurement and total degradation was found in all cases, and consequently, intermediary products were not analyzed.

Figure 6.8 shows the removal of OG as a function of the irradiation time. As it can be observed, very low degradation is obtained using white TiO_2 as catalyst due to its high

band gap (3.2 eV) which limits the activity under visible light. Conversely, activity is observed using coloured TiO₂ as catalysts which increases increasing the solvothermal treatment time. This increasing activity is related with the enhanced visible light adsorption attributed to the effective reduction of Ti⁴⁺ ions of titania into Ti³⁺ by introducing oxygen vacancies. A linear relationship between the time needed to achieve the 50 % of Orange G degradation ($t_{0.5}$) and the photocatalyst band gap is obtained inside each serial (Figure 6.9). Nevertheless, differences between TiN_x and TiH_x series are again observed. Time longer than 200 min are needed for the complete degradation of Orange G in TiN_x serial whereas total degradation is obtained after 80 min of reaction using TiH_x as catalysts. It is true that an activity improvement must be observed in TiH_x samples due to the lower band gap of these samples, but the improvement is much higher than the expected considering the obtained band gap in comparison with TiN_x serial. In these sense, additional factors could contribute to this enhanced behaviour: surface area and specific interactions. It is well known that the photoactivity performance is strongly depended on the adsorption capacity of the photocatalyst, as it is known that the photocatalytic reaction occurs on the photocatalyst surface. As has been commented above, the absorption capacity of TiH_x samples is enhanced regarding TiN_x ones due to the improvement of surface area and electrostatic interactions surface-dye, and thus, the activity is highly improved.

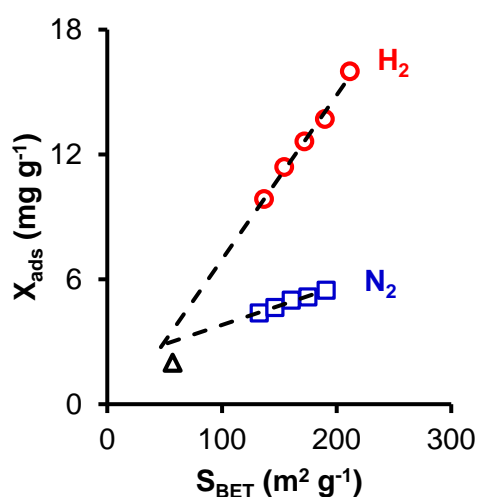


Figure 6.7. Orange G adsorption capacity of samples as a function of surface area. TiH_x (○), TiN_x (□) and TiO₂ (Δ).

The surface disorder is another important factor to consider explaining the better activity of coloured titania. It has been demonstrated that the improved photoactivity of

black TiO_2 results from a synergistic effect of the oxygen vacancies on core and surface disorder, that is the surface localization of defects [15]. In this sense, it was observed that decreasing the relative concentration ratio of bulk defects to surface defects in TiO_2 nanocrystals significantly improves the charge separation efficiency and, thus, enhances the photoactivity [16]. Considering that, the high concentration of Ti^{3+} into the surface of the synthesized as it has been pointed out by TEM and XPS, improves the photocatalytic performance of both TiN_x and TiH_x catalysts. The highest concentration of surface defects (denoted by XPS) and the highest surface area of TiH_x samples results in a highest overall surface disorder resulting in a better photoactivity. So, in TiH_x catalysts, the combination of different factors as improved band gap, surface area and specific interactions and the surface localization of defects results in a superior photoactivity.

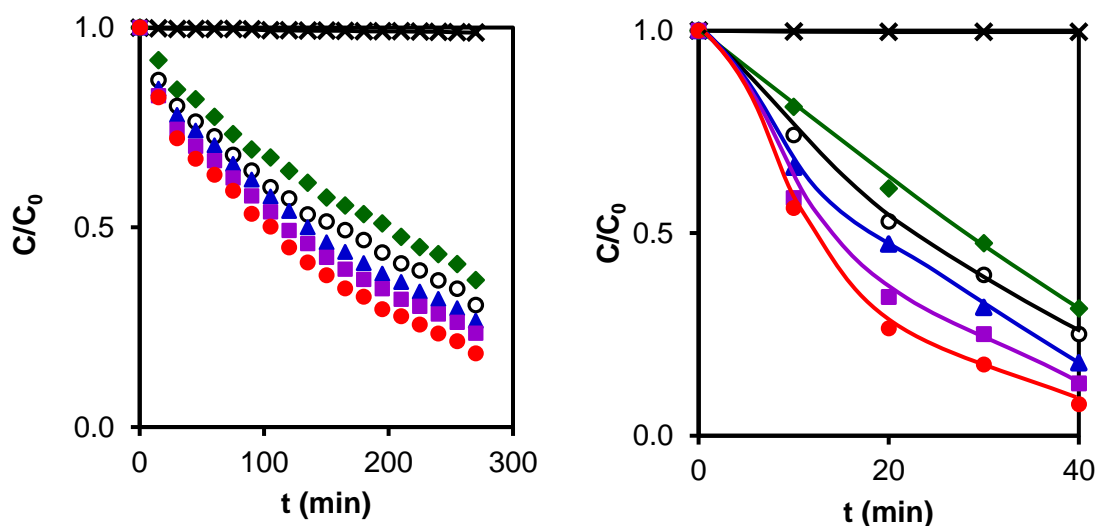


Figure 6.8. Kinetic of Orange G photocatalytic degradation using a) TiN_x and b) TiH_x samples in comparison with white TiO_2 (x). x: 1 (\blacklozenge), 2 (\circ), 3 (\blacktriangle), 4 (\blacksquare) or 5 (\bullet).

In brief, TiH_5 present the best photocatalytic performance. Orange G is almost totally degraded after a very short time of reaction (lower than 40 min) under visible irradiation. This excellent behaviour is due to the optimization of a series of factors by the proposed solvothermal synthesis method with the benefit of softer experimental conditions in comparison with other methods described in bibliography in which temperatures higher than 400°C or pressures higher than 20 bars are required. These factors are: i) the stabilization of low crystal sizes (lower than 5 nm) which improves the accessible surface

area for the pollutants adsorption and minimizes the electron-hole recombination probability. In these senses, in small TiO_2 nanoparticles, the distance that the photogenerated electrons and holes need to travel to surface reaction sites is reduced, thereby reducing the recombination probability; ii) Strong visible light absorption and Band gap reduction. Oxygen vacancies/ Ti^{3+} species confer a black colour to TiO_2 and creates new hybrid states in the band gap, which narrows the band gap and enhances significant visible light adsorption; iii) Ti^{3+} defects or oxygen vacancies increase positive charge on titania surface improving the electrostatic interaction of Orange G, a negatively charged molecule, with the positively charged TiO_2 surface; and iv) the surface localization of defects which significantly improves the electron-hole separation efficiency and thus, significantly enhancing the photocatalytic efficiency.

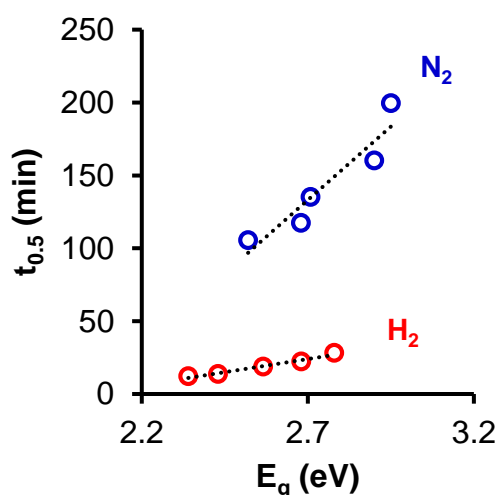


Figure 6.9. Relationship between the time needed to achieve the 50 % of Orange G degradation ($t_{0.5}$) and the photocatalyst band gap. TiH_x (\circ), TiN_x (\square) and TiO_2 (Δ).

6.3. Conclusions.

Coloured TiO_2 was successfully synthesized by the controlled hydrolysis of a titanium alkoxide under controlled atmosphere (N_2 or H_2) with the benefit of softer synthesis conditions in comparison with other methods described in bibliography in which temperatures higher than $400\text{ }^\circ\text{C}$ or pressures higher than 20 bars are required. The colour of samples changes to more intense dark depending of the treatment time suggesting excellent visible light absorption. The material possesses an optimum band gap and visible light adsorption, Ti^{3+} / oxygen vacancies concentration, surface defects, crystal size, surface

area and improved pollutant-surface interactions which significantly enhances the photoactivity under visible light. An industrial textile dye, Orange G, was selected as target molecule. The OG adsorption is controlled by the specific surface area but also the electrostatic interactions of the pollutant with the surface. The increasing positive charge on titania surface due to the increase of Ti^{3+} or oxygen vacancies on the surface improves the electrostatics interactions with OG, a negatively charged molecule, and favour its adsorption. The exceptional photocatalytic behaviour of coloured TiO_2 could be related with the different optimized properties of the samples: i) the stabilization of low crystal sizes (lower than 5 nm) which improves the accessible surface area for the pollutants adsorption and minimizes the electron-hole recombination probability; ii) the strong visible light absorption and band gap reduction and iii) Ti^{3+} defects or oxygen vacancies increase positive charge on titania surface improving the electrostatic interaction of OG favouring its absorption and degradation.

6.4. References.

- [1] G. Zhu, J. Xu, W. Zhao, F. Huang, Constructing black titania with unique nanocage structure for solar desalination, *ACS Appl. Mater. Interfaces*. 8 (2016) 31716–31721.
- [2] C.Y. Wu, K.J. Tu, J.P. Deng, Y.S. Lo, C.H. Wu, Markedly Enhanced Surface Hydroxyl Groups of TiO_2 Nanoparticles with Superior Water-Dispersibility for Photocatalysis, *Materials (Basel)*. 10 (2017).
- [3] G. Wang, H. Wang, Y. Ling, Y. Tang, X. Yang, R.C. Fitzmorris, C. Wang, J.Z. Zhang, Y. Li, Hydrogen-Treated TiO_2 Nanowire Arrays for Photoelectrochemical Water Splitting, *Nano Lett.* 11 (2011) 3026–3033.
- [4] X. Liu, B. Hou, G. Wang, Z. Cui, X. Zhu, X. Wang, Black titania/graphene oxide nanocomposite films with excellent photothermal property for solar steam generation, *J. Mater. Res.* 33 (2018) 674–684.
- [5] C. Fan, C. Chen, J. Wang, X. Fu, Z. Ren, G. Qian, Z. Wang, Black Hydroxylated Titanium Dioxide Prepared via Ultrasonication with Enhanced Photocatalytic Activity, *Sci. Rep.* 5 (2015) 11712.
- [6] J. Su, Y. Liang, S. Yunfei, S. Shuhua, J. Song, Z. Zhuojing, Effects of hydrothermal treatment on the properties of nanoapatite crystals, *Int. J. Nanomedicine*. 7 (2012) 5151.
- [7] N. Muhd Julkapli, S. Bagheri, Applications of Titania as a Heterogeneous Catalyst for Degradation of Landfill Leachates, in: N. Muhd Julkapli, S. Bagheri (Eds.), *Nanocatalysts Environ. Appl.*, Springer International Publishing, Switzerland, 2018.
- [8] A. Sinhamahapatra, J.-P. Jeon, J.-S. Yu, A new approach to prepare highly active and stable black titania for visible light-assisted hydrogen production, *Energy Environ. Sci.* 8 (2015) 3539–3544.
- [9] T. Fröschl, U. Hörmann, P. Kubiak, G. Kučerová, M. Pfanzelt, C.K. Weiss, R.J. Behm, N.

Hüsing, U. Kaiser, K. Landfester, M. Wohlfahrt-Mehrens, High surface area crystalline titanium dioxide: potential and limits in electrochemical energy storage and catalysis, *Chem. Soc. Rev.* 41 (2012) 5313–5360.

[10] K. Kaur, C.V. Singh, Amorphous TiO₂ as a photocatalyst for hydrogen production: A DFT study of structural and electronic properties, *Energy Procedia.* 29 (2012) 291–299.

[11] V.E. Alexandrov, E.A. Kotomin, J. Maier, R.A. Evarestov, First-principles study of bulk and surface oxygen vacancies in SrTiO₃ crystal, *Eur. Phys. J. B.* 72 (2009) 53–57.

[12] H. Qin, Y. Bian, Y. Zhang, L. Liu, Z. Bian, Effect of Ti (III) Surface Defects on the Process of Photocatalytic Reduction of Hexavalent Chromium, *Chinese J. Chem.* 35 (2017) 203–208.

[13] S. Asuha, X.G. Zhou, S. Zhao, Adsorption of methyl orange and Cr(VI) on mesoporous TiO₂ prepared by hydrothermal method, *J. Hazard. Mater.* 181 (2010) 204–210.

[14] H. Lachheb, E. Puzenat, A. Houas, M. Ksibi, E. Elaloui, C. Guillard, J.M. Herrmann, Photocatalytic degradation of various types of dyes (Alizarin S, Crocein Orange G, Methyl Red, Congo Red, Methylene Blue) in water by UV-irradiated titania, *Appl. Catal. B Environ.* 39 (2002) 75–90.

[15] K. Zhang, J.H. Park, Surface Localization of Defects in Black TiO₂: Enhancing Photoactivity or Reactivity, *J. Phys. Chem. Lett.* 8 (2017) 199–207.

[16] M. Kong, Y. Li, X. Chen, T. Tian, P. Fang, F. Zheng, X. Zhao, Tuning the relative concentration ratio of bulk defects to surface defects in TiO₂ nanocrystals leads to high photocatalytic efficiency, *J. Am. Chem. Soc.* 133 (2011) 16414–16417.

The seal of the University of Granada is a circular emblem. It features a central shield with a crown on top, flanked by two eagles with spread wings. The shield is supported by two columns. The entire emblem is enclosed in a circular border containing the Latin text 'UNIVERSITAS GRANATENSIS' and the year '1531'.

**CHAPTER VII - GENERAL
CONCLUSIONS**

In the present Doctoral Thesis, various series of photocatalytic titania-based nanomaterials have been synthesized from various ways, obtaining different types of composites, using functionalized cellulose, carbon, and also the development of non-stoichiometric black titania photocatalysts. All of the prepared materials have been thoroughly characterized, and their behaviour has been studied in photocatalytic degradation of Orange G dye as a target organic pollutant in water. All of the samples present a certain enhancement of photocatalytic activity regarding pure TiO₂ phases, which have been correlated with the physicochemical and textural properties of the developed materials.

The main results draw in this study can be concluded as follows:

1. Successful functionalization of cellulose by H₃PO₄ or HNO₃ as a source of a green, sustainable and cheap materials in order to obtain a high dispersion of TiO₂ nanoparticles on surface of cellulose or carbon after carbonization.
2. MCC is a green, sustainable and cheap support to develop active photocatalysts, but it must be pretreated in order to facilitate the contact with the active phase precursors. Acid treatments completely dissolve the MCC crystalline structure but simultaneously generate different types of oxygen or phosphor functionalities on the cellulose chemical structure.
3. The different interactions between precursors during impregnation leads to microporous cellulose composites with round-shaped anatase TiO₂ microcrystals by using HNO₃ treatments, while H₃PO₄ favours the formation of mesoporous composites with flat and non-crystalline TiO₂ particles.
4. These interactions also allow a band gap narrowing and a developed active surface, and thus, highly active cellulose-TiO₂ composites have been successfully synthesized in particular for the cellulose-HNO₃/TiO₂ composite, thus leading to more active photocatalyst.
5. Carbon-Ti composites are achieved by the carbonization processes of the produced functionalized cellulose-TiO₂ and the transformations are related with the stability of the different functionalities.
6. Phosphorus functionalities lead to carbon-Ti composites with flaky structures of Ti-amorphous, since these groups avoid the crystal growth when are carbonized at low

- temperature (500 °C). On the contrary, oxygen functionalities favour the crystal growth and the transformation of TiO₂ into rutile phase.
7. An increase of the carbonization temperature up to 800 °C favours the progressive crystal growth of rutile and the formation of TiP₂O₇ crystals by reaction between the Ti-precursor and the phosphorous functionalities of the cellulose material.
 8. Carbon-Ti composites with both TiO₂ rutile and TiP₂O₇ nanocrystals present a significant band gap narrowing compared to their corresponding pure Ti-phases.
 9. The physicochemical properties of these carbon-phosphorus-Ti composites vary according to the Ti-content and carbonization temperature.
 10. Carbon-phosphorus-Ti composites with anatase TiO₂ nanoparticles and large surface area seem to be the most active photocatalysts for the OG degradation under UV irradiation.
 11. All composites show a better photocatalytic efficiency performance than commercial TiO₂ (P25) for the degradation of orange-G azo-dye in aqueous solutions.
 12. Black titania (non-stoichiometric Ti_yO_x phases) was successfully synthesized by the controlled hydrolysis of a titanium alkoxide under defined atmosphere (8 bar of N₂, or H₂) at 180 °C. These synthesis conditions are softer in comparison with other methods described in bibliography in which temperatures higher than 400 °C or pressures higher than 20 bars are required.
 13. The exceptional photocatalytic behaviour of coloured TiO₂ could be related with the different optimized properties of the samples: i) the stabilization of low crystal sizes (lower than 5 nm) which improves the accessible surface area for the pollutants adsorption and minimizes the electron-hole recombination probability; ii) the strong solar light absorption and band gap reduction and iii) the oxygen vacancies generate positive charge on titania surface improving the electrostatic interaction of Orange G favouring its absorption and degradation.

